Analysis, Design and Control of LCC Resonant Power Converters

Adam John Gilbert

A thesis submitted for the degree of
PhD in the Department of Electronic
and Electrical Engineering, The
University of Sheffield
October 2007

Summary

Through the judicious and efficient use of energy in both domestic and commercial products, the rate at which the world's fossil fuels and mineral resources are depleted, can be minimised, thereby securing energy reserves for the future. This thesis considers a number energy saving roles the power systems engineer can contribute, with specific emphasis on the impact of improving DC-DC power converters for providing significant energy savings. It is shown that by increasing the efficiency of such converters, through the greater use of switched-mode supplies, huge reductions in the production of green house gases can be obtained. Moreover, resonant converters, a specific subset of switched-mode supply, are identified as a candidate technology for future widespread use.

Since the behavioural dynamics of resonant converters are inherently non-linear, the analysis and design of such systems is extremely complex when compared to other families of converter, and has been a critical factor in impeding their widespread adoption. This thesis therefore aims to provide new tools to aid the designer in overcoming such reservations. Novel analysis and design procedures are developed in Chapters 3 and 4, for the series-parallel inductively-smoothed and capacitively-smoothed resonant converters, respectively, which, unlike previously reported techniques, allows a designer with little knowledge of resonant converter systems to readily select preferred components for the resonant tank based on design specifications. Specifically, the analysis in Chapter 3 develops a new methodology that extends 'Fundamental Mode Analysis' (FMA) techniques, and provides a first-order estimate of component values to meet a given specification. Chapter 4 then considers the steady-state behaviour of the converter, from a state-plane perspective, and provides exact component values and electrical stress analyses based on ideal converter characteristics. The presented methodology normalises the converter behaviour, such that the gain of the resonant tank (at the resonant frequency and minimum load resistance), and the ratio between the two tank capacitances, fully characterises the behaviour of the converter as the load is varied and the output voltage regulated. To further aid the designer, various new design curves are presented that makes the use of traditional, and complicated, iterative calculation procedures, redundant. Chapter 5 further develops a high speed transient analysis technique for resonant converters that is shown to provide a 100× reduction in simulation times compared to integration-based methods, by considering only signal envelopes. The technique is shown to significantly aid in the design of variable frequency controllers. Chapters 6 and 7 further consider the control of resonant converters. Specifically, Chapter 6 derives a novel self-oscillating control methodology, which, unlike previously published techniques, approximately linearises the large-signal dynamics of the converter, and thereby readily enables the robust design of an outer-loop controller for output-voltage/-current regulation purposes. Additionally, in contrast to other methods for the robust control of resonant converters, little knowledge of the converter state-variables is required, thereby minimising the number of high-bandwidth sensors necessary. The technique simply requires the real-time polarity of current-flow through the series-inductor, and output-voltage/-current, to be known. Through additional (optional) measurement of supply-voltage and a feed-forward control component, the effects of supply-voltage disturbance are shown to be greatly attenuated, thereby requiring reduced outer-loop control action and improving overall regulation performance. Finally, Chapter 7 considers the control of resonant converters when the cost of isolated feedback sensors is prohibitive. Unlike traditional techniques, where the output-voltage is estimated under fixed load conditions, through use of an Extended Kalman Filter observer scheme, non-isolated measurements are used to estimate both the output-voltage and the load-resistance. The load resistance estimation is then used to aid in fault-detection and for improving transient dynamic behaviour via the provision of feed-forward action, resulting in safer converter operation and enhanced regulation performance, and, ultimately, reduced cost.

All reported results have been qualified through experimental measurements from candidate converters.

The work presented in this thesis has been reported at international conferences and in learned society journals, details of which are given below:

Journals

Gilbert, A. J.; Bingham, C. M.; Stone, D. A.; Foster, M. P.; 'Self-oscillating control methods for the LCC current-output resonant converter', Submitted for publication to the IEEE Transactions on Power Electronics, 2007.

Gilbert, A. J.; Bingham, Stone, D. A.; C. M.; Foster, M. P; 'Normalised analysis and design of LCC resonant converters', Accepted for Publication in IEEE Transactions on Power Electronics, 2007

Gilbert, A. J.; Stone, D. A.; Bingham, C. M.; 'Rapid design of LCC current-output resonant converters with reduced electrical stresses', Electronics Letters, Volume 41, Issue 6, 17 March 2005, pp.365–366

Conferences

Gilbert, A. J.; Bingham, C. M.; Stone, D. A.; Foster, M. P.; 'Design of an LCC current-output resonant converter for use as a constant current source', European Conference on Power Electronics and Applications, CD proceedings paper number 0206, Aalborg 2-5 Sept. 2007

Gilbert, A. J.; Stone, D. A.; Bingham, C. M.; Foster, M. P.; 'Power factor control of the LCC current-output resonant converter', European Conference on Power Electronics and Applications, CD proceedings paper number 0204, Aalborg 2-5 Sept. 2007

Gilbert, A. J.; Bingham, C. M.; Bhangu, B. S.; Foster, M. P.; Stone, D. A.; 'Observer-based output-voltage regulation for 3rd-order LCC resonant converters with significant load variations', European Conference on Power Electronics and Applications, CD proceedings paper number 0625, Dresden, 11-14 September 2005

Gilbert, A. J.; Stone, D.A.; Bingham, C. M.; 'Rapid design of LCC current-output resonant converters with reduced electrical stresses', European Conference on Power Electronics and Applications, CD proceedings paper number 0627, Dresden, 11-14 September 2005

Gilbert, A. J.; Bingham, C. M.; Bhangu, B. S.; Foster, M. P.; Stone D. A.; Howe, D.; 'EKF-based output voltage estimation of 3rd order LCC resonant converters with significant load variations', EPE-PEMC 2004 Conference, CD proceedings, Latvia, 2-4 September 2004

Acknowledgements

I dedicate this thesis to the people I love.
Their support and encouragement was essential.

I thank my supervisors, Chris, Dave and Martin for their friendship, guidance, and the countless hours they dedicated.

I thank my friends in E125, both new and old, for the laughs, coffee-breaks, trips to pound-land, and every distraction imaginable, without which I'd have clearly gone mad.

Most importantly, I thank the love of my life, Brigitte, for her patience.
It's time to spend my life with you @}--'-,----

Table of Contents

Nomenclature

$\hat{X}$	The peak value of variable X
$\bar{x}(t)$	The complex envelope of a generic signal $x(t)$
$\mathbf{\Gamma Q \Gamma}^T, \mathbf{R}, \mathbf{P}_o$	Extended Kalman Filter covariance matrices
$\mathbf{A}_{M_n}, \mathbf{B}_{M_n}, \mathbf{X}_{M_n}, \mathbf{D}_{M_n}$	State-space matrices describing the piece-wise linear converter behaviour during Mode n (M_n)
θ	Phase shift above resonance, degrees
$\Re()$	The real component of ( )
A	Ratio of parallel to series capacitance, $A=C_p/C_s$
A, B, C, D	Generalised state-space matrices
$\mathbf{A_d}, \mathbf{B_d}$	Discrete-time state-space matrices
$\mathbf{A_{filt}}, \mathbf{B_{filt}}$	State-space matrices describing the dynamics of the output-filter
C_e	Effective capacitance, F
C_f, $C_{f\,norm}$	Filter capacitance, F, normalised filter capacitor
C_p, $C_{p\,norm}$	Parallel capacitance, F, normalised parallel capacitor
C_r	Quasi-resonant tank capacitance, F
C_s	Series capacitor, F
D	Duty-cycle
E_s, E_d	Resonant tank stored energy, Energy dissipated to load per cycle, J
$F_1(G_{tr})$	Mathematical function relating the required parallel capacitance to the converter specifications for the capacitively-smoothed converter variant presented in Chapter 4. $C_p = F_1(G_{tr})\frac{1}{N^2 R_L f_r}$
$F_2(A, G_{tr})$	Mathematical function relating the required series inductance to the converter specifications for the capacitively-smoothed converter variant presented in Chapter 4. $L_s = F_2(A, G_{tr})\frac{N^2 R_L}{f_r}$

$F_3(A,G_{tr})$	Mathematical function relating the tank gain at the resonant frequency (G_{tr}) with an applied load resistance R_L to the tank gain (G_{tr_Ro}) at an alternative nominal load resistance R_o, and a factor increase in load resistance $R_x = \frac{R_L}{R_o}$ for the output-voltage variant presented in Chapter 4 $F_3(A,G_{tr}) = R_x F_3(A,G_{tr\_Ro})$ where $F_3(A,G_{tr}) = \sqrt{\frac{F_1(G_{tr})}{F_2(A,G_{tr})}}$
f_m	Switching frequency to resonant frequency scaling factor, $f_s = f_m f_r$
f_{m_max}	The largest theoretical value of f_m that is required to regulate the tank gain at the required G_o, as the load resistance tends to infinity.
$F_n(\ldots)$	Mathematical function n
f_r, f_{r_Ro}	Resonant frequency, resonant frequency for nominal load, Hz
$f_{r\,max}$	The maximum resonant frequency of the converter that occurs when the load is open-circuit, Hz
f_s	Switching frequency, Hz
$G(\omega)$	The overall converter DC/DC gain at switching frequency ω
G_o	DC/DC voltage gain of tank
G_r	Overall converter DC/DC voltage gain at resonance
G_{tr}'	The required tank voltage gain at resonance to compensate for diode voltage drops
G_{tr}, G_{tr_Ro}	Voltage gain of tank at resonance, voltage gain of tank at resonance for nominal load
I_{Lf}	Output-filter inductor current, A
I_{Ls}	Series inductor current, A
$I_{Ls\,norm1}$	Peak series inductor current normalised to that of a sinusoid at resonance
$I_{Ls\,norm2}$	Peak series inductor current normalised to that at full load ($R_L = R_o$)
I_o	Output current, A
I_{o_min}	The theoretical minimum output current the converter supplies when switching at resonance, A
I_s	Excitation source current, A
I_{tp}	Transformer primary current, A

$I_{tp\_rms(fund)}$	RMS value of the fundamental transformer primary current, A
K	Within Chapter 3, this is the ratio of theoretical maximum output-current at resonance (with the minimum specified load resistance) to the theoretical minimum output-current at resonance (during a near open-circuit). Alternatively within Chapter 6, this is the delay factor.
L_r	Quasi-resonant tank inductance, H
L_s , $L_{s\,norm}$	Series inductance, H, normalised series inductance
Mn	Mode *n*
N	Transformer turns ratio
P_{in}	Input power, W
P_o	Power delivered to load, W
P_{out}	Output power, W
P_s	Excitation source supplied power, W
P_{tw}	Power transferred through transformer primary, W
Q	Quality factor
Q_L	Loaded quality factor at corner frequency
Q_{Mn}	Charge transfer through series inductor during mode n
Q_r	The loaded quality factor at resonance
R_{filt}	Equivalent resistance of the output-filter, Ω
R_i	FMA Effective load resistance, in parallel with parallel capacitor C_p, Ω
R_L	Load resistance, Ω
R_L'	Load resistance compensated for diode voltage drops, Ω
R_o	Nominal load resistance, Ω
R_s	Effective load resistance, in series with series inductor L_s, Ω
R_x	Nominal load scaling factor, $R_L=R_xR_o$
t_{Mn}	Time spent in mode *n, s*
T_s, ΔT	Discrete-time sample period
$u(k)$	Discrete-time input vector
V_{Cf}	Output-filter capacitor voltage, V
V_{Cp}	Parallel capacitor voltage, *V*
V_{Cp_rms}	RMS value of the parallel capacitor voltage waveform, V

V_{Cs}	Series capacitor voltage, V
V_d	Diode voltage drop, V
V_{dc}	DC Input voltage, V
V_{Ls}	Series inductor voltage, V
V_o	DC output voltage, V
V_{pp}	Output ripple voltage (peak-peak), V
V_s	Excitation voltage, V
$w(k)$	Discrete-time state vector
$X_{Mn}(t)$	Variable X expressed over the time period corresponding to Mode n
x_r, x_i	The real and imaginary components of a generic signal x
$y(k)$	Discrete-time output vector
z^{-1}, z	Discrete-time unit delay, and unit advance respectively
Z_{K+1}	Extended Kalman Filter, state estimation vector
α	Reciprocal of the estimated load resistance, Ω^{-1}
ω_o	Un-damped natural frequency/corner frequency, rads/s
ω_r	The resonant frequency, rads/s
$\mathbf{\Phi}, \mathbf{\Gamma}, \mathbf{H}, \mathbf{J}$	Discrete-time state-variable system matrices

Chapter 1 - Introduction

1.1 Renewable energy

High on the international political agenda is the mass produced green-house gas carbon-dioxide (CO_2), with numerous near-term legislation being considered as a result of its great impact on global warming. Significant investment into renewable energy sources is required if emissions are to be reduced whilst satisfying the expected doubling in global energy consumption over the next 20 years [1.1]. Within the European Union (EU) community, negotiations are taking place with respect to binding rates of renewable energy to be produced by each country utilising technologies such as photovoltaic, wind turbines and wave power [1.2]. Governments are therefore offering significant incentives and subsidies to encourage renewable development [1.3]. From an alternative perspective, the depletion of North Sea fossil fuel sources has already forced 50% of Europe's energy supply to be imported [1.1]. Increased use of renewable energy will reduce the necessity for such energy imports. Contrary to popular belief, when considering 'protected' national energy reserves, EU countries contain less than 2% of the world's estimated uranium reserve. Nuclear fission is therefore unlikely to be a long term solution [1.1].

As an example of the current energy market, Figure 1.1 shows the United States huge dependence on fossil fuels (86% in 2005). From this division of resources, it can be seen that renewable sources have significant room for encroaching into the market.

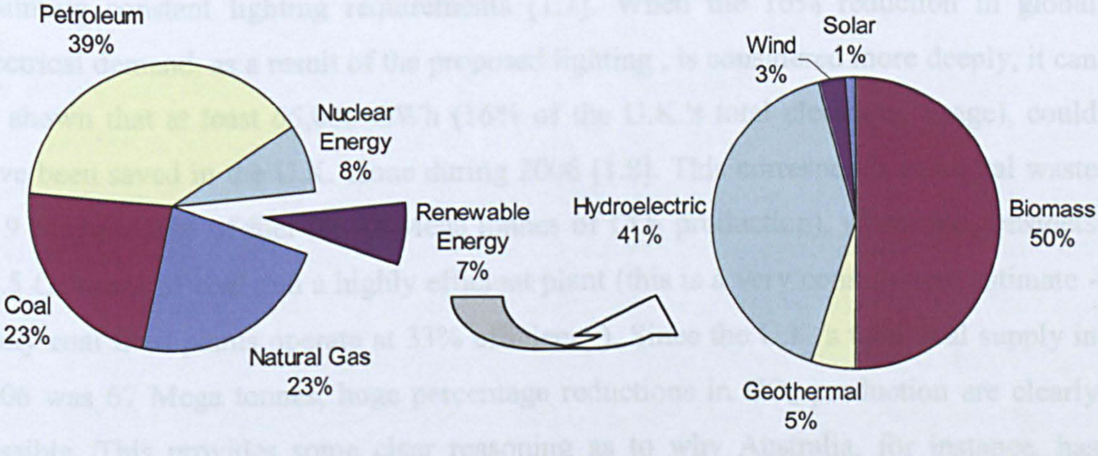

Figure 1.1 - United States energy sources 2005 [1.4]

Although currently providing only a small proportional of the energy quota, the global wind power market is expanding faster than any other alternative renewable source. From 4.8GW in 1995 to 59GW in 2005, the market has on average, enjoyed 28% annual growth [1.1]. Solar energy, on the other hand, is seen to offer the most promise. Solar panel technology is mature, and, under lab conditions can achieve a 20% energy conversion efficiency. In Germany, households are encouraged to install solar panels to supplement their energy needs and sell excess to the domestic market at a government specified premium rate [1.5]. This strategy is likely to be repeated in other countries in due course. To maximise the overall renewable energy supply, however, high efficiency inverter circuits are required to couple the renewable source to the AC supply. Improvements in semiconductor switches, such as reducing MOSFET R_{ds}(on), IGBT tail loss, or diode forward voltage drop, are integral to the more widespread use of renewable sources. Fortunately, improvements in semi-conductor devices are occurring rapidly, for example, with typical on-state resistances R_{ds}(on) of a MOSFET falling by 75% between the years 2000 and 2005 [1.6].

1.2 Energy usage

Lighting

Reducing overall energy requirements, and consumption, is likely to result in the greatest impact on CO_2 production. Lighting, for example, consumes around 20% of the world's total electrical energy demand. Replacing incandescent lamps with fluorescent lamps containing an electronic ballast would reduce this figure to approximately 4% assuming constant lighting requirements [1.7]. When the 16% reduction in global electrical demand, as a result of the proposed lighting , is considered more deeply, it can be shown that at least 65,000 GWh (16% of the U.K.'s total electricity usage), could have been saved in the U.K. alone during 2006 [1.8]. This corresponds to a total waste of 9 Mega tonnes of fuel (or 33 Mega tonnes of CO_2 production), when one considers 25.5 GJ/tonne of coal and a highly efficient plant (this is a very conservative estimate - many coal fired plants operate at 33% efficiency). Since the U.K.'s total coal supply in 2006 was 67 Mega tonnes, huge percentage reductions in CO_2 production are clearly possible. This provides some clear reasoning as to why Australia, for instance, has announced plans to ban incandescent bulbs by the year 2010 [1.9].

Vehicle fuel

The consumption of vehicle fuel also has a direct impact on CO_2 emissions. The automobile industry is currently undergoing a revolution as a direct result of the European Commission imposing a mandatory limit on carbon dioxide emissions for new cars to 130g/ km by 2012, from the 162g/km figure in 2005 [1.10]. To meet the new targets, cars simply have to burn less traditional fuel. Methods such as improving aerodynamic performance, reducing weight, engine design and using alternative fuels are under investigation. Classical 4-stroke (Otto cycle) based piston engines convert approximately 33% of the energy contained in the fuel to mechanical energy (note that additional frictional losses reduce the overall car efficiency to the 10-20% range). New engine designs such as those currently under development by "The Scuderi Group", the Scuderi Split-Cycle Engine [1.11], can improve this to almost 40% whilst reducing toxic emissions by as much as 80%. Hybrid cars take another approach, a hybrid car such as the Toyota Prius, Figure 1.2, combines both an engine (Atkinson cycle based) with a motor/generator.

Figure 1.2 - Toyota Prius - reproduced from online brochure at www.toyota.com

The mechanical energy produced by the engine is converted to electrical energy, then, via a number of inverter stages and an energy storage unit, is used to drive an electric motor/generator. As well as using traditional braking methods, the Prius uses regeneration, in which energy is recovered, via the generator, and temporarily stored for later use in a battery bank. The overall car efficiency is greatly increased, and thus has an emission value of 104g/km, well under the 2012 limit. Power electronics account for around 20% of the hybrid drive system cost [1.12] and since semiconductor losses are of utmost importance in minimising energy losses, Toyota is currently a world leader in Silicon Carbide (SiC) device research. In 2004, Toyota announced a massive breakthrough in SiC material growth, producing virtually defect free wafers and making ultra-high current devices feasible for the first time [1.13]. As a result, the worldwide market for SiC devices is expected to increase to $54 million in 2009 from the $14 million in 2004, corresponding to a 25% annual growth. Interestingly, semiconductor devices based on diamond are also gaining interest as a result of the material's extreme properties and recent developments of high purity single crystal chemical vapour deposition (CVD) diamond [1.14]. Diamond based Schottky diodes potentially offer much higher breakdown voltages (as a result of their large band-gap) than either the currently available 1200V SiC devices, or the ~200V theoretical limit of silicon devices [1.15]. Diamond therefore offers the potential for Schottky barrier diodes ~30 times thinner, in terms of semi-conductor usage, than that of silicon, resulting in lower on-state voltage drops (even than SiC), reduced stored charge, faster switching speeds, and the best thermal conductivity of present technologies [1.16]. Numerous AC-DC power converters are present in Hybrid vehicles. The global AC-DC supply market is forecast to grow from $9.5 billion in 2004 to $12.5 billion in 2009 implying a compound annual growth rate of 5.9% [1.17]. Power converter efficiency savings in this market can therefore provide significant environmental benefit.

Standby electricity

Reducing standby electricity is also of significant in-home and commercial importance. Current estimates indicate that 5% of residential electricity usage in large western countries is accounted for by standby power. Standby power is defined as the power an appliance uses during its least energy consuming mode of operation [1.18]. Maintaining signal reception (as in a cordless telephone), monitoring temperature (as in a refrigerator), powering an internal clock, or charging a battery are all typical uses of stand-by power. Through the use of digital control and advanced power management these losses can be significantly reduced whilst maintaining similar functionality. The inclusion of a Phillips I^2C based power management bus (PMbus) within distributed power networks, for example, provides a methodology for the control of point of load (POL) converter output-voltage levels according to real-time system requirements [1.19]. Within a modern LCD or plasma television, if a distributed network were implemented with power managed POLs, all systems could be shut down with the exception of those providing energy to the remote control interface, clock, and similar constantly running features. Additionally, an interesting concept is the cost of ownership "knowing that most DC-DC converters and regulators are operated in the range of 40 to 70% of the maximum specified by manufacturers, efficiency improvements at lower load levels have a direct impact on the total cost of ownership" [1.20]. The cost of the energy used to supply the hardware over a lifetime may indeed approach or exceed that of the hardware itself. The efficiency of DC-DC converters is, therefore, of great importance [1.20]. As an example, there are approximately 10 billion electronic power supplies worldwide. The typical efficiency of these supplies lies within the 30% to 60% range. The energy loss associated with these supplies amounts to some 350 to 480 GWhrs/year, representing a loss of approximately 2% of the total worlds electricity usage (16.4 TWhrs/year in 2004 [1.21]). Increasing the average efficiency of these supplies by 10%, for instance, would reduce the energy lost by these devices by 40 GWhrs/year, which is the typical yearly output of 4 to 6 generating plants [1.22].

1.3 Regulating power supplies

From the various discussions thus far it can clearly be seen that power electronics can play a significant role in a large number of CO_2 emission reducing activities.

This thesis specifically considers DC-DC power conversion, with the goals of improved design and control techniques for better efficiency, reduced component count, mass and volume.

Regulating power supplies are integral to virtually all electronic equipment. Prior to the development of fast, high voltage power switching transistors, in 1967 [1.23], almost all power supply units (PSUs) were based on linear regulators, where load current is limited by a transistor to maintain the desired output voltage. This method results in large inefficiencies when supply and load voltages are dissimilar. Often, a bulky mains transformer would be employed prior to the linear regulator when stepping voltages down by a large factor. The aerospace industry, where high power density and efficiency are of paramount importance, provided the main drive for the use of switched-mode power supply (SMPS) counterparts [1.24]. They are now in almost all cases the PSU of choice. The large number of new 'must have' consumer products that arrive on the market goes some way to explaining the very high rate at which the SMPS market is growing. The SMPS global market forecast by Frost & Sullivan, is expected to be worth $15.6 billion in 2008 compared to $10.2 billion in 2002 [1.25].

The changing market demands placed on the PSU designer require constant innovation. For instance, the International Technology Roadmap for Semiconductors 2006 [1.26] predicts that by the year 2020, CPU voltages will have decreased to 0.5V from the current minimum of 1.1V, while peak power requirements will have increased to 198W. Maintaining efficiency at such low voltage levels will be a difficult challenge.

Unfortunately in this respect, for the PSU designer, parasitic capacitances inherent in power switching devices require charging and discharging for a switching event to be completed. Since the instantaneous power dissipated within a component is equal to the applied volt-amp product, the slowly changing switching-voltage waveform, coupled with a non-zero switching-current, as in the case of hard-switched converters, results in switching-loss. The benefits of soft-switching can be achieved through shaping of the current and voltage waveforms through and across the power switch, respectively, such that either zero-voltage (ZVS) and/or zero-current switching (ZCS) of the power devices can occur at the switching events, thereby reducing stresses, power-loss, and radiated electro-magnetic interference (EMI). Figure 1.3 provides an example of current and voltage loci for both hard-switched and soft-switched converters. The figure demonstrates the energy saving per switching cycle that can be achieved using soft-switching of the power devices.

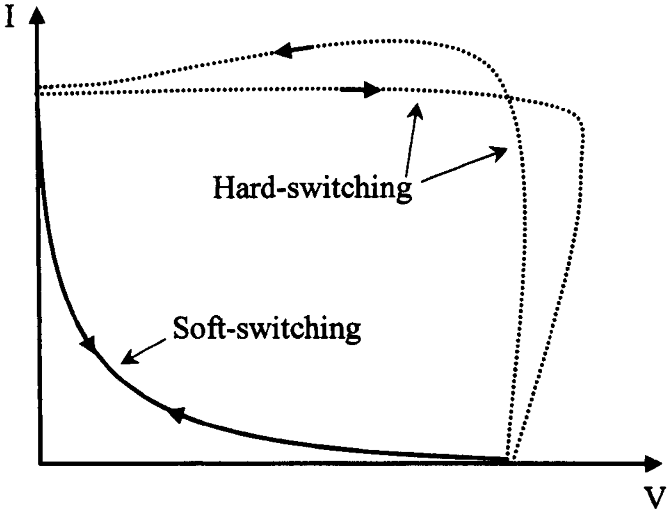

Figure 1.3 - Hard-switching and Soft-switching current/voltage loci

Many topologies of switched-mode power supply are available to the designer, each having their relative merits. Figure 1.4 provides the interrelationships between various configurations.

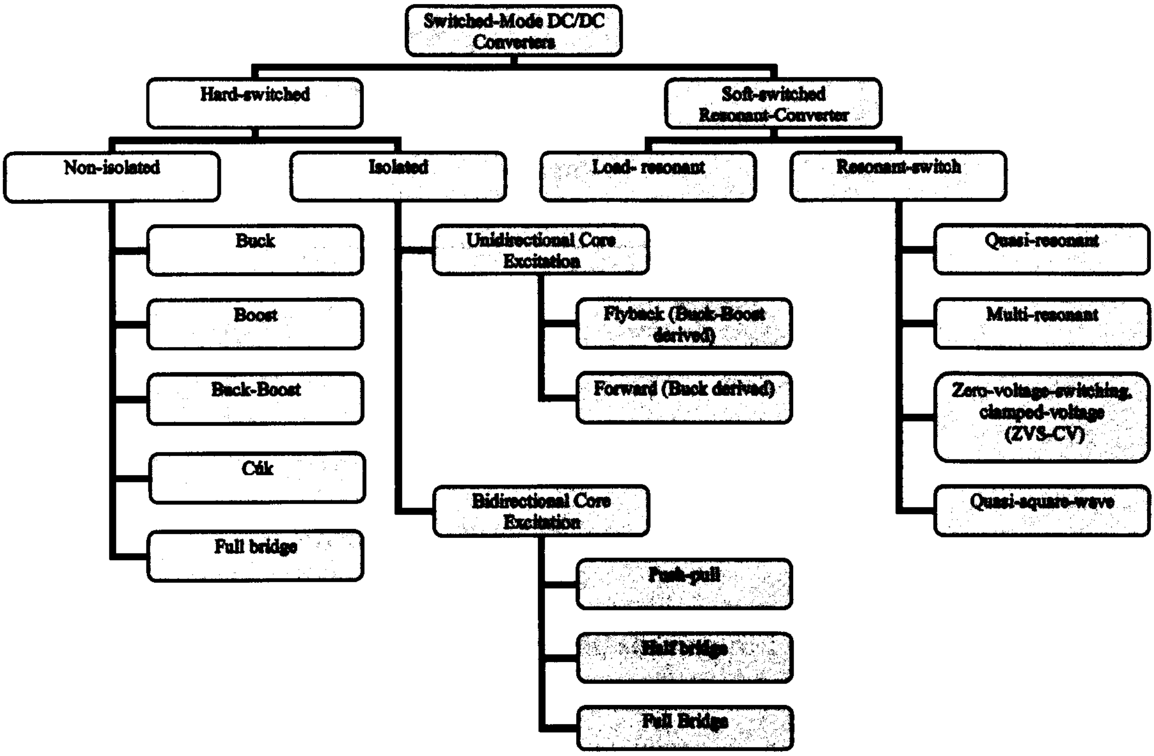

Figure 1.4 - Various converter topologies and their interrelationships

The ultimate choice of topology is based on isolation requirements, cost, power-level, efficiency, size, component stresses and controller complexity and reliability.

As an introduction to switched-mode DC-DC power conversion, the following section demonstrates how a reduction in supply-voltage can be achieved without the losses associated with linear regulators. For simplicity, the behaviour of commonly used hard and soft-switched converter topologies is presented. It should be noted that, for use in switched-mode power converters, the power-devices are never used in their linear operating region; they are either fully on or off.

Buck converter (Hard switched)

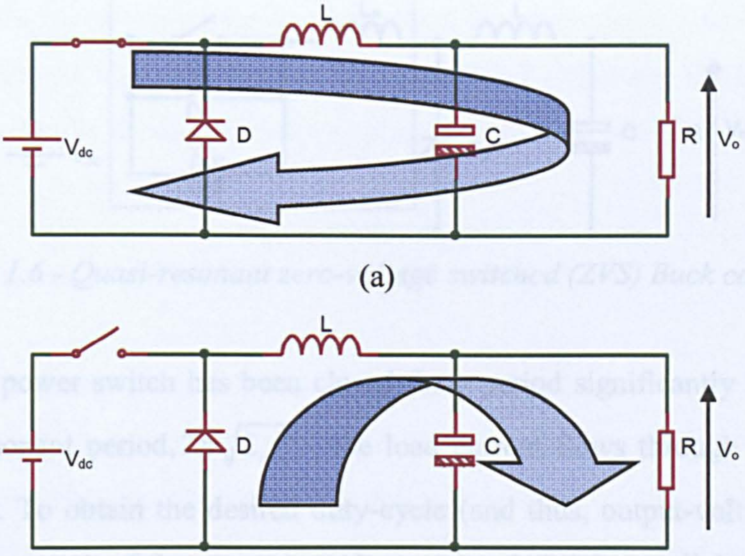

(a)

(b)

Figure 1.5 - Behaviour of a Buck converter

At steady-state, when the switch is turned on, see Figure 1.5(a), V_{dc} reverse biases the diode. The current flowing in the inductor increases linearly as the supply provides energy to the inductor, filter capacitor and load. When the switch is turned off, see Figure 1.5(b), the inductor current circulates through the (now) forward-biased diode. During this period, the inductor current and output capacitance support the output-voltage.

The output-voltage is related to the supply voltage and duty-time (*D*) of the power switch as follows:

$V_o = V_{dc} D$, where V_{dc} and V_o are the input and output voltages, respectively. (1.1)

Quasi-resonant zero-voltage switched (Soft switched)

With any of the hard-switched topologies (specifically the Buck, Boost, Buck-boost, and Cúk configurations) the power switch can be replaced by a resonant-switch power circuit through the addition of a resonant tank consisting of an inductor and capacitor, L_r and C_r, respectively, see Figure 1.6.

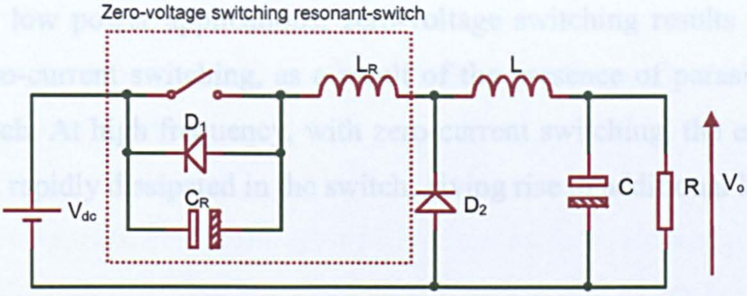

Figure 1.6 - Quasi-resonant zero-voltage switched (ZVS) Buck converter

Assuming the power switch has been closed for a period significantly longer than the un-damped resonant period, $2\pi\sqrt{L_r C_r}$, the load current flows through the switch and both inductors. To obtain the desired duty-cycle (and thus, output-voltage) the switch opens, and, as a result of the resonant tank capacitor being in parallel with the switch, zero-voltage turn off occurs i.e the voltage across the switch is held constant at approximately zero during the switching period by the requirement to charge the capacitor. Current flow occurs momentarily through the resonant capacitor, resonant inductor, and output filter inductor. The voltage across the resonant capacitor increases linearly to V_{dc} as a result of the near constant current being supplied (i.e $V_{Lr}=0$), at which point diode D_2 becomes forward biased. The resonant inductor and capacitor then resonate, the resonant inductor current falling rapidly to a peak below zero before returning to 0A. Note that just before the current reaches 0A, the resonant capacitor becomes fully discharged and the voltage is clamped to 0V as a result of D_1. When current begins to flow through D_1 the switch is turned on once again (zero-voltage switched), and the resonant inductor current linearly increases to the output-current. The off-period of the switch is therefore specified by the choice of resonant tank. The on-period, however, can be varied, thereby enabling almost-linear output voltage/current control. Note that during the majority of the switch off period, diode D_2 is forward-biased, hence, no voltage is applied to the output-filter. Additionally quasi-resonant ZVS converters cannot utilise transformer parasitics. Transformer parasitic utilisation is a very desirable characteristic for power converters since it enables a converter size reduction, and may reduce component count. As discussed later in this chapter, transformer parasitic utilisation is one of the main characteristics of resonant power converters.

In general, for low power applications, zero-voltage switching results in much lower losses than zero-current switching, as a result of the presence of parasitic capacitance across the switch. At high frequency, with zero-current switching, the energy stored in the capacitor is rapidly dissipated in the switch, giving rise to additional loss.

1.4 Synchronous rectification

To improve efficiency in switched-mode supplies, synchronous rectification is now commonplace, where diodes are replaced with high performance MOSFETs, and the power-device switched appropriately to minimise forward on-state voltages to values typically in the range of 50mV to 200mV [1.27]. To simplify the burden of accurate MOSFET turn on and off times, International Rectifier, for instance, have developed the IR1167 IC for automatic switching. The IR1167 measures the drain-source voltage, detects when the body diode begins to conduct and turns on the MOSFET [1.28]. Similarly, ON Semiconductor is developing a device that combines a MOSFET, gate driver, and body-diode conduction sensing circuitry, in a single discrete package [1.27]. Such devices are expected to greatly simplify the future implementation of synchronous rectification by reducing component count and avoiding patent infringement. Although this thesis aims to improve switched-mode power converter efficiency and promote their widespread use, for simplicity, synchronous rectification is not considered further as the technique increases component count and design complexity. Moreover, through the use of the IR1167, implementation of the technique is made trivial. Efficiency improvements prior to synchronous-rectification, via the appropriate selection of components and improved control design, are therefore considered to be of primary importance for this study.

1.5 Resonant converters

Here then, this thesis focuses on a sub-set of resonant converter, specifically load resonant power converters. As a result of their near sinusoidal current waveforms and utilisation of transformer parasitics, they can provide a more compact, power dense/efficient solution than other soft- and hard-switched counterparts, with reduced EMI characteristics [1.33]. For a given switching-loss (implying equivalent heat-sinking requirements), resonant converters are capable of higher switching frequencies, thereby improving power-density compared to other switching topologies, by virtue of requiring smaller reactive components.

However, whilst resonant converters are widely reported to be advantageous in terms of efficiency, EMI and power-density, they possess highly non-linear behaviour and are therefore difficult to analyse, design and control. Moreover, analysis and design methodologies are also uniquely defined by choice of resonant tank configuration, with a very large number of tank configurations being realisable. For instance, with 3 resonant tank elements, 38 possible topologies have been identified [1.29], and with 4 elements, 182 realisable topologies [1.30]. Although many of these topologies are unattractive in terms of circuit behaviour during open- and short-circuit load conditions, a large number are still commercially attractive. Traditionally, designers of resonant converters have largely confined themselves to a 4th order $L_sC_sL_pC_p$ tank configuration, see Figure 1.7, since the tank closely models the parasitic components of a high frequency transformer. Popular lower order converters such as the series-resonant (L_sC_s), parallel-resonant, (L_sC_p), series-parallel resonant ($L_sC_sC_p$), and $L_sC_sL_p$ converter, are obtained, by eliminating various reactive components from the generic 4th order tank. As an example, the magnetising inductance of the transformer, in certain cases, may be assumed sufficiently large to be removed from the model. Alternatively, the inter-winding capacitance of a high-voltage transformer may be significant, thus requiring either the parallel-resonant or series-parallel resonant topologies to fully exploit the transformer parasitics, as opposed to reducing the capacitance's impact by the addition of further inductance. As a result, the series-parallel and parallel-resonant topologies are well suited to applications such as arc-striking or ozone-generation systems [1.39]. The $L_sC_sL_p$ converter, on the other hand, can incorporate the effects of both the leakage- and mutual- inductance of a transformer. Moreover, when dual output voltages are required without additional secondary windings, only those topologies incorporating a parallel-inductor (L_p) are suitable [1.31-1.32].

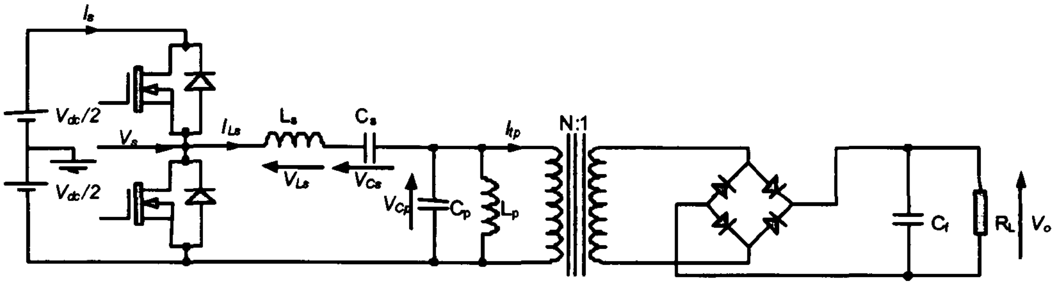

Figure 1.7 - Resonant converter based on the LCLC resonant tank.

The various topologies of resonant converters have well documented relative merits [1.33-1.34]. For instance, the circulating current within a series-resonant converter decreases with reduced load power and the series-capacitor 'blocks' DC voltages being applied across the transformer. It does, however, suffer from the inability to regulate the output-voltage during no load conditions, and provides a maximum tank gain of a half, at the resonant frequency. The parallel-resonant topology is reported to possess inherent short-circuit protection and a tank gain, at resonance, that can far exceed that of the series-resonant converter. Unfortunately, it can also suffer from high circulating currents that are relatively independent of load, and requires bi-polar switching. Nevertheless, through use of the series-parallel resonant topology, all the advantages of the series-resonant and parallel-resonant converters can be combined with none of their respective disadvantages. The $L_sC_sC_p$ (series-parallel) resonant-converter topology, Figure 1.8, is therefore considered a particularly attractive variant for systems where high-efficiency via a reduction in circulating currents, output voltage/current regulation, low component count, inherent short-circuit protection and a voltage boost capability, is required. It is therefore chosen as the focus for the research presented here in this thesis.

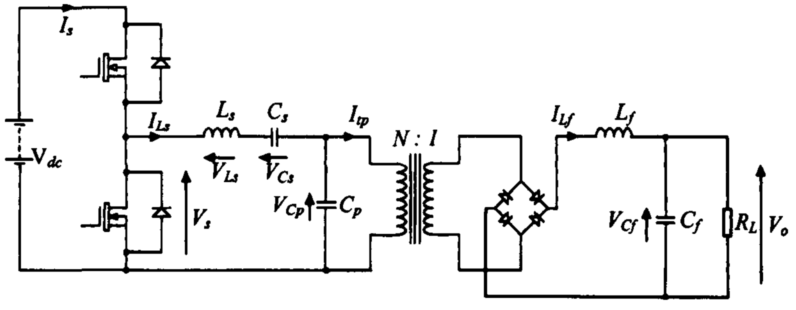

Figure 1.8 - Resonant converter based on the $L_sC_sC_p$ resonant tank. The inductively-smoothed variant is shown. Removing the output-filter inductor L_f results in the capacitively-smoothed variant.

For the benefit of the reader, a basic introduction to the operation principles of the LCC resonant converter is now given.

As with any other DC-DC converter topology, whether hard- or soft-switched, the supply-voltage of the LCC resonant converter is effectively modulated and then rectified. Modulation is achieved through use of either a full-bridge or half-bridge switching network. Via the intermediate resonant tank, between the modulation and rectification stages, resonant converters possess an inherent input/output gain that is a function of excitation frequency. Control of the switching frequency therefore allows for output-voltage/-current regulation, since the switching frequency (and loading conditions) determines the magnitude of the ac waveforms applied to the input of the rectifier. Two distinct topologies for the LCC resonant converter are available. These are the inductively-smoothed and capacitively-smoothed variants; see Figure 1.8 and Figure 1.9, respectively. When comparing the two topologies, the inductively-smoothed variant (Figure 1.8) is seen to include an additional inductor in the output filtering stage.

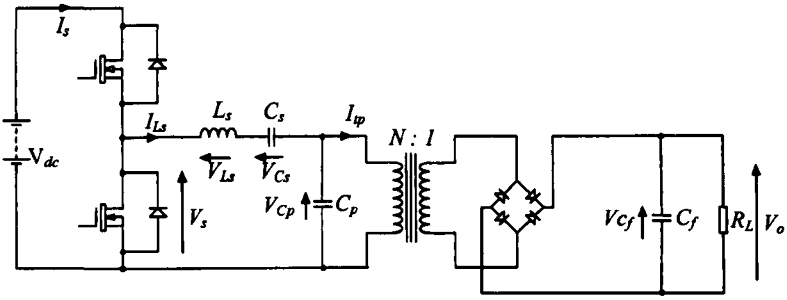

Figure 1.9 - LCC capacitively-smoothed resonant converter

Although this is a subtle difference, the behaviour, and thus the analysis of the converter, is significantly different for the two topologies. For the inductively-smoothed converter (Figure 1.8), the rectifier current or transformer primary current (I_{tp}) can be assumed to take on a squarewave characteristic (since L_f is sufficiently large to support the output current during a full switching cycle) and the parallel capacitor voltage (V_{Cp}) a sinusoidal characteristic, see Figure 1.10. The capacitively-smoothed converter, by contrast, as a result of the voltage-clamping behaviour of the rectifier, has a rectifier current (I_{tp}) that follows the series-inductor (L_s) current during rectifier-conduction periods, and is 0A at other times, see Figure 1.11. The parallel-capacitor voltage for this topology is generally trapezoidal in shape, with the rise and fall times corresponding to the charging of the parallel-capacitor via the series inductor-current, see Figure 1.11.

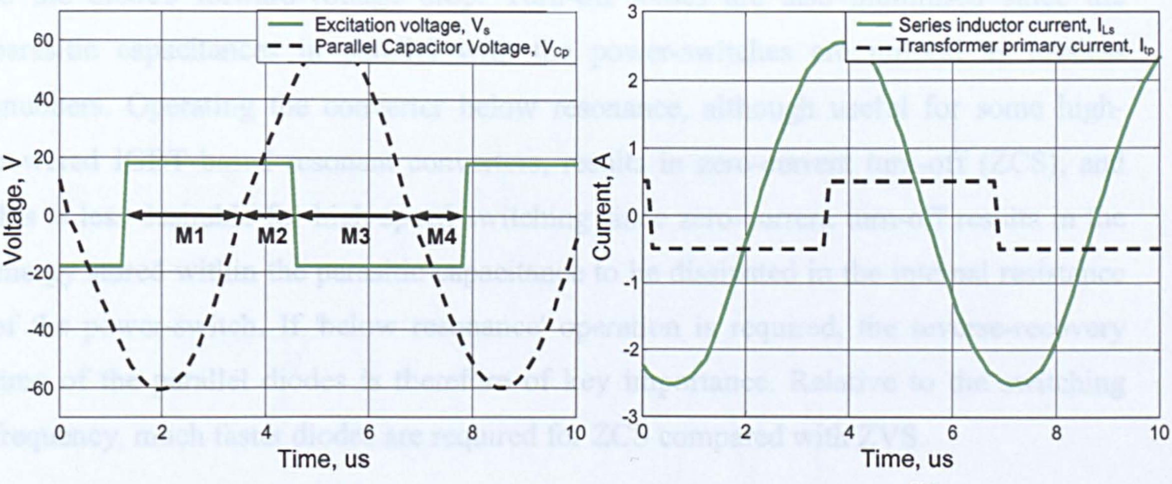

(a) (b)

Figure 1.10 - Typical inductively-smoothed topology waveforms (a) voltages (b) currents

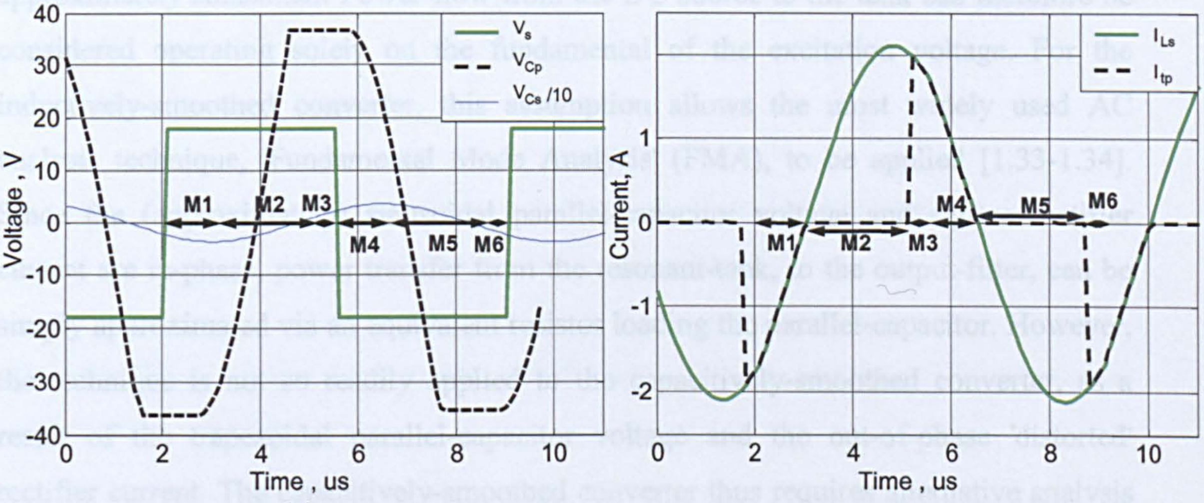

(a) (b)

Figure 1.11 - Typical capacitively-smoothed topology waveforms (a) voltages (b) currents

Note that the operation is subdivided into various modes (M1..M6) of operation which are discussed later.

Resonant converters are generally operated above the resonant frequency to facilitate zero-voltage switching of the power-devices. When operating above resonance, the series-inductor current (I_{Ls}) lags the excitation voltage (V_s) (see Figure 1.11 for instance), hence, when a power-switch is turned on, current is already flowing through the device's reverse biased diode, thereby clamping the voltage across the power-switch to the diode's forward-voltage drop. Turn-off losses are also minimised since the parasitic capacitances in parallel with the power-switches are utilised as lossless snubbers. Operating the converter below resonance, although useful for some high-powered IGBT based resonant converters, results in zero-current turn-off (ZCS), and this is less desirable for high-speed switching since zero-current turn-off results in the energy stored within the parasitic capacitance to be dissipated in the internal resistance of the power-switch. If 'below resonance' operation is required, the reverse-recovery time of the parallel diodes is therefore of key importance. Relative to the switching frequency, much faster diodes are required for ZCS compared with ZVS.

Resonant converters are generally designed to possess a high-quality factor (Q), implying that, as a result of the resonant-tank filtering, the series-inductor current is approximately sinusoidal. Power-flow from the DC source to the tank can therefore be considered operating solely on the fundamental of the excitation voltage. For the inductively-smoothed converter, this assumption allows the most widely used AC analysis technique, 'Fundamental Mode Analysis' (FMA), to be applied [1.33-1.34]. Since the (approximately) sinusoidal parallel-capacitor voltage and square rectifier current are in-phase, power transfer from the resonant-tank, to the output-filter, can be simply approximated via an equivalent resistor loading the parallel-capacitor. However, the technique is not so readily applied to the capacitively-smoothed converter, as a result of the trapezoidal parallel-capacitor voltage and the out-of-phase 'distorted' rectifier current. The capacitively-smoothed converter thus requires alternative analysis techniques to be applied, such as 'Rectifier transformed fundamental analysis' (RTFMA), in which a more complex AC model of the rectifier is generated [1.35].

1.6 Fundamental mode analysis of resonant converters

Since FMA and the resulting equations is used as a benchmark for comparison of the analysis and modelling methods presented throughout the remainder of the thesis, a summary introduction is now given for the benefit of the reader. Figure 1.12 illustrates how the FMA procedure is used to derive an equivalent parallel-capacitor loading resistance for the LCC inductively-smoothed converter and thus demonstrates how to calculate an approximate DC/DC gain for the converter. The 'sinusoidal' voltage across the parallel capacitor (C_p) is applied to the input of the full-bridge rectifier, via a transformer. The output voltage of the rectifier (V_f), which feeds the output-filter, is therefore a full-wave rectified sinusoid, with an average value expressed as follows [1.33]:

$$V_f(avg) = \frac{2}{N\pi}\hat{V}_{Cp} = \frac{2\sqrt{2}}{N\pi}V_{Cp\_rms} = V_o \tag{1.2}$$

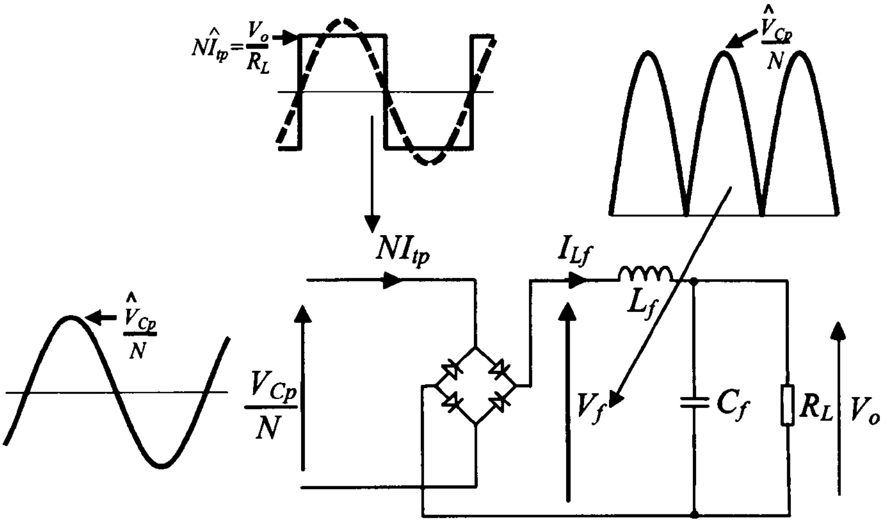

Figure 1.12 - FMA technique depicted graphically for calculation of equivalent load resistance

The rms value of the squarewave transformer primary current (I_{tp}) fundamental component is calculated as:

$$I_{tp\_rms(fund)} = \frac{1}{N}\frac{4}{\pi}\frac{V_o}{R_L}\frac{1}{\sqrt{2}} = \frac{2\sqrt{2}V_o}{N\pi R_L} \tag{1.3}$$

The equivalent load resistance applied in parallel with C_p is therefore calculated from (1.2),(1.3) to be:

$$R_i = \frac{V_{Cp\_rms}}{I_{tp\_rms(fund)}} = \frac{N\pi V_o}{2\sqrt{2}}\frac{N\pi R_L}{2\sqrt{2}V_o} = \frac{N^2\pi^2 R_L}{8} \tag{1.4}$$

As discussed later, the basic analysis presented in this chapter is only valid if the 'Q' factor at the loaded resonant frequency is sufficiently large (Q_r>2.5) to ensure a sufficiently sinusoidal series-inductor current.

The resulting FMA equivalent circuit of the LCC inductively-smoothed converter is therefore shown in Figure 1.13.

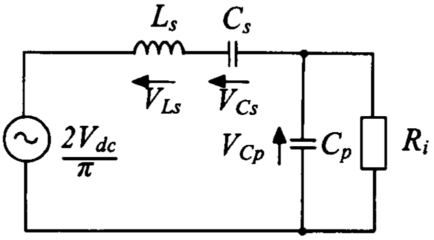

Figure 1.13 - FMA equivalent circuit of an LCC inductively-smoothed resonant converter

An alternative FMA equivalent circuit is provided in Figure 1.14, which is useful when calculating the Q factor and damped resonant frequency of the converter. The parallel branch in Figure 1.13 is transformed into an equivalent series branch, generating a standard series LCR circuit. The equivalent components R_s and C_e are dependent on switching frequency.

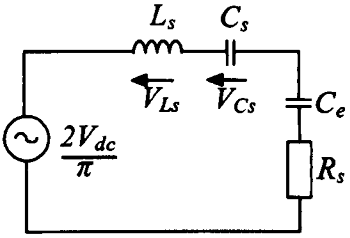

Figure 1.14 - Alternative FMA equivalent circuit of an LCC inductively-smoothed resonant converter

The equivalent resistance R_s and capacitance C_e are found from [1.34]:

$$R_s = \frac{R_i}{(R_i \omega_s C_p)^2 + 1}\ ,\ C_e = C_p\left(1 + \frac{1}{(R_i C_p \omega_s)^2}\right) \tag{1.5}$$

The loaded quality-factor at the un-damped natural resonant frequency (ω_o), is defined as:

$$Q_L = \omega_o\left(\frac{C_s C_p}{C_s + C_p}\right)R_i = \omega_o\left(\frac{C_p}{1+A}\right)R_i, \tag{1.6}$$

where $\omega_o^2 = \frac{1+A}{L_s C_p}$ and $A = \frac{C_p}{C_s}$

The gain of the converter can be most readily extracted via analysis of the circuit in Figure 1.13.

The voltage gain between the ac supply, and parallel-capacitor can be found from:

$$G = \frac{Z_p}{Z_s + Z_p}, \tag{1.7}$$

where Z_s is the impedance of the series branch consisting of L_s and C_s

and Z_p the impedance of the parallel branch consisting of C_p and R_i

Eliminating the series-inductance and series-capacitance from the expressions via (1.6) gives:

$$L_s = \frac{1+A}{\omega_o^2 C_p},\ C_s = \frac{C_p}{A} \tag{1.8}$$

Then, eliminating the parallel-capacitance via:

$$C_p = \frac{Q_L(1+A)}{\omega_o R_i} \tag{1.9}$$

results in

$$\left|\frac{\hat{V}_{Cp}}{V_{dc}}\right| = \frac{2}{\pi\sqrt{(1+A)^2\left(1-\left(\frac{\omega}{\omega_o}\right)^2\right)^2 + \frac{1}{Q_L^2}\left(\frac{\omega}{\omega_o} - \frac{\omega_o A}{\omega(1+A)}\right)^2}} \tag{1.10}$$

which depends on 3 normalised values (A, ω_o, Q_L). Note that it is expressed in magnitude form i.e the expression is no longer complex.

To obtain the gain between the dc input voltage and output voltage, Figure 1.12 can be considered. The output-voltage is the average of the full-wave rectified secondary referred parallel-capacitor voltage, as follows:

$$V_o = \frac{2}{N\pi}\hat{V}_{Cp} \tag{1.11}$$

giving:

$$\frac{V_o}{V_{dc}} = \frac{4}{N\pi^2\sqrt{(1+A)^2\left(1-\left(\frac{\omega}{\omega_o}\right)^2\right)^2 + \frac{1}{Q_L{}^2}\left(\frac{\omega}{\omega_o} - \frac{\omega_o A}{\omega(1+A)}\right)^2}} \tag{1.12}$$

These underlying equations will be used copiously throughout the remainder of the thesis.

1.7 Summary

For environmental and economic reasons, it is vital that power conversion efficiency is maximised. With respect to DC-DC conversion, resonant converters offer the greatest potential as a result of their increased power-density as a result of transformer parasitic utilisation, soft-switching, low EMI and high-frequency operation.

The design of resonant converters, however, is generally a time consuming process, resulting from the many protracted time-domain simulations that are traditionally required. Circuit-approximations, such as the fundamental mode approximation (FMA), are typically used to provide an estimation of the required component values, which are then 'tuned', iteratively, to meet the required specifications when parasitic components are present. Component based analysis packages, such as SPICE [1.36], SABER [1.37] and PLECS [1.38] are often utilised in this process. The lack of literature on robust techniques for resonant converter control also makes many PSU designers reluctant to take advantage of the technology.

Here then, in Chapter 3, an alternative procedure for the design of the LCC inductively-smoothed converter, is presented, that greatly simplifies the complex calculations required for initial proto-type component selection. The aim being to give the designer, whether experienced in resonant converter design, or otherwise, an initial estimate of component values to realise a converter that operates close to the desired specification. Specifically, (1.12) from the FMA procedure previously presented, is used at the resonant frequency, to provide component values for a given set of converter specifications.

Further chapters then consider the design of the LCC capacitively-smoothed variant (Chapter 4), a high speed transient analysis technique for controller design purposes (Chapter 5), and an alternative control technique that (through linearization of the converter's large-signal behaviour) allows simple robust control techniques to be applied (Chapter 6). Finally, the control of resonant converters via nonlinear state-estimation techniques, for cost reduction purposes (Chapter 7), is considered.

To summarise, this thesis aims to improve present analysis, design and control techniques for the series-parallel resonant converter, such that they can be more readily and widely employed. It should be noted, however, that many of the developed techniques presented in the thesis are ultimately more widely applicable to other converter variants.

1.8 References

[1.1]Power Electronics Europe, 'Power Generation and Power Management', November 2006, ISSN: 1748-3530, pp.5

[1.2]Bodo's power systems, Systems Design Motion and Conversion, 'Power Electronics Engineers Needed', April 2007, www.bodospower.com, ISSN: 1863-5598, pp.10

[1.3]Power Electronics Europe, 'More Power Electronics in Renewable Energies', Issue 8, 2005, ISSN: 1748-3530, pp.5

[1.4]Energy Information Administration - Official Energy Statistics from the U.S. Government http://tonto.eia.doe.gov/FTPROOT/renewables/062805.pdf

[1.5]Power Electronics Europe, 'Inverting Energy Concerns by Efficient Design', November 2006, ISSN: 1748-3530, pp.7

[1.6]Power Electronics Europe, 'How to Make a Power Supply Smaller and Cooler', Issue 2, 2005, ISSN: 1748-3530, pp.24

[1.7]Power Electronics Europe, 'Better Times for Power Electronics', p.5, Issue 6, October 2006, ISSN: 1748-3530

[1.8]UK Department for Business Enterprise & Regulatory Reform Energy statistics, 'Electricity supply and consumption', http://www.dti.gov.uk/energy/statistics/source/electricity

[1.9]BBC News, 'Australia pulls plug on old bulbs', February 2007

[1.10]BBC News, 'MEPs back car CO2 emissions cuts', July 2007

[1.11]The Scuderi Group
http://www.scuderigroup.com/technology/the_technology.html

[1.12]Power Electronics Europe, 'On the Road to Better Fuel Efficiency', March 2007, ISSN: 1748-3530, pp.2

[1.13]Power Electronics Europe, 'Power Electronics and Hybrid Cars', Issue 7, 2005, ISSN: 1748-3530, pp.5

[1.14]Isberg. J.; Hammersberg. J.; Johansson. E.; Wikstrom. T.; Twitchen. D.J.; Whitehead. A.J.; Coe. S.E.; Scarsbook. G.A.; 'High carrier mobility in Single-Crystal Plasma-Deposited Diamond', Science, Vol.297, Sept. 2002, pp.1670-1672

[1.15]Power Electronics Europe, 'Power Electronics Saves Electrical Power', August 2006, ISSN: 1748-3530, pp.5

[1.16] Power Electronics Europe, 'Single Crystal Diamond Applied to Schottky Diodes', , August 2006, ISSN: 1748-3530, pp.26

[1.17]Power Electronics Europe, 'Power supply market growth', Issue 2, 2005, ISSN: 1748-3530, pp.12

[1.18]Lawrence Berkeley National Laboratory, 'Standby Power FAQ',
http://standby.lbl.gov/faq.html

[1.19]Power Electronics Europe, 'Integrated Digital Power Conversion for New Communication Systems', Issue 1, 2005, ISSN: 1748-3530, pp.19

[1.20]Power Electronics Europe, 'From Digital Confusion to Digital Conversion', , Issue 7, 2007, ISSN: 1748-3530, pp.21

[1.21]Energy Information Administration, 'International Energy Outlook 2007', Official Energy Statistics from the U.S. Government 2007,
http://www.eia.doe.gov/oiaf/ieo/electricity.html

[1.22]Texas Instruments Power Supply Design Seminar 2006/07, 'Improving power supply efficiency - The Global Perspective',
http://focus.ti.com/download/trng/docs/seminar/Topic1BM.pdf

[1.23]Adler, M.; Owyang, K.; Baliga, B.; Kokosa, R.; 'The evolution of power device technology', IEEE Trans. On electronic devices, vol. Ed-31, no.11, Nov 1984, pp.1570-1591.

[1.24]Furciniti C.A.; Carlson, A.W.; Bach, R.E.; 'Design of highly efficient PWM power supply', IEEE Trans. On aerospace and electronic systems aes-2, Nov 1966.

[1.25]Bodo's power systems, Systems Design Motion and Conversion, 'The Lennox report' April 2007 www.bodospower.com,ISSN: 1863-5598, p.12

[1.26]International technology roadmap for semiconductors, International technology roadmap for semiconductors 2006 update, 'Executive summary', p.25 http://www.itrs.net/links/2006update/finaltopost/00_execsum2006update.pdf

[1.27]Power Electronics Europe, 'Synchronous Rectification Simplified', Issue 8, 2005, ISSN: 1748-3530, pp.29

[1.28]Power Electronics Europe, 'Design of Secondary Side Rectification Using SmartRectifier Control IC', Issue 3, April 2006, ISSN 1748-3530, pp.37

[1.29]Severns, R.P.; 'Topologies for Three-Element Resonant Converter,' IEEE Trans. Power Electronics, vol.7, No.1, Jan. 1992, pp.89-98,

[1.30]Batarseh, I.; 'Resonant Converter Topologies with Three and Four Energy Storage Elements,' IEEE Trans. Power Electronics, vol.9, no.1, Jan. 1994, pp.64-73

[1.31]Yong-Ann Ang; Bingham, C.; Stone, D.; Foster, M.; 'Digital control of dual-load LCLC resonant converters', European Conference on Power Electronics and Applications, 11-14 Sept. 2005

[1.32]Elferich, R.; Duerbaum, T.; 'A new load resonant dual-output converter', Power Electronics Specialists Conference, Volume 3, 23-27 June 2002. pp.1319-1324

[1.33]Steigerwald, R. L.; 'A comparison of Half-Bridge Resonant Converter Topologies', IEEE Trans. Power Electronics, vol.3, no.2, April 1988, pp.174-182.

[1.34]Kazimierczuk, M. K.; Czarkowski, D.; Resonant Power Converters, John Wiley sons, inc 1995, ISBN 0-471-04706-6 , Chapter 8 & 17.

[1.35]Sewell, H.I.; Foster, M.P.; Bingham, C.M.; Stone, D.A.; Hente, D.; Howe, D.; 'Analysis of voltage output LCC resonant converters, including boost mode operation', IEE Proceedings - Electric Power Applications, Vol.50, No.6, Nov. 2003, pp.673-679

[1.36] www.orcad.com

[1.37] www.synopsys.com/saber

[1.38] www.plexim.com

[1.39] Alonso, J.M.; Garcia, J.; Calleja, A.J.; Ribas, J.; Cardesin, J.; 'Analysis, design, and experimentation of a high-voltage power supply for ozone generation based on current-fed parallel-resonant push-pull inverter', IEEE Trans. Industry Applications, Vol.41 , No.5 , Sept. 2005, pp.1364 - 1372

Chapter 2 - Review of Modelling, Analysis and Control Techniques

Having reviewed the current trend for increased use of power converters in Chapter 1, it is now necessary to obtain some familiarity with techniques currently available for their modelling, analysis and design, and identify deficiencies in current available practices.

2.1 Analysis & Design techniques

This literature review provides a summary account of the many design and analysis techniques applicable to switched-mode power supplies. The reviewed techniques can be partitioned into those belonging to the time-domain, the frequency-domain, or some combination of both. As such, the review will be similarly partitioned.

Figure 2.1 shows the interrelationships between the various design and analysis techniques considered.

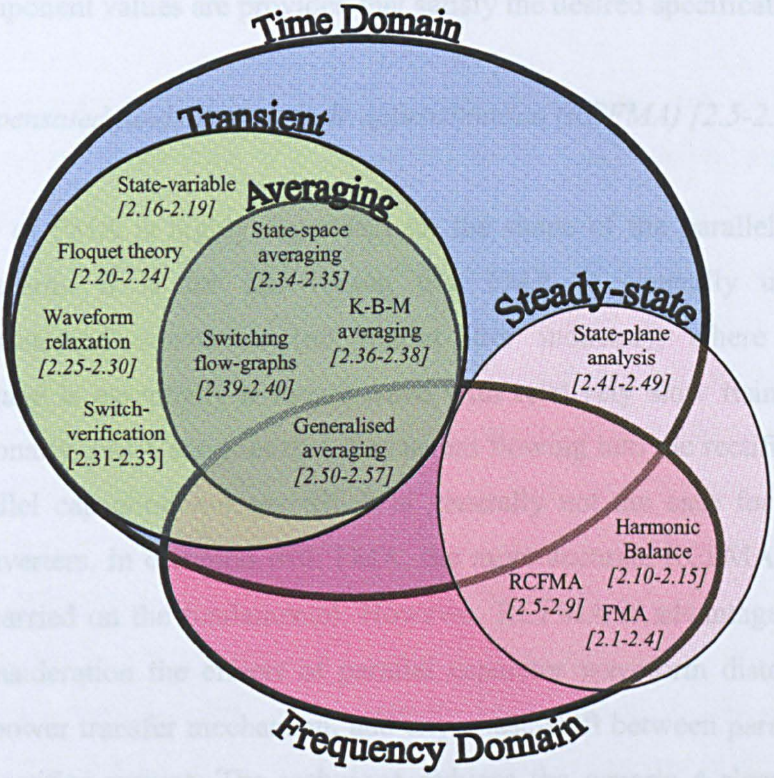

Figure 2.1 - Interrelationships between previously reported analysis and design techniques.

2.1.1 Frequency-domain techniques

Fundamental mode approximation (FMA) [2.1-2.4]

In general, the quality factor of the resonant tank is designed such that the series-inductor current is approximately sinusoidal. In practice, the quality factor (Q_r) is chosen to be in the range 2.5 to 20. Low Q factors result in poorly sinusoidal waveforms whilst larger values result in physically large resonant tank components. Techniques based on Fundamental Mode Approximation (FMA) therefore assume that the power transfer mechanism within the converter takes place solely due to the fundamental, allowing the rectifier and output-filter to be modelled by a single equivalent resistor. This technique is only practically applicable to inductively-smoothed resonant converter variants i.e those converters that include an output-filter inductor (L_f), see Chapter 1. Although additional distortion in the current waveform can impart significant modelling error as the switching frequency is increased beyond resonance, FMA nevertheless remains the most commonly employed technique for the provision of initial converter behaviour. In Chapter 3, FMA is reformulated such that an estimate of the required converter component values are provided that satisfy the desired specifications.

Rectifier compensated fundamental mode approximation (RCFMA) [2.5-2.9]

The accuracy of FMA is highly dependent on the shape of the parallel capacitor C_p voltage waveform. It is for this reason that FMA is generally unsuitable for capacitively-smoothed converters (no output-filter inductor), where the parallel capacitor voltage is essentially a square-wave with relatively slow rising and falling edges. Additionally, FMA assumes that the current flowing into the rectifier is in phase with the parallel capacitor voltage, which is generally not the case for capacitively-smoothed converters. In common with FMA, the more accurate RCFMA assumes that all power is carried on the fundamental. However, RCFMA is advantageous in that it takes into consideration the effects of parallel capacitor waveform distortion, on the fundamental power transfer mechanism, and any phase-shift between parallel capacitor voltage and rectifier current. The technique reduces the generic 4-element $L_sC_sL_pC_p$ resonant tank, and any derivatives thereof, into an equivalent 2nd order parallel resonant tank $L_s'C_p'$ (L_s' and C_p' representing the inductance and capacitance of the series and parallel branches respectively, calculated at the switching frequency) see Figure 2.2. This is achieved by virtue of the series tank being operated inductively to obtain zero-voltage switching, and the parallel branch being operated capacitively to obtain a voltage-gain [2.5]. An equivalent impedance, is then calculated to accurately model the combined interaction of the transformer, rectifier and load, see Figure 2.2. Traditional AC analysis is then performed on the new converter equivalent circuit to calculate both the converter's electrical stresses and output-voltage. The methodology is slightly more complex than FMA but substantially more accurate for the analysis of inductively-smoothed converter.

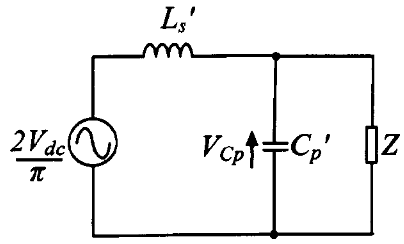

Figure 2.2 - RCFMA equivalent circuit

Harmonic balance techniques [2.10-2.15]

Here, the converter is analysed on a harmonic contribution basis, and, via superposition, the overall response is the sum of the contributions for each individual harmonic. A source representing the n^{th} harmonic of the switching voltage, and rectifier response, are placed on the input and output side of the resonant tank, respectively, see Figure 2.3. The switching source is easily decomposed into its individual harmonics. The model of the rectifier harmonics, however, is not as readily obtained. For each of these harmonics to be determined, the general shape of rectifier input-current, or applied-voltage must be pre-defined (as an approximation, the rectifier voltage may be assumed sinusoidal, trapezoidal or square depending on the choice of output-filter and resonant-tank). For example, in [2.10] a series resonant capacitively-smoothed converter is analysed. The voltage applied across the rectifier input is square, as a result of the rectifier clamping action, with an amplitude equal to the output-voltage and an unknown phase-shift. Likewise in [2.11], the $L_sC_sL_pC_p$ - inductively-smoothed converter is analysed and the rectifier input current is assumed trapezoidal with an unknown phase-shift and rise-time, and an amplitude equal to the steady-state load current. In each of these examples the unknowns must be determined for an accurate application of the harmonic balance technique. As a result, it is necessary to:

1) estimate one of the unknowns, for instance, the phase-shift
2) calculate the remainder of the unknowns (e.g output-voltage amplitude and/or parallel-capacitor voltage raise-time) via various physical constraints
3) sum the response of the converter to the individual harmonics
4) check for consistency with the initial assumption via the evaluation of an error function. A typical error function uses the difference between the input and output power.
5) continue iterating the process until the estimate no longer needs refining, i.e the error tends to zero.

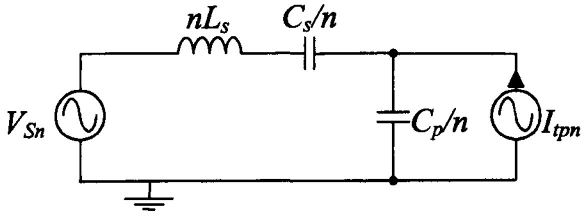

Figure 2.3 - n^{th} harmonic LCC inductively-smoothed equivalent circuit

Although, in theory, the process requires the response to an infinite number of harmonics to be summed to obtain peak accuracy, more realistically, it is only necessary to sum harmonics until the results converge. The author estimates that summing the responses from fundamental to a maximum of the 9th harmonic will result in near peak model accuracy since even a second-order resonant tank (e.g L_sC_s) would attenuate the 9th harmonic by a factor of -40dB. This coupled with a 9th harmonic switching-voltage that is approximately -20dB lower in amplitude than the fundamental, the resulting 9th harmonic response is likely to be at least -60dB lower than that of the fundamental, which corresponds to approximately ±0.1% error between the results of the infinite and truncated series. Converters consisting of larger order tanks, such as the series-parallel ($L_sC_sC_p$) resonant converter, will undergo a greater attenuation.

Very rapid steady-state solutions can be obtained with better accuracy than that of RCFMA. However, since the general shape of the waveforms are approximated as sinusoidal or piece-wise linear, the method may not provide sufficient accuracy, which is of significant importance and thus limits the ultimate applicability for these methods.

2.1.2 Time-domain techniques

Time-domain techniques can be further subdivided viz. those that provide the full response of the converter at all times (Transient), those which provide only the steady-state waveform envelopes (Steady-state), and those that provide the signal-envelopes at all times (Transient-Averaging).

Transient analysis

State-variable [2.16-2.19]

Although the behaviour of resonant switching converters is nonlinear, the converters themselves operate piece-wise linearly. At any specific moment, the converter can be described by an equivalent linear circuit, with diodes and switches being either open- or short-circuit. When diodes or switches change state, the converter is said to enter a new mode in the switching cycle.

The converter can therefore be represented in piece-wise linear state-space form with each mode being described by:

$$\begin{aligned} \dot{x} &= \mathbf{A}_{M_n} x + \mathbf{B}_{M_n} u \\ y &= \mathbf{C}_{M_n} x + \mathbf{D}_{M_n} u \end{aligned} \tag{2.1}$$

where $\mathbf{A}_{M_n}, \mathbf{B}_{M_n}, \mathbf{C}_{M_n}, \mathbf{D}_{M_n}$, correspond to the circuit model of the converter during mode n (M_n), as the various current paths in the converter are changed through the conduction / non-conduction of the switches and rectifier diodes

Through the use of simulation packages such as SIMULINK, for instance, the converter can be simulated in state-variable form, a key advantage being that the matrices themselves provide additional insight into the system's dynamic behaviour, observability and controllability. Furthermore, the state-trajectory can be represented on an n-dimensional graph, thereby providing information on equilibrium points, limit-cycles and stability. Nevertheless, such techniques, whilst being very accurate, suffer from the requirement for integration, and therefore require a computation overhead that can lead to protracted simulation times.

Floquet theory [2.20-2.24]

A switching converter in steady-state operation does not fulfil the traditional definition of steady-state in that as time tends to infinity, the system state derivatives do not tend to zero when perturbed by a step or impulse. Instead, the system states at the beginning and end of a switching cycle are considered identical, as if the system were in a limit cycle for a long period of time. Floquet theory considers that a periodic system, such as a switching-converter, may be represented by a periodic-describing function in conjunction with a damping term describing the transient behaviour. The technique, described in [2.20], is applied to a hard-switched boost converter. The method is demonstrated to provide significant improvements in transient modelling accuracy when compared to state-space averaging (see later) and provides the system eigenvalues and eigenvectors, which are useful for controller design purposes.

A resonant-converter analysis technique based on Floquet theory, known as 'cyclic-averaging', is documented in [2.20]. Since integration of the analytical equations describing the system is not required, extremely rapid steady-state results are achieved.

Waveform relaxation [2.25-2.30]

Waveform relaxation techniques were developed in 1982 as an alternative to the computationally expensive incremental-time analysis methods for VLSI circuit simulations [2.25]. The methodology reduces large systems into multiple subsystems each utilising the largest feasible integration step. Significant improvements in computation overhead are therefore possible. For example, the low bandwidth output-filter of a resonant converter can be accurately modelled at a much larger time-step than that of the resonant tank. The non-linear differential equations governing each sub-system are further reduced to a set of linear equations and solved to the required accuracy in an iterative manner [2.26]. Methodical system partitioning and the choice of maximum time-step (windowing) are demonstrated in [2.27]. Additionally [2.27] shows that for a series resonant-converter only 25% of the computation time is required when compared to traditional integration based methods. The technique is considered no further since it offers little benefit when compared to Floquet theory based techniques.

Step-wise switch verification techniques [2.31-2.33]

Many variable-step solvers are susceptible to problems when simulating around converter switching events, such as when a diode begins to change state or when feed-back is used to govern the MOSFET switching pattern, for instance. Often, somewhat counter intuitively, resulting simulations times are then reduced by utilising fixed-step solvers. Fixed-step solvers, however, require a very fine step-size, such that, if the switching-event is missed by an entire step, accuracy is not unduly affected. Step-wise switch verification techniques specifically aim to improve the simulation accuracy around switching events. For instance, quadratic-extrapolation and compensation methodologies are used to provide a predictor/corrector-type mechanism to verify the state of switches, such as MOSFETs or diodes. For example, when analysing diodes in a circuit, it is initially assumed that they are non-conducting. The potentials across the diode's location are then determined and the initial assumption is tested and modified accordingly. Specifically, quadratic-extrapolation estimates the nodal voltages and current for the next time instant based on a discretised version of the system, and verifies if the switch state throughout the time-step would be constant. If not, the methodology back-tracks to the switching instant, then resumes normal time-stepping until the next switching instant. In [2.31] the methodology is demonstrated on a candidate PWM switching regulator. Compensation theory represents power switches by a low- or high-valued piecewise resistance during the on- and off-periods, respectively. If the current through one of the resistances changes polarity, it provides an indication that a switching event is imminent. The technique has been applied to a buck-boost DC-DC converter in [2.32]. Switch-verification techniques result in improved accuracy around switching-events whilst providing improved simulation speed when compared to traditional fixed-step integration based methods. However, the technique does not eliminate integration requirements, thereby still resulting in protracted simulation times.

Transient-Averaging analysis

State-space averaging [2.34-2.35]

This technique, pioneered by Middlebrook and Cuk in 1976, remains one of the most widely used analysis methodologies for switching converters. A state-variable description of the converter under analysis is formed for each mode of operation, such as when a power switch is either in the on- or off-state. These models are then averaged with respect to the time spent in each specific mode i.e the duty-cycle. The resulting state-space description provides both the steady-state and transient behaviour of the converter as duty-cycle is varied, allowing traditional robust linear control methodologies to be readily applied. The technique's underlying assumption is that the highest corner frequency of interest is much lower than the switching frequency. Whilst this is widely applicable to hard-switched converters, it is unsuitable for resonant converters, where circulating currents in the resonant tank generally operate at the switching-frequency.

Krylov-Bogoliubov-Miltropolsky (KBM) averaging [2.36-2.38]

Here, the state vector of a system is expressed as a sum of an averaged variable and a ripple series [2.36]. For converters such as the buck-boost, for instance, where the switching frequency is much higher than the largest corner frequency of interest, the resulting averaged variables, such as the output voltage, converge to that obtained using state-space averaging. However, since the ripple correction term is utilised, this analysis methodology, unlike state-space averaging is applicable to resonant converters, as demonstrated by [2.36]. Although the ripple series is, in theory, infinite in length, generally only the first three terms need to be employed. A high level of symbolic manipulation must be undertaken in order to calculate these ripple series terms, however. Traditional integration based methods must then simulate the averaged system. Although accurate, the method can again incur significant computational overhead.

Switching-flow graph [2.39-2.40]

Here, the switching circuit is reduced to a series of signal paths and node-variables, each signal-path having an associated transformation, in a similar way to that traditionally used in classical control theory. Signals entering each node are summed to solve the required node-variables. Possible path transformations are switches or traditional transfer-functions. The switching-flow graph, in essence, allows for a time varying control structure, and can be manipulated to find large-signal, small-signal and steady-state system models. If the 'averaged' system behaviour is required, the various states of a switch can be modelled by a signal-path with a gain (0→1) corresponding to the duty-cycle of switch in that specific position. The resulting analysis would then be identical to that for state-space averaging. The switching-flow graph method can therefore provide significant insight into the construction of state-variable based simulation models.

Steady-state analysis

State-plane [2.41-2.49]

It is generally considered that any form of time-domain analysis specifically aimed at obtaining a steady-state solution for systems with multiple modes that repeat periodically, such as those demonstrated by Batarseh in [2.41-2.43], operates on the following basis: as the structure of the switching-converter varies, the state of the system, i.e capacitor voltages and inductor currents, must be identical at the end of one mode, and the start of the next. This also implies that the state of a converter at the very beginning, and end, of each switching-cycle must be identical. In effect, the states must follow a closed contour with a period equal to the switching time. All such converter analysis methods therefore belong to the more general state-plane analysis technique. The account given in Chapter 4 develops a new steady-state state-plane analysis methodology specifically for the LCC capacitively-smoothed converter, such that the converter characteristics (part-load efficiency, required switching frequency range, component-stresses) are fully defined by the capacitor ratio and tank-gain, at resonance, when the minimum load resistance is applied. The technique allows for the simple 'graphical' design of converters given a series of converter specifications. To determine the usefulness and applicability of the technique it is incorporated into a readily useable graphical user interface.

2.1.3 Hybrid Time and Frequency-domain techniques

Generalised averaging (Phasor transform) [2.50-2.58]

These techniques, like waveform relaxation, aim to decouple a system into 'slow' and 'fast' sub-systems. An equivalent frequency domain-model is then generated for each of these sub-systems with the model complexity ultimately depending on the number of harmonics included i.e an index-0 model corresponds to time averaged behaviour, whereas an index-0,1 models the time-averaged characteristics and behaviour at the switching frequency (an index-0,1,2 model simply includes the next harmonic in its behavioural analysis). By way of example, a resonant converter can be decoupled into the resonant tank and output-filter representing the 'fast' and 'slow' sub-systems respectively. The resonant tank requiring at least an index-0,1 model and the output filter utilising an index-0 model since virtually no switching harmonics are normally apparent in the states. The index-0 model is simply the state-space description of the circuit. The index-0,1 model, on the other hand, can be represented via a component transformation. An inductor, for example, is transformed into an inductor in series with an imaginary resistance [2.50-2.52]. Techniques for modelling these combinations of components with imaginary resistors, in SPICE, via two coupled networks are given in [2.53-2.54]. As opposed to considering the higher indexed models and including additional harmonic content (as in a Fourier series), some generalised averaging techniques consider the higher order indexed models to simply include additional derivative terms when the decoupled systems are linearised about their moving operating points [2.55-2.57]. Generalised averaging allows the user to effectively trade simulation speed with accuracy by including or removing higher-order harmonics/derivatives. For resonant converters, an index-0 output filter and an index-0,1 tank model effectively performs a transient FMA analysis. Chapter 5 explores such techniques, and enhances them, resulting in a very high speed analysis methodology. The account in Chapter 6 then further develops this technique to provide a large/small-signal control model for a novel form of phase-angle control (the angle between the switching voltage and series-inductor current). The resulting control technique ultimately linearises the large-signal behaviour of the converter, and thereby allows simple robust linear control techniques to be applied.

2.2 Resonant converter control techniques

To provide a realisable 'system' solution for the use of resonant converters, it is necessary to appreciate the possible resonant converter control methodologies available to the designer. Methods that have been previously explored include:

Variable frequency [2.59-2.62]

The complex impedance of the resonant tank varies with switching frequency, and thereby allows for the adjustment of real power-flow through the converter. This facilitates a low-cost and simplistic solution for controlling converters and remains the most popular method to date. A voltage-controlled oscillator (VCO) provides the required square-wave gate signals. The voltage applied to the VCO is varied such that the output voltage/current is regulated. A number of papers have examined the small- and large-signal behaviour of the converters under such control for necessity of robust design [2.60-2.62].

Bi-frequency [2.63-2.64]

Here, the converter is switched between two discrete frequencies. In effect a 2-state variable frequency control methodology is employed, one frequency being close to resonance where the tank impedance is minimised and real power flow is maximised, and the other, at a much higher frequency where power flow is mostly reactive. The technique allows for simple pulse-width modulation control schemes to be implemented.

Phase-shift control [2.65-2.73]

In most published literature on the subject, a full-bridge switch configuration is used to control the converter at a constant switching frequency with a phase-shift between the switching-voltages of each leg. This results in a 3-state excitation voltage consisting of $+V_{dc}$, $-V_{dc}$ and 'Ground'-potential. It can therefore be considered a form of pulse-width modulation (PWM). Many papers provide alternative control strategies to govern the gate switching patterns. For example, in [2.72], a phase-shift technique is presented that maximises the number of switching events occurring on current-zero crossings thereby reducing switching-losses. Various small- and large-signal models to aid controller design, are presented in [2.67-2.70]. As a result of the constant switching-frequency, EMI produced by the converter is very well defined. Unfortunately however, the topology suffers from increased electrical stresses as a result of significant circulating currents.

Fuzzy-logic [2.76-2.78]

Fuzzy logic control methodologies provide inexpensive nonlinear control with the aim of obtaining good robust performance. Once their underlying principles are understood, they generally have a much reduced development time and deployment cost. The methodology presented in [2.76] describes a fuzzy-based variable frequency controller applied to a resonant converter. In a similar manner, fuzzy-based controllers could compliment many other resonant converter control techniques, such as quantum control (see later under the "self-oscillating" heading) where a PWM signal controls whether to switch the converter at resonance or simply stop switching altogether for a period [2.77]. With the advent of low-cost fuzzy-logic control ICs, fuzzy-logic control should now readily be considered a candidate control technique.

Optimal trajectory [2.79-2.85]

The highest performance in resonant converter control is achieved through optimal trajectory control, where the switching-signals are adjusted on a cycle-by-cycle basis such that the converter enters steady-state in the least number of cycles. Optimal switching events are calculated from analysis of the state-plane. For a reduction in computation and sensor requirements the method can be linearised resulting in a near time-optimal technique [2.81]. Small- and large-signal models are provided in [2.82-2.85] for the purpose of controller design. The method provides the ultimate in performance, at the cost of a large number of sensors and high calculation overhead during each and every switching-cycle.

Self-oscillating [2.86- 2.91]

Self-oscillating controllers for resonant converters are a class of techniques that use a measured converter state variable (such as series-inductor current) to provide the required gate switching-signals after some intermediate processing. They can be divided into a number of distinct categories. The most popular of these is phase-shift control. Timing signals are generated in the controller via measurement of the series-inductor current, and the gate signals switched such that the phase-shift between switching-voltage and measured current is maintained at a pre-determined value. Quantum control, on the other hand, a much simpler technique, always switches the converter on the current zero-crossings, such that zero-voltage and zero-current switching occurs. This results in much improved efficiency and low EMI. To control the output current/voltage level, entire switching cycles are purposefully missed. A sliding mode or hysteresis controller is used to govern when to skip cycles out or simply switch at resonance. The paper [2.91], linearises the large- and small-signal behaviour of the converter via this technique. Self-oscillating controllers are usually very robust, and can be readily applied to converters with significantly different resonant tanks. As a result, Chapter 7 considers a novel form of self-oscillating control where the phase (θ) between the excitation voltage and series-inductor current is adjusted on a cycle-by-cycle basis such that a desired power-factor ($cos(\theta)$), is obtained. The methodology is shown to linearise the large- and small-signal behaviour of the power-factor controlled converter, such that a simple, linear and robust outer-loop can be designed.

Component control [2.92-2.95]

Here the component values present in the resonant tank are either adjusted via an applied control signal (in the case of the voltage controlled capacitor) [2.92-2.93] or modified by switching additional reactive components in or out of the circuit when necessary [2.95]. Such methods allow constant frequency switching to be employed, whilst varying the resonant tank frequency and gain. Interestingly, self-oscillating schemes based on these techniques have yet to be reported, such as locking onto the resonant frequency to maximise efficiency (switching on zero-current crossing results in purely real power flow, reduced electrical stresses and minimised switching losses), and varying the tank gain via resonant tank component control. Such methods offer the potential for greatly enhancing the part-load operating efficiency of the converter.

Energy based control [2.96-2.98]

The converter is analysed from an energy or charge transfer per switching-cycle perspective. From this viewpoint, and, by application of certain control theorems such as passivity [2.96], the potential to generate very robust controllers with high performance is possible. Additionally, in [2.97], an energy based controller is shown to have a similar form to optimal trajectory control, albeit with reduced sensor measurement requirements.

Switched-rectifier techniques [2.99-2.100]

Here, the resonant tank is switched at a constant frequency, and control of the output-voltage is achieved through additional power switches forming part of the rectifier. In [2.99], the rectifier behaves as a simple diode-based full-bridge when no rectifier power switches are in the 'on' state. Through gate turn-on of the rectifier power switches, the voltage across the parallel capacitor is clamped to 0V, thereby eliminating power-flow from the resonant tank to the load.

Non-isolated measurement control [2.101]

When the cost of isolated sensing is prohibitive, a form of output-voltage prediction is required based on primary side measurements. A paper describing such a technique, based on a linear observer, is presented in [2.101], which is extended in Chapter 8 for varying load conditions, via output resistance estimation.

Additional contributions [2.102-2.103]

The account in [2.102] compares a number of the above techniques on a candidate $L_sC_sC_p$ inductively-smoothed resonant converter. Additionally, a useful tool for stability analysis, known at state-plane animation, is described in [2.103]. The tool allows for the generation of a state-plane as the converter is regulated, providing an insight into control dynamics, and overall system behaviour. For instance, various types of instability can easily be explained in geometric terms.

2.3 References

Fundamental mode approximation

[2.1] Steigerwald, R. L. ; 'A Comparison of Half-Bridge Resonant Converter Topologies', IEEE Trans. Power Electronics, Vol.3, No.2, pp 174-182, April 1988

[2.2] Kazimierczuk, M. K.; Czarkowski, D.; 'Resonant Power Converters', Wiley, April 1995, ISBN 0-471-04706-6 , Chapter 8 & 17.

[2.3] Kazimierczuk, M. K.; Wang, S.; 'Frequency-domain Analysis of Series-Resonant Converter for Continuous Conduction Mode,' IEEE Trans. Power Electronics, Vol.7, No.2, April 1992, pp.270-279

[2.4] Ang, Y.; Foster, M.P.; Sewell, H.I.; Bingham, C.M.; Stone, D.A.; 'Stress analysis of fourth-order LLCC resonant converters', Electronics Letters, Vol.38, No.24, 21 Nov. 2002, pp.1585-1586

Rectifier compensated fundamental mode approximation

[2.5] Hayes, J.G. Egan, M.G.; 'Rectifier-compensated fundamental mode approximation analysis of the series parallel LCLC family of resonant converters with capacitive output filter and voltage-source load', PESC'99 Record IEEE Power Electronics Specialists Conference, Vol.2, June 1999, pp.1030-1036

[2.6] Forsyth, A.J.; Mollov, S.V.; 'Simple equivalent circuit for the series-loaded resonant converter with voltage boosting capacitor', IEE Proceedings - Electric Power Applications, Vol.145, No.4, July 1998, pp.301-306

[2.7] Sewell, H.I.; Foster, M.P.; Bingham, C.M.; Stone, D.A.; Hente, D.; Howe, D.; 'Analysis of voltage output LCC resonant converters, including boost mode operation', IEE Proceedings - Electric Power Applications, Vol.50, No.6, Nov. 2003, pp.673-679

[2.8] Ivensky, G.; Kats, A.; Ben-Yaakov, S.; 'An RC load model of parallel and series-parallel resonant DC-DC converters with capacitive output filter', IEEE Trans. Power Electronics, Vol.14, No.3, May 1999, pp.515-521

[2.9] Foster, M.P.; Sewell, H.I.; Bingham, C.M.; Stone, D.A.; Howe, D.; 'Methodologies for the design of LCC capacitively-smoothed resonant converters', IEE Proceedings - Electric Power Applications, Vol.153, No.4, July 2006, pp.559-567

Harmonic balance

[2.10]Roy, P.P.; Doradla, S.R.; Deb, S.; ' Analysis of the series resonant converter using a frequency domain model', PESC '91 Record IEEE Power Electronics Specialists Conference, June 1991, pp.482-489

[2.11]Jain, P.; Quaicoe, J.E.; 'Generalized modelling of constant frequency DC/DC resonant converter topologies', INTELEC '92 Telecommunications Energy Conference, 1992, 4-8 Oct. 1992, pp.180-185

[2.12]Mandhana, O.P.; Hoft, R.G.; 'Steady state frequency domain analysis of parallel-series resonant converter', APEC '92 record IEEE Applied Power Electronics Conference and Exposition, 1992, Feburary, pp.229-236

[2.13]Bhat, A.K.S.; 'Analysis and design of a fixed-frequency LCL-type series-resonant converter with capacitive output filter', IEE Proceedings Circuits, Devices and Systems, Vol.144, No.2, April 1997, pp.97-103

[2.14]Deb, S.; Joshi, A.; Doradla, S.R.; 'A novel frequency-domain model for a parallel-resonant converter', IEEE Trans. Power Electronics, Vol.3, No.2, April 1988, pp.208-215

[2.15]Nelms, R.M.; 'Harmonic analysis of a parallel-loaded resonant converter', IEEE Trans. Aerospace and Electronic Systems, Vol.27, No.4, July 1991, pp.683-688

Transient - State-variable

[2.16]Fiorella, L.; Di Miceli, C.; Raimondi, T.; Cutrona, C.; 'Analysis of a series resonant converter', INTELEC '89 record Telecommunications Energy Conference, Oct. 1989, vol.2, pp.20.3/1-20.3/6

[2.17]de Jesus Silva, A.R.; Cruz Martins, D.; 'Numerical simulation of power static converters: diagonalization method of dynamical matrix', PESC '96 Record IEEE Power Electronics Specialists Conference, Vol.2, June 1996, pp.1655-1660

[2.18]Foster, M.P.; Sewell, H.I.; Bingham, C.M.; Stone, D.A.; 'State-variable modelling of LCC voltage-output resonant converters', Electronics Letters, Vol.37, No.17, 2001, pp.1065-1066

[2.19]Agarwal, V.; Bhat, A.K.S.; 'Large signal analysis of the LCC-type parallel resonant converter using discrete time domain modelling', Proceedings of the IECON '93., International Conference on Industrial Electronics, Control, and Instrumentation, Vol.2, Nov. 1993, pp.836-841

Transient - Floquet theory

[2.20]Visser, H.R.; van den Bosch, P.P.J.; 'Modelling of periodically switching networks', PESC '91 Record IEEE Power Electronics Specialists Conference, June 1991, pp.67-73

[2.21]Foster, M.P.; Sewell, H.I.; Bingham, C.M.; Stone, D.A.; Hente, D.; Howe, D.; 'Cyclic-averaging for high-speed analysis of resonant converters', IEEE Trans. Power Electronics, Vol.18, No.4, July 2003, pp.985-993

[2.22]Ang, Y.A.; Foster, M.P.; Bingham, C.M.; Stone, D.A.; Sewell, H.I.; Howe, D.; 'Analysis of 4th-order LCLC resonant power converters', IEE Proceedings - Electric Power Applications, Vol.151, No.2, Mar 2004, pp.169-181

[2.23]Foster, M.P.; Sewell, H.I.; Bingham, C.M.; Stone, D.A.; Hente, D.; Howe, D.; 'High-speed analysis of resonant power converters', IEE Proceedings - Electric Power Applications, Vol.150, Issue.1, Jan. 2003, pp.62-70

[2.24]Gould, C.; Bingham, C.M.; Stone, D.A.; Foster, M.P.; 'CLL resonant converters with output short-circuit protection', IEE Proceedings-Electric Power Applications, Vol.152, No.5, Sept. 2005, pp.1296-1306

Transient - Waveform relaxation

[2.25]Saviz, P.; Wing, O.; 'Circuit simulation by hierarchical waveform relaxation', IEEE Trans. Computer-Aided Design of Integrated Circuits and Systems, Vol.12, No.6, June 1993, pp.845-860

[2.26]Erdman, D.J.; Rose, D.J.; 'Newton waveform relaxation techniques for tightly coupled systems', IEEE Transactions on Computer-Aided Design of Integrated Circuits and Systems, Vol.11, No.5, May 1992, pp.598-606

[2.27]Sun, J.; Grotstollen, H.; 'Fast time-domain simulation by waveform relaxation methods', PESC '96 Record IEEE Power Electronics Specialists Conference, Vol.2, June 1996, pp.1634-1640

[2.28]Wang, Q.; Marti, J.R.; 'A waveform relaxation technique for steady state initialization of circuits with nonlinear elements and ideal diodes', IEEE Trans.Power Delivery, Vol.11, No.3, July 1996, pp.1437-1443

[2.29]Yao-Lin Jiang; 'A general approach to waveform relaxation solutions of nonlinear differential-algebraic equations: the continuous-time and discrete-time cases', IEEE Trans. Circuits and Systems I, Vol.51, No.9, Sept. 2004, pp.1770-1780

[2.30]Sun, J.; Grotstollen, H.; 'Fast time-domain simulation by waveform relaxation methods', IEEE Trans. Circuits and Systems I, Vol.44, No.8, Aug 1997, pp.660-666

Stepwise switch verification

[2.31]Tse, K.K.; Chung, H.; 'Fast time-domain analysis of PWM switching regulators', PESC '96 Record IEEE Power Electronics Specialists Conference, Vol.2, June 1996 , pp.1363-1369

[2.32]Femia, N.; 'A fast method to find the state of switches after forced commutations in switching converters', PESC '96 Record IEEE Power Electronics Specialists Conference, Vol.2, June 1996, pp.1356-1362

[2.33]Femia, N.; 'Understanding commutations in switching converters. Basic theory and application of the Compensation Theorem', IEEE Trans. Aerospace and Electronic Systems, Vol.39, No.1, Jan. 2003, pp.282-297

State-space averaging

[2.34]Middlebrook, R. D., Cuk, S; 'A general unified approach to modelling switching-converter power stages', PESC '76 Record IEEE Power Electronics Specialists Conference, June 1976, pp.18-34.

[2.35]Dirkman, R. J., 'Generalized state space averaging', PESC'83 Record IEEE Power Electronics Specialists Conference, 1983, pp. 283-294

Krylov-Bogoliubov-Miltropolsky

[2.36]Krein, P.T.; Bass, R.M.; 'A new approach to fast simulation of periodically switching power converters', IEEE Industry Applications Society Annual Meeting, Vol.2, Oct. 1990, pp.1185-1189

[2.37]Bass, R.M.; Sun, J.; 'Large-signal averaging methods under large ripple conditions [for power converters]', PESC'98 Record IEEE Power Electronics Specialists Conference, Vol.1, May 1998, pp.630-632

[2.38]Krein, P.T.; Bentsman, J.; Bass, R.M.; Lesieutre, B.L.; 'On the use of averaging for the analysis of power electronic systems', IEEE Trans. Power Electronics, Vol.5, No.2, April 1990, pp.182-190

Switching-flow graphs

[2.39]Smedley, K.; Cuk, S.; 'Switching Flow-Graph nonlinear modelling technique', IEEE Trans. Power Electronics, Vol.9, No.4, July 1994, pp.405-413

[2.40]Yunhong Ma; Smedley, K.M.; 'Switching flow-graph nonlinear modelling method for multistate-switching converters', IEEE Trans. Power Electronics, Vol.12, No.5, Sept. 1997, pp.854-861

State-plane analysis

[2.41]Batarseh, I.; 'State-plane approach for the analysis of half-bridge parallel resonant converters', IEE Proceedings Circuits, Devices and Systems,Vol.142, No.3, June 1995, pp.200-204

[2.42]Batarseh, I.; Liu, R.; Lee, C.Q.; Upadhyay, A.K.; 'Theoretical and experimental studies of the LCC-type parallel resonant converter', IEEE Trans. Power Electronics, Vol.5, No.2, April 1990, pp.140-150

[2.43]Batarseh, I.; Lee, C.Q.; Upadhyay, A.K.; 'Multi-output LLCC-type parallel resonant converter', IECON '90 record IEEE Industrial Electronics Society, Vol.2, Nov. 1990, pp.850-856

[2.44]Batarseh, I.; Liu, R.; Lee, C.Q.; Upadhyay, A.K.; '150 Watts and 140 kHz multi-output LCC-type parallel resonant converter', APEC' 89 record IEEE Applied Power Electronics Conference and Exposition, March 1989, pp.221-230

[2.45]Bhat, A.K.S.; 'Analysis and design of a series-parallel resonant converter with capacitive output filter', IEEE Trans. Industry Applications, Vol.27, No.3, June 1991, pp.523-530

[2.46]Bhat, A.K.S., Dewan, S.B.; 'Analysis and design of a high-frequency resonant converter using LCC-type commutation', IEEE Trans. Power Electronics, Vol.2, No.2, October 1987, pp.291-300

[2.47]Fu-Sheng Tsai; Lee, F.C.Y.; 'State-plane analysis of a constant-frequency clamped-mode parallel-resonant converter', IEEE Trans. Power Electronics, Vol.3, No.3, July 1988, pp.364-378

[2.48]Fu-Sheng Tsai; Materu, P.; Lee, F.C.Y.; 'Constant-frequency clamped-mode resonant converters', IEEE Trans. Power Electronics, Vol.3, No.4, October 1988, pp.460-473

[2.49]Raju, G.S.N.; Doradla, S.; 'An LCL resonant converter with PWM control-analysis, simulation, and implementation', IEEE Trans. Power Electronics, Vol.10, No. 2, March 1995, pp.164-174

Generalised averaging

[2.50]Rim, C.T.; Cho, G.H.; 'Phasor transformation and its application to the DC/AC analyses of frequency phase-controlled series resonant converters (SRC)', IEEE Trans. Power Electronics, Vol.5, No.2, April 1990, pp.201-211

[2.51]Noworolski, J.M.; Sanders, S.R.; 'Generalized in-plane circuit averaging', APEC '91 record Applied Power Electronics Conference and Exposition, March 1991, pp.445-451

[2.52]Sanders, S.R.; Noworolski, J.M.; Liu, X.Z.; Verghese, G.C.; 'Generalized averaging method for power conversion circuits', IEEE Trans. Power Electronics, Vol.6, No.2, April 1991, pp.251-259

[2.53]Ben-Yaakov, S.; Glozman, S.; Rabinovici, R.; 'Envelope simulation by SPICE-compatible models of linear electric circuits driven by modulated signals', IEEE Trans. Industry Applications, Vol.37, No.2, March-April 2001, pp.527-533

[2.54]Ben-Yaakov, S.; Glozman, S.; Rabinovici, R.; 'Envelope simulation by SPICE-compatible models of electric circuits driven by modulated signals', IEEE Trans. Industrial Electronics, Vol.47, No.1, Feb. 2000, pp.222-225

[2.55]Sun, J.; Grotstollen, H.; 'Symbolic analysis of switching power converters based on a general averaging method', PESC '96 Record IEEE Power Electronics Specialists Conference, Vol.1, June 1996, pp.543-549

[2.56]Sun, J.; Grotstollen, H.; 'Symbolic analysis methods for averaged modeling of switching power converters',IEEE Trans. Power Electronics, Vol.12, No.3, May 1997, pp.537-546

[2.57]Sun, J.; Grotstollen, H.; 'Averaged modelling of switching power converters: reformulation and theoretical basis', PESC '92 Record IEEE Power Electronics Specialists Conference, Vol.2, June 1992, pp.1165-1172

[2.58]Yingqi Zhang; Sen, P.C.; 'D-Q models for resonant converters', PESC'04 record IEEE Power Electronics Specialists Conference, Vol.3, June 2004, pp.1749-1753

Variable frequency control

[2.59]Lin, Ray-Lee; Ju, Wei-Cheng; 'LLC DC/DC Resonant Converter with PLL Control Scheme', APEC 2007 record IEEE Applied Power Electronics Conference, Feb. 2007, pp.1537-1543

[2.60]Witulski, A.F.; Hernandez, A.F.; Erickson, R.W.; 'Small signal equivalent circuit modeling of resonant converters', IEEE Trans.Power Electronics, Vol.6, No.1, Jan. 1991, pp.11-27

[2.61]Yang, E.X.; Lee, F.C.; Jovanovic, M.M.; 'Small-signal modeling of series and parallel resonant converters', APEC '92 record IEEE Applied Power Electronics Conference and Exposition, Feb. 1992, pp.785-792

[2.62]Yang, E.X.; Lee, F.C.; Jovanovic, M.M.; 'Small-signal modeling of LCC resonant converter', PESC '92 Record IEEE Power Electronics Specialists Conference, Vol.2, June 1992, pp.941-948

Bi-frequency control

[2.63]Yuefeng Zhang; Xubin Sun; Lee, C.Q.; 'Bi-frequency control for quasi-resonant converters', PESC '94 Record IEEE Power Electronics Specialists Conference, Vol.1, June 1994, pp.309-314

[2.64]Sun, X.; Zhang, Y.; Gegner, J.; Lee, C.Q.; 'Bi-frequency control for DC-to-DC converters', IECON'93 record Industrial Electronics, Control, and Instrumentation, Vol.2, November 1993, pp.848-851

Phase control

[2.65]Jacobson, B.S.; Weil, T.A.; 'Sequential switching series resonant converter with phase shift control', APEC '88 record IEEE Applied Power Electronics Conference and Exposition, Feb. 1988, pp.190-199

[2.66]Kazmierczuk, M.K.; Czarkowski, D.; Thirunarayan, N.; 'A new phase-controlled parallel resonant converter', IEEE Trans. Industrial Electronics, Vol.40, No.6, Dec. 1993, pp.542-552

[2.67]Tsai, M.-C.; 'Analysis and implementation of a full-bridge constant-frequency LCC-type parallel resonant converter', IEE Proceedings- Electric Power Applications, Vol.141, No.3, May 1994, pp.121-128

[2.68]So, W.C.; Lee, Y.S.; Tse, C.K.; 'Dynamic modelling of phase-shifted full-bridge series resonant converter', PESC '97 Record IEEE Power Electronics Specialists Conference, Vol.1, June 1997, pp.460-465

[2.69]Sanbao Zheng; Czarkowski, D.; 'Dynamics of a phase-controlled series-parallel resonant converter', ISCAS 2002 record IEEE International Symposium on Circuits and Systems, Vol.3, May 2002, pp.819-822

[2.70]Sanbao Zheng; Czarkowski, D.; 'Modeling and Digital Control of a Phase-Controlled Series–Parallel Resonant Converter', IEEE Trans. Industrial Electronics, Vol.54, No.2, April 2007, pp.707-715

[2.71] Lu, Y.; Cheng, K.W.E.; Ho, S.L.; 'Auto-disturbance-rejection control for phase-shifted resonant converter', IEE Proceedings - Electric Power Applications, Vol.153, No.5, September 2006, pp.711-718

[2.72]Ranstad, P.; Nee, H.-P.; Linner, J.; 'A novel control strategy applied to the series loaded resonant converter', 2005 European Conference on Power Electronics and Applications, Sept. 2005.

[2.73]Bhat, A.K.S.; 'Fixed-frequency PWM series-parallel resonant converter', IEEE Trans. Industry Applications, Vol. 28, No.5, Sept 1992, pp.1002-1009

[2.74]Tanaka, H.; Ninomiya, T.; Shoyama, M.; Zaitsu, T.; 'Novel PWM-controlled resonant converter', INTELEC '96 record IEEE Telecommunications Energy Conference, Oct. 1996, pp.823-828

[2.75]Ngo, K.D.T.; 'Analysis of a series resonant converter pulse width-modulated or current-controlled for low switching loss', IEEE Trans. Power Electronics, Vol.3, No.1, Jan. 1988, pp.55-63

Fuzzy logic control

[2.76]Bonissone, P.P.; Khedkar, P.S.; Schutten, M.J.; 'Fuzzy logic control of resonant converters for power supplies', Proceedings of the 4th IEEE Conference on Control Applications, Sept. 1995 pp.323-328

[2.77]Correa, J.M.; Hutto, E.D.; Farret, F.A.; Simoes, M.G.; 'A fuzzy-controlled pulse density modulation strategy for a series resonant inverter with wide load range', PESC '03 record IEEE Power Electronics Specialist Conference, Vol. 4, June 2003, pp.1650-1655

[2.78]Sivakumaran, T.S.; Natarajan, S.P.; Venkatachalam, P.; 'Simulation and Real-Time Implementation of Fuzzy Logic Controller for Parallel Loaded Resonant Converter', Annual IEEE INDICON conference, Dec. 2005, pp.127-132

Optimal trajectory control

[2.79]Oruganti, R.; Yang, J.J.; Lee, F.C.; 'Implementation of optimal trajectory control of series resonant converter', IEEE Trans. Power Electronics, Vol.3, No.3, July 1988, pp.318-327

[2.80]Sivakumar, S.; Natarajan, K.; Sharaf, A.M.; 'Optimal trajectory control of series resonant converter using modified capacitor voltage control technique', PESC '91 Record IEEE Power Electronics Specialists Conference, June 1991, pp.752-759

[2.81]Oruganti, R.; How, T.C.; 'Resonant-tank control of parallel resonant converter', IEEE Trans. Power Electronics, Vol. 8, No. 2, April 1993, pp.127-134

[2.82]Kim, M.G.; Kim, J.S.; 'Modeling and optimal-trajectory control of the series resonant converter pulsewidth-modulated or current-controlled for low switching loss', APEC '93 record IEEE Applied Power Electronics Conference and Exposition, March 1993, pp.752-758

[2.83]Natarajan, K.; Sivakumar, S.; 'Optimal trajectory control of constant frequency series resonant converter', PESC '93 Record IEEE Power Electronics Specialists Conference, June 1993, pp.215-221

[2.84]Chen, H.; Sng, E.K.K.; Tseng, K.J.; 'Generalized optimal trajectory control for closed loop control of series-parallel resonant converters', PESC'04 record IEEE Power Electronics Specialists Conference, Vol. 3, June 2004, pp.1786-1791

[2.85]Hernandez-Guzman, V.M.; 'On the Phase Plane Stability Analysis for DC to DC Series Resonant Converters', 2006 IEEE International Symposium on Industrial Electronics, Vol. 2, July 2006, pp.733-738

Self-oscillating control

[2.86]Pinheiro, H.; Jain, P.; Joos, G.; 'Self-sustained oscillating resonant converters operating above the resonant frequency', APEC '97 record IEEE Applied Power Electronics Conference and Exposition,Vol. 2, Feb. 1997, pp.993 -999

[2.87]Youssef, M.Z.; Pinheiro, H.; Jain, P.K.; 'Analysis & modelling of a self-sustained oscillation series-parallel resonant converter with capacitive output filter using sampled-data analytical technique', INTELEC '03 record IEEE Telecommunications Energy Conference, Oct. 2003, pp.282-289

[2.88]Youssef, M.Z.; Pinheiro, H.; Jain, P.K.; ' Self-sustained phase-shift modulated resonant converters: modeling, design, and performance', IEEE Trans. Power Electronics, Vol. 21, No. 2, March 2006, pp.401-414

[2.89]Joung, G.B.; Rim, C.T.; Cho, G.H.; 'An integral cycle mode control of series resonant converter', PESC '88 Record IEEE Power Electronics Specialists Conference, Vol.2, April 1988, pp.575-582

[2.90]Kwon, W.H.; Cho, G.H.; 'Modified quantum and phase control of series resonant converter', PESC '91 record IEEE Power Electronics Specialists Conference, June 1991, pp.498-503

[2.91]Castilla, M.; Garcia de Vicuna, L.; Lopez, M.; Lopez, O.; Matas, J.; 'Dynamic response optimization of quantum series-parallel resonant converters using sliding mode control', PESC'00 record IEEE Power Electronics Specialists Conference, Vol.2, June 2000, pp.702-707

Component control

[2.92]Harada, K.; Katsuki, A.; Fujiwara, M.; Nakajima, H.; Matsushita, H.; 'Resonant converter controlled by variable capacitance devices', IEEE Trans, Power Electronics, Vol. 8, No. 4, Oct. 1993, pp.404-410

[2.93]Harada, K.; Katsuki, A.; Fujiwara, M.; Nakajima, H.; Matsushita, H.; 'Resonant converter controlled by variable capacitance devices', PESC '90 Record IEEE Power Electronics Specialists Conference, June 1990, pp.273-280

[2.94]Hernandez Cid, J.M.; Rizo Diaz, F.de.J.; Design of an electronic ballast based on a resonant converter controlled by a variable capacitance strategy', ISIE'2000 record Industrial Electronics, Vol. 2, Dec. 2000, pp.365-369

[2.95]Wen-Jian Gu; Harada, K.; 'A new method to regulate resonant converters', IEEE Trans. Power Electronics, Vol. 3, No.4, Oct. 1988, pp.430-439

Energy-based control

[2.96]Lu, Y.; Cheng, K.W.E.; Ho, S.L.; Pan, J.F.; 'Passivity-based control of a phase-shifted resonant converter', IEE Proceedings-Electric Power Applications, Vol. 152, No. 6, Nov. 2005, pp.1509-1515

[2.97]Marn-Go Kim; Myung-Joong Youn;' An energy feedback control of series resonant converter', IEEE Trans. Power Electronics, Vol. 6, No.3, July 1991, pp.338-345

[2.98]Nguyen, V.; Lee, C.Q.; 'A tracking control method for series-resonant converters', PESC 98 Record IEEE Power Electronics Specialists Conference, Vol. 1, May 1998, pp.348-353

Controlled rectifier

[2.99]Conesa, A.; Pique, R.; Fossas, E.; 'The serial resonant converter with controlled rectifier stage', 2005 European Conference on Power Electronics and Applications, Sept. 2005

[2.100]Conesa, A.; Pique, R.; Fossas, E.; Velasco, G.; 'Steady state analysis of parallel-loaded resonant converter with one-cycle control', PESC 04 record IEEE Power Electronics Specialists Conference, Vol. 3, June 2004, pp.1761-1767

Non-isolated measurement control

[2.101]Foster, M.P, Sewell, H.I., Bingham, C.M., Stone, D.A.; 'Observer based feedback control of 3rd order LCC resonant converters', EPE'03 record European Conference on Power Electronics and Applications, 2003, CD-ROM proceedings.

Additional contributions

[2.102]Youssef, M.Z.; Jain, P.K.; 'A review and performance evaluation of control techniques in resonant converters', IECON 2004 record IEEE Industrial Electronics Society, Vol.1, Nov. 2004, pp.215-221

[2.103]Bass, R.M.; Krein, P.T.; 'State-plane animation of power electronic systems: a tool for understanding feedback control and stability', APEC'90 record IEEE Applied Power Electronics Conference and Exposition, March 1990, pp.641-648

Chapter 3 - Rapid design of LCC Inductively-smoothed Resonant Converters

Chapter 2 has outlined many previously reported tools for the analysis and design of resonant converters. None of these, however, provide a simple intuitive design process for the LCC inductively-smoothed resonant converter (see Figure 3.1). To address the issue, this chapter presents, and practically validates, a straightforward and novel design methodology [3.1-3.3] for this type of converter for use in both voltage-source and current-source applications, with the aim of reducing tank currents, and hence, electrical stresses on resonant components, with a minimum of calculation overhead. The methodology provides component values directly from a set of converter specifications and is ideally suited for preliminary pre-production designs.

3.1 Introduction

The design procedure assumes that the converter is operated about a specified resonant frequency for a given load and gain. The aim is to provide a converter that minimises tank currents for a given set of converter specifications. A number of the underlying equations have been taken from previously reported design methodologies (see Chapter 1) - the reader will be referred to these wherever possible, for brevity to aid the reader's understanding. The design process utilises the accuracy of Fundamental Mode Approximation (FMA) at the resonant frequency, and the potential for rapid analysis that it provides.

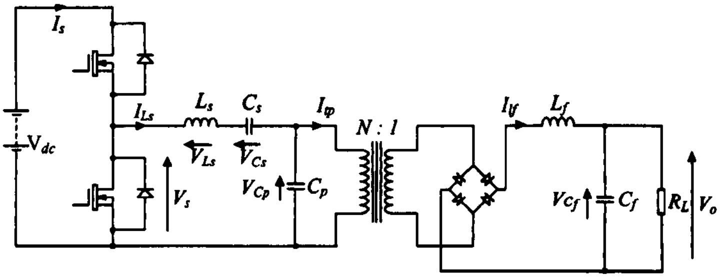

Figure 3.1 - LCC Inductively-smoothed resonant converter

3.2 Operation at resonance

Operation at resonance minimises reactive power flow around the tank and therefore reduces electrical stresses and improves efficiency. Figures 3.2(a) and 3.2(b) show example switching voltage and tank current waveforms for two resonant converters, of the type shown in Figure 3.1, both operated with constant output power and input voltage, at, and above resonance, respectively. Current only flows to or from the supply when the switching voltage is positive (i.e with the upper MOSFET or upper body diode conducting, in Figure 3.1). To maintain a constant output power, and hence, constant input power for an efficient converter, the time integral of the supply current both at, and above resonance, must be the same, assuming negligible losses in either case. This can be seen in Figure 3.2(b) and 3.2(d) for operation at, and above the resonant frequency, respectively. Note that during excitation above resonance the supply current during part of the cycle becomes negative. This requires that the positive current peak will have to increase to maintain a constant time integral.

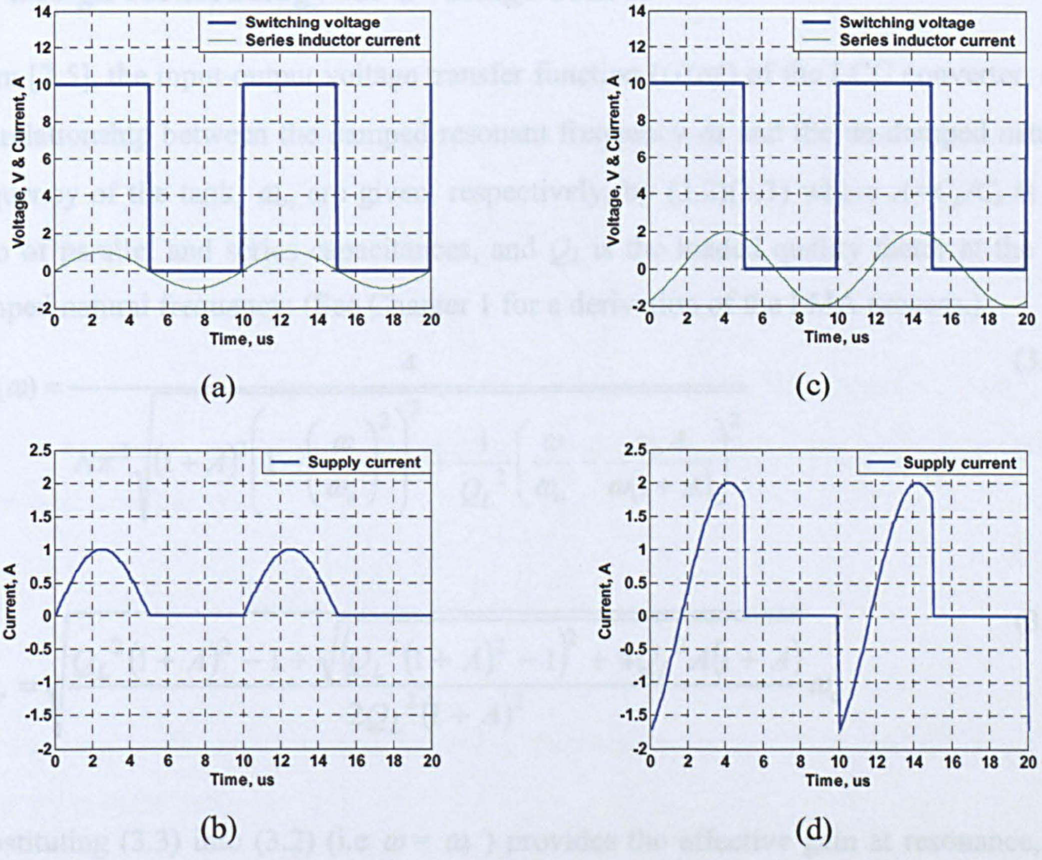

(a) (c)

(b) (d)

Figure 3.2 - Comparison between at resonance (a,b) and above resonance operation (c,d) in-terms of resonant current, supply current and switching voltage

For a sinusoidal tank current and square wave excitation voltage, when considering the supply input power at the fundamental frequency, it can be shown that:

$$P_{in} = \frac{\hat{I}_{Ls(above\ resonance)}\cos(\theta)2V_{dc}}{\pi} = \frac{\hat{I}_{Ls(at\ resonance)}2V_{dc}}{\pi} \tag{3.1}$$

therefore giving $\hat{I}_{Ls(above\ resonance)} = \dfrac{\hat{I}_{Ls(at\ resonance)}}{\cos(\theta)}$

where θ is the phase shift between the excitation voltage and series-inductor current

Notably, for the conditions depicted in Figures 3.2(b) and 3.2(d), a phase shift of 60° is used, hence, from (3.1), the required peak current is double what is required for operation at the resonant frequency resulting in higher losses and increased component stresses (thus requiring a greater cost to manufacture).

3.3 Design methodology for a voltage-source

From [3.5], the input-output voltage transfer function ($G(\omega)$) of the LCC converter, and the relationship between the damped resonant frequency ω_r and the un-damped natural frequency of the tank, ω_o, are given, respectively, by (3.2)(3.3) where $A=C_p/C_s$ is the ratio of parallel and series capacitances, and Q_L is the loaded quality factor at the un-damped natural frequency: (See Chapter 1 for a derivation of the FMA process.)

$$G(\omega) = \frac{4}{N\pi^2\sqrt{(1+A)^2\left(1-\left(\frac{\omega}{\omega_o}\right)^2\right)^2 + \frac{1}{Q_L{}^2}\left(\frac{\omega}{\omega_o} - \frac{\omega_o A}{\omega(1+A)}\right)^2}} \tag{3.2}$$

$$\omega_r = \sqrt{\frac{Q_L{}^2(1+A)^2 - 1 + \sqrt{\left(Q_L{}^2(1+A)^2-1\right)^2 + 4Q_L{}^2A(1+A)}}{2Q_L{}^2(1+A)^2}}\,\omega_o \tag{3.3}$$

Substituting (3.3) into (3.2) (i.e $\omega = \omega_r$) provides the effective gain at resonance, G_r, and subsequently rearranging the resulting gain expression to give the quality factor Q_L at the un-damped resonant frequency ω_o gives:

$$Q_L = \frac{NG_r\pi^2}{4}\sqrt{\frac{\left(G_rN\pi^2-4\right)\left(G_rN\pi^2+4\right)}{\left(1+A\right)\left(AG_r^{\,2}N^2\pi^4+G_r^{\,2}N^2\pi^4-16\right)}} \tag{3.4}$$

The overall gain G_r can be written as a combination of the resonant tank gain and the transformer gain:

$$G_r = \frac{G_{tr}}{N} \text{ where } G_{tr} \text{ is the resonant tank gain i.e } G_{tr} = \frac{NV_o}{V_{dc}} \tag{3.5}$$

Substituting (3.5) into (3.4) gives:

$$Q_L = \frac{\pi^2 G_{tr}}{4}\sqrt{\frac{\left(G_{tr}\pi^2-4\right)\left(G_{tr}\pi^2+4\right)}{\left(1+A\right)\left(AG_{tr}^{\,2}\pi^4+G_{tr}^{\,2}\pi^4-16\right)}} \tag{3.6}$$

From (3.6), a constraint on the minimum value of tank gain can be found that ensures Q_L (3.6) remains real i.e,

$$G_{tr} > \frac{4}{\pi^2} \tag{3.7}$$

Substituting (3.6) into (3.3), the expression for ω_r becomes:

$$\omega_r = \frac{\omega_o\sqrt{AG_{tr}^{\,2}\pi^4+G_{tr}^{\,2}\pi^4-16}}{G_{tr}\pi^2\sqrt{1+A}} \tag{3.8}$$

The input power and output power are equated, as in (3.9). The equations assume a lossless converter operating at the resonant frequency with a 50% duty cycle, and a sinusoidal tank current.

$$P_{in} = \left(\frac{V_{dc}}{2}\right)\left(\frac{2\hat{I}_L}{\pi}\right),\ P_{out} = \frac{\left(V_{dc}G_{tr}\right)^2}{N^2R_L},\ P_{in} = P_{out} \tag{3.9}$$

Rearranging (3.9) results in the following expression for the peak magnitude of the resonant tank current:

$$\hat{I}_L = \frac{\pi V_{dc}G_{tr}^{\,2}}{N^2R_L} \tag{3.10}$$

An alternative expression for Q_L is also given in [3.5] as:

$$Q_L = \frac{\pi^2 N^2 R_L}{8\omega_o L_s} \tag{3.11}$$

which, when equated to (3.6) can provide the required series-inductance as a function of converter specifications.

Rearranging (3.11) for L_s and multiplying by $\omega_r/(2\pi f_r)$ gives:

$$L_s = \frac{\pi N^2 R_L}{16 Q_L f_r}\frac{\omega_r}{\omega_o} \tag{3.12}$$

and substituting (3.5),(3.6),(3.8) into (3.12) gives:

$$L_s = \frac{N^2 R_L \left(A G_{tr}^{\ 2} \pi^4 + G_{tr}^{\ 2} \pi^4 - 16\right)}{4\pi^3 f_r G_{tr}^{\ 2} \sqrt{G_{tr}^{\ 2} \pi^4 - 16}} \tag{3.13}$$

The un-damped natural frequency of the converter is expressed as:

$$\omega_o = \sqrt{\frac{1+A}{L_s C_P}} \tag{3.14}$$

and substituting (3.14) into (3.11) and rearranging for C_P gives:

$$C_p = \frac{64 Q_L^{\ 2}(1+A)L_s}{N^4 \pi^4 R_L^{\ 2}} \tag{3.15}$$

and substituting (3.5),(3.6),(3.13) into (3.15) gives:

$$C_p = \frac{\sqrt{G_{tr}^{\ 2}\pi^4 - 16}}{\pi^3 N^2 R_L f_r} \tag{3.16}$$

Finally, from $C_s = C_p/A$ and (3.16):

$$C_s = \frac{\sqrt{G_{tr}^{\ 2}\pi^4 - 16}}{\pi^3 N^2 R_L f_r A} \tag{3.17}$$

It is also important to consider the quality factor at the damped resonant frequency:

$$Q_r = \frac{\omega_r L_s}{R_s} \tag{3.18}$$

where R_s, the effective loading on the series resonant tank, is defined in [3.5] as follows:

$$R_s = \frac{R_i}{1+\left(\omega_r C_p R_i\right)^2} \tag{3.19}$$

where R_i, the effective loading on the parallel capacitor, for the inductively-smoothed converter is:

$$R_i = \frac{\pi^2 N^2 R_L}{8} \tag{3.20}$$

Substituting (3.19),(3.20) into (3.18) now gives:

$$Q_r = \frac{\omega_r L_s\left(64+\pi^4 \omega_r{}^2 C_P{}^2 R_L{}^2 N^4\right)}{8\pi^2 N^2 R_L} \tag{3.21}$$

and substituting (3.5),(3.13),(3.16) and $\omega_r = (2\pi f_r)$ into (3.21) gives:

$$Q_r = \frac{A G_{tr}{}^2 \pi^4 + G_{tr}{}^2 \pi^4 - 16}{4\sqrt{G_{tr}{}^2 \pi^4 - 16}} \tag{3.22}$$

In order for FMA to accurately estimate the output voltage, the inductor current must be near sinusoidal. In [3.5], it is specified that $Q_r > 2.5$ will provide near sinusoidal waveforms. Figure 3.3 provides the minimum value of A for a given G_{tr} value in order that $Q_r > 2.5$. [Note that the terms Q_L and Q_r are easily confused in the literature. Q_L is generally a normalisation term, used to compare various converter designs, see equation (1.12). Q_r on the other hand is a measure of how sinusoidal the series-inductor current is]

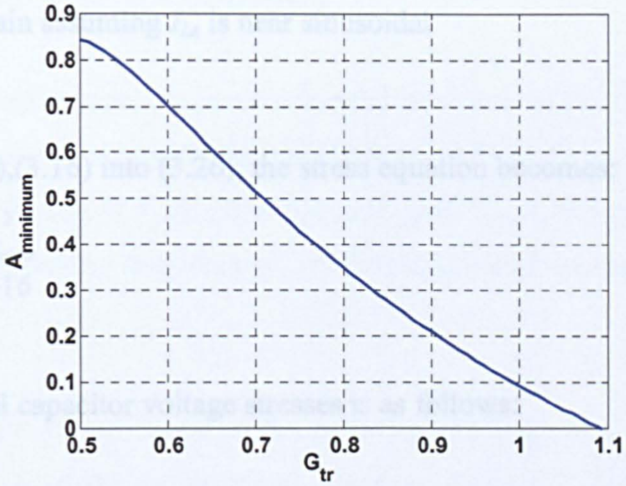

Figure 3.3 - Plot of $A_{minimum}$ vs G_{tr} for $Q_r>2.5$

Electrical Stresses

It is important to consider the component voltage stresses during the design process since this ultimately dictates the voltage ratings. The peak resonant inductor voltage stress is found from:

$$\hat{V}_{Ls} = 2\pi f_r L_s \hat{I}_L \text{ (assuming } I_{Ls} \text{ is near sinusoidal)} \tag{3.23}$$

Substituting (3.10),(3.13) into (3.23) the expression can be rearranged to:

$$\hat{V}_{Ls} = \frac{V_{dc}\left(AG_{tr}{}^2\pi^4 + G_{tr}{}^2\pi^4 - 16\right)}{2\pi\sqrt{G_{tr}{}^2\pi^4 - 16}} \tag{3.24}$$

Since FMA only considers the fundamental component of waveforms, it often provides inaccurate estimates of the inductor voltage stress. A significant contribution to this is the supply voltage level, since, at the switching instants, the inductor voltage is increased by the level of the supply voltage. The ultimate peak stress is therefore higher by V_{dc} volts i.e:.

$$\hat{V}_{Ls} = \frac{V_{dc}\left(AG_{tr}{}^2\pi^4 + G_{tr}{}^2\pi^4 - 16\right)}{2\pi\sqrt{G_{tr}{}^2\pi^4 - 16}} + V_{dc} \tag{3.25}$$

The series capacitor voltage stress is as follows:

$$\hat{V}_{Cs} = \frac{A\hat{I}_L}{2\pi f_r C_p} \text{ again assuming } I_{Ls} \text{ is near sinusoidal} \tag{3.26}$$

Substituting (3.10),(3.16) into (3.26), the stress equation becomes:

$$\hat{V}_{Cs} = \frac{AV_{dc}\pi^3 G_{tr}^{\ 2}}{2\sqrt{G_{tr}^{\ 2}\pi^4 - 16}} \tag{3.27}$$

Finally the parallel capacitor voltage stresses is as follows:

$$\hat{V}_{Cp} = \frac{\pi V_{dc} G_{tr}}{2} \tag{3.28}$$

Thus far it has been assumed that G_{tr} should be greater than ≈0.4. However, a more stringent requirement is obtained when considering the reduced accuracy of FMA in the discontinuous parallel capacitor mode (i.e when the parallel capacitor voltage is clamped to 0V by action of the rectifier for a period during each switching cycle). A constraint should therefore be added that ensures operation (for reasons of model accuracy) in the continuous parallel capacitor mode (normal operation). Discontinuous parallel capacitor voltage mode typically occurs for high output powers when voltage regulating [3.6]. From [3.6], to ensure a continuous parallel capacitor voltage characteristic, the following must be satisfied:

$$\pi^2 N^2 C_p R_L f_s > 1 \text{ where } f_s \text{ is the switching frequency} \tag{3.29}$$

Some authors, such as that in [3.6], aim to increase power-density through use of the discontinuous parallel capacitor voltage mode.

Substituting (3.5),(3.16) into (3.29), equating ($f_s = f_r$), and solving for G_{tr} gives:

$$G_{tr} \geq 0.52 > \frac{\sqrt{\pi^2 + 16}}{\pi^2} \tag{3.30}$$

Note that, in general, the load resistance and switching frequency are greater than the minimum load and resonant frequency, respectively. From (3.29) increasing R_L and/or f_s serves to further satisfy the constraint (i.e the minimum G_{tr} reduces). This therefore implies that (3.30) will always ensure continuous operation.

3.4 Voltage-source design examples

The proposed design procedure is summarised by equations (3.5),(3.13),(3.16),(3.17) and based on initial design constraints of i) selecting $G_r = V_{o\_max}/V_{dc\_min}$ ii) selecting a transformer gain N such that the resonant tank gain G_{tr} is as desired iii) choosing a desired nominal switching frequency f_r, iv) the minimum load resistance R_{L_min}, v) the value of A.

To provide a degree of validation of the proposed methodology, various designs have been created based on the requirements given in Table 3.I. Table 3.II(a) shows the percentage difference in gain G_{tr} and resonant frequency of the converters obtained through use of the design methodology, with respect to the desired values specified in Table 3.I. The data are based on the results of SPICE simulation studies. Clearly, component requirements generated by the design methodology will not provide preferred values. However, by judicious choice of preferred values, about those calculated by the design method, the resulting gain errors are shown to be around 6% or less (see Table 3.II(b)), which is typical of the accuracy normally obtained when employing standard industrial grade off-the-shelf components.

Table 3.I: Design requirements

Design No.	G_{tr} (V/V)	N(V/V)	f_r (kHz)	R_{Lmin} (Ω)	A (F/F)
(1)	0.8	0.1	25	50	2
(2)	1	0.3	125	2	1.5
(3)	1.5	0.05	100	500	5
(4)	2.5	5	50	0.3	0.5
(5)	5	1	75	20	1

Table 3.II: SPICE simulation results when using (a) ideal and (b) preferred component values

	Components			Simulation		% Error	
No.	L_s	C_p	C_s	G_{tr} (V/V)	f_r(kHz)	G_{tr}	f_r
(1)	6.33u	17.6u	8.8u	0.82	24.8	2.5	-0.4
(2)	293n	12.9u	8.6u	1.02	124.3	2.0	-0.6
(3)	4.08u	3.68u	736n	1.46	100.2	-2.7	0.2
(4)	7.13u	2.09u	4.18u	2.49	49.9	-0.4	-0.2
(5)	8.49u	1.06u	1.06u	4.99	74.9	-0.2	-0.1

(a)

	Components			Simulation		% Error	
No.	L_s	C_p	C_s	G_{tr} (V/V)	f_r(kHz)	G_{tr}	f_r
(1)	6.8u	18u	8.2u	0.83	24.6	3.8	-1.6
(2)	330n	12u	8.2u	0.94	119.4	-6.0	-4.5
(3)	4.7u	3.9u	680n	1.48	96.2	-1.3	-3.8
(4)	6.8u	2.2u	4.7u	2.60	49.3	4.0	-1.4
(5)	8.2u	1.0	1.0u	4.94	78.4	-1.2	4.5

(b)

There are other ways in which the design equations may be utilised. For instance, it is entirely possible to specify some components in advance and solve the design equations for the remaining components and variables. The constraints that G_{tr}>0.52 and Q_r>2.5 are still necessary to maintain accuracy. The designer may also wish to design with a specific Q_L and/or Q_r. In this case (3.6),(3.22) then provide further constraints on A and G_{tr} such that a design may be found.

3.5 Voltage-source part load performance

In general, for this converter topology, it can be shown [3.5] that if Q_L is chosen to have a relatively low value at full load, then operation at part load implies a reduction in tank current (Part load being defined as operation below maximum rated power, whilst voltage regulating at the specified level). Providing (3.30) is satisfied (to ensure a continuous parallel capacitor voltage, and hence, model accuracy), then from (3.6), choosing the lower permissible value of resonant tank gain will result in a low Q_L. By way of example, Figure 3.4 shows a 3D plot of Q_L vs. G_{tr} and A.

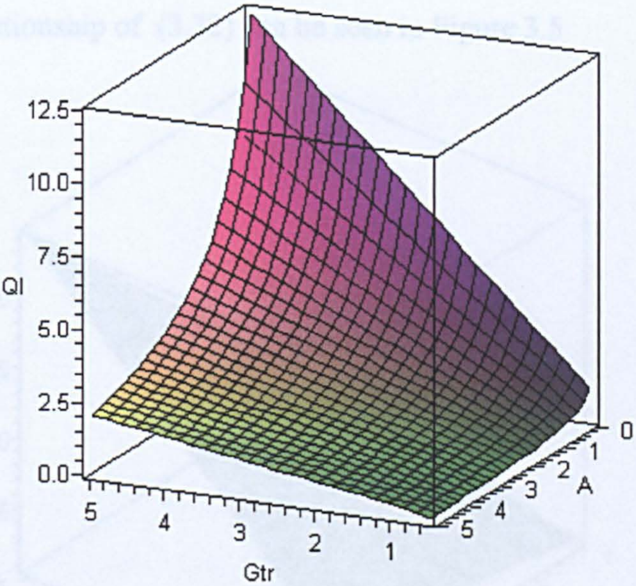

Figure 3.4 - 3D plot of Q_L vs. G_{tr} and A

Figure 3.4 is also consistent with equation (3.16). Solving (3.16) for G_{tr} gives:

$$G_{tr} = \frac{\sqrt{16+\left(C_p \pi^3 N^2 R_L f_r\right)^2}}{\pi^2} \tag{3.31}$$

From (3.31), the closer the resonant tank gain is to $4/\pi^2$, and the less sensitive the resonant frequency is to load changes (i.e A large), the smaller the dependence of resonant tank gain, G_{tr}, on the load. Hence, for any given load, the phase shift between excitation voltage and series-inductor current, necessary to maintain the output voltage during above resonance operation, will remain small. However, from (3.1), the dependence of series-inductor current to load is much greater.

From (3.13), (3.5) the following expression can be written:

$$\frac{L_s f_r G_r^{\,2}}{R_L} = \frac{A G_{tr}^{\,2}\pi^4 + G_{tr}^{\,2}\pi^4 - 16}{4\pi^3\sqrt{G_{tr}^{\,2}\pi^4 - 16}} \tag{3.32}$$

This expression implies that for a given overall converter gain G_r and load resistance R_L, a relationship exists between the $L_s f_r$ product of the tank at the resonant frequency, and the A and G_{tr} values. Reducing the $L_s f_r$ product can aid in the reduction of iron losses in the inductor.

A 3D plot of the relationship of (3.32) can be seen in Figure 3.5

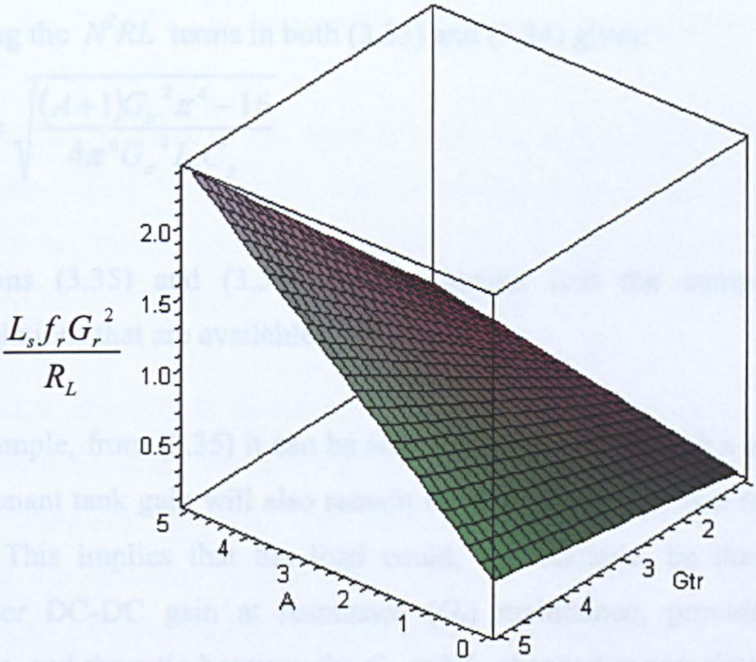

Figure 3.5 - 3D plot of normalised $L_s f_r$ product vs. G_{tr} and A

From Figure 3.5 it can be seen that for a given load resistance R_L and overall gain at resonance (G_r), lower resonant tank gains (G_{tr}) provide a lower $L_s f_r$ product. Hence, for a given L_s the resonant frequency is lower. This facilitates reduced iron losses in the inductors and transformers.

3.6 Insight given by proposed voltage-source design methodology

From (3.16), the required parallel capacitor was found to be:

$$C_p = \frac{\sqrt{G_{tr}^2 \pi^4 - 16}}{\pi^3 N^2 R_L f_r} \tag{3.33}$$

and from (3.13) the required series inductor was calculated as:

$$L_s = \frac{N^2 R_L \left(A G_{tr}^2 \pi^4 + G_{tr}^2 \pi^4 - 16\right)}{4\pi^3 f_r G_{tr}^2 \sqrt{G_{tr}^2 \pi^4 - 16}} \tag{3.34}$$

Equating f_r terms in (3.33) and (3.34) gives:

$$\frac{L_s}{N^4 R_L^2 C_p} = \frac{(A+1)G_{tr}^2\pi^4 - 16}{4G_{tr}^2\left(G_{tr}^2\pi^4 - 16\right)} \qquad (3.35)$$

Equating the N^2RL terms in both (3.33) and (3.34) gives:

$$f_r = \sqrt{\frac{(A+1)G_{tr}^2\pi^4 - 16}{4\pi^6 G_{tr}^2 L_s C_p}} \qquad (3.36)$$

Equations (3.35) and (3.36) provide insight into the component and parameter manipulations that are available.

For example, from (3.35) it can be seen that, providing the l.h.s and A remain constant, the resonant tank gain will also remain constant since only one real solution for $G_{tr} > 0$ exists. This implies that the load could, for example, be doubled and the overall converter DC-DC gain at resonance (G_r) maintained, providing N and A remain constant, and the ratio between the C_p and L_s changed appropriately. In this example C_p could be quartered and L_s left as is. From (3.36) this would result in the resonant frequency doubling.

Alternatively, it may be desired that the overall gain be doubled. The simplest way in which to achieve the alteration in gain is via the turns ratio of the transformer. If the resonant tank gain G_{tr} is maintained constant, the transformer gain simply has to double, i.e N must half. From (3.35) it can be seen that this action by itself would require an appropriate increase in the r.h.s in order to maintain the resonant tank gain, other components on the l.h.s must vary also. For example, the load resistance could be quadrupled. From (3.36) this manipulation would also result in the same resonant frequency. This is because the resonant components and resonant tank gain have remained unchanged.

Increasing the overall converter DC-DC gain at resonance (G_r) while maintaining the resonant frequency (f_r), and load, is also possible by considering the relationships provided by equations (3.35),(3.36).

For example, doubling G_r whilst maintaining G_{tr} and A, the transformer gain must double i.e N will halve. Since we require the resonant frequency to remain unchanged, from (3.36), the C_pL_s product must also remain constant. From (3.35), however, if N were to half the L_s/C_p ratio would need to reduce by a factor of 16. Achieving this requires that C_p and C_s are increased by a factor of 4 and L_s reduced by the same factor.

Equation (3.35) is also useful when considering the conversion from ideal to preferred component values. From (3.35) preferred components should be chosen such that L_s/C_p and A are as close to the ideal as possible. The penalty for any difference in component value will be an alteration in resonant frequency f_r.

The design process, as it stands, assumes that the resulting converter has a high efficiency (i.e through the use of diodes with low forward voltage drop in the rectifier). A low efficiency converter will have severely reduced output-voltage/current thus reducing the accuracy of the design process. The method can be easily modified, however, to accommodate for the loss in output voltage due to the rectifier diodes.

In this case, the diodes can simply be viewed as a parasitic load resistor. Thus the overall load resistance will appear larger, and the gain reduced (compared to that used in the design equations (3.13)(3.16)) due to the effective potential divider network that is present.

The following expressions can be utilised to compensate for the rectifier voltage drop:

$$R_L{}' = R_L\left(1+\frac{2V_d}{V_o}\right) \text{ since } R_L{}' = \frac{V_o+2V_d}{I_o} \text{ and } I_o = \frac{V_o}{R_L} \tag{3.37}$$

similarly:

$$G_{tr}{}' = G_{tr}\left(1+\frac{2V_d}{V_o}\right) \tag{3.38}$$

where R_L' and G_{tr}' are the effective load resistance and resonant tank gain, respectively, required (for substitution into (3.13) and (3.16)) to achieve the specifications, and V_d, V_o are the diode forward-voltage drop and converter output-voltage, respectively.

3.7 Design methodology for a Current-source

Section 3.3 has shown that the tank component values (L_s, C_s, C_p) are related to the tank gain at resonance G_{tr}, the transformer turns ratio N, the resonant switching frequency f_r, the parallel to series capacitor ratio ($A=C_p/C_s$) and load resistance R_L.

It is now shown that, as the load resistance is increased, the converter output current tends to a constant value. Solving both (3.13) and (3.16) for f_r, equating the results and further solving for G_{tr} then gives:

$$G_{tr} = \frac{\sqrt{2}}{4\pi^2\sqrt{L_s}}\sqrt{64L_s + N^4 R_L{}^2 C_p \pi^4 (A+1) + X} \tag{3.39}$$

where $X = \sqrt{4096L_s{}^2 + 128L_s N^4 R_L{}^2 C_p \pi^4 (A-1) + N^8 R_L{}^4 C_p{}^2 \pi^8 (A+1)^2}$

Now, for a given G_{tr} the output current I_o can be calculated as follows:

$$I_o = \frac{V_{dc} G_{tr}}{R_L N} \tag{3.40}$$

Substituting (3.39) into (3.40) gives an expression for the output current as a function of load, when operated about the resonant frequency.

Under ideal circumstances, the output current, at the resonant frequency, ideally tends to a constant minimum value as the load resistance is increased. This can be shown theoretically by taking the limit of (3.40) as $R_L \to \infty$ (open-circuit) after G_{tr} is eliminated through the use of (3.39) giving:

$$I_{o\_\min} = \frac{V_{dc} N \sqrt{C_p}\sqrt{A+1}}{2\sqrt{L_s}} \tag{3.41}$$

This is the minimum output current a theoretically ideal converter will provide when excited about the resonant frequency (assuming no losses). As the load resistance is increased towards open-circuit, whilst switching at resonance, the large converter stresses (implying a reduced efficiency) will reduce the ability of the converter to provide the current in (3.41) to near open-circuit loads.

With lower R_L, the output current will be larger. If we relate the maximum current (at minimum load resistance) to the 'open-circuit' current via the expression $I_{o\_max}=K.I_{o\_min}$, the required value of A can be calculated. Solving (3.41) for C_p/L_s then yields:

$$\frac{C_p}{L_s}=\frac{4I_{o\_\min}{}^2}{N^2(A+1)V_{dc}{}^2} \tag{3.42}$$

Dividing (3.16) by (3.13) , eliminating G_{tr} through the use of (3.40), replacing I_o with $K.I_{o\_min}$ and R_L with R_{L_min}, equating the result with (3.42) and finally solving for A gives:

$$A=-\frac{I_{o\_\min}{}^2N^2R_{L\_\min}{}^2\pi^4K^2\left(K^2-1\right)+16V_{dc}{}^2(1-K^2)}{K^2\left(I_{o\_\min}{}^2N^2R_{L\_\min}{}^2\pi^4\left(K^2-1\right)-16V_{dc}{}^2\right)} \tag{3.43}$$

It is now possible to generate boundaries on the minimum and maximum allowed values of N for a given design specification. To generate the minimum, the value of A must never be *-ve*, hence, solving for N in (3.43) at $A=0$ gives:

$$\frac{4V_{dc}}{I_{o\_\min}R_{L\_\min}K\pi^2}<N \tag{3.44}$$

To generate the maximum value, solving (3.43) for the limit of N as $A \to \infty$ gives the following constraint:

$$N<\frac{4V_{dc}}{\pi^2R_{L\_\min}I_{o\_\min}\sqrt{K^2-1}} \tag{3.45}$$

Hence, for a given specification, the range of N must first be calculated, the transformer turns ratio N specified, the capacitor ratio A calculated from (3.43), the G_{tr} calculated at the minimum load by assuming $I_o=K.I_{o\_min}$ and solving (3.40), and finally, computing the required components from (3.13) and (3.16). Note that f_r corresponds to the minimum resonant frequency of the converter, i.e at the minimum load resistance.

3.8 Current-source design example

The methodology is now applied to the design of a constant output-current converter. The specifications for the supply are provided in Table 3.III.

Table 3.III – DC-DC Converter Specifications

DC Input Voltage	Current source Range	Output voltage Range
18V	0→1A	10→20V

The theoretical open circuit output current, at resonance, is selected to be 10% larger than the required peak current, thereby ensuring that parasitic effects (such as losses in the resonant tank) will not reduce the current so as to make the design ineffective and will ensure above-resonance operation at the required peak output current. Therefore $I_{o\_min}=1.1A$. Now, selecting $K = 1.1$ ensures that, at the minimum specified load resistance, the output current at resonance will not exceed 1.21A. Equations (3.44) and (3.45) provide a constraint on the range of N. At 1A output, the minimum load resistance is 10Ω, hence $0.60<N<1.45$. Selecting an N of 1 for simplicity and reduction in converter cost, gives a $G_{tr}=0.672$ and from (3.45) the value of A is therefore found to be 0.582. Assuming a minimum switching resonant frequency of 133kHz, the required tank components from (3.13) and (3.16) are $C_p=128\text{nF}$ $C_s=220\text{nF}$ and $L_s=13.6\text{uH}$.

3.9 Experimental results

A prototype converter, Figure 3.6(a), based on the component values given in (3.8), is switched via a self-oscillating controller, Figure 3.6(b), at the resonant frequency, to verify the design methodology. See Appendix D for hardware details.

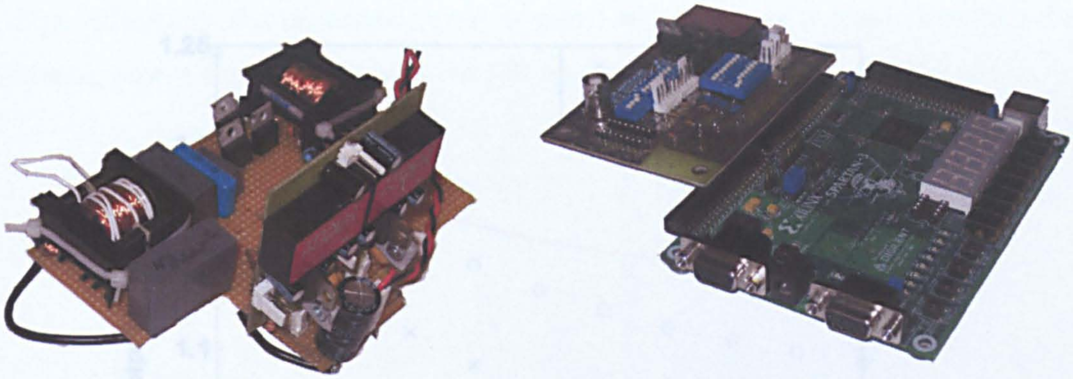

(a) (b)

Figure 3.6 - LCC inductively-smoothed resonant converter

(a) prototype converter (b) self-oscillating phase lock controller

Figure 3.7(a) provides the steady-state output current I_o when the converter is switched at the resonant frequency, for various loads. Included on the figure is the simulated converter output current and the output current predicted by the design process (see equations (3.39) & (3.40)) for comparison.

It can be seen that I_o does not change significantly over the load range when the converter is switched at the resonant frequency. Since a series-inductor resistance of 0.15Ω is present in the converter, it is expected that the experimental output-current data will be slightly lower than that of the ideal simulated converter. Note that, from an idealised perspective, the presence of a forward voltage drop should not reduce the output current below the theoretical open-circuit current since the diodes effectively make the load resistance appear larger, thereby forcing the converter to naturally compensate by increasing the resonant tank current.

Additionally, during open-circuit operation, and switching at resonance, the output-current from a practical perspective is clearly 0A. As a result of very high component stresses, and all the input-power being dissipated within parasitic elements, the converter will over-heat and ultimately fail. Figure 3.7(b) provides a measure of error in the proposed analysis. The largest error between the analysis and simulated converter is approximately 4%. The maximum error between measured output-current and that predicted from the presented analysis, occurs at the highest output power, and is approximately 10%. This makes the design process ideal for prototype component selection, especially when the simplicity of the underlying equations is considered.

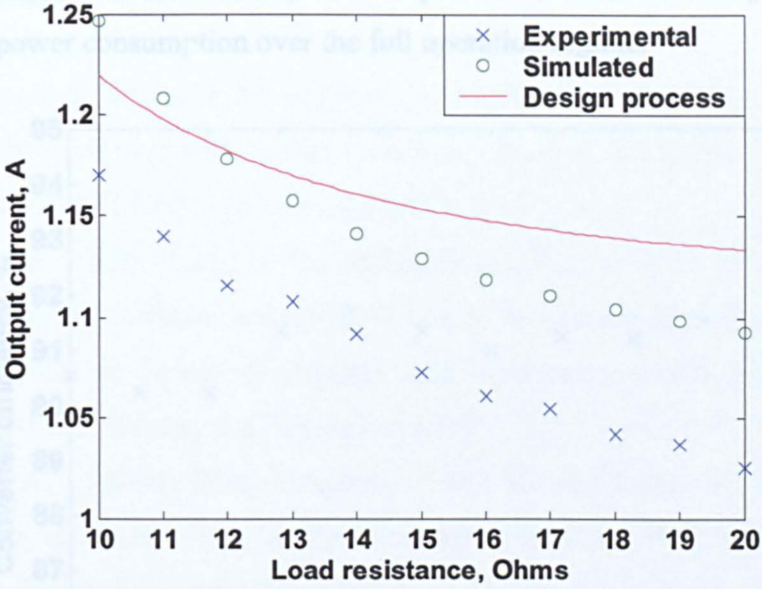

(a)

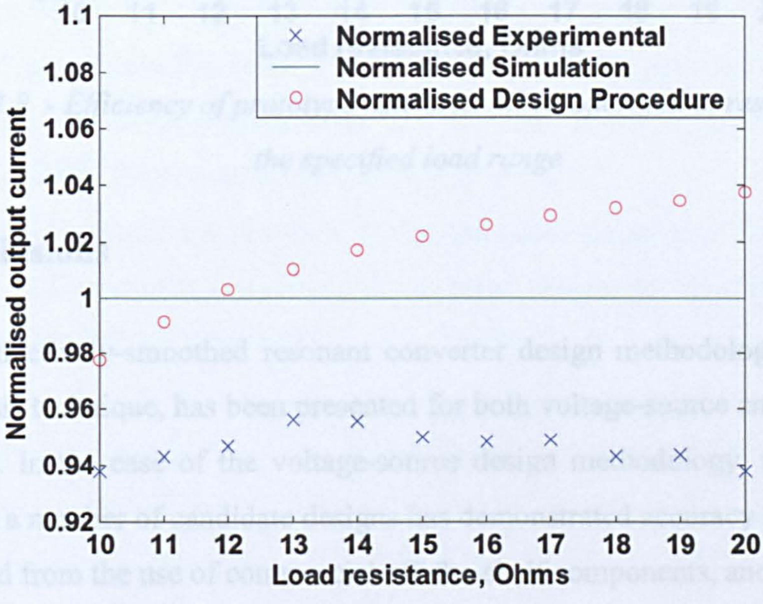

(b)

Figure 3.7 - (a) Output current (b) normalised output current w.r.t ideal converter simulation as the load is varied from 5Ω to 10Ω when switched at resonance

A benefit of the proposed design procedure, when a constant load current is desired, is the ability to operate near resonance across the full load range. This maximises the converter efficiency since less reactive power is circulated by the resonant tank. By way of example, Figure 3.8 provides the efficiency of the prototype converter for the load range specified in Table 3.III, when switched at the resonant frequency. It can be seen that high efficiency is maintained, even at part-load, which is a major benefit when considering power consumption over the full operation regime.

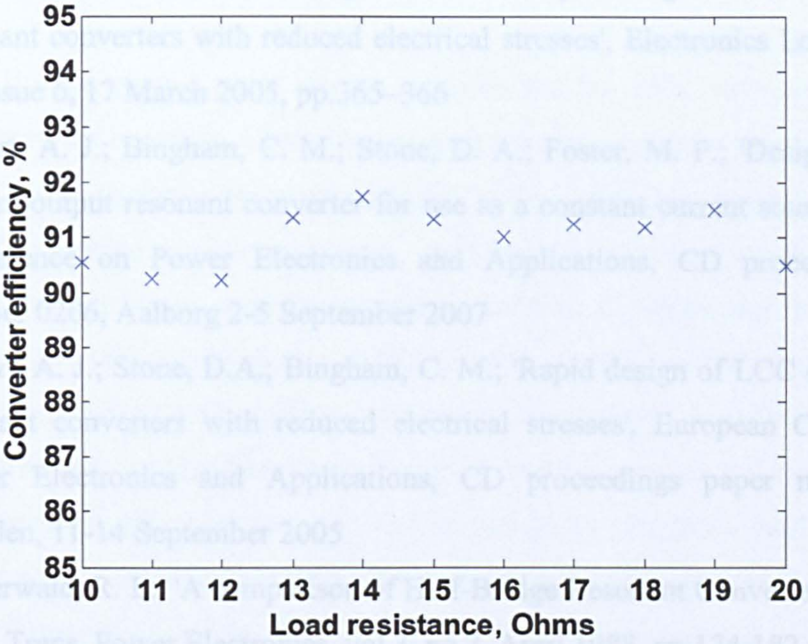

Figure 3.8 - Efficiency of prototype converter when operated at resonance over the specified load range

3.10 Conclusions

An LCC inductively-smoothed resonant converter design methodology, based on the FMA analysis technique, has been presented for both voltage-source and current-source applications. In the case of the voltage-source design methodology, a comparison of results from a number of candidate designs has demonstrated accuracy comparable with that expected from the use of commercial off-the-shelf components, and their associated tolerances. The current-source design methodology, on the other hand, has demonstrated near constant steady-state output current over an extended load range when switched at the resonant frequency. If supplied by a constant input voltage, the converter is capable of virtually constant output-current regulation in open-loop, via a self-oscillating switching mechanism. Results from a prototype converter have validated the proposed benefits. Both design methodologies are suitable for use in a rapid iterative design environment e.g. as part of a GUI, and aim to reduce resonant tank currents—thereby reducing the electrical stresses on components and improving tank efficiency.

3.11 References

[3.1] Gilbert, A. J.; Stone, D. A.; Bingham, C. M.; 'Rapid design of LCC current-output resonant converters with reduced electrical stresses', Electronics Letters, Volume 41, Issue 6, 17 March 2005, pp.365–366

[3.2] Gilbert, A. J.; Bingham, C. M.; Stone, D. A.; Foster, M. P.; 'Design of an LCC current-output resonant converter for use as a constant current source', European Conference on Power Electronics and Applications, CD proceedings paper number 0206, Aalborg 2-5 September 2007

[3.3] Gilbert, A. J.; Stone, D.A.; Bingham, C. M.; 'Rapid design of LCC current-output resonant converters with reduced electrical stresses', European Conference on Power Electronics and Applications, CD proceedings paper number 0627, Dresden, 11-14 September 2005

[3.4] Steigerwald, R. L.; 'A comparison of Half-Bridge Resonant Converter Topologies', IEEE Trans. Power Electronics, vol.3, no.2, April 1988, pp.174-182.

[3.5] Kazimierczuk, M. K.; Czarkowski, D.; Resonant Power Converters, John Wiley sons inc 1995, ISBN 0-471-04706-6 , Chapter 8 & 17.

[3.6] Forsyth, A.J; Ward G.A.; Mollov, S.V.; 'Extended fundamental frequency analysis of the LCC resonant converter', IEEE Trans. Power electronics, Vol.18, No.6, November 2003, pp.1286-1292

Chapter 4 - Rapid design and analysis of LCC Capacitively-smoothed Resonant Converters

Chapter 3 has developed novel design methods for the LCC inductively-smoothed resonant converter based on a behavioural analysis for operation around the resonant frequency. These concepts are now extended to be applicable to the more complex capacitively-smoothed converter variant, resulting in a new, easy to use, design methodology. Once again, component values are directly calculated from converter specifications. A full steady-state analysis for operation at, and above, the resonant frequency, normalised to the tank gain at resonance and the resonant tank capacitor ratio, is presented. Unlike previously reported steady-state analysis techniques for resonant converters, this methodology is computationally straightforward and intuitive. Graphical design curves are derived, and the use of preferred component values, is considered. Through use of the proposed normalised analysis technique, design regions are identified for the reduction of electrical stresses on components, and for the use of harmonics to transfer real power [4.1].

4.1 Introduction

The series-parallel ($L_sC_sC_p$) capacitively-smoothed resonant converter topology, shown in Figure 4.1, combines the advantages of the series resonant converter topology (C_p omitted) with that of the parallel resonant converter (C_s omitted). The series-resonant converter, for example, can only provide a gain (V_o/V_{dc})<½ when no transformer is used. Conversely the parallel-resonant converter contains a 'boost capacitor' C_p thereby allowing for the provision of gains >½, with no transformer [4.2-4.3].

This chapter concerns itself with the design and analysis of the capacitively-smoothed ($L_sC_sC_p$) topology [4.2-4.5], identified by the absence of an output filter inductor L_f, see Figure 4.1.

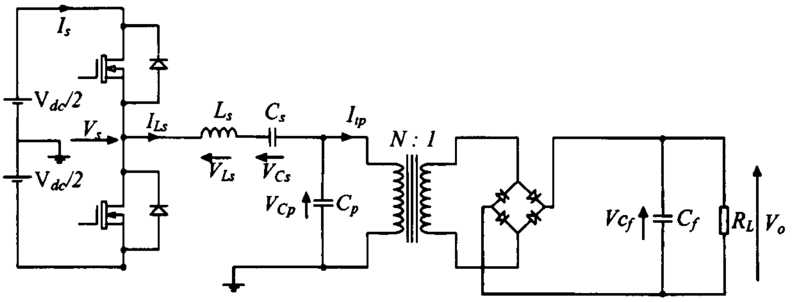

Figure 4.1 - LCC capacitively-smoothed resonant converter

This variant (Figure 4.1) is often selected in preference to the inductively-smoothed counterpart for its lower component count and reduced output filter order. Moreover, as a result of omitting L_f, output-voltage regulation is also made easier. During a transient open-circuit load, for example, the inclusion of a filter inductor forces the output voltage to rise momentarily even when switching has ceased. The capacitively-smoothed converter variant however, does not suffer from such problems. It is often used in high-voltage supplies where the forward voltage drop of the diodes does not unduly reduce overall efficiency.

Typical resonant tank waveforms, for a converter operating above the resonant frequency, are shown in Figure 4.2. The behaviour can generally be divided into 6 modes (M1, M2 ... M6), as shown, over one switching period.

Whilst having good part-load efficiency characteristics, the capacitively-smoothed topology is significantly more difficult to analyse as a result of the finite time taken to charge and discharge the parallel capacitor C_p. Fundamental Mode Approximation (FMA), the most widely used technique for analysis, assumes that the parallel capacitor waveform V_{Cp} is a square-wave, see Figure 4.2, which can therefore significantly degrade analysis accuracy [4.6-4.10].

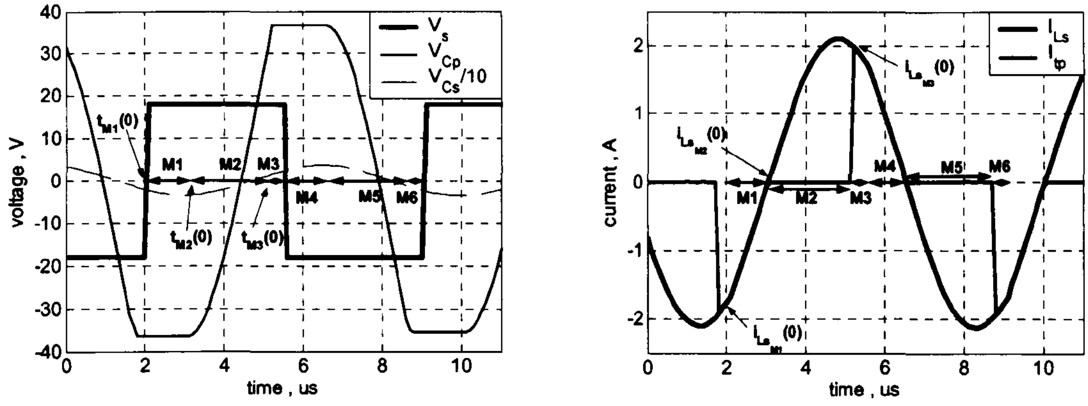

(a) (b)

Figure 4.2 - Typical above resonance operation of a heavily loaded converter excited above the resonant frequency (a) steady-state voltage waveforms (b) current waveforms

Considering operation of the converter during each mode, it can be seen that the parallel capacitor is charging during M2 and discharging during M5. In this chapter a full steady-state solution (component stresses, output voltage etc..) will be formed that incorporates the effects of these parallel-capacitor charging periods. For analysis and design simplicity, the methodology normalises the $L_sC_sC_p$ capacitively-smoothed resonant converter performance characteristics, in terms of the tank gain at resonance and parallel- to series-capacitor ratio. This is in contrast to previously published normalisation techniques [4.11-4.13] based on the un-damped or series resonant frequency, which leads to the actual system resonant frequency and gain being unknown, thereby not guaranteeing operation above the resonant frequency for a specific design. The resulting equations and graphical design curves are also more readily employed than those previously reported since it is not necessary to numerically solve simultaneous equations, as required in [4.11], for instance. Moreover, unlike previously reported techniques, the normalised converter analysis is used to identify design regions for reducing the electrical stresses on components, and the use of harmonics to transfer real power. Consideration of the use of preferred component values is also given. Both simulation results and experimental measurements from a prototype converter are included to demonstrate the attributes of the proposed analysis and design methodologies. The underlying methodology is incorporated into a software suite for use as part of a rapid interactive design tool.

Three converter operating scenarios are considered viz. operation at the resonant frequency; and operation above resonance for low and high loading conditions.

4.2 Converter operation at the resonant Frequency

When operating at the resonant frequency, 4 modes (M1..M4) describe the converter's behaviour over a single switching period in steady-state, as defined by the example waveforms in Figure 4.3. Mode M1 corresponds to the period when C_p is charging, whilst M2 corresponds to the rectifier conduction period - during this period the parallel capacitor voltage (V_{Cp}) is clamped to the referred DC output voltage. Through symmetry, M3 and M4 are similarly defined for the second half cycle.

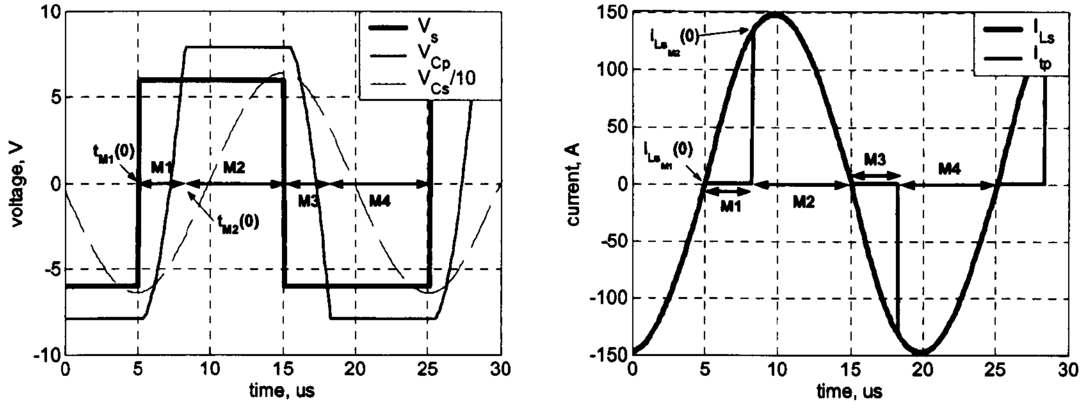

(a) (b)

Figure 4.3 – Definition of modes for operation at resonance (a) voltages (b) currents

The converter behaviour can be described by equivalent electrical networks, which, for operation during M1 and M2, are given in Figures 4.4(a) and 4.4(b), respectively, which can be used to derive a piece-wise description of steady-state operation.

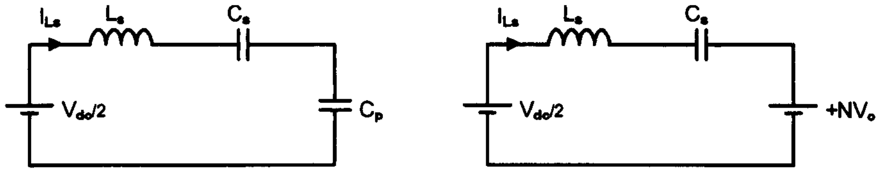

(a) (b)

Figure 4.4 – Equivalent circuits for operation at the resonant frequency during (a) M1 (b) M2

For simplicity, charge transfer through the series inductor during the various modes will be written as follows:

$$Q_{Mn} = \int_{t_{Mn}(0)}^{t_{Mn}+t_{Mn}(0)} i_{Ls_{Mn}}(t)\ dt \tag{4.1}$$

where t_{Mn} is the total time spent in mode n and $t_{Mn}(0)$ is the initial time of the mode.

When operating at resonance, the output voltage (V_o) is given by:

$$V_o = \frac{G_{tr} V_{dc}}{N} \tag{4.2}$$

where G_{tr} is the voltage gain of the tank ($\hat{V}_{Cp} / V_{dc}$). From Figure 4.3(a), it can be seen that during M1 the parallel capacitor C_p charges from the most negative clamped voltage to the most positive. The magnitude of the clamping voltage is equal to the output voltage referred to the primary winding of the transformer (NV_o). From (4.1), (4.2), the total charge supplied to C_p during M1 is:

$$\begin{gathered} \Delta V_{Cp_{M1}} = \frac{Q_{M1}}{C_p} = 2NV_o = 2G_{tr}V_{dc} \\ \rightarrow Q_{M1} = 2G_{tr}V_{dc}C_p \end{gathered} \tag{4.3}$$

To provide the initial conditions for each mode it is instructive to consider expressions for the power flow in the converter. Assuming high efficiency (negligible losses) operation, and that sufficient filter capacitance exists such that V_o can be considered constant over a single switching period (consideration of rectifier losses will be addressed in Section 4.8), the power provided by the square wave excitation source, P_s, and the power entering the transformer primary winding, P_{tw}, are both approximately equal to the output power, P_o giving:

$$P_s = V_{dc} f_r \left(Q_{M1} + Q_{M2}\right) \tag{4.4}$$

$$P_{tw} = 2V_{dc} G_{tr} f_r Q_{M2} \quad , \quad P_s \approx P_{tw} \approx P_o$$

$$P_o = \frac{G_{tr}^{\ 2} V_{dc}^{\ 2}}{N^2 R_L}$$

[Note that Q_{M1} and Q_{M2} are the charge transfers during mode 1 and 2 respectively from the excitation source]

From (4.4), equating P_{tw} and P_o provides an expression for the total charge transferred through the primary of the transformer during a half cycle, as follows:

$$Q_{M2} = \frac{G_{tr} V_{dc}}{2N^2 R_L f_r} \tag{4.5}$$

Now, equating P_s and P_{tw} in (4.4), eliminating Q_{M1} and Q_{M2} using (4.3),(4.5), and solving for C_p gives:

$$C_p = \frac{2G_{tr} - 1}{4N^2 R_L f_r} = \frac{F_1(G_{tr})}{N^2 R_L f_r} \text{ where } F_1(G_{tr}) = \frac{2G_{tr} - 1}{4} \tag{4.6}$$

Since $C_p > 0$, (4.6) provides a constraint on the minimum permissible resonant tank gain i.e $G_{tr} > ½$.

Equation (4.6) is one of the primary converter design equations. It will provide the required value of C_p for a given G_{tr}, N, R_L and f_r.

The parallel- to series-capacitor ratio, A, is defined as:

$$A = \frac{C_p}{C_s} \tag{4.7}$$

For convenience, designers of LCC converters often assume A=1 as a good compromise between bandwidth, component sizing, electrical stresses and impedance matching. It will be shown, however, that the proposed normalisation procedure can readily provide performance characteristics for alternative values of A, with additional benefits.

The voltage across C_s at the start of M1 is equal to the negative of the voltage at the end of M2:

$$V_{Cs_{M2}}(t_{M2}) = -V_{Cs_{M1}}(0) = V_{Cs_{M1}}(0) + \frac{1}{C_s}(Q_{M1} + Q_{M2}) \tag{4.8}$$

Substituting (4.3),(4.5) into (4.8) and solving for V_{Cs} at the start of M1 then gives:

$$V_{Cs_{M1}}(0) = -\frac{2AV_{dc}G_{tr}^{\ 2}}{2G_{tr} - 1} \tag{4.9}$$

During M1, the rectifier is non-conducting and the system consists of a basic series LC-network, Figure 4.4(a). The series and parallel capacitances effectively present a series combination, C_e, as seen from the perspective of the power devices, where:

$$C_e = \frac{C_p}{1 + A} \tag{4.10}$$

From Figure 4.4, the general solution for i_{Ls} during Mode n (Mn) is:

$$I_{Ls_{Mn}}(t) = I_{Ls_{Mn}}(0)\cos\left(\frac{t}{\sqrt{L_s C_e}}\right) + V_{Ls_{Mn}}(0)\sqrt{\frac{C_e}{L_s}}\sin\left(\frac{t}{\sqrt{L_s C_e}}\right) \tag{4.11}$$

with the inductor voltage at the start of M1 being given by:

$$V_{Ls_{M1}}(0) = \frac{V_{dc}}{2} - V_{Cs_{M1}}(0) - V_{Cp_{M1}}(0) \tag{4.12}$$

Substituting (4.9) into (4.12) and recalling that $V_{Cp_{M1}}(0) = -NV_o$ now gives:

$$V_{Ls_{M1}}(0) = \frac{V_{dc}\left(4(A+1)G_{tr}^{\,2} - 1\right)}{2(2G_{tr} - 1)} \tag{4.13}$$

From Figure 4.3(b), it can be seen that $I_{Ls_{M1}}(0) = 0$. Therefore, substituting (4.6),(4.10),(4.13) into (4.11) gives:

$$I_{Ls_{M1}}(t) = \frac{V_{dc}\left(4(A+1)G_{tr}^{\,2} - 1\right)}{4N\sqrt{R_L f_r (A+1) L_s (2G_{tr} - 1)}}\sin\left(2N\sqrt{\frac{R_L f_r (A+1)}{L_s(2G_{tr} - 1)}}\,t\right) \tag{4.14}$$

and substituting (4.6),(4.14),(4.3) into (4.1) and solving for $t = t_{M1}$ provides:

$$t_{M1} = \frac{1}{2}\sqrt{\frac{L_s(2G_{tr} - 1)}{N^2 R_L f_r (A+1)}}\left(\pi - \cos^{-1}\left(\frac{(A+1)(2G_{tr} - 1)^2 - A}{4(A+1)G_{tr}^{\,2} - 1}\right)\right) \tag{4.15}$$

To determine the initial conditions for M2, (4.15) is substituted into (4.14), for $t = t_{M1}$ giving:

$$I_{Ls_{M2}}(0) = \frac{V_{dc}}{N}\sqrt{\frac{G_{tr}(2(A+1)G_{tr} - 1)}{2R_L f_r L_s}} \tag{4.16}$$

and by differentiating (4.14) and inserting (4.15):

$$V_{Ls_{M2}}(0) = L_s \frac{d}{dt} I_{Ls_{M1}}(t_{M1}) = -\frac{V_{dc}\left((A+1)(2G_{tr} - 1)^2 - A\right)}{2(2G_{tr} - 1)} \tag{4.17}$$

During M2, the rectifier is conducting and V_{Cp} is clamped to NV_o, see Figure 4.4(b), and C_e as seen from the perspective of the power switches is given by:

$$C_e = \frac{C_p}{A} \tag{4.18}$$

Substituting the initial conditions (4.16),(4.17), and C_e, into (4.11), and eliminating C_p using (4.6), leaves:

$$\begin{aligned} I_{Ls_{M2}}(t) = {} & \frac{V_{dc}}{N}\sqrt{\frac{G_{tr}\left(2G_{tr}(A+1) - 1\right)}{2L_s R_L f_r}}\cos\left(t\,2N\sqrt{\frac{R_L f_r A}{L_s(2G_{tr} - 1)}}\right) \\ & \ldots - \frac{V_{dc}\left(G_{tr}4(A+1)(G_{tr} - 1) + 1\right)}{4N\sqrt{(2G_{tr} - 1)L_s R_L f_r A}}\sin\left(t\,2N\sqrt{\frac{R_L f_r A}{L_s(2G_{tr} - 1)}}\right) \end{aligned} \tag{4.19}$$

Now, M2 ends when i_{Ls}=0, hence, equating (4.19) to 0, and solving for $t=t_{M2}$ gives:

$$t_{M2} = \frac{1}{2N}\sqrt{\frac{L_s(2G_{tr}-1)}{AR_L f_r}}\cos^{-1}\left(\frac{(1+A)(2G_{tr}-1)^2 - A}{(1+A)(2G_{tr}-1)^2 + 2A(2G_{tr}-1) + A}\right) \tag{4.20}$$

Due to symmetry, the resonant frequency is related to the mode times by:

$$f_r = \frac{1}{2(t_{M1}+t_{M2})} \tag{4.21}$$

Substituting (4.15) and (4.20) into (4.21) gives a design value for L_s:

$$L_s = \frac{N^2 R_L}{f_r} F_2(A, G_{tr}) \tag{4.22}$$

where $F_2(A,G_{tr}) = \dfrac{1}{N^2 R_L 4 f_r \left(\dfrac{t_{M1}}{\sqrt{L_s}} + \dfrac{t_{M2}}{\sqrt{L_s}}\right)^2}$

and F_2 becomes solely a function of A and G_{tr} from the use of (4.15) and (4.20).

[note: the $\sqrt{L_s}$, N, R_L and f_r terms in $F_2(A,G_{tr})$ are cancelled by the respective terms in (4.15) and (4.20) hence as stated $F_2(A,G_{tr})$ depends explicitly on A and G_{tr} after the substitutions]

Equation (4.22) is another primary converter design equation. It will provide the required value of L_s for a given G_{tr}, A, N, R_L and f_r.

A key factor in the operation of resonant converters is the effective quality factor 'Q', at resonance, defined at the beginning of M1 as:

$$Q = 2\pi\frac{Energy\,Stored}{Energy\,Dissipated\,/\,cycle} = 2\pi\frac{E_s}{E_d} \tag{4.23}$$

The energy stored at the beginning of M1 (i_{Ls}=0) is given by:

$$E_s = \frac{C_p V_{Cs_{M1}}{}^2(0)}{2A} + \frac{C_p V_{Cp_{M1}}{}^2(0)}{2} \tag{4.24}$$

and the energy dissipated per cycle is:

$$E_d = \frac{V_{dc}{}^2 G_{tr}{}^2}{N^2 R_L f_r} \tag{4.25}$$

Substituting (4.9),(4.24),(4.25) into (4.23) and recalling that $V_{Cp_{M1}}(0) = -NV_o$, gives:

$$Q = \frac{\pi\left(4G_{tr}\left((A+1)G_{tr}-1\right)+1\right)}{4(2G_{tr}-1)} \tag{4.26}$$

It should be noted that the stored energy changes during each mode, as energy is first stored and then transferred to the load during respective modes. The effective 'Q' therefore changes during each mode. The 'energy profile' in steady-state therefore consists of a dc- value upon which a triangular-type energy profile is imposed. For the analysis presented here, the dc-baseline value at the start of M1 is therefore used.

To consider the accuracy of the design equations (4.6),(4.22) at resonance, various converter designs have been generated satisfying the specifications given in Table 4.I. The resulting ideal component values, given in Table 4.II, are used for simulating each converter in SPICE. Also given in Table 4.II are the values of G_{tr} and f_r obtained from the simulations using the calculated component values, from which it can be seen that an excellent correlation between them exists.

Table 4.I – Converter specifications at resonance

Design No.	G_{tr} *(V/V)*	*N (V/V)*	*A (F/F)*	f_r *(kHz)*	R_L *(Ω)*
(1)	0.55	0.1	10	25	0.1
(2)	0.6	0.75	5	125	5
(3)	0.7	0.33	0.5	100	10
(4)	0.8	10	1	15	0.3
(5)	0.9	20	4	75	20
(6)	1	0.25	5	60	100
(7)	2	1	2	20	10
(8)	5	10	0.5	100	2
(9)	10	0.1	20	200	10
(10)	20	0.25	10	50	1000

Table 4.II - SPICE simulation results when using ideal component values

	Designed Components			Simulation		% Error	
Design No.	L_s *(H)*	C_p *(F)*	C_s *(F)*	G_{tr} *(V/V)*	f_r *(kHz)*	G_{tr}	f_r
(1)	407n	1.00m	100u	0.535	25.0	-2.7	0.0
(2)	58.2u	142n	28.4n	0.599	125.2	-0.2	0.2
(3)	2.00u	900n	1.80u	0.700	100.1	0.0	0.1
(4)	447u	333n	333n	0.778	15.1	-2.8	0.6
(5)	59.8m	333p	83.3p	0.879	75.2	-2.3	0.3
(6)	58.0u	667n	133n	1.00	60.1	0.0	0.1
(7)	47.3u	3.75u	1.88u	2.01	20.1	0.5	0.0
(8)	32.6u	113n	225n	4.98	99.9	-0.4	-0.1
(9)	559n	9.50m	475u	9.98	20.0	-0.2	0
(10)	35.7u	3.12u	312n	20.1	50.0	0.5	0

4.2.1 Load dependent tank current

To maintain high part-load efficiency, it is desirable that the tank current (I_{Ls}) reduces as R_L increases. From (4.6):

$$G_{tr} - \frac{1}{2} = 2N^2 R_L f_r C_p \tag{4.27}$$

Since f_r increases for increasing R_L, doubling R_L results in at least a doubling of the r.h.s of (4.27). Note that with a near short-circuit load, C_p is effectively short-circuited and the resonant frequency is given by the series tank components. Conversely, with an open-circuit output, the rectifier is effectively disconnected and f_r is a function of both C_p and C_s, resulting in a higher resonant frequency. Consequently, if the r.h.s of (4.27) is initially large, doubling R_L will result in G_{tr} approximately doubling, thereby requiring operation far above the resonant frequency to regulate the output voltage. The resulting I_{Ls} will therefore be much larger than necessary. Conversely, if the r.h.s of (4.27) is made relatively small, for the minimum R_L, providing f_r is only modified slightly with an increase in resistance, G_{tr} will remain approximately constant, and operation can remain close to resonance. This implies two conditions for good loading performance. Firstly, A should be chosen to be large to provide good resonant frequency stability, and secondly, G_{tr} should be chosen to be ≈½ for the maximum load (minimum R_L). The penalty for this, is that, from (4.22) a higher value for L_s is required, and from (4.26) a larger effective '*Q*'.

4.2.2 Real power transfer by harmonic excitation

For applications where only very limited changes in load are expected (in some lighting applications, for instance) and a regulated output voltage is required, it is now shown that it is possible to reduce the peak current stresses on the tank components using harmonic power transfer. Considering (4.14) and (4.19) which describe the tank current, the peak can occur in either M1 or M2. If the derivative of I_{Ls} at the end of M1, is positive i.e. $V_{Ls_{M2}}(0)>0$, see (4.17), the peak current occurs in M2. Conversely, if the gradient is negative, the current has already peaked during M1. The peak current can therefore be expressed as:

$$\hat{I}_{Ls} = \frac{V_{dc}}{8N\sqrt{R_L f_r L_s (2G_{tr} - 1)}} \times \left(\frac{\left(\operatorname{sgn}\left(4AG_{tr}{}^2 - 4AG_{tr} + 4G_{tr}{}^2 - 4G_{tr} + 1\right) + 1\right)\left(4AG_{tr}{}^2 + 4G_{tr}{}^2 - 1\right)}{\sqrt{A+1}} \ldots\ldots + \frac{\left(1 - \operatorname{sgn}\left(4AG_{tr}{}^2 - 4AG_{tr} + 4G_{tr}{}^2 - 4G_{tr} + 1\right)\right)\left|4AG_{tr}{}^2 + 4G_{tr}{}^2 - 4G_{tr} + 1\right|}{\sqrt{A}} \right) \tag{4.28}$$

For a particular converter operating at high efficiency, about the resonant frequency, with a 50% duty cycle, I_{Ls} can be assumed sinusoidal, and all power supplied to the converter can therefore be assumed to be real. Therefore, to a first approximation, the input and output power can be equated:

$$P_{in} = \left(\frac{V_{dc}}{2}\right)\left(\frac{2\hat{I}_p}{\pi}\right), P_{out} = \frac{(V_{dc}G_{tr})^2}{N^2 R_L}, P_{in} = P_{out} \tag{4.29}$$

Simple rearrangement then leads to $\hat{I}_p$ being given by:

$$\hat{I}_p = \frac{\pi V_{dc} G_{tr}{}^2}{N^2 R_L} \tag{4.30}$$

where $\hat{I}_p$ corresponds to the minimum sinusoidal current peak that can be achieved for a given design specification and load R_L.

Using (4.28), (4.30) gives:

$$\hat{I}_{Ls_{norm1}} = \left(\frac{\hat{I}_{Ls} - \hat{I}_p}{\hat{I}_p}\right) \tag{4.31}$$

where $\hat{I}_{Ls_{norm1}}$ is the peak current normalised to an equivalent sinusoid, about the resonant frequency, and from (4.15),(4.20),(4.22),(4.28),(4.30) is solely a function of A and G_{tr}.

A 3-D plot showing the characteristic of (4.31) is given in Figure 4.5, from where it can be seen that $\hat{I}_{Ls}$ tends to the value described by (4.30), i.e. (4.31) tends to zero. It can also be seen that in certain regions of the A, G_{tr} plane, significant variations in current stress is evident.

For completeness, Figure 4.6 provides a magnified view of Figure 4.5 in the region of low G_{tr} and low A.

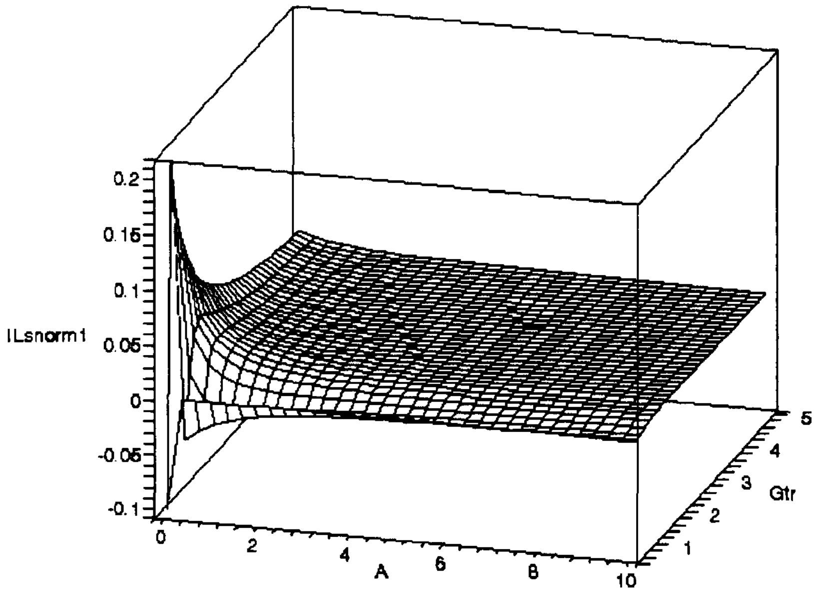

Figure 4.5 – 3-D plot of normalised inductor current at resonance

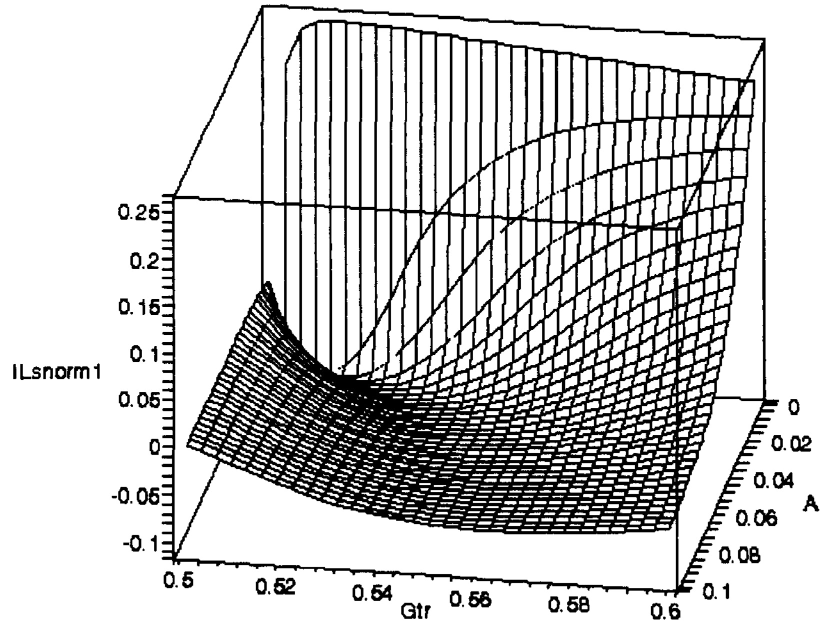

Figure 4.6 – 3-D plot of normalised inductor current, at resonance, in the low G_{tr} and low A regions.

It is clear that a region exists where $\hat{I}_{Ls}$ is lower than would be expected if sinusoidal tank currents were induced, thereby indicating that significant real power is being transferred on harmonics. Also, from Figure 4.6, it can be seen that as G_{tr} is varied, the minimum peak current occurs at a particular value of A that can be numerically calculated. The result is given in Figure 4.7. The corresponding percentage reduction in peak tank current is plotted in Figure 4.8. Although the peak current reduces, as a result of harmonic excitation, the overall rms current remains the same. See Table 4.VI for the practically measured power factor of various harmonics when operating above resonance.

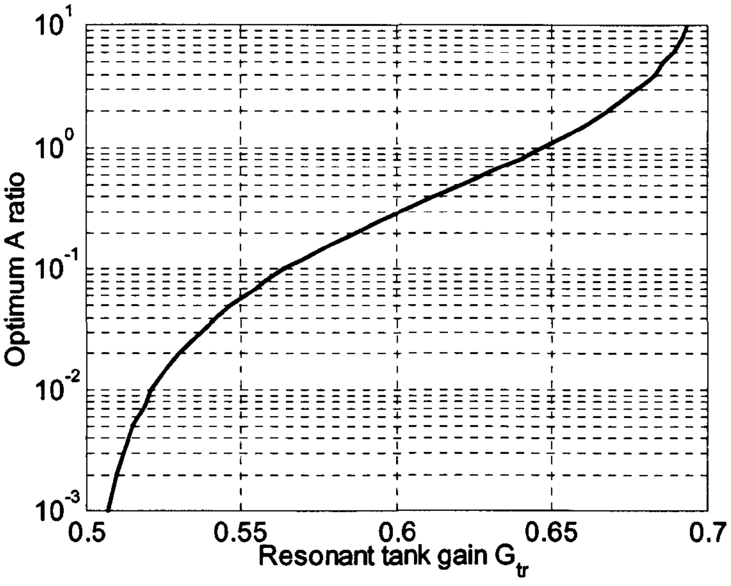

Figure 4.7 – Optimum A for peak current reduction vs G_{tr}

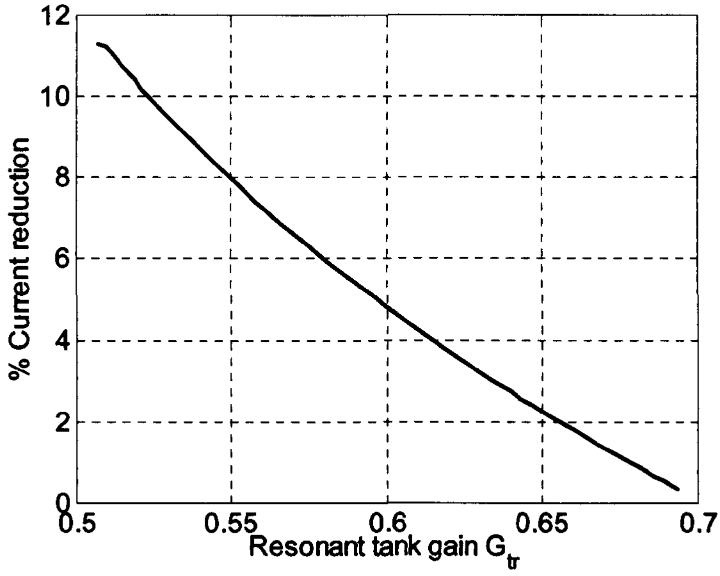

Figure 4.8 – % Current reduction at optimum A vs. G_{tr}

Again, it can be seen from Figure 4.8 that the penalty for reducing the current stresses on the tank components is that G_{tr} and A are small, thereby incurring a large variation in resonant frequency as the load changes, and reducing part-load efficiency. This design principle is therefore preferred when load variations are expected to be small.

4.2.3 Impact of component value choice

From (4.6):

$$C_p = \frac{F_1(G_{tr})}{N^2 R_L f_r} \tag{4.32}$$

and the required series inductor from (4.22) can be written:

$$L_s = \frac{N^2 R_L}{f_r} F_2(A, G_{tr}) \tag{4.33}$$

Equating f_r terms in both (4.32) and (4.33) provides the relationship:

$$\frac{L_s}{4N^4 R_L{}^2 C_p} = \frac{F_2(A, G_{tr})}{F_1(G_{tr})} \tag{4.34}$$

and equating the N^2R_L terms in both (4.32) and (4.33) gives:

$$f_r = \frac{1}{2}\sqrt{\frac{F_1(G_{tr})F_2(A, G_{tr})}{L_s C_p}} \tag{4.35}$$

Equations (4.34) and (4.35) provide important insight into the impact of component and parameter choices that are available to the designer. It will ultimately be shown that converters with similar values of A and G_{tr} possess similar properties, such as their normalised frequency responses. Moreover, it may be desirable to maintain certain favourable properties of a previously used design, with a new specification of converter. The following section therefore demonstrates how one can simply change i) the minimum load, ii) the overall gain and iii) the resonant frequency, of an existing design, to accommodate a different application requirement.

Scenario 1 - From (4.34) it can be seen that the converter's component values can be varied whilst maintaining a specific G_{tr} by ensuring that both the l.h.s of (4.34) and A remain constant. This implies that R_L can, for example, be doubled and G_{tr} maintained providing N remains constant, and L_s/C_p quadrupled. However, in general, this will result in a change of f_r. If this is not desired, maintaining f_r, from (4.35), requires a constant $C_p L_s$ product. Doubling L_s and halving C_p is therefore necessary.

Scenario 2 - Alternatively, it may be desirable that the overall converter gain (G_{tr}/N) be doubled, for instance. The most straightforward method to achieve this is via N. Whilst maintaining G_{tr}, N simply has to be halved. However, since A and G_{tr} are to remain constant, the resonant tank components must be appropriately selected i.e. from (4.34)

L_s/C_p must reduce by a factor of 16, generally resulting in a change of resonant frequency. Again, if this is not desirable, maintaining the resonant frequency, from (4.35), requires a constant $C_p L_s$ product. Consequently, C_p has to be quadrupled and L_s quartered.

Scenario 3 - Changing f_r, whilst maintaining N, G_{tr}, and A, for a nominal load, is achieved through the appropriate choice of tank component values. From (4.34) and (4.35) doubling f_r is achieved by halving both L_s and C_p. Equation (4.34) is also useful when considering the conversion from ideal to preferred component values, since the gain is usually the determining factor in a converter design. From (4.34) the preferred values can be chosen to satisfy component value ratio constraints, such as L_s/C_p and A, giving greater flexibility.

4.3 Heavily loaded operation ($1 \le f_m \le \frac{2G_o+1}{2G_{tr}-1}$)

Some fundamental definitions are:

$$V_o = \frac{G_o}{N} V_{dc} \tag{4.36}$$

$f_s = f_m f_r$ f_m relates the resonant frequency to the switching frequency (4.37)

where f_r is the resonant frequency, f_s is the switching frequency, $f_m > 1$ for operation above resonance and G_o is the resonant tank gain at f_s. [Note that f_m is dimensionless]

Figure 4.9 shows typical current and voltage waveforms for converter operation above resonance. The behaviour can now be divided into 6 modes (M1, M2 ... M6). Due to symmetry, it is sufficient to restrict the analysis to the first half cycle of operation.

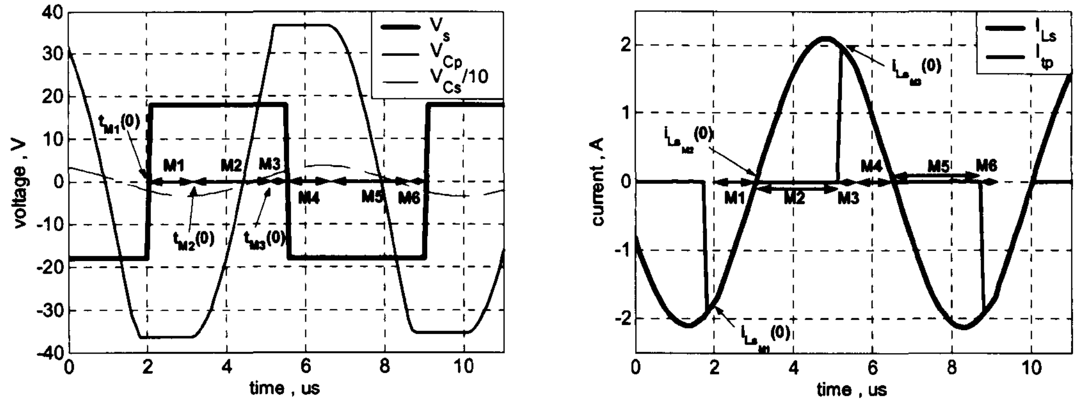

(a) (b)

Figure 4.9 - Modes for operation above the resonant frequency of a heavily loaded converter (a) voltage waveforms (b) current waveforms

Equivalent circuits for M1, M2 and M3 are given, respectively, in Figures 4.11 (a),(b) and (c), and can be used to form a piece-wise steady-state solution of the converter's behaviour.

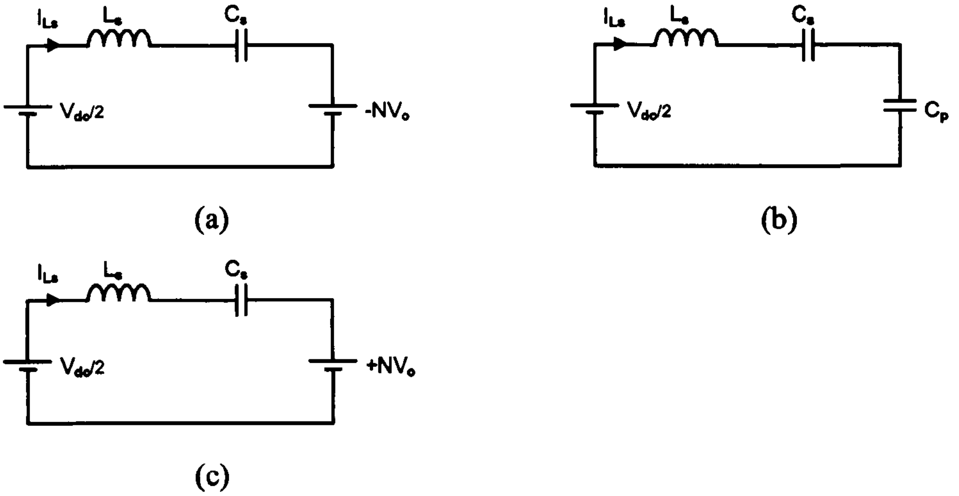

(a) (b) (c)

Figure 4.11 - Equivalent circuits for (a)M1 (b)M2 (c)M3 for a heavily loaded converter operating above resonance

It is important to consider the power transfer mechanisms in the converter. For high efficiency operation, as a first approximation, P_s, P_{tw} and P_o, are considered equal. From Figure 4.9, the following expressions can be written, where t_{M1}, t_{M2}, t_{M3} are the total times spend in M1, M2, M3 respectively:

$$P_s = V_{dc} f_m f_r \left(Q_{M1} + Q_{M2} + Q_{M3}\right)$$

$$P_{tw} = 2G_o V_{dc} f_m f_r \left(-Q_{M1} + Q_{M3}\right) \ , \ P_s \approx P_{tw} \approx P_o \tag{4.38}$$

$$P_o = \frac{V_{dc}^{\ 2} G_o^{\ 2}}{N^2 R_L}$$

Also from Figure 4.9, it can be seen that no power transfer from the supply to the load occurs during M2 since no current enters the primary of the transformer.

During M2 all the tank current charges C_p from $-NV_o$ to $+NV_o$, then, when (4.6) is used as a substitution for C_p the total charge is given as:

$$Q_{M2} = \frac{V_{dc} G_o \left(2G_{tr} - 1\right)}{2 f_r N^2 R_L} \tag{4.39}$$

Since the procedure to calculate the mode times for heavy loading is similar to that used previously, when the converter is operating at resonance, the derivation and mode time expressions are summarised in Appendix A for brevity.

4.4 Lightly loaded operation ($f_m \geq \frac{2G_o + 1}{2G_{tr} - 1}$)

The methodology presented in this section is similar to that for heavy loading. Figure 4.11 shows example current and voltage waveforms for operation above resonance under light loading conditions. The behaviour of the converter can be divided into 6 modes (M1, M2 … M6). Once again, it is sufficient to analyse the converter during the first half cycle only.

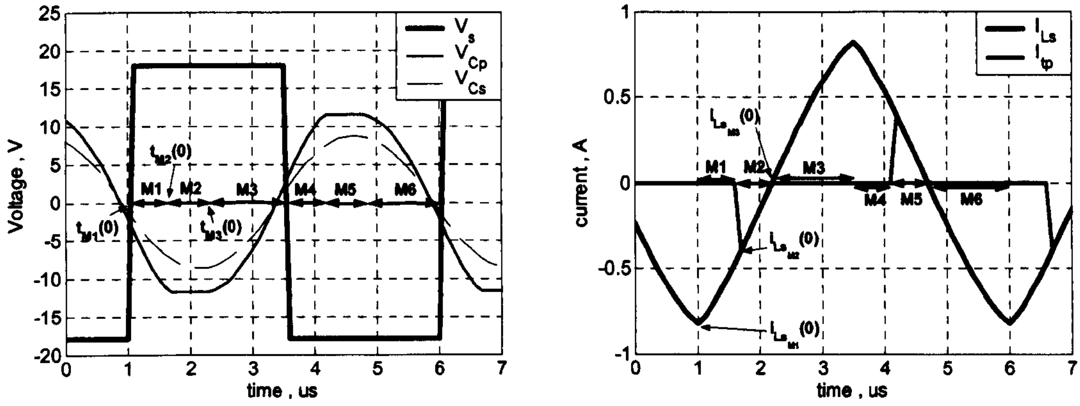

(a) (b)

Figure 4.11 – Modes of operation of a lightly loaded converter (a) voltage waveforms (b) current waveforms

Equivalent circuits for M1,M2,M3 are given in Figure 4.12 (a),(b),(c) respectively.

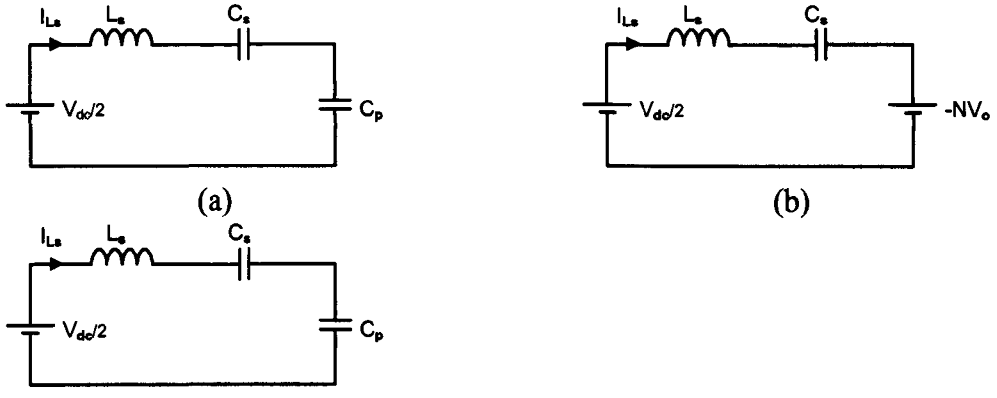

(a) (b) (c)

Figure 4.12 – Equivalent circuits during modes (a) M1 (b) M2 (c) M3 for a lightly loaded converter operating above resonance

From Figure 4.11, the following expressions for P_s, P_{tw} and P_o can be derived (note that all power transfer to the load occurs during M2):

$$P_s = V_{dc} f_m f_r \left(Q_{M1} + Q_{M2} + Q_{M3}\right)$$

$$P_{tw} = -2G_o V_{dc} f_m f_r Q_{M2} \qquad , \; P_s \approx P_{tw} \approx P_o \tag{4.40}$$

$$P_o = \frac{V_{dc}^{\;2} G_o^{\;2}}{N^2 R_L}$$

During M3, M4 all the tank current charges C$_p$ from $-NV_o$ to $+NV_o$ Volts, and the following relationship is obtained when (4.6) is used as a substitution for C_p:

$$\frac{V_{dc} G_o \left(2G_{tr} - 1\right)}{2 f_r N^2 R_L} = -Q_{M1} + Q_{M3} \tag{4.41}$$

Since the procedure to calculate the mode times for light loading is similar to that used previously, when the converter is operating at resonance, the derivation and mode time expressions are again summarised in Appendix B for brevity.

4.5 Normalised frequency response

During steady-state operation, the half-cycle switching period is the sum of the mode times:

$$t_{M1} + t_{M2} + t_{M3} - \frac{1}{2 f_m f_r} = 0 \tag{4.42}$$

The expressions for the mode times given in the Appendices, equations {(A.9), (A.12), (A.17)} and {(B.10), (B.15), (B.22)}, can be substituted into (4.42) to provide the half-cycle solution for the heavily and lightly loaded cases, respectively. When L_s is eliminated from the mode time expressions through the use of (4.15), (4.20) and (4.22), the converter frequency response can be extracted from (4.42) and is explicitly dependent on only 4 variables viz. G_{tr}, A, G_o, f_m

Equation (4.42) can be used to generate a frequency response to aid in the design of converters. For example, a designer may choose to nominally operate at a specific percentage above f_r, with a given G_o and A, the only unknown then being G_{tr}. Once the particular G_{tr} is calculated, the required converter component values can be simply generated from (4.2), (4.6), (4.7), (4.15), (4.20), (4.22).

Whilst generating a frequency response it is necessary to identify whether the converter is heavily or lightly loaded so that the correct set of equations can be utilised. This is achieved through analysis of the mode times. At the transition between the two conditions, when the converter is critically loaded, $t_{M3(heavy\ loading)} = t_{M1(light\ loading)} = 0$. Equating the charge transfer through the series inductor during either of these two modes, to zero, (appendix equations (A.2), (B.1)), and solving for f_m provides the following inequality for heavy loading operation (note: using mode time expressions (A.17), (B.22) also leads to the same result, although the calculation is more complex):

$$f_m < \frac{2G_o + 1}{2G_{tr} - 1} \tag{4.43}$$

Hence, if heavy loading is initially assumed, after solving f_m for a given G_o and G_{tr}, if (4.43) is satisfied then the heavy loading assumption is valid. Interestingly, setting $t_{M3} = 0$ during heavy loading, see equation (A.17), and utilising equations (4.22) and (4.43) to eliminate L_s and f_m, respectively, provides an expression relating G_o directly to G_{tr} and A at this critical loading point.

As an example of computation overhead, Figure 4.13 shows (a) the resonant tank frequency response and (b) phase response, for $G_{tr}=A=1$—the results show 50-point curves that were calculated in 2 seconds on a P4 2.4GHz, running MATLAB.

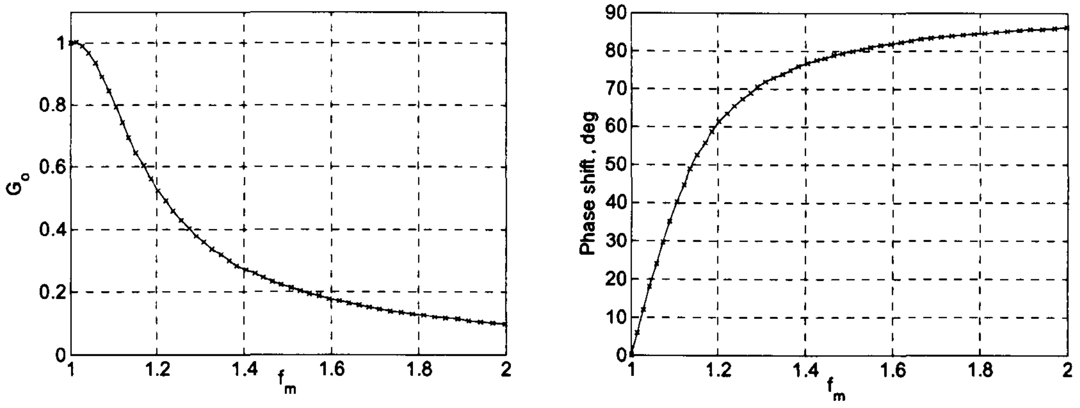

(a) (b)

Figure 4.13 - Tank frequency response (a) magnitude (b) phase response for $G_{tr}=A=1$

4.6 Normalised converter - output regulation

The behaviour of the converter, as a function of the load, is now investigated. For convenience, the applied load, R_L, and the nominal load, R_o, are related by the load scaling factor, R_x, as follow:

$$R_L = R_o R_x \tag{4.44}$$

From (4.6), (4.22), expressions for G_{tr} and f_r can be obtained by virtue of the resonant tank components remaining unchanged as the load is varied (where G_{tr_Ro}, f_{r_Ro} are the resonant tank gain and resonant frequency, respectively, when the load is at its nominal value ($R_x=1$)). From (4.6):

$$C_p = \frac{F_1(G_{tr\_Ro})}{N^2 R_o f_{r\_Ro}} = \frac{F_1(G_{tr})}{N^2 R_x R_o f_r} \quad \therefore \quad \frac{f_r}{f_{r\_Ro}} = \frac{F_1(G_{tr})}{R_x F_1(G_{tr\_Ro})} = \frac{(2G_{tr}-1)}{(2G_{tr\_Ro}-1)R_x} \tag{4.45}$$

Similarly, from (4.22) and using (4.45) to eliminate f_r/f_{r_Ro} gives:

$$\begin{gathered} \frac{L_s f_r}{N^2 R_o} = \frac{f_r}{f_{r\_Ro}} F_2(A,G_{tr\_Ro}) = R_x F_2(A,G_{tr}) \\ \rightarrow \sqrt{\frac{F_2(A,G_{tr\_Ro})}{F_1(G_{tr\_Ro})}} = R_x \sqrt{\frac{F_2(A,G_{tr})}{F_1(G_{tr})}} \end{gathered} \tag{4.46}$$

and

$$R_x = \sqrt{\frac{F_2(A,G_{tr\_Ro})F_1(G_{tr})}{F_1(G_{tr\_Ro})F_2(A,G_{tr})}} = \frac{F_3(A,G_{tr})}{F_3(A,G_{tr\_Ro})} \text{ where } F_3(A,G_{tr}) = \sqrt{\frac{F_1(G_{tr})}{F_2(A,G_{tr})}} \tag{4.47}$$

Since (4.47) is dependent only on G_{tr}, G_{tr_Ro}, R_x and A, a function numerically exists that provides the tank gain at resonance G_{tr} for a given A, G_{tr_Ro} and R_x obeying the constraint:

$$R_x F_3(A, G_{tr\_Ro}) - F_3(A, G_{tr}) = 0 \qquad (4.48)$$

From (4.48) it can be seen that as R_x is varied, the change in G_{tr}, and hence, f_r/f_{r_Ro} (see (4.45)) is identical for converters with the same A and G_{tr_Ro} at nominal load. In (4.42) it was also established that the frequency response of a converter is fully defined by its G_{tr} and A, hence, as load is varied, for a given A and G_{tr_Ro} at nominal load, the converter's normalised frequency response for all values of R_x is also fully defined, thereby implying that the normalised regulation performance of converters with similar G_{tr_Ro} and A, are identical. Consequently, assuming high efficiency operation, it is not necessary to analyse cases on an individual basis, even if respective converters differ in f_{r_Ro}, N, and R_o.

It is notable, however, that when the converter is regulated above resonance at nominal load and $G_o > ½$ (the normal condition), performance curves for $G_{tr\_Ro} = G_o$ can be used, since the converter can be thought to be operating with $R_{Lmin} > R_o$. For $G_o < ½$ this analogy cannot be used since converters cannot be generated with $G_{tr} \leq ½$ at any load.

Figure 4.14 provides the regulation performance curves for $G_{tr\_Ro}=A=1$ (the 50-point curves are calculated in 2.5 seconds on a P4 2.4GHz running MATLAB). Figure 4.14(a) is particularly useful when assessing the part load efficiency of converters. Ideally, $I_{Ls_{norm1}}$ would remain at, or below, unity for all loads, since this corresponds to a sinusoidal current at resonance. From Figure 4.14(a), when R_x=10, $\hat{I}_{Ls}$ is 7.5 times larger than for a sinusoidal current at resonance, see (4.30). Therefore, improved part-load efficiency occurs at lower gradients on the plot.

Figure 4.15 provides an example frequency response for $G_{tr}=A=1$. When generating the frequency response, if f_m is numerically calculated for a given G_o, care must be taken since two solutions are present. From a practical perspective it is necessary that the gradient of the transfer function remains –ve (for operation above resonance) over the whole load range, thereby ensuring that positive feedback at the controller never occurs. In the example considered, operating below $f_m \approx 1.01$ may result in instability. In a practical converter, the effects of parasitics may eliminate this potential problem, or indeed accentuate it.

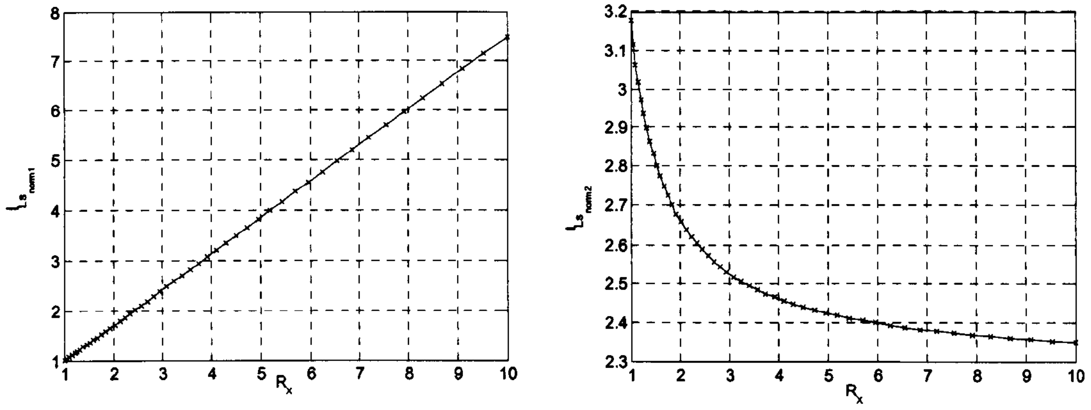

(a) Peak resonant current normalised to a sinusoid at resonance

$(\hat{I}_{Ls} = I_{Ls_{norm1}} \frac{V_{dc}}{N^2 R_o} \frac{\pi}{R_x})$

(b) Peak resonant current normalised to nominal load $(\hat{I}_{Ls} = I_{Ls_{norm2}} \frac{V_{dc}}{N^2 R_o})$

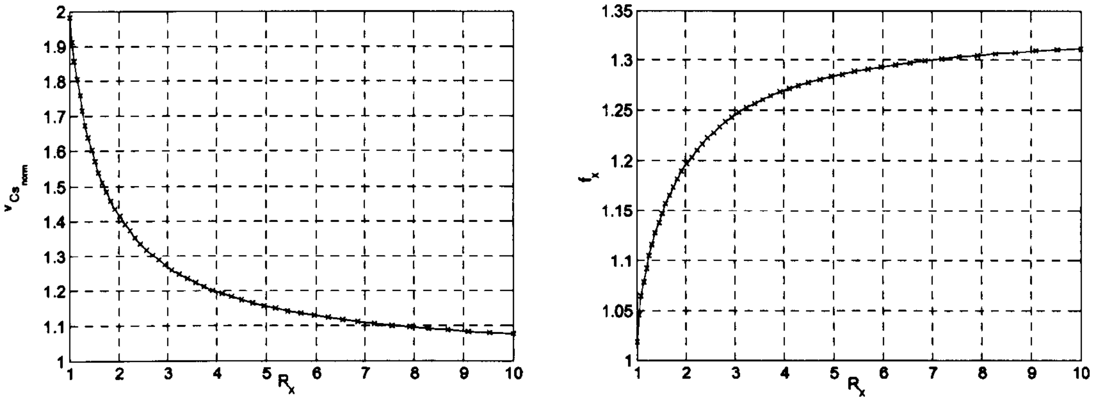

(c) Peak series capacitor voltage stress

$(\hat{V}_{Cs} = V_{Cs_{norm}} V_{dc})$

(d) Normalised Switching frequency wrt nominal load $(f_s = f_x f_{ro})$

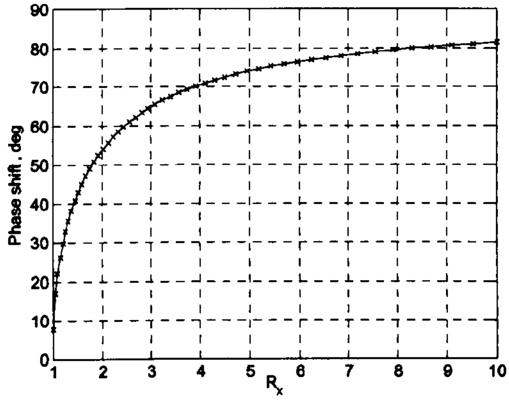

(e)Phase shift required for output regulation

Figure 4.14 - (a),(b),(c),(d),(e) provides the regulation performance curves for $G_{tr\_Ro}=G_o=A=1$.

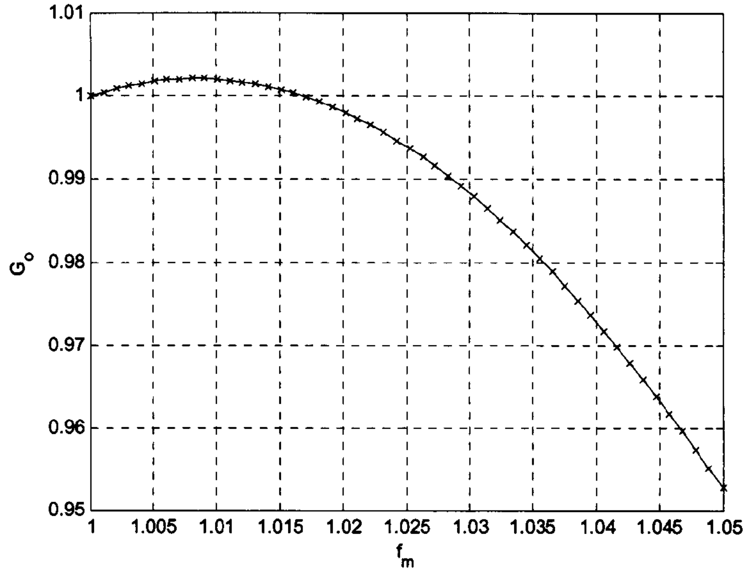

Figure 4.15 – Frequency response showing peak gain occurring above resonance

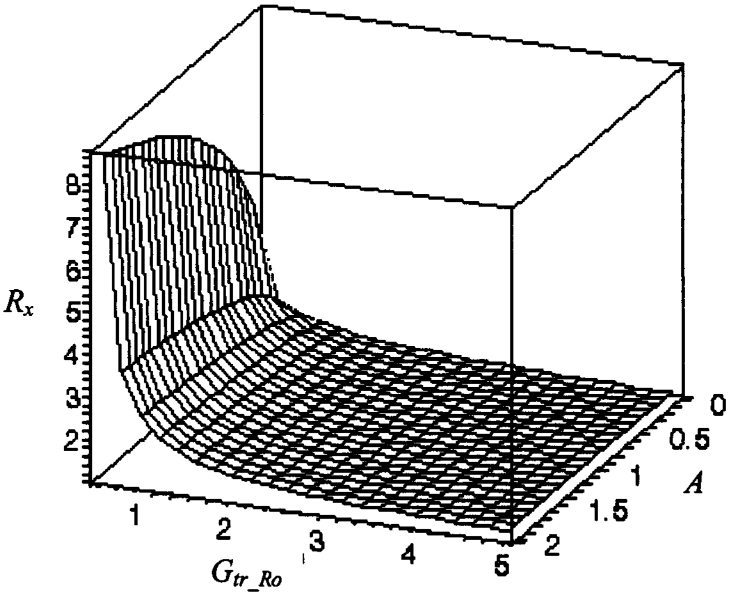

Figure 4.16 – Critical loading point (R_x) for converter regulated at nominal resonant tank gain G_{tr_Ro} and given A.

Converter operation has been previously described with respect to being either heavily or lightly loaded, the transition between the two being a critical point for analysis. Whilst generating the frequency response it has been necessary to find an expression for this borderline condition, see (4.43). In a similar manner, it is now also possible to derive an expression for the regulatory behaviour of the converter (i.e maintaining G_o while varying R_L through control of f_s). If it is assumed that the converter G_o is regulated at G_{tr_Ro}, as the load resistance is increased operation passes through the critical loading point into light loading. Setting $t_{M3} = 0$ in the heavy loading condition of (4.42) and utilising equations (4.43),(4.44),(4.45) gives an analytical expression relating R_x to G_{tr_Ro} and A. Figure 4.16 provides a plot of the resulting expression. From Figure 4.16, for instance, it can be seen that when a converter is regulated about its nominal resonant tank gain of $G_{tr\_Ro}=1$ and $A=2$, R_L can increase by a factor of 2.7 from its nominal level prior to light loading occurring. Also from Figure 4.16 it can be seen that for $G_{tr\_Ro} <1$, the heavy loading condition dominates the characteristic, and that light loading is more prevalent for large G_{tr_Ro}.

4.7 Normalised converter design curves

Here, normalised design curves for several G_{tr} values (see Figures 4.17&4.18) are presented for the common case A=1 using the majority of the equations presented in Appendices A and B, and those provided in section 4.2. For completeness, design curves for alternative A values are presented in Appendix C. From the curves, the converter's magnitude and phase response can be obtained, and additionally component values and electrical component stresses derived. Finally, a degree of insight into the steady state bandwidth of the converter is also identified. {note that the vertical axis on a number of the figures are in terms of G_o. The tank gain at resonance, G_{tr}, corresponds to the value of G_o when $f_m=1$, i.e the peak value of G_o}

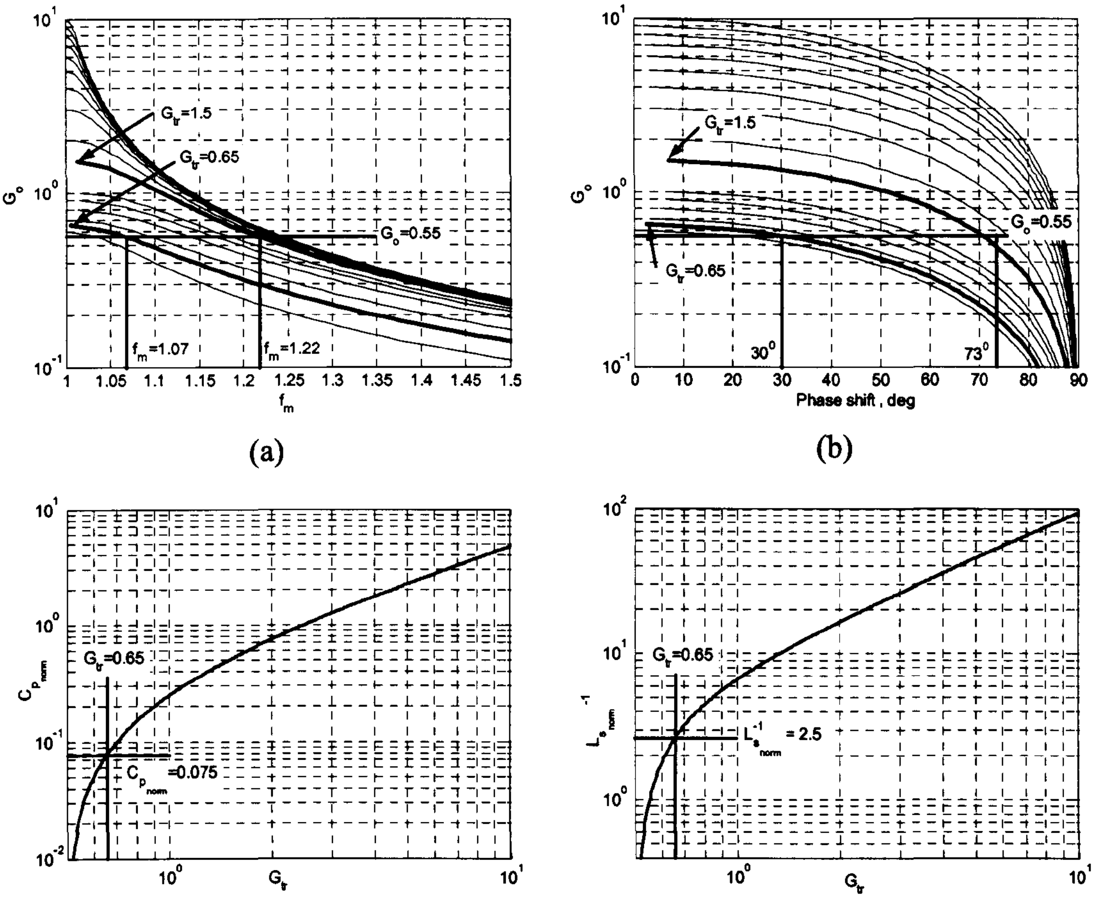

(a) (b)

(c) (d)

$$C_p = C_{p_{norm}} \frac{1}{N^2 R_L f_r} = \frac{2G_{tr}-1}{4N^2 R_L f_r}$$

$$L_s = L_{s_{norm}} \frac{N^2 R_L}{f_r} \approx \frac{N^2 R_L}{f_r(9.755G_{tr}-3.061)}, G_{tr} > 1$$

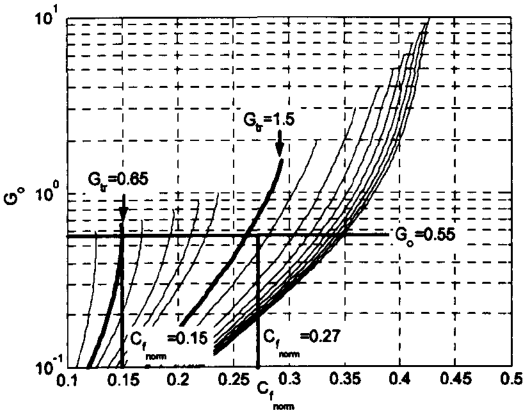

(e)

$$C_f = C_{f_{norm}} \frac{V_o}{R_L f_r V_{pp}}$$

Figure 4.17 –Design curves for A=1. (a) magnitude response (b) phase response (c) required parallel capacitor (d) required inductor (e) required filter capacitor

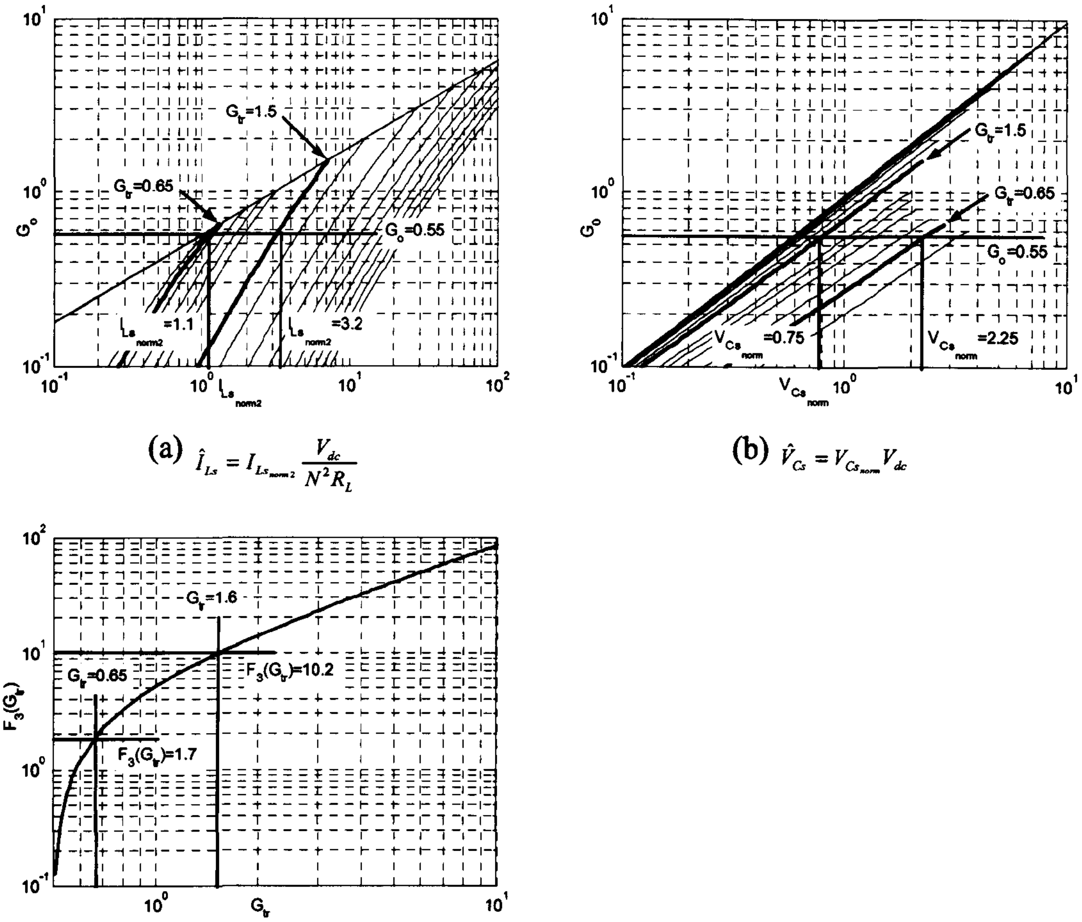

(a) $\hat{I}_{Ls} = I_{Ls_{norm2}} \frac{V_{dc}}{N^2 R_L}$

(b) $\hat{V}_{Cs} = V_{Cs_{norm}} V_{dc}$

(c)

Figure 4.18 –Design curves for A=1. (a) resonant inductor peak current (b) peak series capacitor voltage stress (c) resonant tank gain calculation curve

For steady-state regulation of the converter, G_{tr} should be considered as a function of load. The resonant frequency can then be calculated from (4.45). Once these parameters are known, Figure 4.17(a) allows the necessary value of f_m to maintain output voltage regulation, to be calculated, and subsequently, the associated switching frequency.

Figure 4.18(a) provides the peak series inductor current stress. The 'low gradient' asymptote added to the graph provides the peak inductor current stress that would be obtained had the current been a sinusoid at the resonant frequency, see (4.30). This is useful when considering converter efficiency.

From (4.48) it can be seen that $F_3(A,G_{tr}) = R_x F_3(A,G_{tr\_Ro})$. Since G_{tr_Ro} at R_L=R_o is well defined, $F_3(A,G_{tr\_Ro})$ can be readily evaluated. Now, if R_L is doubled from the nominal value (R_x=2), for example, the converter G_{tr} will vary. The value of G_{tr} obtained after this doubling can most easily be found graphically. Figure 4.18(c) provides a plot of $F_3(A, G_{tr})$ for $A=1$.

Figure 4.17(e) provides the necessary filter capacitance (C_f) to obtain a certain percentage output voltage ripple. During periods when C_p is charging, the output current is maintained by the charge stored on C_f. Assuming a constant load current implies a linear reduction in output voltage, which can be calculated from knowledge of the mode times.

From Figure 4.17(a) it can be seen that as G_{tr} increases, the necessary f_m for output voltage regulation is bounded. The highest value of f_m occurs during light loading, when G_{tr} is high. Finding the limit of (4.42) for light loading, as $G_{tr} \rightarrow \infty$ and solving for f_m gives the following:

$$f_{m_{\max}} \rightarrow \frac{\pi}{2\cos^{-1}\left(\dfrac{1}{1+2G_o(A+1)}\right)} \tag{4.49}$$

As the load tends to open circuit the resonant frequency tends to:

$$f_{r_{\max}} \rightarrow \frac{1}{2\pi}\sqrt{\frac{A+1}{L_s C_p}} \tag{4.50}$$

Equations (4.49),(4.50) can therefore be used to calculate the theoretical maximum steady-state control bandwidth to regulate the converter from nominal load to open circuit. The peak switching frequency required to regulate the converter tank gain at $G_o=G_{tr\_Ro}$ occurs at $f_{s_{\max}} = f_{m_{\max}} f_{r_{\max}}$ when the load resistance is assumed infinite. If G_o>½, which is the usual case, then the minimum switching frequency required to regulate the converter output voltage occurs at resonance when the load is at its nominal value. Solving (4.6) for R_L and substituting this into (4.22) provides an L_sC_p product. Substituting this product into the expression for $f_{s_{\max}}$ and dividing by f_r provides a measure of the steady-state control bandwidth dependent on G_{tr} at the nominal load (G_{tr_Ro}) and A only. Figure 4.19 provides a measure of the steady-state bandwidth (maximum frequency / minimum frequency) as G_{tr_Ro} is varied, for several A values ranging from 0.2 to 2 in steps of 0.2.

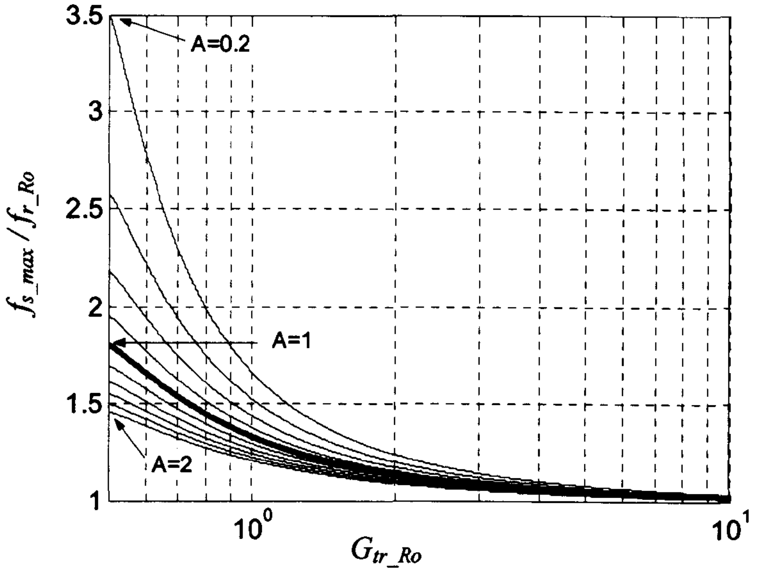

Figure 4.19 - provides a measure of the steady-state bandwidth (maximum frequency / minimum frequency) as G_{tr_Ro} is varied from >½ to 10, for several A values ranging from 0.2 to 2 in steps of 0.2. Note that for A=1 the maximum value is 1.8.

4.8 Design example with experimental results

Use of the design curves in Figures 4.17 & 4.18 will now be demonstrated by example. A converter specification is given in Table 4.III, from where it can be seen that the specification includes rectifier on-state voltages that can be modelled by parasitic load resistors, effectively making the overall load resistance appear larger. The overall gain is therefore reduced due to the potential divider network that is then present. The following expressions can be used to compensate for the rectifier voltage drop: (where R_L' and G_o' are the required effective load resistance and tank gain to achieve the specifications)

$$R_L' = R_L\left(1+\frac{2V_d}{V_o}\right) \quad \text{[Note: see (3.37) for the derivation]} \tag{4.51}$$

$$G_o' = G_o\left(1+\frac{2V_d}{V_o}\right) \tag{4.52}$$

Table 4.III – Converter specifications

Input voltage	V_{dc}	36V
Output voltage	V_o	18V
Load range	R_L	15→90Ω , (21W→4W)
Switching frequency range	$f_{s_{\min}} \to f_{s_{\max}}$	100kHz→150kHz
Parallel to series capacitor ratio	A	1
Ripple voltage	V_{pp}	0.18V

For use with the design curves, from (4.51) and (4.52), the minimum load and tank gain are therefore R_L'=16.5Ω, G_o'=0.55, respectively.

From (4.6), $G_{tr} > ½$, therefore it can be shown that providing $N \geq 0.5V_{dc}/\left(V_{o_{\max}} + 2V_d\right)$ a converter design exists meeting the specifications. To ensure that the converter operates above resonance at the desired output voltage, the converter shall be designed for a maximum output voltage (at resonance) of 21V (≈ 20% larger than required). A minimum value of N is therefore 0.8 (assuming at this stage V_d = 0.7V). However, for cost and volume reduction, the converter is not considered to include a transformer, and therefore, for calculation purposes, it is assumed that $N=1$. MUR1560 diodes are used for the full-bridge rectifier. When the converter is operated at the peak output power, I_f =1.2A, giving, from datasheets V_d = 0.9V. From Figure 4.17(a), the first curve that meets the specification corresponds to G_{tr}=0.65, as highlighted (0.65*V_{dc}-2V_d= 21.6V), and from Figure 4.17(b), the phase shift is approximately 30° above resonance. Also, from Figure 4.17(a) f_m =1.07. To ensure that the nominal gain occurs at the specified switching frequency, the resonant frequency is chosen to be f_r=93.5kHz. From Figures 4.17(c)(d), the normalised parallel capacitor and series inductor are found to be 0.075 and 2.5^{-1}, respectively, corresponding to idealised values of 48.6nF and 70.6μH. To obtain preferred values, whilst maintaining G_{tr}, component values should be chosen to maintain L_s/C_p and A constant (see (4.34)). If C_p = C_s=47nF and L_s=68uH, the requirement is satisfied. The new resonant frequency must now be calculated. From (4.35), since A and G_{tr} have remained constant, the resonant frequency will increase by a factor of 1.036 to 96.9kHz. The switching frequency will therefore have to be also increased to 103.6kHz. Finally, from Figure 4.17(e) the normalised filter capacitor required to limit the output voltage ripple to 10% is 0.15, corresponding to 10μF.

From Figures 4.18(a), 4.17(b) an indication of electrical component stresses can be found. The normalised peak inductor current and peak series capacitor voltage, are 1.1 and 2.25, respectively, corresponding to actual values of 2.4A and 81V.

Equation (4.47), $F_3(A,Gtr)$, provides a useful tool for the estimation of G_{tr} at an alternative load resistance R_L given the tank gain at resonance G_{tr_Ro} at the nominal load R_o. Figure 4.18(c) depicts (4.47) graphically for $A=1$. From Figure 4.18(c) an estimate of the switching frequency to maintain the output voltage for the minimum load (90Ω) can be obtained. An increase from 15Ω to 90Ω gives bounds for R_x i.e. R_x=1 to R_x=6. When G_{tr}=0.65, Figure 4.18(c) gives a value of 1.7 for $F_3(A,G_{tr})$, see (4.47). Since the load increases by a factor of 6 the resonant tank gain needs to be found to give a $F_3(A,G_{tr})$ value of 10.2 (=1.7×6), which from Figure 4.18(c) corresponds to G_{tr}=1.6. From (4.45) the 'new' resonant frequency is a factor of 1.22 higher than that at nominal load, giving 118.2kHz. Now, from Figure 4.17(a), extrapolating from the highlighted G_{tr}=1.5 curve, for G_{tr}=1.6, $f_m \approx 1.22$, and, from Figure 4.17(b) the phase shift is approximately 73°. The 'new' switching frequency is therefore 144.2kHz. Furthermore, from Figures 4.18(a)(b), the normalised peak current stress is 3.2 and normalised peak series capacitor voltage is 0.75, corresponding to 1.2A and 27V, respectively. Note that the 90Ω load is scaled to compensate for the rectifier diode losses using (4.52) to give 99Ω. From Figure 4.17(e) the normalised filter capacitance is now approximately 0.27, giving a peak-to-peak output voltage ripple of 42mV. Of note, in this case, is that if the 'new' switching frequency had exceeded the specifications, from Figure 4.19, given $A=1$, the value of G_{tr_Ro} would need to be increased to regulate the converter. In this case, it would be prudent incorporate a transformer to increase the effective turns ratio.

To verify the design procedure experimentally, a prototype converter has been commissioned with the calculated preferred component values, see Figure 4.20. Results from experiments are summarised in Table 4.IV, from where it can be seen that a high degree of correlation exists between the experimental and theoretical performance characteristics obtained from the analysis results and design procedure.

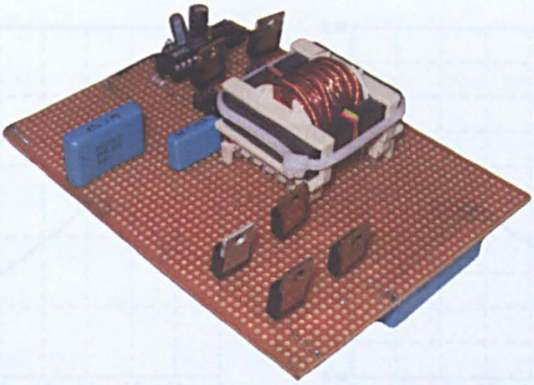

Figure 4.20 - Prototype LCC capacitively-smoothed resonant converter

Table 4.IV– Experimental measurements vs. theoretical estimates

	15Ω Load		90Ω Load	
	Theoretical	Experimental	Theoretical	Experimental
f_s (kHz)	103.6	101.3	144.2	143
$\hat{I}_{Ls}$ (A)	2.4	2.3	1.2	1.2
$\hat{V}_{cs}$ (V)	81	85	27	27
θ (°)	30	27	73	77
V_{pp} (V)	0.18	0.25	0.04	0.05

4.9 Using harmonics to transfer power

The possibility to transfer real power on harmonics, at the resonant frequency, has been previously discussed in section 4.2.2 to provide a mechanism for reducing peak current stresses. Here, similar curves to those presented in section 4.6, are given, for an A and G_{tr} that produce a peak current reduction. Regulation performance can then be determined. Component stress and regulation curves have been generated for a converter with A=0.1 and G_{tr}=0.55, in Figure 4.21, once again using the equations presented in section 4.2 and those from Appendices A and B. Within this section two designs will be compared, one utilising harmonic power transfer the other without. Design 1, with $A=1$, $G_{tr}=1$, will be referred to as the 'standard' design, whereas Design 2, utilising harmonic power transfer, has $A=0.1$ and $G_{tr}=0.55$, and will be referred to as the 'harmonic power transfer' design.

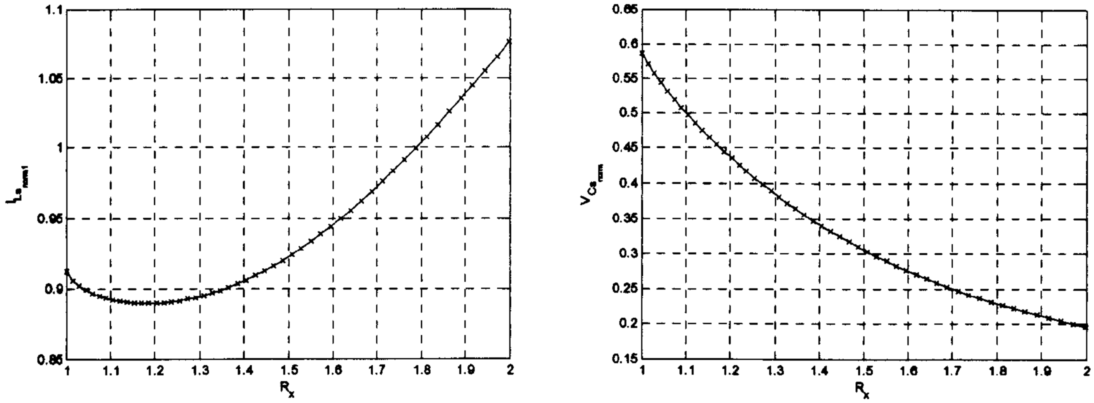

Peak resonant current normalised to a sinusoid at resonance

$(\hat{I}_{Ls} = I_{Ls_{norm1}} \frac{V_{dc}}{N^2 R_o} \frac{\pi}{R_x})$

(b) Peak series capacitor voltage stress

$(\hat{V}_{Cs} = V_{Cs_{norm}} V_{dc})$

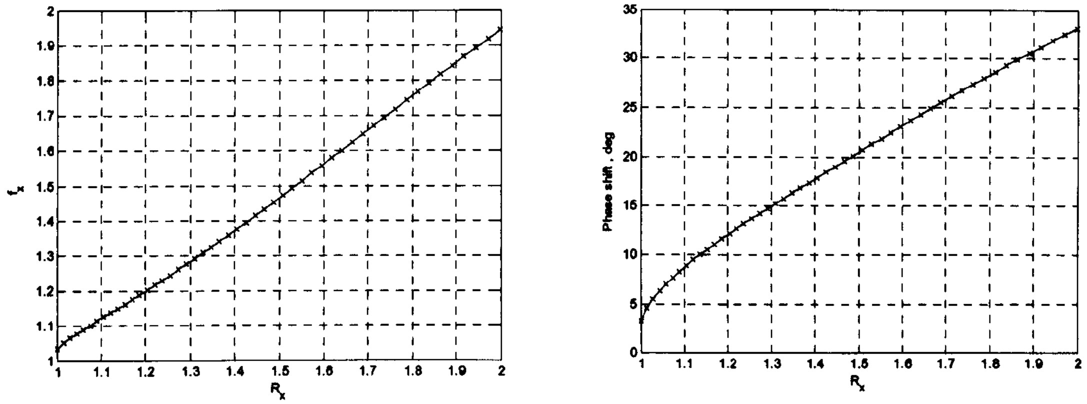

Regulation switching frequency normalised to nominal load ($f_s = f_x f_{ro}$)

(d) Phase shift required for output regulation

Figure 4.21 (a),(b),(c),(d) provide the regulation performance, G_o=0.55, curves for a converter with A=0.1 and G_{tr}=0.55 at nominal load ('harmonic power transfer' design).

Although peak series-inductor current naturally reduces as load resistance is increased and output-voltage regulated, the peak current in Figure 4.21(a) is falling lower than that for a sinusoid at resonance ($I_{Ls_{norm1}} = 1$) whilst delivering the same power to the load. The reduction in normalised peak current, occurring as R_L is increased, indicates that the tank current wave-shape is becoming increasingly 'square'. Comparing the peak normalised series-inductor current at R_x=*1* between the 'standard' design, Figure 4.14(a), and the 'harmonic power transfer' design, Figure 4.21(a), it can be seen that the peak current is ≈9% lower ($I_{Lsnorm1}$ =0.91). Similarly the 'harmonic power transfer' design has

≈22% lower peak current stress at R_x=1.2 and a ≈37% reduction at R_x=2. This implies that the 'harmonic power transfer' converter design will have improved part-load efficiency (over the load range R_x=1→2) compared to that of the 'standard' design. Alternatively designing the converter such that the nominal load occurs at the minimum normalised current could reduce stresses further at nominal load and enhance overall efficiency. Furthermore, by comparing the series capacitor stresses, from Figures 4.14(a) and 4.20(a), it can be seen that the series-capacitor voltage stress is approximately 70% lower at nominal load in the 'harmonic power transfer' converter design. From Figure 4.21(a) it can be seen that at R_x=2, the normalised current >1, hence, the harmonic power transfer is no longer able to compensate for the reduced power factor. The stress reduction at this load is therefore mainly due to the much reduced phase angle between switching voltage and series inductor current (23°) compared with (53°) for the 'standard' design, see Figures 4.21(d) and 4.14(e), respectively.

To verify the normalised stress reduction using an ideal SPICE model, the two designs have been generated around the input-/output-voltage and minimum load specifications provided in Table. 4.III. For the 'standard' design, where A=1 and G_{tr}=1, the ideal components required were N=2, L_s=91.6uH, C_s=C_p=42.4nF and the 'harmonic power transfer' design where A=0.1 and G_{tr}=0.55 the components required are N=1.1, L_s=25.5uH, C_s=142.2nF and C_p=14.22nF.

Table 4.V – SPICE simulation stress comparison between 'standard' and 'harmonic power transfer' converter design

	R_L (Ω)	f_s (kHz)	$\hat{I}_{Ls}$(A)	$\hat{V}_{Cs}$(V)
A=1, G_{tr}=1	15	100	1.91	71.4
'Standard' Design	30	117.4	1.60	51.1
A=0.1, G_{tr}=0.55	15	100	1.72	21.1
'Harmonic power transfer' Design	30	188.1	1.01	7.1

It can be seen that the data in Table 4.V closely matches that predicted from the normalised analysis, when considering the percentage reductions and increases in component stress and switching frequency respectively for the 'harmonic power transfer' design compared to that for the 'standard' design.

To show the ability of harmonics to carry power, Table 4.VI provides the harmonic content when the output is regulated at R_x=1 and R_x=1.2 for the 'new' converter design, along with the proportion of power transferred to the load. In particular, it can be seen that for the 22.5Ω case, the 3rd harmonic transfers approximately 3% of the total output power, although, importantly, this corresponds to an effective reduction in the peak electrical stresses incurred due to $\hat{I}_{Ls}$ of ≈10%.

Table 4.VI – Harmonic content of 'harmonic power transfer' converter design at various loads

Harmonic	R_L (Ω)	$\hat{I}_{Ls}$ (A)	$\hat{V}_s$ (V)	Phase (°)	Real Power (W)	% Power
Fundamental	15	1.83	22.9	6	20.9	96.8%
	22.5	1.54	22.9	8.4	17.4	96.7%
3rd	15	0.17	7.64	25.4	0.59	2.7%
	22.5	0.22	7.64	49.9	0.55	3.1%
5th	15	0.086	4.58	-50	0.13	0.6%
	22.5	0.093	4.58	84.6	0.02	0.1%

A consequence of reducing the electrical stresses, however, is that the switching bandwidth required to provide regulation over the whole load range also increases. Specifically, the 'standard' converter design required only ≈ 20% increase in switching frequency to maintain the gain, whereas the 'harmonic power transfer' converter design requires ≈ 90% increase in switching frequency over the same load range. This again indicates that utilising harmonics to carry power is more suited to applications were the load is expected to have limited variability.

4.10 Simplifying the design equation

By assuming large values of G_{tr}, an approximation to (4.22) can be found,

$$L_{s\,approx} = \frac{(A+1)N^2 R_L}{(2G_{tr}-1)\pi^2 f_r} \qquad (4.53)$$

Figure 4.22 presents a contour plot demonstrating the accuracy of the approximation. For each contour, the approximation (4.53) provides results that are a given percentage larger than those given by (4.22). The contours presented in the figure are 1% , 2%, 3%, … ,10%. The 10% contour being closest to the origin. Through use of both (4.53) and the contour plot, a very close approximation to (4.22) can be obtained.

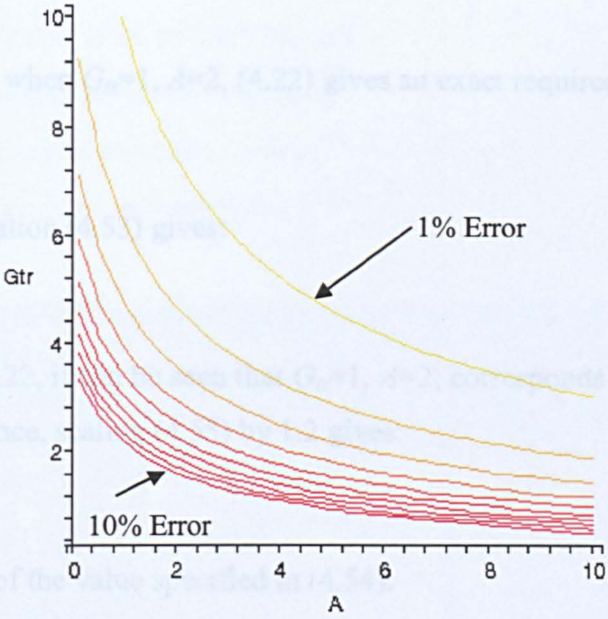

Figure 4.22 - Contours demonstrating approximation accuracy for various G_{tr}'s and A's –Contour closest and furthest away from origin corresponding to 10% and 1% error, respectively.

Similarly, Figure 4.23 provides contours at 10%, 20%, 30%, … , 100%, once again with the greatest error being closer to the origin.

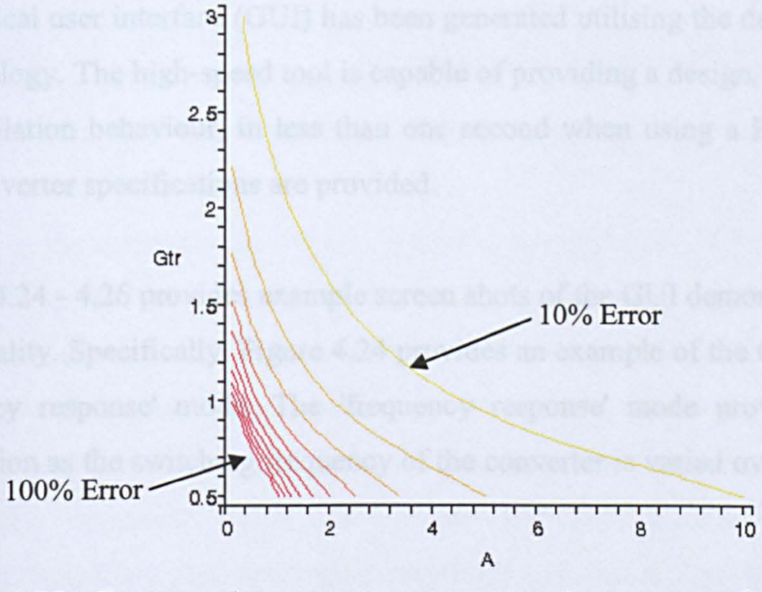

Figure 4.23 - Contours demonstrating approximation accuracy for various G_{tr}'s and A's –Contour closest and furthest away from origin corresponding to 100% and 10% error, respectively.

Since results from the approximation (4.53) are always larger than the 'exact' results obtained from (4.22), one can use equation (4.53) and, via the use of Figures 4.22 and 4.23, rapidly compensate for the error.

By way of example, when G_{tr}=1, A=2, (4.22) gives an exact required inductance of:

$$L_s = \frac{0.247\,N^2 R_L}{f_r} \tag{4.54}$$

whilst the approximation (4.53) gives:

$$L_s = \frac{0.203\,N^2 R_L}{f_r} \tag{4.55}$$

Now, from Figure 4.22, it can be seen that G_{tr}=1, A=2, corresponds to a contour slightly larger than 20%. Hence, scaling (4.55) by 1.2 gives:

$$L_s = \frac{0.243\,N^2 R_L}{f_r} \tag{4.56}$$

which is within 2% of the value specified in (4.54).

Generally, the exact design equation (4.22) is the more suitable for most applications. However, through use of Figures 4.22, 4.23 and (4.53), the designer may calculate the required L_s accurately and simply with a hand calculator.

4.11 Rapid interactive design tool

A graphical user interface (GUI) has been generated utilising the demonstrated analysis methodology. The high-speed tool is capable of providing a design, frequency response, and regulation behaviour, in less than one second when using a Pentium P4 2.8GHz, after converter specifications are provided.

Figures 4.24 - 4.26 provides example screen shots of the GUI demonstrating its versatile functionality. Specifically, Figure 4.24 provides an example of the GUI operating in the 'frequency response' mode. The 'frequency response' mode provides the following information as the switching frequency of the converter is varied over a specified range, viz.

- Output voltage
- Phase shift between
- Peak / RMS series inductor current
- Peak / RMS transformer primary current
- Peak / RMS series capacitor voltage
- Peak / RMS parallel capacitor voltage
- Transformer primary volt-seconds

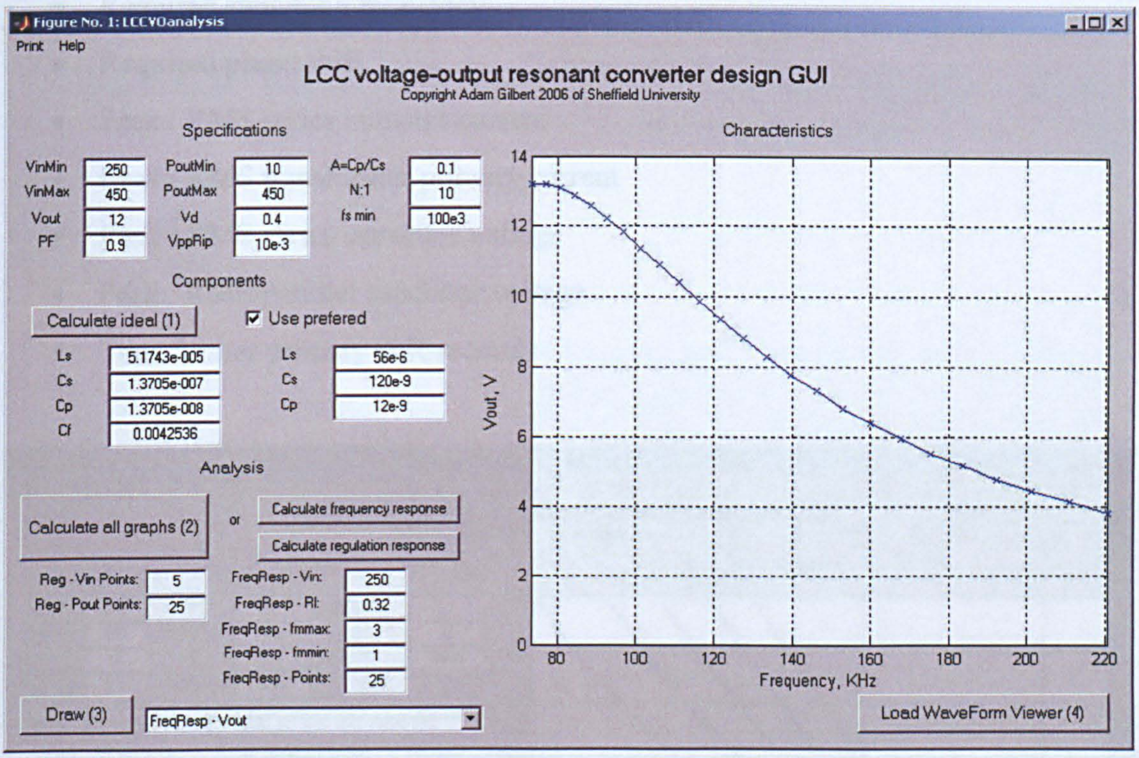

VinMin 250
VinMax 450
Vout 12
PF 0.9
PoutMin 10
PoutMax 450
Vd 0.4
VppRip 10e-3
A=Cp/Cs 0.1
N:1 10
fs min 100e3

Ls 5.1743e-005
Cs 1.3705e-007
Cp 1.3705e-008
Cf 0.0042536

☑ Use prefered
Ls 56e-6
Cs 120e-9
Cp 12e-9

Reg - Vin Points: 5
Reg - Pout Points: 25
FreqResp - Vin: 250
FreqResp - Rl: 0.32
FreqResp - fmmax: 3
FreqResp - fmmin: 1
FreqResp - Points: 25

FreqResp - Vout

Figure 4.24 - Screen shot of design GUI in 'frequency response' mode

Included in the converter specifications are the power-factor (*PF*) and peak-peak output voltage ripple. The power factor scales the maximum output voltage to V_{out} / PF at the resonant frequency under minimum supply-voltage and load resistance conditions. The *PF* specification provides a useful way of ensuring operation above the resonant frequency at the minimum specified switching frequency. Note that, for converters with sufficiently sinusoidal series-inductor currents (high *Q*-factor) at the minimum switching frequency, minimum load resistance and desired output voltage, the phase angle between the switching voltage and series inductor current is approximately $\theta \approx \cos^{-1}(PF)$ (above resonance); thereby justifying the use of the 'power factor' terminology. From the peak-peak output voltage ripple specification the user provides, the required output filter capacitance is recommended.

Figure 4.25 provides an example of the GUI operating in the 'output-voltage regulation' mode. This mode provides the following information as load resistance is varied over a specified range. Note that several curves are provided for each, over the specified supply-voltage range, viz.

- Required switching frequency
- Required phase shift
- Peak / RMS series inductor current
- Peak / RMS transformer primary current
- Peak / RMS series capacitor voltage
- Peak / RMS parallel capacitor voltage
- Transformer primary volt-seconds

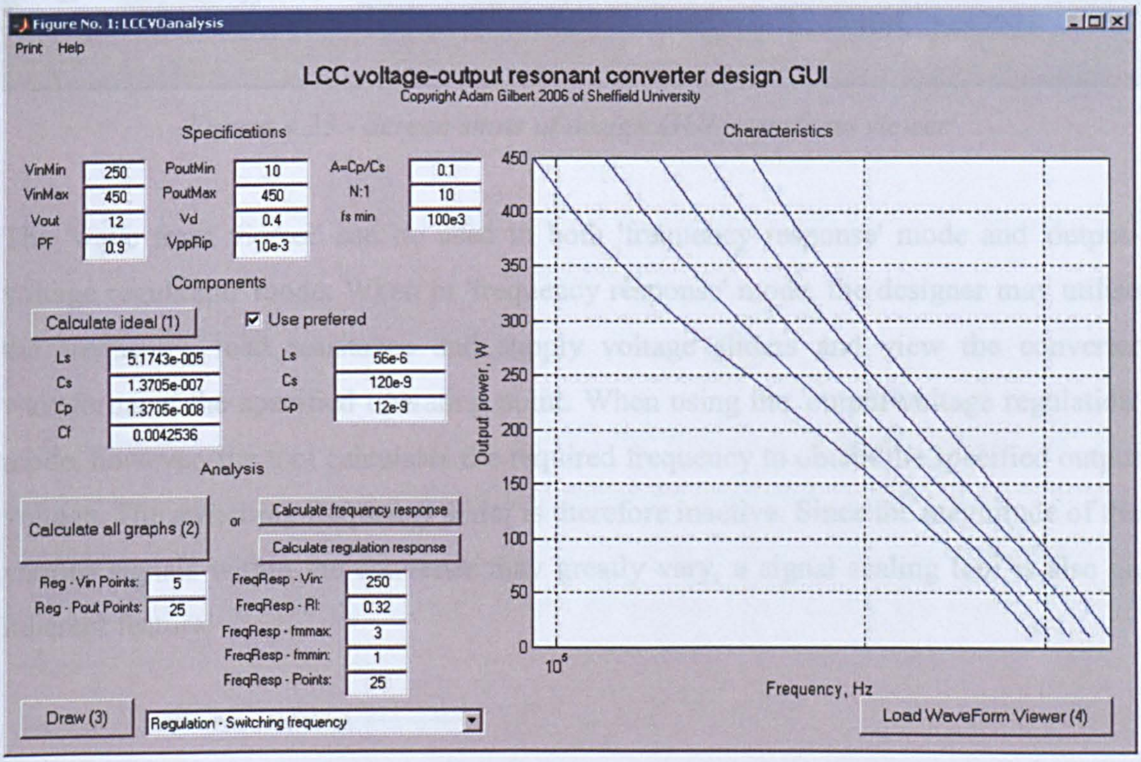

Figure No. 1: LCCVOanalysis

LCC voltage-output resonant converter design GUI

Copyright Adam Gilbert 2006 of Sheffield University

Specifications

VinMin 250
VinMax 450
Vout 12
PF 0.9
PoutMin 10
PoutMax 450
Vd 0.4
VppRip 10e-3
A=Cp/Cs 0.1
N:1 10
fs min 100e3

Components

☑ Use prefered

Ls 5.1743e-005
Cs 1.3705e-007
Cp 1.3705e-008
Cf 0.0042536

Ls 56e-6
Cs 120e-9
Cp 12e-9

Analysis

Reg - Vin Points: 5
Reg - Pout Points: 25
FreqResp - Vin: 250
FreqResp - Rl: 0.32
FreqResp - fmmax: 3
FreqResp - fmmin: 1
FreqResp - Points: 25

Regulation - Switching frequency

Figure 4.25 - Screen shots of design GUI in 'output-voltage regulation' mode

Finally, Figure 4.26 provides a screen-shot of the 'waveform viewer'. The tool permits a designer to view the shape of the current and voltage waveforms present in the converter, once again under a regulation and frequency response mode of operation.

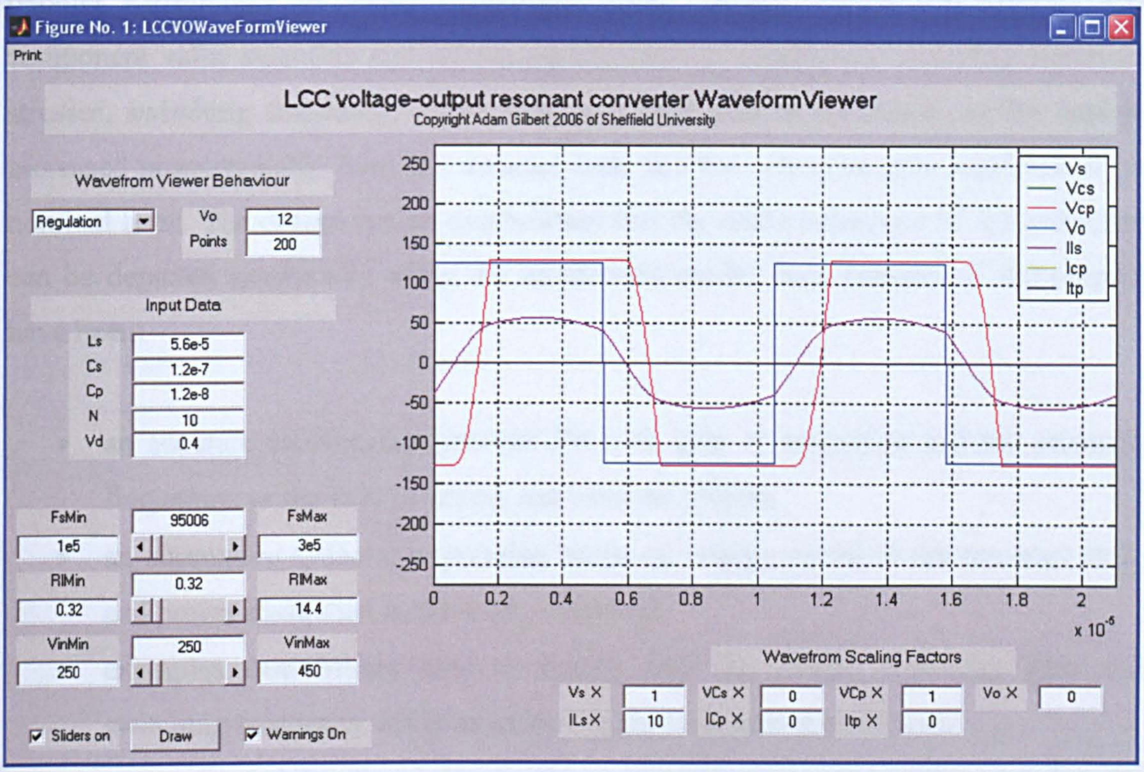

LCC voltage-output resonant converter WaveformViewer
Copyright Adam Gilbert 2006 of Sheffield University

Wavefrom Viewer Behaviour
Regulation
Vo 12
Points 200

Input Data
Ls 5.6e-5
Cs 1.2e-7
Cp 1.2e-8
N 10
Vd 0.4

FsMin 1e5 | 95006 | FsMax 3e5
RlMin 0.32 | 0.32 | RlMax 14.4
VinMin 250 | 250 | VinMax 450

☑ Sliders on
Draw
☑ Warnings On

Wavefrom Scaling Factors
Vs X 1
VCs X 0
VCp X 1
Vo X 0
ILs X 10
ICp X 0
Itp X 0

Figure 4.23 - Screen shots of design GUI 'waveform viewer'

The 'wave form viewer' can be used in both 'frequency response' mode and 'output-voltage regulation' mode. When in 'frequency response' mode, the designer may utilise the frequency, load resistance and supply voltage sliders and view the converter waveforms at the specified operating point. When using the 'output-voltage regulation' mode, however, the tool calculates the required frequency to obtain the specified output voltage. The switching frequency slider is therefore inactive. Since the magnitude of the various signals within the converter may greatly vary, a signal scaling tool is also an inherent feature.

4.12 Conclusion

This chapter has considered the normalised behaviour of the LCC capacitively-smoothed converter characteristics, in terms of the tank gain at resonance and the parallel capacitance to series capacitance ratio. Design curves are derived and component value selection and related performance is considered, including electrical stresses, switching frequency, phase shift, and tank gain at resonance, as the load is increased proportionally from the nominal load and the converter gain regulated at its nominal level. The design curves demonstrate that the entire behaviour of the converter can be depicted graphically using the normalised model. Key features of the chapter have been:

- an accurate relationship between the tank gain at resonance and the resonant frequency, as the load is varied, has been developed.
- an alternative Q-factor expression based on energy stored in the resonant tank, and power dissipated in the load, is derived.
- examples demonstrate how to simply alter the overall converter gain and switching frequency whilst maintaining the tank gain at resonance.
- expressions giving the maximum theoretical switching bandwidth to regulate the converter gain from nominal load to open circuit, are provided.
- an investigation into how the choice of nominal resonant tank gain and capacitor ratio affects part load efficiency, is given.
- a high-speed GUI is developed.

The presented methodology clearly defines the boundary between heavy and light loading conditions, in terms of normalised switching frequency or normalised load, and, as shown, is ideally suited for use in a graphical user interface. The underlying analysis has also identified operating regions where harmonics can transfer real power, thereby reducing peak current and component stresses. A design example has been provided and results compared with experimental measurements on a prototype converter demonstrating a high degree of correlation between theoretical and experimental performance characteristics. The design example also demonstrates how to select preferred component values and how the effects of rectifier voltage drop can be included in the design procedure.

Finally, it should be noted that although the analysis is derived for a bipolar input voltage, ultimately, the results are equally applicable to converters considered to have a uni-polar input by simply adding half the dc supply voltage to the steady-state series-capacitor voltage waveforms.

4.13 References

[4.1] Gilbert, A. J.; Stone, D. A.; Bingham, C. M.; Foster, M. P; 'Normalised analysis and design of LCC resonant converters', Accepted for Publication in IEEE Trans. Power Electronics, 2007

[4.2] Steigerwald, R. L.; 'A comparison of Half-Bridge Resonant Converter Topologies', IEEE Trans. Power Electronics, vol.3, no.2, April 1988, pp.174-182.

[4.3] Kazimierczuk, M. K.; Czarkowski, D.; 'Resonant Power Converters', John Wiley sons, inc 1995, ISBN 0-471-04706-6 , Chapter 8 & 17.

[4.4] Bhat, A. K. S.; 'Analysis and design of Series-Parallel Resonant Power Supply', IEEE Trans. Aerospace and Electronic Systems, vol. AES-28, January 1992, pp.249-258.

[4.5] Kazimierczuk, M. K.; Thirunarayan, N.; Shan, S.; 'Analysis of Series-Parallel Resonant Converter', IEEE Trans. Aerospace and Electronic Systems, vol. AES-29, January 1993, pp.88-99.

[4.6] Foster, M. P.; Sewell, H. I.; Bingham, C.M; Stone, D.A.; Howe, D.; 'Methodologies for the design of LCC voltage-output resonant converters', IEE Proceedings - Electrical Power Applications, vol.153 , no.4 , July 2006, pp.559-567.

[4.7] Forsyth, A. J.; Mollov, S.V.; 'Simple equivalent circuit for the series-loaded resonant converter with voltage boosting capacitor', IEE Proceedings on Electrical Power Applications, 1998, vol. 145, no. 4, pp.301-306

[4.8] Bhat, A.K.S.; 'A Generalized Steady-State Analysis of Resonant Converters Using Two-Port Model and Fourier-Series Approach', IEEE Trans. Power Electronics, vol. 13, no. 1, January 1998, pp. 142-151.

[4.9] Wong, S.C. ; Brown, A.D.; 'Analysis, modelling, and simulation of series-parallel resonant converter circuits', IEEE Trans. Power Electronics, vol. 10, no. 5, September 1995, pp. 605-614.

[4.10]Foster, M.P.; Sewell, H.I.; Bingham, C.M.; Stone, D.A.; 'State-variable modelling of LCC voltage output resonant converters', IEE Electronic Letters 2001, vol. 37, no. 17, pp. 1065-1066

[4.11]Bhat, A.K.S.; 'Analysis and Design of a Series-Parallel Resonant Converter with Capacitive Output Filter', IEEE Trans. Industrial Applications, vol.27, no.3, May 1991, pp.523-530

[4.12]Bhat, A.K.S.; Dewan, S.B.; 'Analysis and Design of a High Frequency Resonant Converter using LCC-type Commutation', IEEE Trans. Power Electronics, vol. PE-2, October 1987, pp.291-301.

[4.13]Batarseh, I.; Lie, R.; Lee, C.Q.; Upadhyay,A.K.; 'Theoretical and Experimental Studies of the LCC-type parallel resonant converter', IEEE Trans. Power Electronics, vol. PE-5, April 1990, pp.140-150.

Chapter 5 - Rapid analysis of LCC Inductively-smoothed Resonant Converters via the Phasor Transform Method

Chapters 3 and 4 have focused on generating alternative user-friendly and intuitive design and analysis methodologies for the LCC current- and capacitively-smoothed converter topologies, respectively. Here, tools for the high speed transient analysis of the LCC inductively-smoothed resonant converter, are explored. Specifically, through use of waveform envelope analysis, it is shown that the LCC inductively-smoothed resonant converter can be analysed transiently with a simulation time typically 100 times faster than that obtained when using previously reported state-variable and network simulator methods. Moreover, the underlying principles form a central feature of the small-signal converter analysis [5.1] presented in Chapter 6, facilitating the development of a robust controller design methodology.

5.1 Introduction

Traditionally, the *d-q* axis transformation has been widely used for modelling and analysis of 3-phase machines and power systems. However, a similar but infrequently used phasor-transform technique also exists for single-phase systems based on the assumption that the signals are sinusoidal in nature but vary in amplitude, frequency and phase [5.2] - the same features that are characteristic of resonant converters operating near resonance with sufficiently high quality factor.

The phasor-transform technique is now shown to be applicable to the LCC inductively-smoothed resonant converter, see Figure 5.1, providing much lower transient simulation times when compared to other network simulator methods.

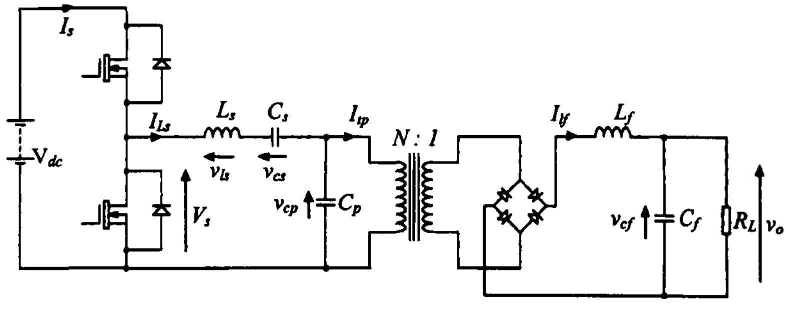

Figure 5.1- LCC inductively-smoothed resonant converter

5.2 Phasor transform

A mathematical derivation follows, demonstrating how the component transformations from rotating(switching) to stationary(envelope) frame are obtained, see Figure 5.2.

From [5.2], a sinusoidal voltage or current can be approximated by a sinusoid whose frequency and amplitude vary with time:

$$x(t) = \Re\left(\bar{x}(t) e^{j\int_0^t \omega_s(t)dt} \right) \tag{5.1}$$

where $\bar{x}(t)$ is the complex envelope of $x(t)$. Consider the differential equation governing the behaviour of an ideal inductor:

$$v(t) = L\frac{d\,i(t)}{dt} \tag{5.2}$$

Substituting (5.1) into (5.2) for current and voltage gives:

$$\Re\left(\bar{v}(t) e^{j\int_0^t \omega_s(t)dt} \right) = L\frac{d}{dt}\Re\left(\bar{i}(t) e^{j\int_0^t \omega_s(t)dt} \right) \tag{5.3}$$

and simplifying gives [5.3]:

$$\bar{v}(t) = L\frac{d\,\bar{i}(t)}{dt} + jL\omega_s(t)\bar{i}(t) \tag{5.4}$$

In a similar manner, capacitors and resistors are described by:

$$\bar{i}(t) = C\frac{d\,\bar{v}(t)}{dt} + jC\omega_s(t)\bar{v}(t)\,,\quad \bar{v}(t) = R\,\bar{i}(t) \tag{5.5}$$

More generally, therefore, the signal envelope $\bar{x}(t)$ can be expanded into its constituent real and imaginary components, donated by '*r*' and '*i*' subscripts, respectively.

$$\bar{x}(t) = x_r(t) + jx_i(t) \tag{5.6}$$

For the inductor, substituting (5.6) into (5.4) gives:

$$v_r(t) + jv_i(t) = L\frac{d}{dt}\left(i_r(t) + j\,i_i(t)\right) + jL\omega_s(t)\left(i_r(t) + j\,i_i(t)\right) \tag{5.7}$$

Separating the real and imaginary components in (5.7) gives:

$$v_r(t) = L\frac{d\,i_r(t)}{dt} - L\omega_s(t)\,i_i(t) \tag{5.8}$$

$$v_i(t) = L\frac{d\,i_i(t)}{dt} + L\omega_s(t)\,i_r(t)$$

Similarly for the capacitor and resistor,

$$\begin{aligned} i_r(t) &= C\frac{d\,v_r(t)}{dt} - C\omega_s(t)\,v_i(t) \\ i_i(t) &= C\frac{d\,v_i(t)}{dt} + C\omega_s(t)\,v_r(t) \end{aligned} \tag{5.9}$$

and

$$\begin{aligned} v_r(t) &= R\,i_r(t) \\ v_i(t) &= R\,i_i(t) \end{aligned} \tag{5.10}$$

For use in network simulators such as SPICE, for instance, the complex components can be eliminated through use of two coupled equivalent circuits, one describing the real domain and the other the imaginary domain [5.4]. Figure 5.2 demonstrates how to directly generate the coupled equivalent circuits from the original circuit diagram.

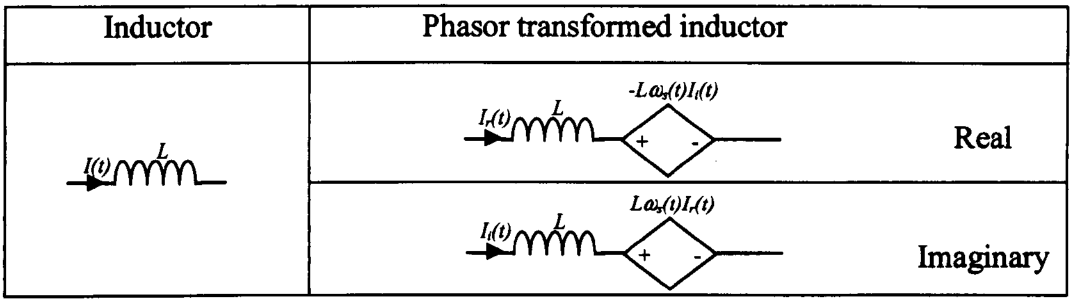

[note that the diamond shaped components here are variable voltage sources]

(a)

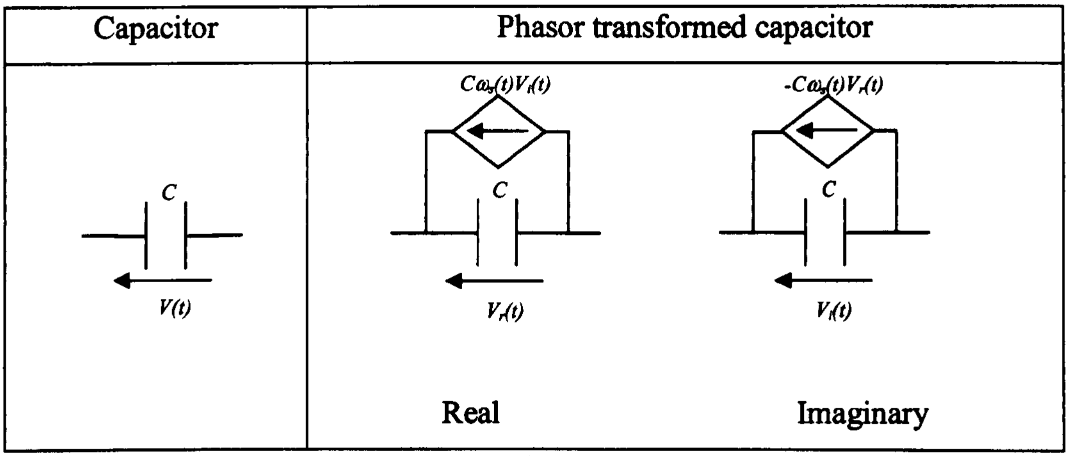

(b)

[note that the diamond shaped components here are variable current sources]

Resistor	Phasor transformed resistor	
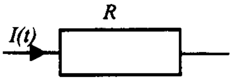 	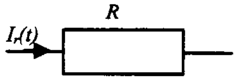 	Real
	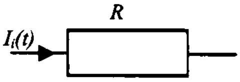 	Imaginary

(c)

Figure 5.2 – Phasor transformed components (a) inductor (b) capacitor (c) resistor

5.3 Applying Phasor transform to LCC inductively-smoothed converter

The rectifier in Figure 5.1 is not readily modelled using the phasor-transform, and requires the resonant tank and output filter to be modelled separately and then combined. This is justified since the output filter bandwidth is much lower than that of the resonant tank, and, as a result of the rectifier action, the filter effectively reacts only to envelope of the resonant tank waveforms. From basic FMA, the resonant tank is modelled as in Figure 5.3—see [5.5].

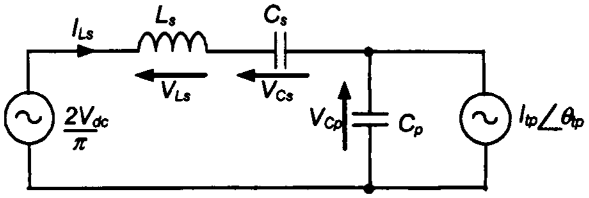

Figure 5.3 –FMA of LCC Resonant tank

After phasor-transforming the components in Figure 5.3, through use of Figure 5.2, the coupled networks shown in Figure 5.4 are obtained.

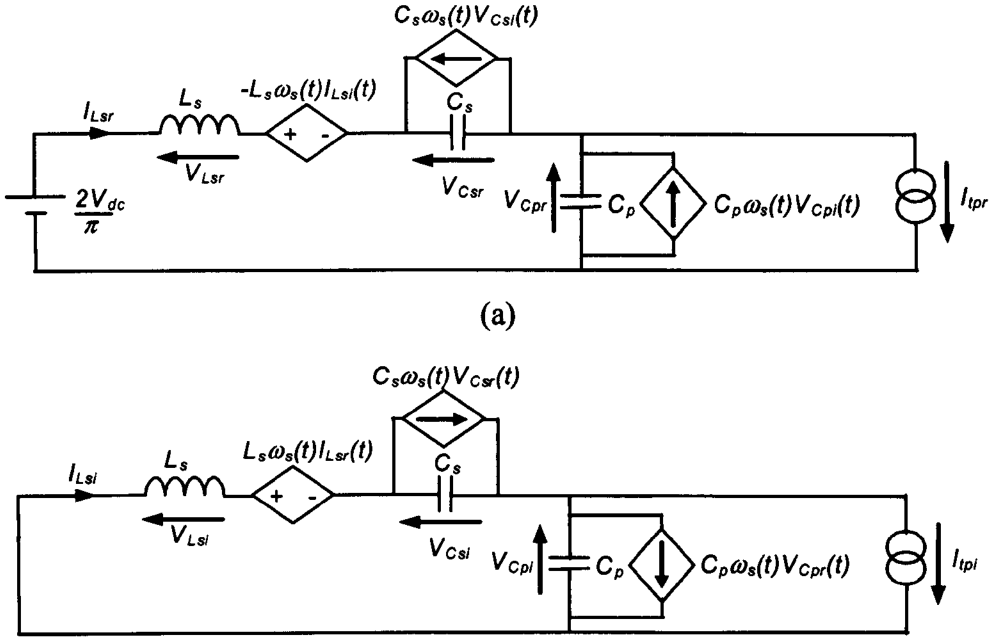

(a)

(b)

Figure 5.4 – Phasor transformed LCC resonant tank model

(a) real circuit (b) imaginary circuit

A state-space representation for both the real and imaginary circuits in Figure 5.4 are given by (5.11) and (5.12), respectively:

$$\begin{bmatrix} \dot{I}_{Ls_r} \\ \dot{V}_{Cs_r} \\ \dot{V}_{Cp_r} \end{bmatrix} = \begin{bmatrix} 0 & \frac{-1}{L_s} & \frac{-1}{L_s} \\ \frac{1}{C_s} & 0 & 0 \\ \frac{1}{C_p} & 0 & 0 \end{bmatrix} \begin{bmatrix} I_{Ls_r} \\ V_{Cs_r} \\ V_{Cp_r} \end{bmatrix} - \omega_s(t) \begin{bmatrix} 1 & 0 & 0 \\ 0 & 1 & 0 \\ 0 & 0 & 1 \end{bmatrix} \begin{bmatrix} I_{Ls_i} \\ V_{Cs_i} \\ V_{Cp_i} \end{bmatrix} + \begin{bmatrix} \frac{2}{\pi L_s} & 0 \\ 0 & 0 \\ 0 & -\frac{1}{C_p} \end{bmatrix} \begin{bmatrix} V_{dc} \\ I_{tp_r} \end{bmatrix} \tag{5.11}$$

$$\begin{bmatrix} \dot{I}_{Ls_i} \\ \dot{V}_{Cs_i} \\ \dot{V}_{Cp_i} \end{bmatrix} = \begin{bmatrix} 0 & \frac{-1}{L_s} & \frac{-1}{L_s} \\ \frac{1}{C_s} & 0 & 0 \\ \frac{1}{C_p} & 0 & 0 \end{bmatrix} \begin{bmatrix} I_{Ls_i} \\ V_{Cs_i} \\ V_{Cp_i} \end{bmatrix} + \omega_s(t) \begin{bmatrix} 1 & 0 & 0 \\ 0 & 1 & 0 \\ 0 & 0 & 1 \end{bmatrix} \begin{bmatrix} I_{Ls_r} \\ V_{Cs_r} \\ V_{Cp_r} \end{bmatrix} + \begin{bmatrix} 0 & 0 \\ 0 & 0 \\ 0 & -\frac{1}{C_p} \end{bmatrix} \begin{bmatrix} V_{dc} \\ I_{tp_i} \end{bmatrix} \tag{5.12}$$

Both (5.11) and (5.12) can be readily expressed as a partitioned state-space equation:

$$\begin{bmatrix} \dot{I}_{Ls_r} \\ \dot{V}_{Cs_r} \\ \dot{V}_{Cp_r} \\ \dot{I}_{Ls_i} \\ \dot{V}_{Cs_i} \\ \dot{V}_{Cp_i} \end{bmatrix} = \begin{bmatrix} 0 & \frac{-1}{L_s} & \frac{-1}{L_s} & -\omega_s & 0 & 0 \\ \frac{1}{C_s} & 0 & 0 & 0 & -\omega_s & 0 \\ \frac{1}{C_p} & 0 & 0 & 0 & 0 & -\omega_s \\ \omega_s & 0 & 0 & 0 & \frac{-1}{L_s} & \frac{-1}{L_s} \\ 0 & \omega_s & 0 & \frac{1}{C_s} & 0 & 0 \\ 0 & 0 & \omega_s & \frac{1}{C_p} & 0 & 0 \end{bmatrix} \begin{bmatrix} I_{Ls_r} \\ V_{Cs_r} \\ V_{Cp_r} \\ I_{Ls_i} \\ V_{Cs_i} \\ V_{Cp_i} \end{bmatrix} + \begin{bmatrix} \frac{2}{\pi L_s} & 0 & 0 \\ 0 & 0 & 0 \\ 0 & \frac{-1}{C_p} & 0 \\ 0 & 0 & 0 \\ 0 & 0 & 0 \\ 0 & 0 & \frac{-1}{C_p} \end{bmatrix} \begin{bmatrix} V_{dc} \\ I_{tr_r} \\ I_{tp_i} \end{bmatrix} \tag{5.13}$$

$$\dot{x} = A_{PT}x + B_{PT}u$$

The waveform envelopes are extracted from the real and imaginary components using the output equation:

$$\begin{bmatrix} \hat{I}_{Ls} \\ \hat{V}_{Cr} \\ \hat{V}_{Cs} \end{bmatrix} \equiv \left| \begin{bmatrix} 1 & 0 & 0 & j & 0 & 0 \\ 0 & 1 & 0 & 0 & j & 0 \\ 0 & 0 & 1 & 0 & 0 & j \end{bmatrix} \begin{bmatrix} I_{Ls_r} \\ V_{Cs_r} \\ V_{Cp_r} \\ I_{Ls_i} \\ V_{Cs_i} \\ V_{Cp_i} \end{bmatrix} \right| \tag{5.14}$$

Finally, the output filter is described in state-variable form by:

$$\begin{bmatrix} \dot{I}_{Lf} \\ \dot{V}_o \end{bmatrix} = \begin{bmatrix} 0 & \frac{-1}{L_f} \\ \frac{1}{C_f} & \frac{-1}{R_L C_f} \end{bmatrix} \begin{bmatrix} I_{Lf} \\ V_o \end{bmatrix} + \begin{bmatrix} \frac{1}{L_f} \\ 0 \end{bmatrix} \begin{bmatrix} V_f \end{bmatrix} \tag{5.15}$$

$$\dot{x} = \mathbf{A}_{filt}x + \mathbf{B}_{filt}u$$

The voltages of the phasor-transformed tank model and the output filter are coupled by noting that the average voltage presented to the output filter, via the rectifier, is given by (5.16) since V_{Cp} is assumed sinusoidal.

$$V_f = \frac{2\hat{V}_{Cp}}{N\pi} \tag{5.16}$$

Coupling of the currents is achieved by replacing the current source in Figure 5.3 by a time varying resistor, Figure 5.5, with the imaginary and real components of I_{tp} given by:

$$I_{tp_r} = \frac{V_{Cp_r}}{R_{filt}} \qquad I_{tp_i} = \frac{V_{Cp_i}}{R_{filt}} \tag{5.17}$$

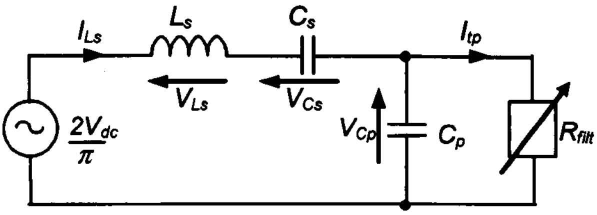

Figure 5.5 – Modelling output filter by a time varying load

Since the transformer primary current is a squarewave, and the fundamental is used in the phasor-transformed model, the peak of the squarewave current is increased by the factor 4/π. Notably, if the resonant tank current is not sufficient to support the output-filter inductor current, the rectifier turns off and the parallel capacitor voltage remains constant. The two operating states are, therefore:

$$\hat{I}_{tp} = \sqrt{I_{tp_r}^{\;2} + I_{tp_i}^{\;2}} = \begin{cases} \dfrac{4I_{Lf}}{N\pi} & \text{for } \hat{I}_{Ls} \geq \dfrac{4I_{Lf}}{N\pi} \\ \sqrt{I_{Ls_r}^{\;2} + I_{Ls_i}^{\;2}} & \text{otherwise} \end{cases} \tag{5.18}$$

The effective time-varying load resistance is now calculated from:

$$R_{filt} = \frac{\hat{V}_{Cp}}{\hat{I}_{tp}} \tag{5.19}$$

From (5.17),(5.18) and (5.19) the transformer primary phasor currents are found algebraically:

$$I_{tp_r} = \begin{cases} \dfrac{4I_{Lf}}{N\pi}\dfrac{V_{Cp_r}}{\hat{V}_{Cp}} & \text{for} \quad \hat{I}_{Ls} > \dfrac{4I_{Lf}}{N\pi} \\ I_{Ls_r} & \text{otherwise} \end{cases} \qquad I_{tp_i} = \begin{cases} \dfrac{4I_{Lf}}{N\pi}\dfrac{V_{Cp_i}}{\hat{V}_{Cp}} & \text{for} \quad \hat{I}_{Ls} > \dfrac{4I_{Lf}}{N\pi} \\ I_{Ls_i} & \text{otherwise} \end{cases} \tag{5.20}$$

The model is therefore described by (5.13),(5.14),(5.15),(5.16),(5.20).

A further constraint is required to fully characterise the output filter behaviour for simulation purposes. The filter current may never go negative. It is therefore necessary to limit the output filter current to ≥ 0 and to ensure no integral windup. This is achieved by ensuring that when that output-filter inductor current is zero, the derivative of the output-filter current is ≥0.

For use in 'signal-conservative' simulation packages, the integrator shown in Figure 5.6 can be used in place of the output-filter current integrator to ensure that the filter current never falls below 0A and prevents integral windup.

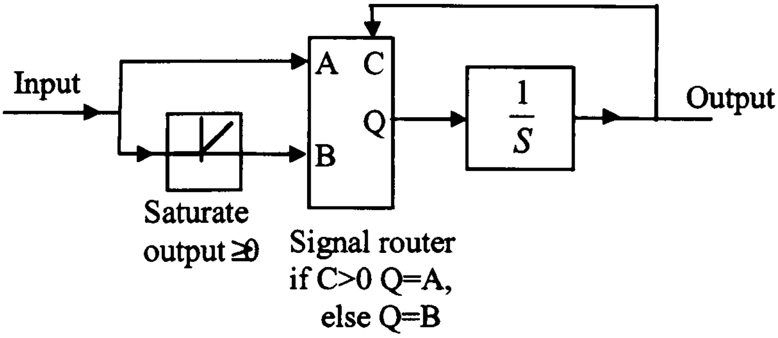

Figure 5.6 – Integrator model to prevent negative filter current and integral windup

5.4 Results

As with classical FMA, the phasor-transform method can be used to rapidly obtain the frequency response of a converter. An example design with parameters is given in Table 5.I. A comparison of results with those from a non-linear state-variable model [5.5] and FMA are given in Figure 5.7, from where it can be seen that the phasor-transform method provides commensurate accuracy with FMA.

Table 5.I Component values

Input voltage	V_{dc}	100V
Load resistance	R_L	10Ω
Series tank inductor	L_s	8μH
Series tank capacitor	C_s	620nF
Parallel tank capacitor	C_p	620nF
Transformer turns ratio	$N:1$	1 : 1
Filter inductor	L_f	1mH
Filter capacitor	C_f	20μF

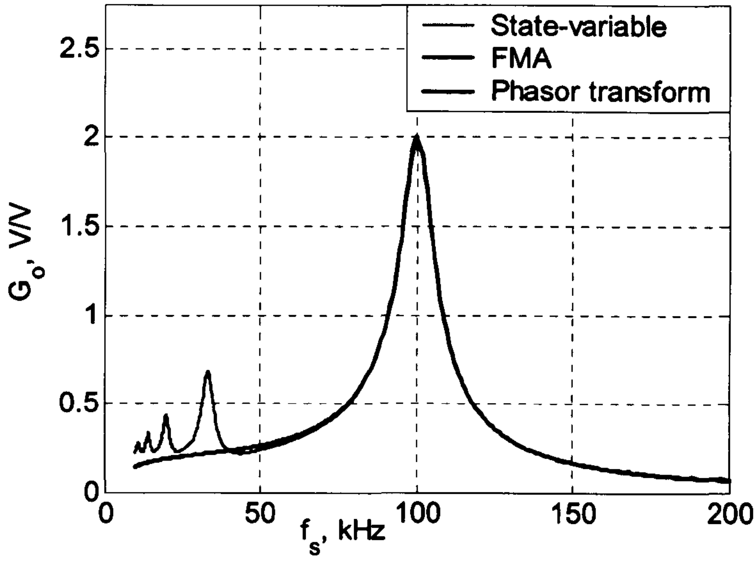

Figure 5.7 – Steady-State model comparison (all curves computed through use of Simulink) [Note: G_o is the effective DC voltage gain of the resonant tank]

A key advantage of the presented phasor-transform methodology, however, is that it also readily allows transient solutions to be rapidly obtained. By way of example, Figure 5.8 shows the input/output voltage ratio from both the phasor-transform model, and the non-linear state-variable model, when subjected to turn-on transients at various switching frequencies. It can be seen that a high degree of correlation exists between the results indicating that the phasor-transform accurately captures the dynamic behaviour of the converter.

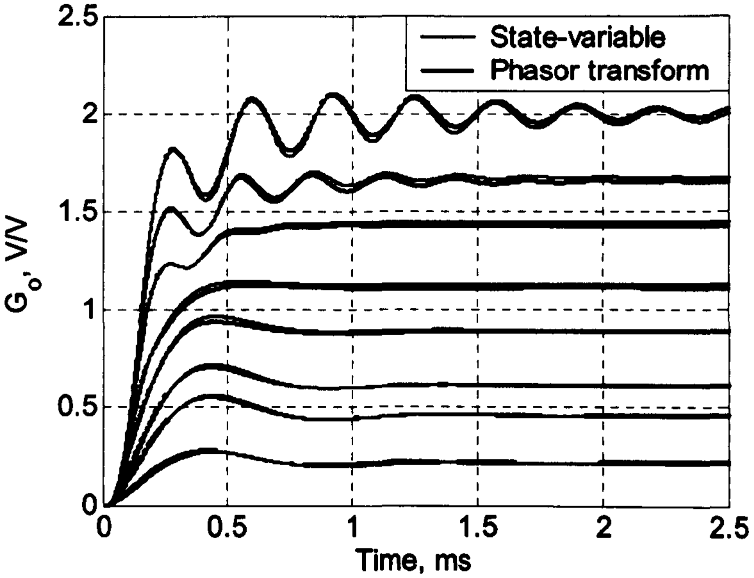

Figure 5.8 – Dynamic response comparison between state-variable and phasor-transformed model (all curves computed through use of Simulink)

Now, to provide a comparison of computation requirements, the switching frequency exciting the converter is varied in a sinusoidal manner, as described by the equation, $\omega_s(t)=2\pi(120\times10^3+10\times10^3\sin(2\pi10\times10^3t))$, and applied to both the phasor-transform and non-linear state-variable models. Figure 5.9 shows the resulting output voltage from each model, from where it can be seen that commensurate accuracy is obtained. However, notably, to provide comparable accuracy to SPICE simulation results, the sample-time step of the state-variable model was required to be set no greater than 10ns, whilst the commensurate results from the phasor-transform model were readily obtained using a sample time of 1.4μs, thereby significantly reducing the overall simulation time. This advantage is a direct consequence of only modelling the envelope behaviour.

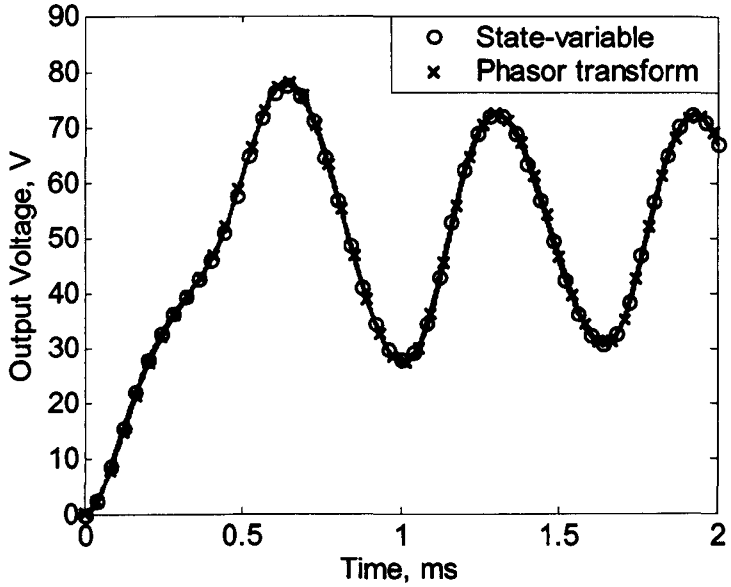

Figure 5.9 – Dynamic response of state-variable and phasor-transform model under varying switching frequency conditions (both curves computed through use of Simulink)

For completeness, a comparison of results of the series inductor current, is given in Figure 5.10, from which it is demonstrated that the phasor-transform method accurately captures the envelope of the high-frequency tank waveforms, as required.

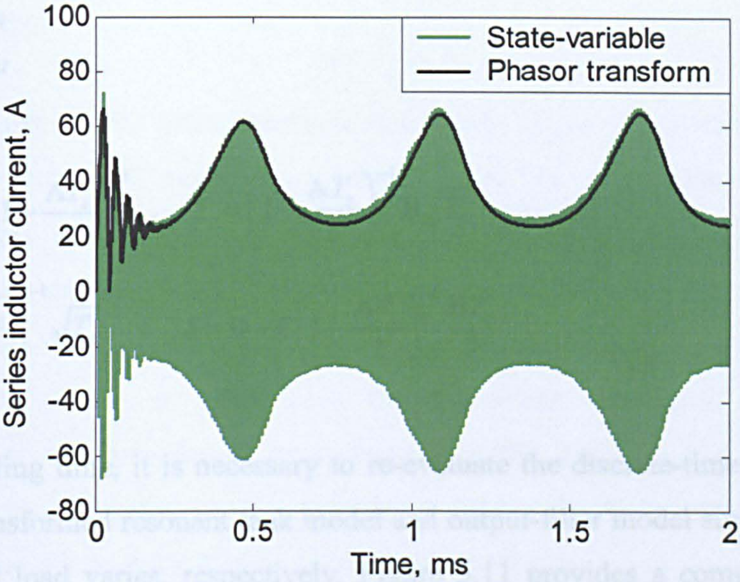

Figure 5.10 – State-variable response compared with phasor-transform envelope under varying switching frequency conditions (all curves computed through use of Simulink)

5.5 Discretisation of the Phasor transform model

Further increase in simulation speed may be obtained through discretisation of both the phasor transform tank model and output filter model.

For both the resonant tank and output filter model a discrete-time model with the following form is required:

$$\begin{aligned} w(k+1) &= \mathbf{\Phi}\, w(k) + \mathbf{\Gamma}\, u(k) \\ y(k) &= \mathbf{H}\, w(k) + \mathbf{J}\, u(k) \end{aligned} \tag{5.21}$$

To maintain accuracy, the bilinear transform is utilised to transform the continuous-time state-variable model to discrete-time.

$$s = \frac{2}{T}\frac{z-1}{z+1} \tag{5.22}$$

To transform from the continuous-time state-space form (5.23) to the discrete-time state-space form (5.21) utilizing the bilinear transform (5.22), requires use of the equations in (5.24), [5.6].

$$\dot{x} = \mathbf{A}x + \mathbf{B}u$$
$$y = \mathbf{C}x + \mathbf{D}u \tag{5.23}$$

$$\mathbf{\Phi} = \left(\mathbf{I} + \frac{\mathbf{A}T_s}{2}\right)\left(\mathbf{I} - \frac{\mathbf{A}T_s}{2}\right)^{-1} \quad , \quad \mathbf{\Gamma} = \left(\mathbf{I} - \frac{\mathbf{A}T_s}{2}\right)^{-1}\mathbf{B}\sqrt{T_s} \tag{5.24}$$
$$\mathbf{H} = \mathbf{C}\left(\mathbf{I} - \frac{\mathbf{A}T_s}{2}\right)^{-1}\sqrt{T_s} \quad , \quad \mathbf{J} = \mathbf{D} + \mathbf{C}\left(\mathbf{I} - \frac{\mathbf{A}T_s}{2}\right)^{-1}\frac{\mathbf{B}T_s}{2}$$

At each sampling time, it is necessary to re-evaluate the discrete-time model for both the phasor-transformed resonant tank model and output-filter model since the switching frequency and load varies, respectively. Figure 5.11 provides a comparison between both the continuous-time model simulated with a fixed step of 1μs and the discrete-time model sampled at 1μs intervals. Note how both curves are virtually identical.

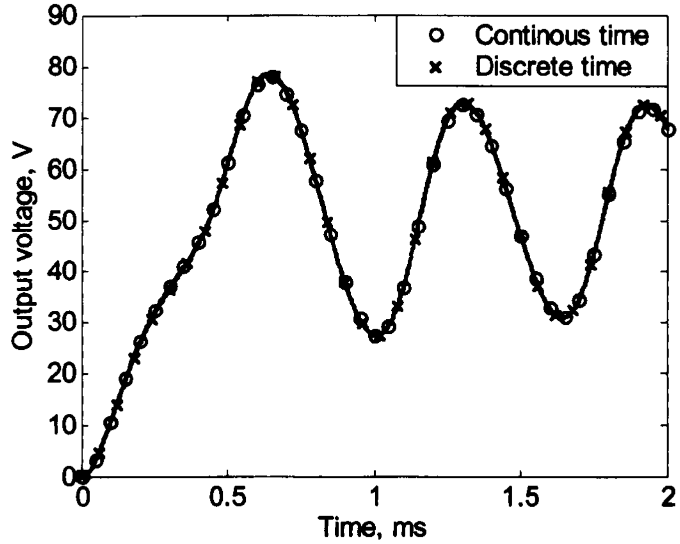

Figure 5.11 – Continuous-time model response compared with discrete-time model response under varying switching frequency conditions (all curves computed through use of Simulink)

To compare model speed, an ode3 solver was utilised for the continuous-time model since this was found to be the fastest solver resulting in an equivalent performance with SPICE. The continuous-time model was found to take 1.5×longer than that of the discrete-time model, therby demonstrating that the discrete-time model is ≈50% faster.

5.6 Conclusion

The phasor-transform has been presented as a means of rapidly obtaining the transient characteristics of the LCC resonant converter. It has been shown that sample times at least two orders of magnitude longer than state-variable techniques can often be employed, at the expense of only obtaining the envelopes of the high-frequency tank waveforms. Nevertheless, this presents a significant advantage to the designer of resonant converters as it ameliorates the protracted simulation times that are characteristic of iterative design procedures. Finally, although the LCC converter variant has been presented as an example, it should be noted that the method is ultimately applicable to other resonant converter topologies.

5.7 References

[5.1]Gilbert, A. J.; Stone, D. A.; Bingham, C. M.; Foster, M. P.; 'Power factor control of the LCC current-output resonant converter', European Conference on Power Electronics and Applications, CD proceedings paper number 0204, Aalborg 2-5 Sept. 2007

[5.2]Yin, Y.; Zane, R.; Erickson. R.; Glaser. J.; 'Dynamic analysis of frequency-controlled electronic ballasts,' Industry Applications Conference, vol. 1, 13-18 Oct. 2002 pp.685-691

[5.3]Rim, C. T; Cho, G.H.; 'Phasor Transformation and its Application to the DC/AC Analyses of Frequency Phase-Controlled Series Resonant Converters (SRC)', IEEE Trans. Power Electronics, vol.5, no.2, April 1990, pp.201-211

[5.4]Ben-Yaakov, S.; Glozman, S.; Rabinovici, R.; 'Envelope Simulation by SPICE-Compatible Models of Electric Circuits Driven by Modulated Signals', IEEE Trans. Industrial Electronics, vol.47, no.1, February 2000, pp.222-225

[5.5]Steigerwald, R. L.; 'A comparison of Half-Bridge Resonant Converter Topologies', IEEE Trans. Power Electronics, vol.3, no.2, April 1988, pp.174-182

[5.5]Foster, M. P.; Sewell, H. I.; Bingham, C. M.; Stone, D. A.; 'State-variable modelling of LCC voltage-output resonant converters', Electronic Letters, vol. 37, issue. 17, 16th August 2001 pp.1065-1066

[5.6]Franklin, G. F.; Powell, J. D.; Workman, M.; 'Digital Control of Dynamic Systems', Pearson International 3rd edition 1998

Chapter 6 - Power-factor Control of the LCC Inductively-smoothed Resonant Converter

To this point, the thesis has reported on, and addressed problems in the analysis and design of resonant converters. Ultimately, however, most converters to be practically useful, require some form of closed loop control to facilitate good voltage or current regulation. An improved strategy for the control of LCC inductively-smoothed resonant converters is therefore now formulated [6.1], based on varying the phase-angle between the fundamental of the input voltage and current. Unlike other commonly employed control methodologies, the proposed technique is shown to provide a convenient, linear system input-output characteristic suitable for the design of regulators. Put simply, the method is shown to have a similar impact as being able to vary the DC-link supply voltage, in terms of output-voltage/current control. The LCC converter variant is used as an application focus for demonstrating the presented techniques, with simulation and experimental measurements from a prototype converter being used to show the practical benefits. 3rd-order small and large-signal models are developed, based on the results of Chapter 5, and employed in the formulation of robust output-voltage and output-current control schemes. Notably, the presented techniques are ultimately generic and readily applicable to other resonant converter variants.

6.1 Introduction

It is well established that resonant converter-based supplies are advantageous in terms of size and efficiency [6.2-6.3] compared to hard-switched counterparts. One of the main impediments to their use, however, is the lack of design techniques to provide simple yet robust control. This is primarily due to the highly non-linear dynamic characteristics that are normally associated with such systems. Here then, a novel control strategy is proposed that approximately linearises the behaviour of the converter such that well-known control techniques can be readily applied. Although other methods have been previously reported [6.4-6.5] that aim to linearise the converter's behaviour, the mechanism presented here provides a convenient and cohesive framework that is very widely applicable. To focus the development, the LCC inductively-smoothed converter variant, shown in Figure 6.1, is used as an example.

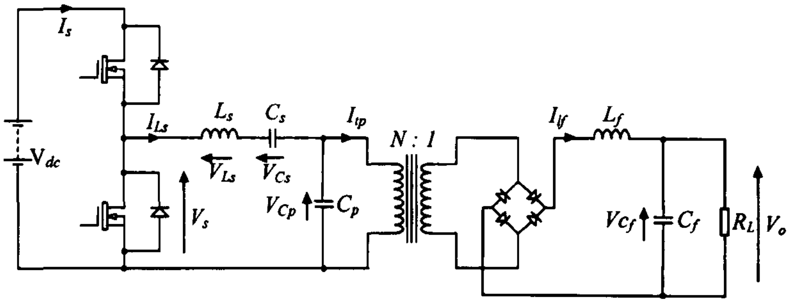

Figure 6.1 - LCC Inductively-smoothed resonant converter

6.2 Equivalence of power-factor and supply voltage control

During normal operation, the resonant tank is excited above the resonant frequency by an applied square-wave voltage, V_s, that results in an approximately sinusoidal series inductor current, I_{Ls}, see Figure 6.2(a). The fundamental component of the square-wave is also shown, and can be sub-divided into two components, one in phase with the resonant current, I_{Ls}, and one in quadrature, Figure 6.2(b).

The following identity can be used to derive the magnitude of the switching voltage component that is in-phase with the series inductor current,

$$\sin(A+B)=\sin(A)\cos(B)+\cos(A)\sin(B) \tag{6.1}$$

The switching voltage can be approximated by its fundamental component as follows:

$$V_s=\frac{V_{dc}}{2}\operatorname{sgn}(\sin(\omega_s t))\approx\frac{2V_{dc}}{\pi}\sin(\omega_s t) \tag{6.2}$$

with the series inductor current assumed to be a sinusoid:

$$I_{Ls}=\hat{I}_{Ls}\sin(\omega_s t-\theta) \tag{6.3}$$

Using the identity (6.1) the fundamental component of the excitation voltage can be re-expressed as:

$$\frac{2V_{dc}}{\pi}\sin(\omega_s t)=\frac{2V_{dc}}{\pi}\cos(\theta)\sin(\omega_s t-\theta)+\frac{2V_{dc}}{\pi}\sin(\theta)\cos(\omega_s t-\theta) \tag{6.4}$$

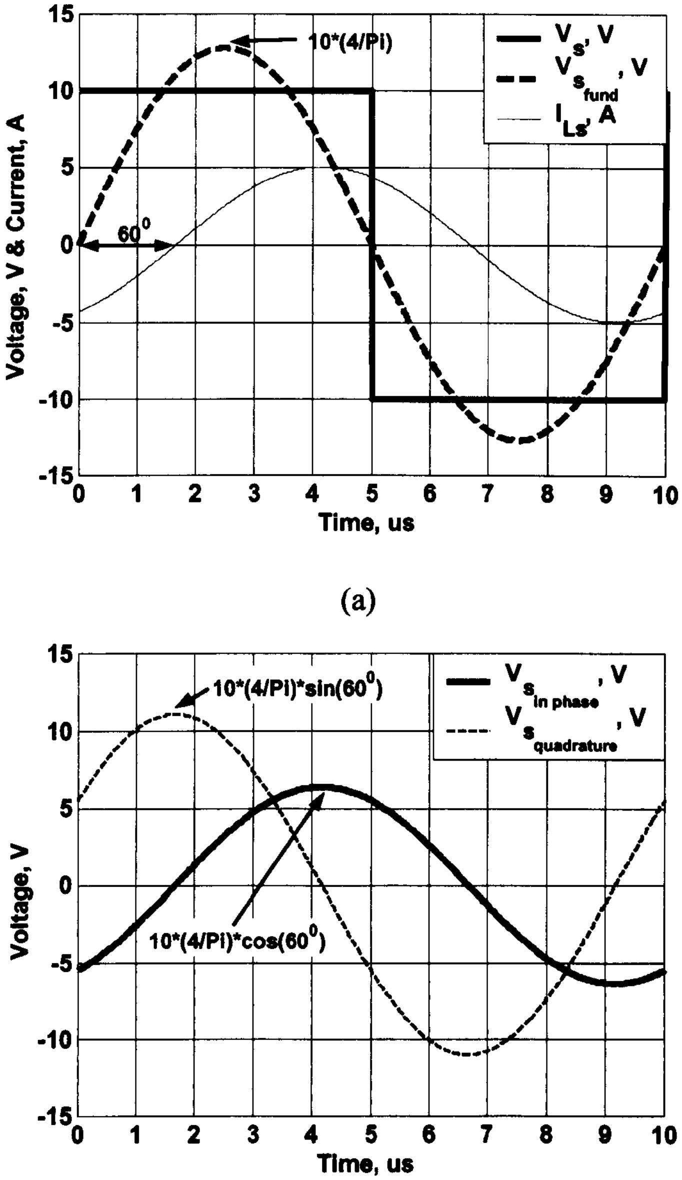

(a)

(b)

Figure 6.2 - (a) Switching voltage and resonant tank current

(b) phase components of switching voltage wrt. resonant tank current

(Curves generated through the use of Simulink)

To maintain the real power flow into the converter, assuming an equivalent square-wave switching voltage in-phase with the series inductor current, the 'equivalent' square-wave is approximated to:

$$V_s = \frac{V_{dc}}{2}\cos(\theta)\,\mathrm{sgn}(\sin(\omega_s t-\theta)) = \frac{V_{dc}PF}{2}\,\mathrm{sgn}(\sin(\omega_s t-\theta)) \tag{6.5}$$

where the electrical power-factor $PF=cos(\theta)$

It can now be seen that varying the instantaneous power-factor (*PF*) is equivalent to varying the instantaneous supply-voltage, from a fundamental mode approximation (FMA) perspective—that is, the current waveform is assumed sinusoidal. When deriving a small-signal model, this allows the converter to be considered as being excited at the resonant frequency whilst varying the power factor—in this case, power-factor can be included in the model as an effective supply-voltage scaling factor, and therefore does not alter the model structure.

6.3 Small-signal analysis

The phasor-transformed large-signal model presented in Chapter 5 is now extended to provide a small-signal model to facilitate power-factor control. For convenience, it is assumed that the converter is switched at resonance (i.e a constant switching frequency for a given load resistance) with a controllable supply voltage, to mimic the effects of power-factor control. [Note that as the power factor is controlled, the switching frequency of the converter will indeed vary. It is not necessary however to model the varying in frequency, since the effects have already been modelled by the power factor i.e as a reduction in supply voltage]

Equation (5.13) is modified such that power factor becomes the input, giving:

$$\begin{bmatrix} \dot{I}_{Ls_r} \\ \dot{V}_{Cs_r} \\ \dot{V}_{Cp_r} \\ \dot{I}_{Ls_i} \\ \dot{V}_{Cs_i} \\ \dot{V}_{Cp_i} \end{bmatrix} = \begin{bmatrix} 0 & \frac{-1}{L_s} & \frac{-1}{L_s} & \omega_s & 0 & 0 \\ \frac{1}{C_s} & 0 & 0 & 0 & \omega_s & 0 \\ \frac{1}{C_p} & 0 & 0 & 0 & 0 & \omega_s \\ -\omega_s & 0 & 0 & 0 & \frac{-1}{L_s} & \frac{-1}{L_s} \\ 0 & -\omega_s & 0 & \frac{1}{C_s} & 0 & 0 \\ 0 & 0 & -\omega_s & \frac{1}{C_p} & 0 & 0 \end{bmatrix} \begin{bmatrix} I_{Ls_r} \\ V_{Cs_r} \\ V_{Cp_r} \\ I_{Ls_i} \\ V_{Cs_i} \\ V_{Cp_i} \end{bmatrix} + \begin{bmatrix} \frac{2V_{dc}}{\pi L_s} & 0 & 0 \\ 0 & 0 & 0 \\ 0 & \frac{-1}{C_p} & 0 \\ 0 & 0 & 0 \\ 0 & 0 & 0 \\ 0 & 0 & \frac{-1}{C_p} \end{bmatrix} \begin{bmatrix} PF \\ I_{tp_r} \\ I_{tp_i} \end{bmatrix} \tag{6.6}$$

The equations underpinning the phasor-transformed model (6.6) (5.14) (5.15) (5.16) (5.20) are linearised about the resonant frequency, and (5.16) is re-expressed as follows:

[note that at resonance $\hat{I}_{Ls} \geq \dfrac{4I_{Lf}}{N\pi}$].

$$V_f = \frac{2\sqrt{{V_{Cp_r}}^2 + {V_{Cp_i}}^2}}{N\pi} \qquad \text{(6.7}$$

For a generic variable *X(t)*, the steady-state and small-signal components are separated as follows:

$$X = X_o + \Delta x \qquad (6.8)$$

where X_o and Δx are the steady-state and small-signal components, respectively. Using this, (6.7) can be written as:

$$V_f = \frac{2\sqrt{\left(V_{Cp_ro} + \Delta v_{Cp_r}\right)^2 + \left(V_{Cp_io} + \Delta v_{Cp_i}\right)^2}}{N\pi} \qquad (6.9)$$

and linearising about a steady-state operating point gives:

$$\Delta v_f = \frac{2}{N\pi\sqrt{{V_{Cp_ro}}^2 + {V_{Cp_io}}^2}}\left(V_{Cp_ro}\Delta v_{Cp_r} + V_{Cp_io}\Delta v_{Cp_i}\right) \qquad (6.10)$$

The transformer primary currents (6.20) are also modified accordingly:

$$I_{tp_r} = \frac{4\left(I_{Lf_o} + \Delta I_{Lf}\right)}{N\pi}\frac{\left(V_{Cp_{r0}} + \Delta v_{Cp_r}\right)}{\sqrt{\left(V_{Cp_{r0}} + \Delta v_{Cp_r}\right)^2 + \left(V_{Cp_{i0}} + \Delta v_{Cp_i}\right)^2}} \qquad \text{(6.11a}$$

$$I_{tp_i} = \frac{4\left(I_{Lf_0} + \Delta I_{Lf}\right)}{N\pi}\frac{\left(V_{Cp_{i0}} + \Delta v_{Cp_i}\right)}{\sqrt{\left(V_{Cp_{r0}} + \Delta v_{Cp_r}\right)^2 + \left(V_{Cp_{i0}} + \Delta v_{Cp_i}\right)^2}} \qquad \text{(6.11b}$$

Linearising (6.11) about the steady-state operating point gives:

$$\Delta i_{tp_r} = \frac{4I_{Lf_0}{V_{Cp_{i0}}}^2\Delta v_{Cp_r}}{N\pi\left({V_{Cp_{r0}}}^2 + {V_{Cp_{i0}}}^2\right)^{(3/2)}} - \frac{4I_{Lf_o}V_{Cp_{i0}}V_{Cp_{r0}}\Delta v_{Cp_i}}{N\pi\left({V_{Cp_{r0}}}^2 + {V_{Cp_{i0}}}^2\right)^{(3/2)}} + \frac{4V_{Cp_{r0}}\Delta i_{Lf}}{N\pi\sqrt{{V_{Cp_{r0}}}^2 + {V_{Cp_{i0}}}^2}} \qquad \text{(6.12a}$$

$$\Delta i_{tp_i} = \frac{4I_{Lf_0}{V_{Cp_{r0}}}^2\Delta v_{Cp_i}}{N\pi\left({V_{Cp_{r0}}}^2 + {V_{Cp_{i0}}}^2\right)^{(3/2)}} - \frac{4I_{Lf_o}V_{Cp_{i0}}V_{Cp_{r0}}\Delta v_{Cp_r}}{N\pi\left({V_{Cp_{r0}}}^2 + {V_{Cp_{i0}}}^2\right)^{(3/2)}} + \frac{4V_{Cp_{i0}}\Delta i_{Lf}}{N\pi\sqrt{{V_{Cp_{r0}}}^2 + {V_{Cp_{i0}}}^2}} \qquad \text{(6.12b}$$

To develop the small-signal model, expressions for the steady-state components $V_{Cp_{r0}}$, $V_{Cp_{i0}}$ and I_{Lf_0} need to be derived. From (6.7), the steady-state output inductor current is simply written:

$$I_{Lf_0} = \frac{2\sqrt{{V_{Cp_{r0}}}^2 + {V_{Cp_{i0}}}^2}}{N\pi R_L} \qquad \text{(6.13}$$

with the transformer primary current components, from (5.20) and (6.13), becoming:

$$I_{tp_r} = \frac{4I_{Lf}}{N\pi}\frac{V_{Cp_r}}{\sqrt{V_{Cp_r}{}^2+V_{Cp_i}{}^2}} = \frac{8V_{Cp_r}}{N^2\pi^2R_L} \tag{6.14a}$$

$$I_{tp_i} = \frac{4I_{Lf}}{N\pi}\frac{V_{Cp_i}}{\sqrt{V_{Cp_r}{}^2+V_{Cp_i}{}^2}} = \frac{8V_{Cp_i}}{N^2\pi^2R_L} \tag{6.14b}$$

Steady-state conditions are obtained by equating the time derivatives in (6.6) to zero. Equation (6.14) is used to replace the I_{tp} components, thereby giving:

$$\dot{I}_{Ls_{r0}} = 0 = -\frac{1}{L_s}V_{Cs_{r0}} - \frac{1}{L_s}V_{Cp_{r0}} + \omega_s I_{Ls_{i0}} + \frac{2V_{dc}}{\pi L_s}PF \tag{6.15a}$$

$$\dot{V}_{Cs_{r0}} = 0 = \frac{1}{C_s}I_{Ls_{r0}} + \omega_s V_{Cs_{i0}} \tag{6.15b}$$

$$\dot{V}_{Cp_{r0}} = 0 = \frac{1}{C_p}I_{Ls_{r0}} + \omega_s V_{Cp_{i0}} - \frac{1}{C_p}\left(\frac{8V_{Cp_{r0}}}{N^2\pi^2R_L}\right) \tag{6.15c}$$

$$\dot{I}_{Ls_{i0}} = 0 = -\frac{1}{L_s}V_{Cs_{i0}} - \frac{1}{L_s}V_{Cp_{i0}} - \omega_s I_{Ls_{r0}} \tag{6.15d}$$

$$\dot{V}_{Cs_{i0}} = 0 = \frac{1}{C_s}I_{Ls_{i0}} - \omega_s V_{Cs_{r0}} \tag{6.15e}$$

$$\dot{V}_{Cp_{i0}} = 0 = \frac{1}{C_p}I_{Ls_{i0}} - \omega_s V_{Cp_{r0}} - \frac{1}{C_p}\left(\frac{8V_{Cp_{i0}}}{N^2\pi^2R_L}\right) \tag{6.15f}$$

As previously shown, the power factor, in steady-state, does not alter the small-signal analysis. Consequently, it can be assumed that *PF=1* (i.e. operation at resonance) to simplify the analysis. At resonance, therefore, $I_{Ls_{i0}} = 0$, since all the series-inductor current is real. From (6.15e) this also implies that $V_{Cs_{r0}} = 0$. Substituting $I_{Ls_{i0}} = 0$ and $V_{Cs_{r0}} = 0$ into equation (6.15a) now allows the calculation of $V_{Cp_{r0}}$

$$V_{Cp_{r0}} = \frac{2V_{dc}}{\pi} \tag{6.16}$$

Now, the design equations for the LCC inductively-smoothed resonant converter, based on FMA, from Chapter 3, can be utilised to simplify the analysis. Specifically it is shown that, at resonance, the output voltage of the converter is given by:

$$V_o = \frac{V_{dc} G_{tr}}{N} \tag{6.17}$$

where G_{tr} is the voltage gain of the resonant tank and N is transformer turns ratio (when expressed as $N{:}1$), and the steady-state output-filter current is given by:

$$I_{Lf_0} = \frac{V_{dc}\, G_{tr}}{N R_L} \tag{6.18}$$

Equating (6.13) and (6.18), eliminating $V_{Cp_{r0}}$ via use of (6.16), and solving for $V_{Cp_{i0}}$ ultimately gives:

$$V_{Cp_{i0}} = -\frac{V_{dc}\sqrt{G_{tr}^{\;2}\pi^4 - 16}}{2\pi} \tag{6.19}$$

Note that two solutions exist for (6.19), having opposing polarities. The solution presented in (6.19) is selected such that the phase of V_{Cp} w.r.t I_{Ls}, is negative i.e $\arctan(V_{Cp_{i0}} / V_{Cp_{r0}}) < 0$.

In Chapter 3, it is also shown that, from a given converter specification, the resonant tank components can be chosen as follows:

$$C_p = \frac{2\sqrt{G_{tr}^{\;2}\pi^4 - 16}}{\pi^2 N^2 R_L \omega_r} \tag{6.20a}$$

$$C_s = \frac{2\sqrt{G_{tr}^{\;2}\pi^4 - 16}}{A\pi^2 N^2 R_L \omega_r} \tag{6.20b}$$

$$L_s = \frac{N^2 R_L\left((A+1)G_{tr}^{\;2}\pi^4 - 16\right)}{2\pi^2 \omega_r G_{tr}^{\;2}\sqrt{G_{tr}^{\;2}\pi^4 - 16}} \tag{6.20c}$$

where $A = C_p/C_s$, and ω_r is the resonant frequency. These equations will be used to simpify the remaining analysis. Substituting (6.16) and (6.19), into (6.15c), and eliminating C_p in (6.15c) via (6.20a) gives:

$$I_{Ls_{r0}} = \frac{V_{dc}\, G_{tr}^{\;2}\pi}{N^2 R_L} \tag{6.21}$$

Eliminating C_s in (6.15b) via (6.20b), substituting in (6.21) and solving for $V_{Cs_{i0}}$ then gives:

$$V_{Cs_{i0}} = -\frac{A V_{dc} G_{tr}{}^2 \pi^3}{2\sqrt{G_{tr}{}^2 \pi^4 - 16}} \tag{6.22}$$

Since the steady-state conditions are all now known (at PF=1) the small-signal equations expressed in (6.10), (6.12) can be determined:

$$\Delta v_f = \frac{2}{N\pi^3 G_{tr}}\left(4\Delta v_{Cp_r} - \sqrt{G_{tr}{}^2\pi^4 - 16}\,\Delta v_{Cp_i}\right) \tag{6.23}$$

$$\Delta i_{tp_r} = \frac{8}{\pi^2 N^2 R_L}\left(1 - \frac{16}{G_{tr}{}^2\pi^4}\right)\Delta v_{Cp_r} + \frac{32\sqrt{G_{tr}{}^2\pi^4 - 16}}{G_{tr}{}^2\pi^6 N^2 R_L}\Delta v_{Cp_i} + \frac{16}{G_{tr}\pi^3 N}\Delta i_{Lf} \tag{6.24a}$$

$$\Delta i_{tp_i} = \frac{32\sqrt{G_{tr}{}^2\pi^4 - 16}}{G_{tr}{}^2\pi^6 N^2 R_L}\Delta v_{Cp_r} + \frac{128}{G_{tr}{}^2\pi^6 N^2 R_L}\Delta v_{Cp_i} - \frac{4\sqrt{G_{tr}{}^2\pi^4 - 16}}{G_{tr}\pi^3 N}\Delta i_{Lf} \tag{6.24b}$$

The resulting state-space small-signal model can now be written from (5.15), (6.6),(6.20),(6.23) and (6.24) giving (6.25):

$$\mathbf{A} = \begin{bmatrix} 0 & -1/L_s & -1/L_s & \omega_r & 0 & 0 & 0 & 0 \\ 1/C_s & 0 & 0 & 0 & \omega_r & 0 & 0 & 0 \\ 1/C_p & 0 & K_{33} & 0 & 0 & (\omega_r + K_{36}) & K_{37} & 0 \\ -\omega_r & 0 & 0 & 0 & -1/L_s & -1/L_s & 0 & 0 \\ 0 & -\omega_r & 0 & 1/C_s & 0 & 0 & 0 & 0 \\ 0 & 0 & (-\omega_r + K_{63}) & 1/C_p & 0 & K_{66} & K_{67} & 0 \\ 0 & 0 & K_{73} & 0 & 0 & K_{76} & 0 & -1/L_f \\ 0 & 0 & 0 & 0 & 0 & 0 & 1/C_f & -1/(C_f R_L) \end{bmatrix} \tag{6.25}$$

$$\mathbf{B} = [2V_{dc}/(\pi L_s) \quad 0 \quad 0 \quad 0 \quad 0 \quad 0 \quad 0 \quad 0] \; \mathbf{C} = [0 \quad 0 \quad 0 \quad 0 \quad 0 \quad 0 \quad 0 \quad 1]$$

$$x = [\Delta I_{Ls_r} \quad \Delta V_{Cs_r} \quad \Delta V_{Cp_r} \quad \Delta I_{Ls_i} \quad \Delta V_{Cs_i} \quad \Delta V_{Cp_i} \quad \Delta I_{Lf} \quad \Delta V_o]^T$$

$$\begin{aligned} \dot{x} &= \mathbf{A}.x + \mathbf{B}.u \\ y &= \mathbf{C}.x \end{aligned} \quad \text{where} \quad \begin{aligned} y &= \Delta V_o \\ u &= \Delta PF \end{aligned} \quad \text{and,}$$

$$K_{33} = -\frac{4\omega_r\sqrt{G_{tr}{}^2\pi^4 - 16}}{G_{tr}{}^2\pi^4} \qquad K_{36} = -\frac{16\omega_r}{G_{tr}{}^2\pi^4} \qquad K_{37} = -\frac{8NR_L\omega_r}{G_{tr}\pi\sqrt{G_{tr}{}^2\pi^4 - 16}}$$

$$K_{63} = -\frac{16\omega_r}{G_{tr}{}^2\pi^4} \qquad K_{66} = -\frac{64\omega_r}{G_{tr}{}^2\pi^4\sqrt{G_{tr}{}^2\pi^4 - 16}} \qquad K_{67} = \frac{2NR_L\omega_r}{G_{tr}\pi}$$

$$K_{73} = \frac{8}{L_f G_{tr}\pi^3 N} \qquad K_{76} = \frac{-2\sqrt{G_{tr}{}^2\pi^4 - 16}}{L_f G_{tr}\pi^3 N}$$

To use the model, (6.25), the converter tank gain and resonant frequency must first be calculated. These are obtained by solving (6.20) for $A=C_p/C_s$, G_{tr} and ω_r. For instance, to calculate G_{tr}, equate the ω_r term in both (6.20a) and (6.20c), and solve for G_{tr}.

6.4 Realisation of a Power-factor controller

A key factor for providing good self-oscillating control of the power factor is determining when changes of polarity of the series-inductor current occur - for simplicity, the series-inductor voltage is measured, integrated (through use of low pass filter with relatively low break frequency), and fed into a low-offset comparator, as shown in Figure 6.3.

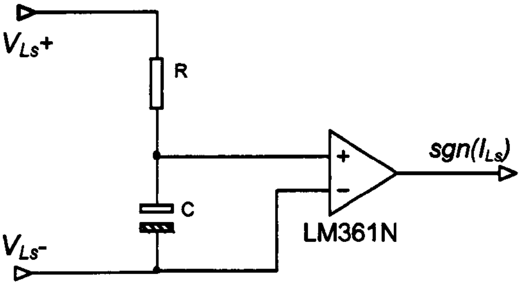

Figure 6.3 - Series inductor current zero-crossing detection via series inductor voltage integration

Equation (6.43) is used to choose the values of C and R in the low-pass filter. The time-constant (CR) of the lower-pass filter is chosen such that at the lowest switching frequency, the phase shift θ, closely approximates $-\pi/2$ and that the filter gain G is sufficiently small such that the voltage applied across the comparator is within the limits of its specifications at all times (for instance ±5V).

$$\theta = -\tan^{-1}(2\pi fCR) \approx -\frac{\pi}{2} \quad , \quad G = \frac{1}{\sqrt{1+(2\pi fCR)^2}} \tag{6.26}$$

Having obtained the polarity of the current, an FPGA is used to generate the required switching signals based on the demanded power-factor. Figure 6.4 demonstrates the required functionality of the FPGA delay mechanism. A background process on the FPGA measures the period (T_p) of the current waveform. At time t_1 a rising edge on *sgn*(I_{Ls}) is detected, after a delay time (T_d), at time t_2 the FPGA forces a falling-edge on the switching voltage. Similarly, the opposite occurs when a falling edge *sgn*(I_{Ls}) is detected, and after the delay T_d, the FPGA forces a rising-edge on the switching voltage.

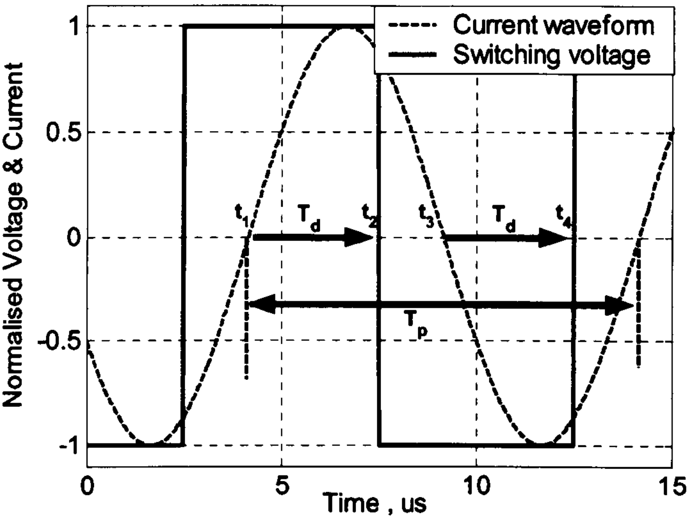

Figure 6.4 - FPGA delay methodology

Delaying the 'edges' in the proposed manner reduces the delays necessary by the FPGA and, secondly, ensures that the duty cycle of the current-waveform is maintained.

The required delay-time T_d is calculated from the power-factor (*PF*) and the period T_p as follows:

$$T_d = \frac{T_p}{2}\left(1 - \frac{\cos^{-1}(PF)}{\pi}\right) \tag{6.27}$$

Since the FPGA, in fact, measures the number of clock-cycles across the period n_p, and delays the signal by n_d samples, (6.27) can be re-written as:

$$n_d = K n_p \quad \text{where } K = \frac{1}{2}\left(1 - \frac{\cos^{-1}(PF)}{\pi}\right) \text{and } \frac{1}{4} \geq K \geq \frac{1}{2} \tag{6.28}$$

For a given *PF*, the delay factor *K* is obtained through use of a look-up table.

Additional features to the FPGA based power-factor controller include a user selectable dead-time between high and low gate-drive signals and a propagation delay compensation feature that reduces the calculated delay by a fixed number of clock cycles.

The functionality of the power factor controller, and the FPGA with interface board, is depicted in Figure 6.5.

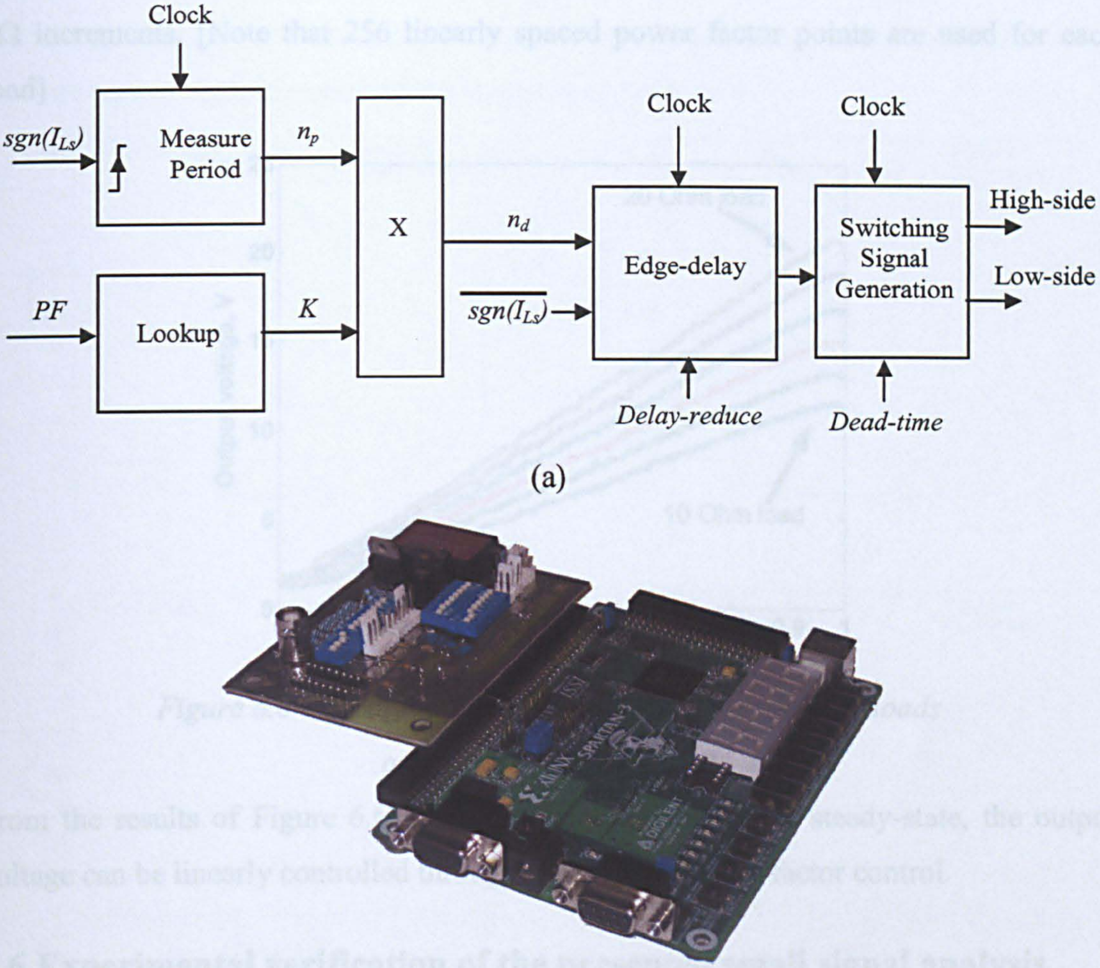

(a)

(b)

Figure 6.5 - FPGA based Power-factor controller (a) block diagram (b) photo

See Appendix E for FPGA code details.

Note that although a Spartan-3 demonstration board was chosen for simplicity, very little of the FPGA is actually utilised.

6.5 Steady-state behaviour of the power-factor control scheme

For a converter specified by: V_{dc}=18, L_s=13.6µH, C_s=220nF, C_p=130nF, N=1, L_f=24µH, C_f=220µF (see section 3.8 for design specifications), Figure 6.6 provides results from experimental measurements of the steady-state output voltage, as the power-factor is varied through use of the power-factor controller, for loads varying from 10Ω to 20Ω in 2Ω increments. [Note that 256 linearly spaced power factor points are used for each load]

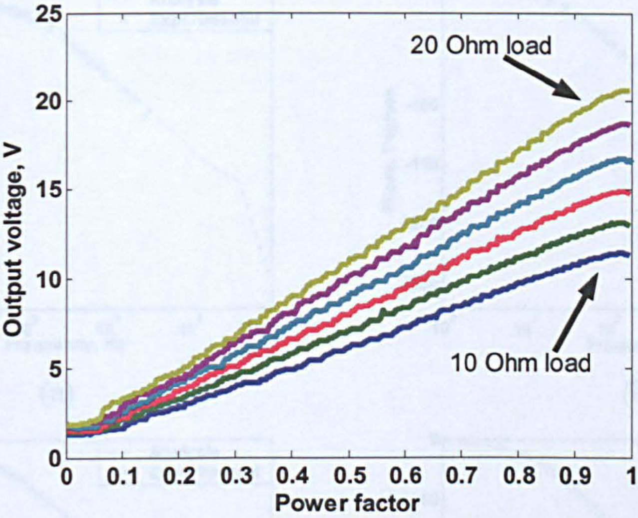

Figure 6.6 - Steady-state output voltage across various loads at specified power-factors

From the results of Figure 6.6 it can clearly be seen that, at steady-state, the output voltage can be linearly controlled through appropriate power-factor control.

6.6 Experimental verification of the presented small signal analysis methodology

Figure 6.7 shows experimental measurements of the small-signal frequency response of the converter along with those from the proposed analysis (6.25). The power factor is perturbed around PF_{bias}=0.75 through use of the self-oscillating power-factor controller considered previously. A note about the scaling is in order here. When R_L=10Ω, the converter gain at resonance is 0.674, hence, with the specified input voltage, V_{out}=12.1V, implying a steady-state gain of +21.7dB at 0Hz between PF and V_{out}. Similarly, when R_L=20Ω, the converter gain at resonance is 1.26, hence, with the specified input voltage, V_{out}=22.7V, implying a steady-state gain of +27.1dB at 0Hz between PF and V_{out}. It can be seen that, in general, very good agreement between the results exists. Moreover, from Figure 6.8, it can also be seen that both the simulated and experimental output voltage dynamics closely follow a scaled version of the input power factor, thereby further demonstrating the controller's linear behaviour, and, although the underlying state-variable model is 8th order, the system is dominantly 3rd order. Furthermore, since the small-signal response is found to be constant across the full steady-state power-factor range, the small-signal response can also be considered to provide a good approximation of the large-signal behaviour.

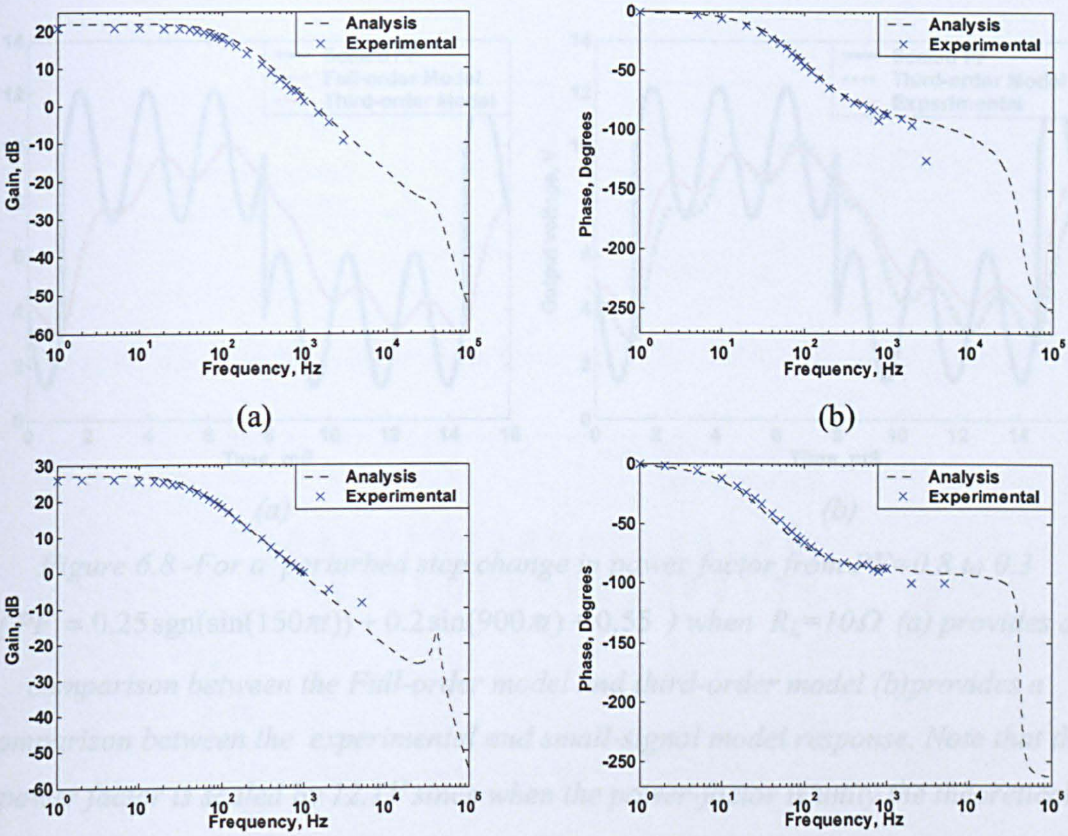

(a) (b)

(c) (d)

Figure 6.7 - Small-signal frequency response comparison between proposed analysis and experimental results for 10Ω load (a-b) and 20Ω load (c-d). [Note that when the perturbation in power factor is above 2kHz, the phase response measurements become inaccurate as a result of the signal-level becoming comparable in amplitude with noise and output-voltage ripple].

Third order approximations for:

$$10\Omega \text{ load} \rightarrow G(s)=\frac{-0.0072S^3+5.0437\times10^3S^2-2.4286\times10^9S+1.0087\times10^{15}}{S^3+2.4732\times10^5S^2+1.1960\times10^{11}S+8.3174\times10^{13}}$$

$$20\Omega \text{ load} \rightarrow G(s)=\frac{-0.0041S^3+738.7S^2-3.3788\times10^8S+3.9480\times10^{13}}{S^3+3.3494\times10^4S^2+7.0662\times10^{10}S+1.7524\times10^{13}}$$

Table 6.I - Open loop gain and phase margins

	Gain Margin	Phase Margin
10 Ω load	28.29dB	92.57
20 Ω load	16.67dB	92.12

The controller must be designed for the higher load resistance since the open-loop gain margin reduces with increasing load resistance.

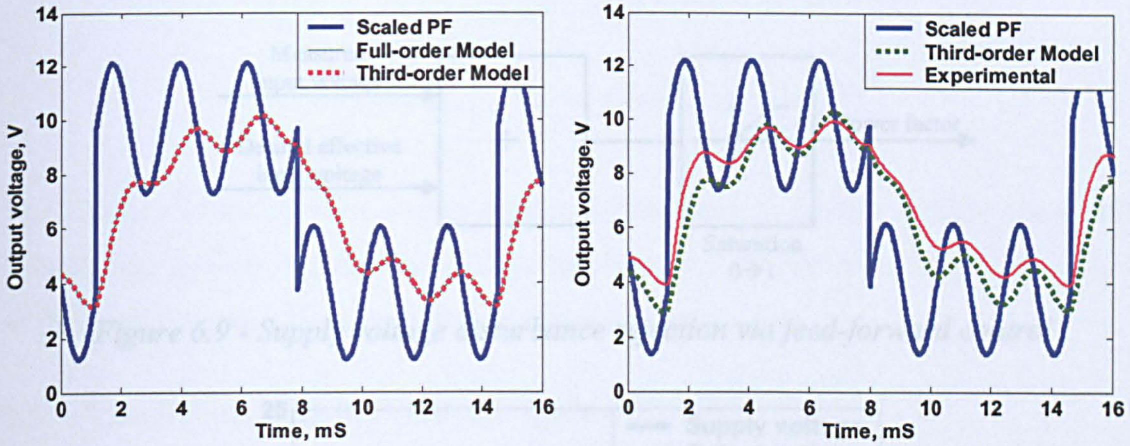

(a) *(b)*

Figure 6.8 -For a perturbed step change in power factor from PF=0.8 to 0.3 ($PF = 0.25\,\mathrm{sgn}(\sin(150\pi t)) + 0.2\sin(900\pi t) + 0.55$) when $R_L=10\Omega$ (a) provides a comparison between the Full-order model and third-order model (b)provides a comparison between the experimental and small-signal model response. Note that the power factor is scaled by 12.1V since when the power-factor is unity the theoretical ideal output-voltage of the converter is 12.1V

Note that the full order model and third order model overlay each other in Figure 6.8(a). Additionally differences between the third order model and experimental data in Figure 6.8(b) are a result of converter parasitics.

6.7 Supply-voltage disturbance rejection via feed-forward control

To demonstrate the supply voltage disturbance rejection properties, the converter (detailed in section 6.5) is initially excited such that the power factor is controlled to be *PF=0.79*. Then, intermittently, the product $V_{dc}PF$ is controlled to be maintained at $V_{dc}PF=14.2$ through use of feed-forward action, see Figure 6.9. With a DC supply voltage of 18V both strategies provide $V_{out}=9V$ output when applied across a 10Ω load. Figure 6.10 shows the ability of the latter method to provide improved regulation characteristics when $V_{dc}=18+2\sin(2\pi 100t)$–the choice of 100Hz disturbance reflecting the use of a full-bridge mains rectifier. In particular, it can be seen that during constant power-factor operation, the peak-peak output voltage ripple (1.66V) is much larger than that obtained when utilising feed-forward control action (0.26V), thereby demonstrating the potential for improving regulation performance.

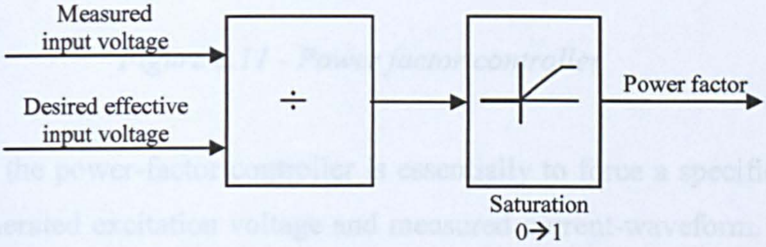

Figure 6.9 - Supply voltage disturbance rejection via feed-forward control

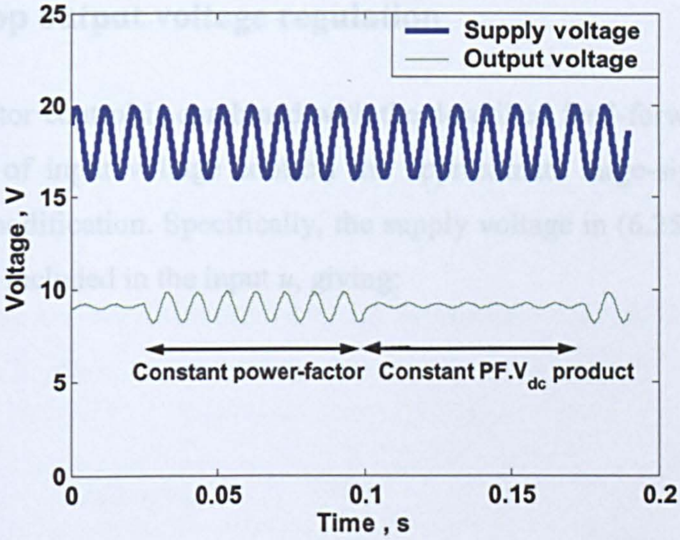

Figure 6.10 - Supply-voltage rejection with and without feed-forward action

6.8 Modelling the power-factor controller characteristics

To investigate the behaviour of the converter under power-factor control, a SIMULINK based compensator is developed. Figure 6.11 provides the top-level power-factor controller structure.

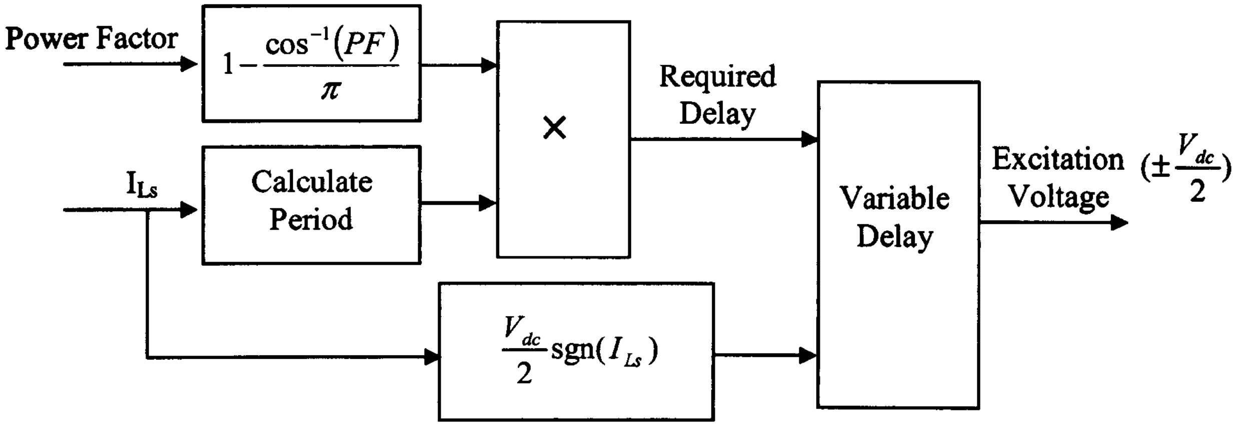

Figure 6.11 - Power factor controller

The function of the power-factor controller is essentially to force a specific phase shift between the generated excitation voltage and measured current-waveform. The amount of phase shift being a function of the demanded power-factor.

6.9 Closed-loop output voltage regulation

When power factor control is combined with the described feed-forward action (giving the equivalence of input voltage control) the approximate large-signal model (6.25) requires minor modification. Specifically, the supply voltage in (6.25) is removed from the **B** matrix and included in the input u, giving:

$$\mathbf{A}=\begin{bmatrix} 0 & -1/L_s & -1/L_s & \omega_r & 0 & 0 & 0 & 0 \\ 1/C_s & 0 & 0 & 0 & \omega_r & 0 & 0 & 0 \\ 1/C_p & 0 & K_{33} & 0 & 0 & (\omega_r+K_{36}) & K_{37} & 0 \\ -\omega_r & 0 & 0 & 0 & -1/L_s & -1/L_s & 0 & 0 \\ 0 & -\omega_r & 0 & 1/C_s & 0 & 0 & 0 & 0 \\ 0 & 0 & (-\omega_r+K_{63}) & 1/C_p & 0 & K_{66} & K_{67} & 0 \\ 0 & 0 & K_{73} & 0 & 0 & K_{76} & 0 & -1/L_f \\ 0 & 0 & 0 & 0 & 0 & 0 & 1/C_f & -1/(C_f R_L) \end{bmatrix} \qquad (6.29)$$

$$\mathbf{B}=\begin{bmatrix} 2/(\pi L_s) & 0 & 0 & 0 & 0 & 0 & 0 & 0 \end{bmatrix} \mathbf{C}=\begin{bmatrix} 0 & 0 & 0 & 0 & 0 & 0 & 0 & 1 \end{bmatrix}$$

$$x=\begin{bmatrix} \Delta I_{Ls_r} & \Delta V_{Cs_r} & \Delta V_{Cp_r} & \Delta I_{Ls_i} & \Delta V_{Cs_i} & \Delta V_{Cp_i} & \Delta I_{Lf} & \Delta V_o \end{bmatrix}^T$$

$$\begin{aligned} \dot{x} &= \mathbf{A}.x+\mathbf{B}.u \\ y &= \mathbf{C}.x \end{aligned} \quad \text{where} \quad \begin{aligned} y &= V_o \\ u &= V_{dc}PF \end{aligned} \quad \text{and,}$$

$$K_{33}=-\frac{4\omega_r\sqrt{G_{tr}^2\pi^4-16}}{G_{tr}^2\pi^4} \qquad K_{36}=-\frac{16\omega_r}{G_{tr}^2\pi^4} \qquad K_{37}=-\frac{8NR_L\omega_r}{G_{tr}\pi\sqrt{G_{tr}^2\pi^4-16}}$$

$$K_{63}=-\frac{16\omega_r}{G_{tr}^2\pi^4} \qquad K_{66}=-\frac{64\omega_r}{G_{tr}^2\pi^4\sqrt{G_{tr}^2\pi^4-16}} \qquad K_{67}=\frac{2NR_L\omega_r}{G_{tr}\pi}$$

$$K_{73}=\frac{8}{L_fG_{tr}\pi^3N} \qquad K_{76}=\frac{-2\sqrt{G_{tr}^2\pi^4-16}}{L_fG_{tr}\pi^3N}$$

For output voltage control, with feed-forward mechanism described in section 6.7, the overall system will take a form similar to that shown in Figure 6.12.

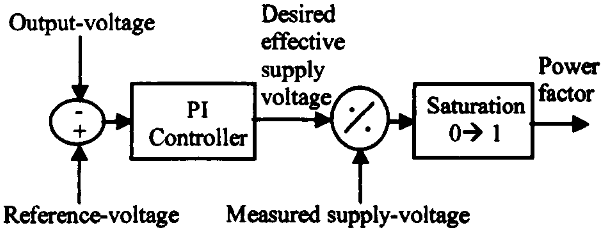

Figure 6.12 - Closed loop output voltage regulation utilising feed-forward action.

For stability, the loop-gain must never exceed unity magnitude when the phase shift crosses -180°, for all possible load conditions.

The loop-gain is found from:

$$L(s) = G(s)F(s) \tag{6.30}$$

where $G(s)$ is the third-order reduced model of the converter and $F(s)$ is the controller model.

The converter will regulate the output voltage across a load ranging from 10'sΩ to 100Ω. For robustness, the controller gains are selected such that the converter remains stable with a phase margin >20°, with an applied load of 100Ω.

Table 6.II - Controller gains and associated 100Ω load Gain/Phase Margins

Controller Gains	Gain/Phase Margins
$K_i=1\times10^3$ $K_p=2$	$GM=9.25$ $PM=57.4°$
$K_i=1\times10^3$ $K_p=10$	$GM=1.85$ $PM=88.8°$
$K_i=10\times10^3$ $K_p=2$	$GM=9.24$ $PM=20.3°$
$K_i=10\times10^3$ $K_p=10$	$GM=1.85$ $PM=71.8°$

See section 6.6 for the open loop gain and phase margins. Note that the higher order poles in the higher order model have insignificant loop gain compared to the lower 3 poles hence, the 3rd order model is sufficient for closed-loop controller design.

Before utilising the model presented in (6.29) for controller design purposes, the behaviour of the proposed model is compared in closed loop with that of the actual system (PLECS component based simulation) under identical closed loop control to a moving output voltage demand. Ideally the behaviour of the proposed model and the actual system under identical control are the same. Figure 6.13 provides the comparison when a PI controller ($K_p=2$, $K_i=1e3$) is used to regulate the output voltage to a moving voltage reference. From the figure, it can be seen that both the converter (a PLECS model) and the proposed model, behave very similarly in closed loop, thus justifying the use of the model for controller design purposes.

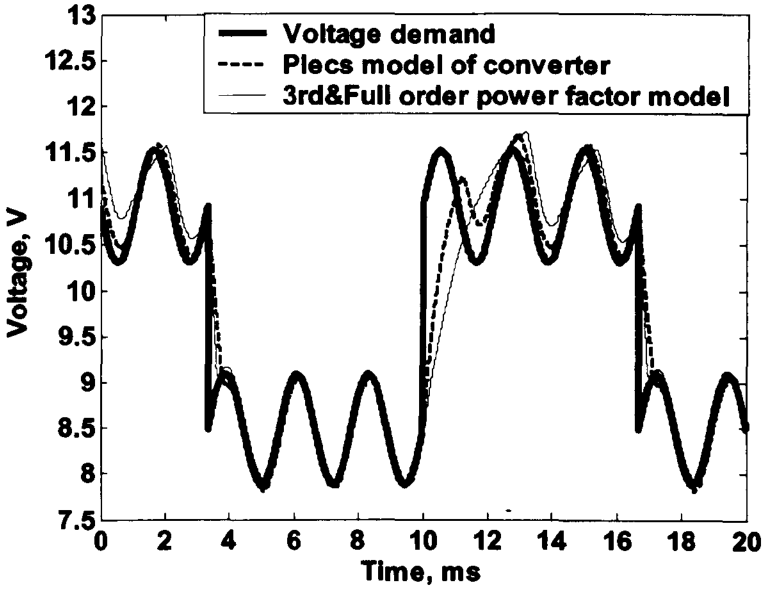

Figure 6.13 - Behavioural comparison between closed loop PLECS converter model and proposed model under varying output demand conditions.

Implementing the control gains in Table 6.II on the prototype converter, and stepping the load between 10Ω and 20Ω, at 20Hz through use of an electronic load, whilst regulating the output-voltage at 9V gives the responses presented in Figures 6.14 and 6.15, for the two cases, respectively.

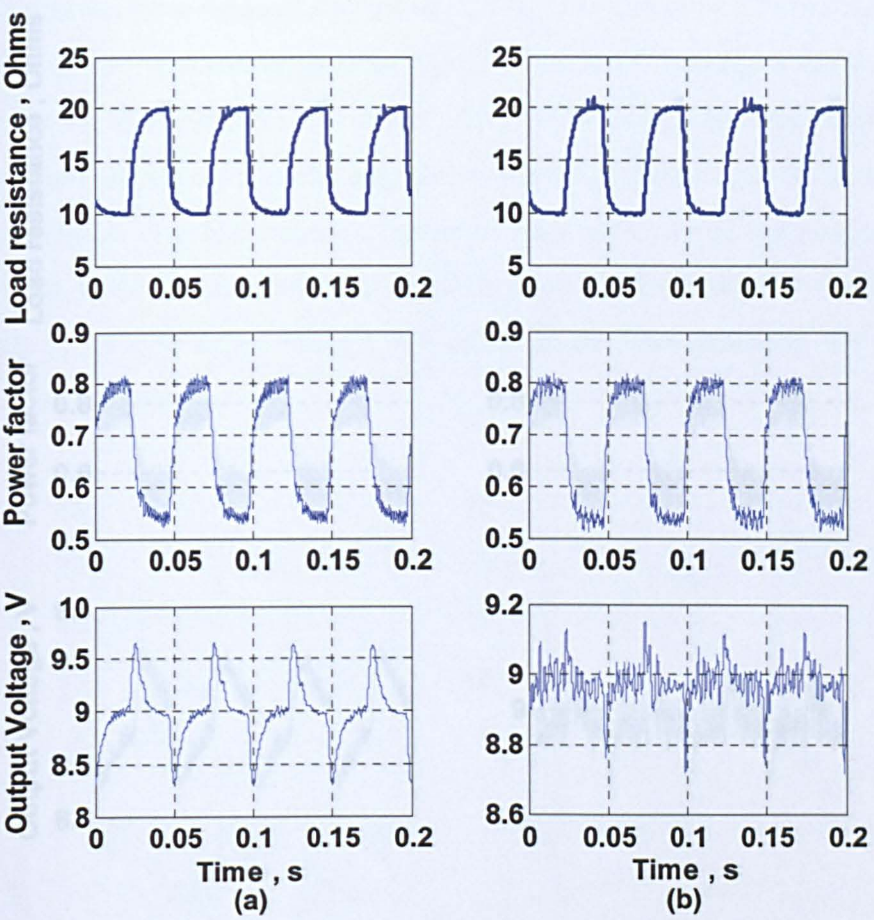

Figure 6.14 - Closed loop output-voltage regulation waveforms

(a) $K_p=2$ $K_i=1\times10^3$ (b) $K_p=2$ $K_i=10\times10^3$

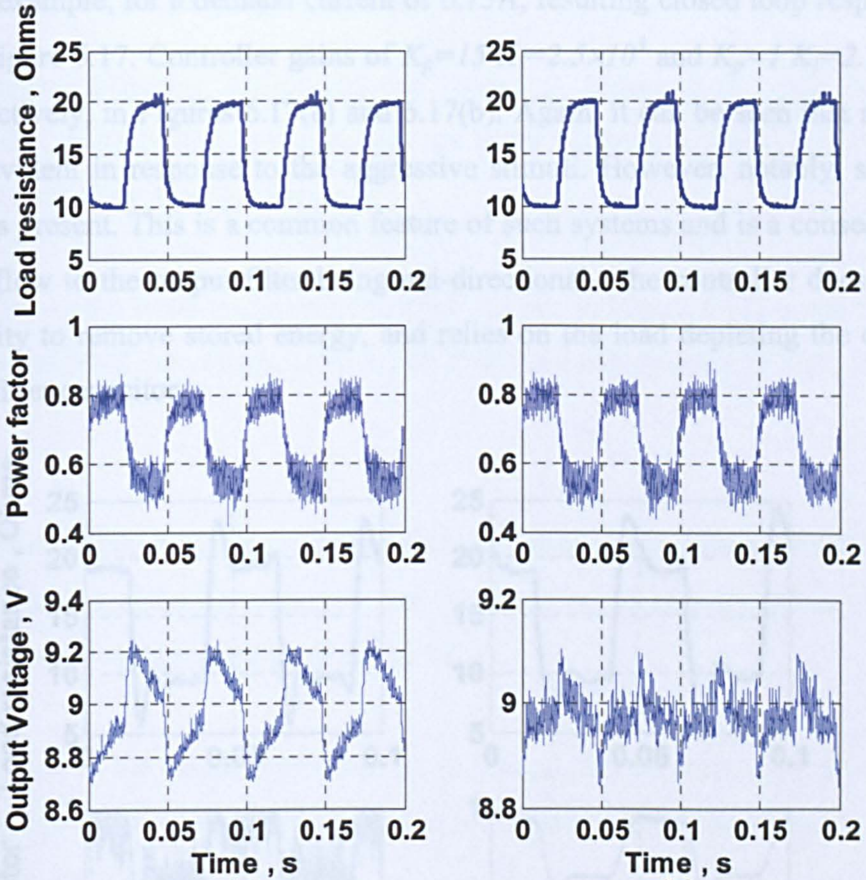

(a) (b)

Figure 6.15 - Closed loop output-voltage regulation waveforms

(a) $K_p=10$ $K_i=1\times10^3$ (b) $K_p=10$ $K_i=10\times10^3$

It can be seen that the output-voltage regulation is being obtained, in each case, in response to the relatively aggressive disturbance stimuli.

The converter can also be operated as a constant-source by feeding back a measurement of output current, see Figure 6.16.

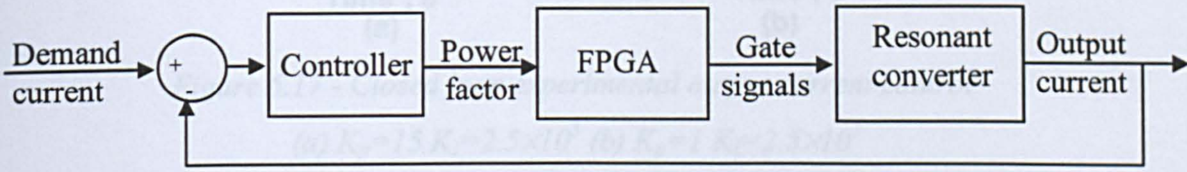

Figure 6.16 - Closed loop current regulation block diagram

By way of example, for a demand current of 0.75A, resulting closed loop responses are shown in Figure 6.17. Controller gains of $K_p=15$ $K_i=2.5\times10^3$ and $K_p=1$ $K_i=2.5\times10^3$ are used, respectively, in Figures 6.17(a) and 6.17(b). Again, it can be seen that regulation is clearly evident in response to the aggressive stimuli. However, notably, significant overshoot is present. This is a common feature of such systems and is a consequence of the power flow to the output filter being uni-directional—the controller does not have the capability to remove stored energy, and relies on the load depleting the charge on the output filter capacitor.

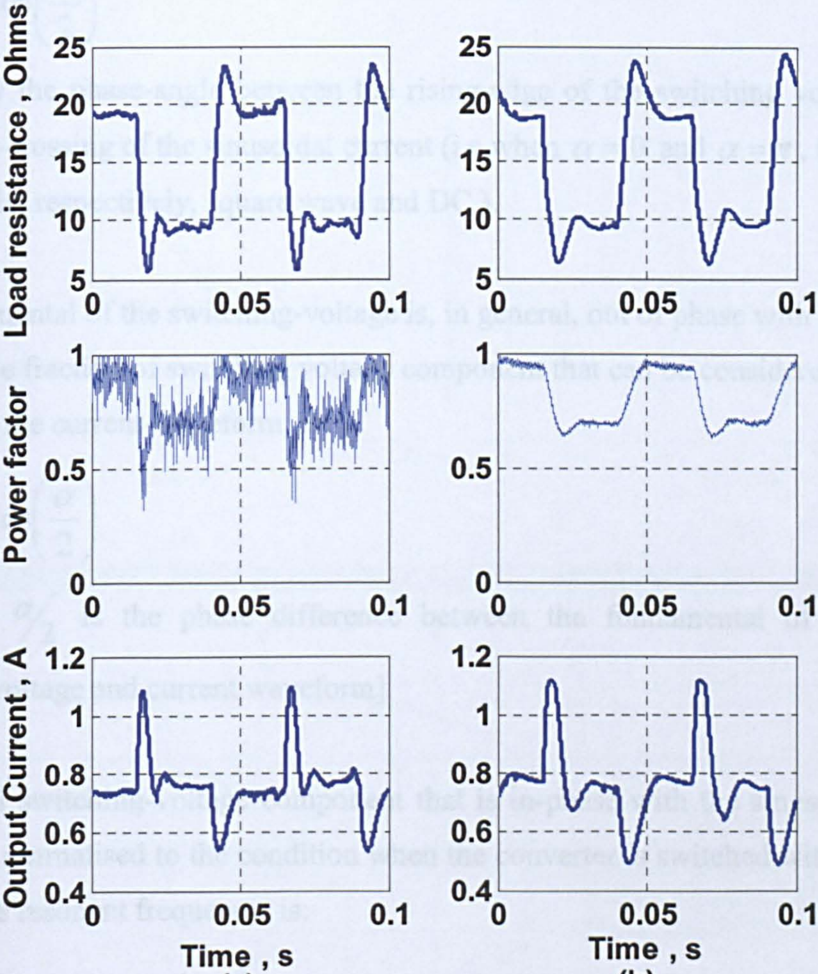

(a) (b)

Figure 6.17 - Closed loop experimental output current control

(a) $K_p=15$ $K_i=2.5\times10^3$ *(b)* $K_p=1$ $K_i=2.5\times10^3$

6.10 Alternative switching technique

Two alternative switching techniques are shown in Figure 6.18, each having the advantage that a switching event occurs on a zero-current crossing point, thereby facilitating reduced switching losses.

When employing the fixed falling-edge method, shown in Figure 6.18(a), the magnitude of the fundamental of the voltage, normalised to that for a duty-cycle of 50% is:

$$G_1(\alpha) = \cos\left(\frac{\alpha}{2}\right) \tag{6.31}$$

where α is the phase-angle between the rising-edge of the switching voltage and the rising zero-crossing of the sinusoidal current (i.e when $\alpha = 0$ and $\alpha = \pi$, the switching-waveform is, respectively, square wave and DC).

The fundamental of the switching-voltage is, in general, out of phase with the sinusoidal current. The fraction of switching voltage component that can be considered as being in-phase with the current-waveform, is:

$$G_2(\alpha) = \cos\left(\frac{\alpha}{2}\right) \tag{6.32}$$

[note that $\alpha/2$ is the phase difference between the fundamental of the switching voltage and current waveform]

The overall switching-voltage component that is in-phase with the sinusoidal current-waveform, normalised to the condition when the converter is switched with a 50% duty cycle, at the resonant frequency, is:

$$G = G_1(\alpha)G_2(\alpha) = \cos\left(\frac{\alpha}{2}\right)^2 \tag{6.33}$$

The time T_d is therefore calculated as follows:

$$T_d = T_p\left(\frac{1}{2} - \frac{\cos^{-1}(G)}{\pi}\right) \tag{6.34}$$

Similarly:

$$n_d = K n_p \quad \text{where } K = \left(\frac{1}{2} - \frac{\cos^{-1}(G)}{\pi}\right) \text{ and } 0 \ge K \ge \frac{1}{2},\ 0 \ge G \ge 1 \tag{6.35}$$

When employing the fixed rising-edge method, as shown in Figure 6.18(b), a similar mathematical treatment can be performed, leading to:

$$n_d = K n_p \quad \text{where } K = \frac{\sin^{-1}(G)}{\pi} \text{ and } 0 \ge K \ge \frac{1}{2},\ 0 \ge G \ge 1 \tag{6.36}$$

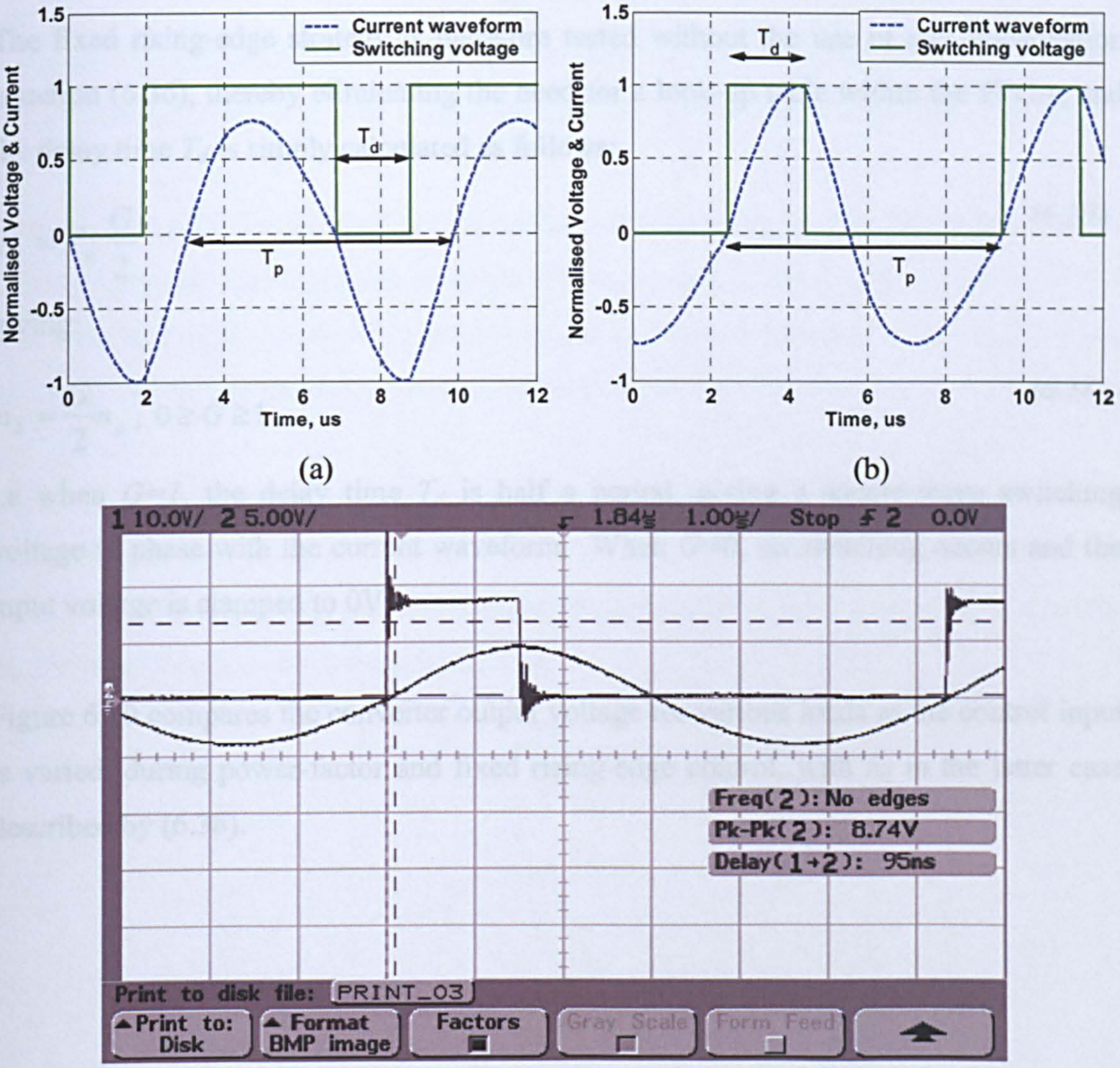

(a) (b)

(c)

Figure 6.18 - Alternative self-oscillating switching strategies - series inductor current zero-crossing fixed (a) falling-edge (b) rising-edge (c) practical implementation of rising-edge strategy - notice that the delay time between the zero-crossing of the current waveform and rising edge of the excitation voltage is approximately 100ns, insignificant compared to the switching period of approximately 6.3uS

Note that the zero current detection method has been presented in section 6.4, see Figure 6.3.

From Figure 6.18 it can be seen that the current waveforms are asymmetric about the positive and negative half-cycles, and are therefore not sinusoidal, which was the underlying assumption for the analysis. Simulation studies have shown that, generally, (6.35) and (6.36) do not provide a sufficiently accurate linearisation mechanism for the respective switching strategies. Nevertheless, the resulting behaviour for each is found to be similar.

The fixed rising-edge strategy is therefore tested without the use of any linearisation equation (6.36), thereby eliminating the need for a look-up table within the FPGA, and the delay time T_d is simply calculated as follows:

$$T_d = T_p \frac{G}{2} \tag{6.37}$$

giving:

$$n_d = \frac{G}{2} n_p \, , \; 0 \geq G \geq 1 \tag{6.38}$$

i.e when $G=1$, the delay time T_d is half a period, giving a square-wave switching voltage in phase with the current waveform. When $G=0$, no switching occurs and the input voltage is clamped to 0V.

Figure 6.19 compares the converter output voltage for various loads as the control input is varied, during power-factor and fixed rising-edge control, with n_d in the latter case described by (6.38).

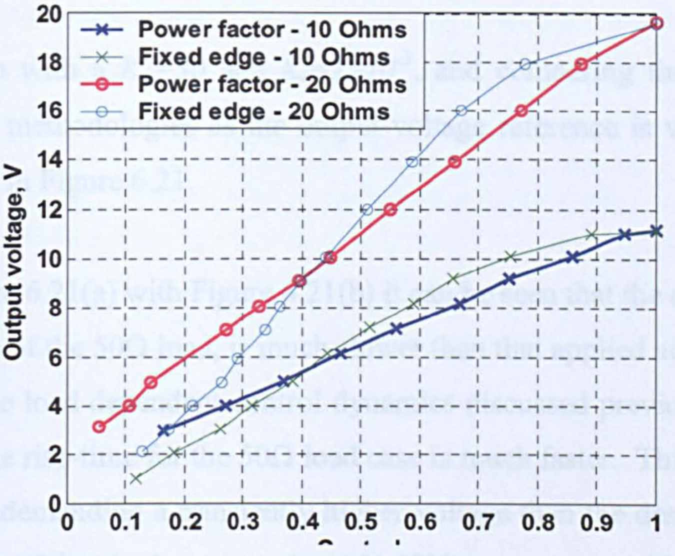

Figure 6.19 - Comparison between control input and output-voltage for two different loads under power-factor control and the alternative fixed rising-edge control

From Figure 6.19 the fixed-edge methodology can be shown to provide approximately linear behaviour. The large-signal model for power-factor control, approximated by the small-signal model presented in section 6.3, may therefore provide a reasonable large-signal model for the fixed rising-edge control scheme.

Figure 6.20 compares the converter output-voltage and control-input for both power-factor control and fixed-edge control (with no lookup table). Both methods result in similar output-voltage waveform characteristics, and, for control purposes the power-factor large-signal model may be sufficient.

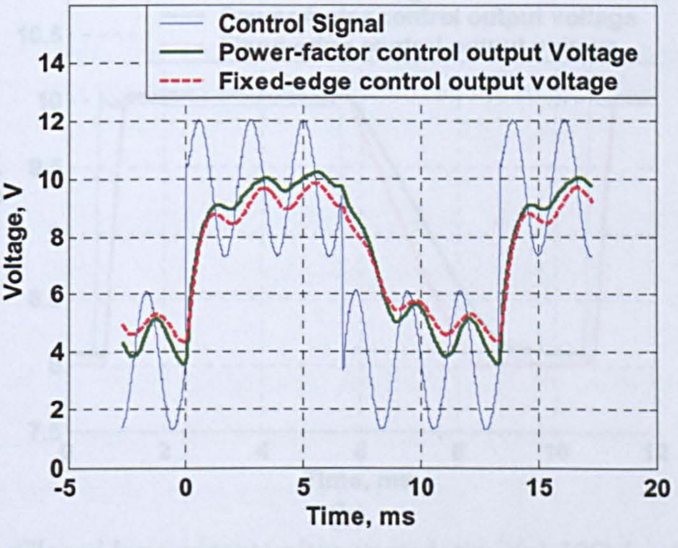

Figure 6.20 - Output voltage as control signal is varied for both power-factor and fixed edge control with an applied 10Ω load

Closing the loop with a $K_p=30$ and $K_i=1\times10^{-3}$, and comparing the converter output voltage for both methodologies as the output-voltage reference is varied provides the responses shown in Figure 6.21.

Comparing Figure 6.21(a) with Figure 6.21(b) it can be seen that the output-voltage fall-time, for the case of the 50Ω load, is much slower than that applied across the 10Ω load, demonstrating the load dependent control dynamics discussed previously. Conversely, the output-voltage rise-time for the 50Ω load case is much faster. This is a consequence of the controller demanding a transiently higher voltage than the desired 10V, with the converter capable of developing approximately 50V at resonance with a 50Ω load.

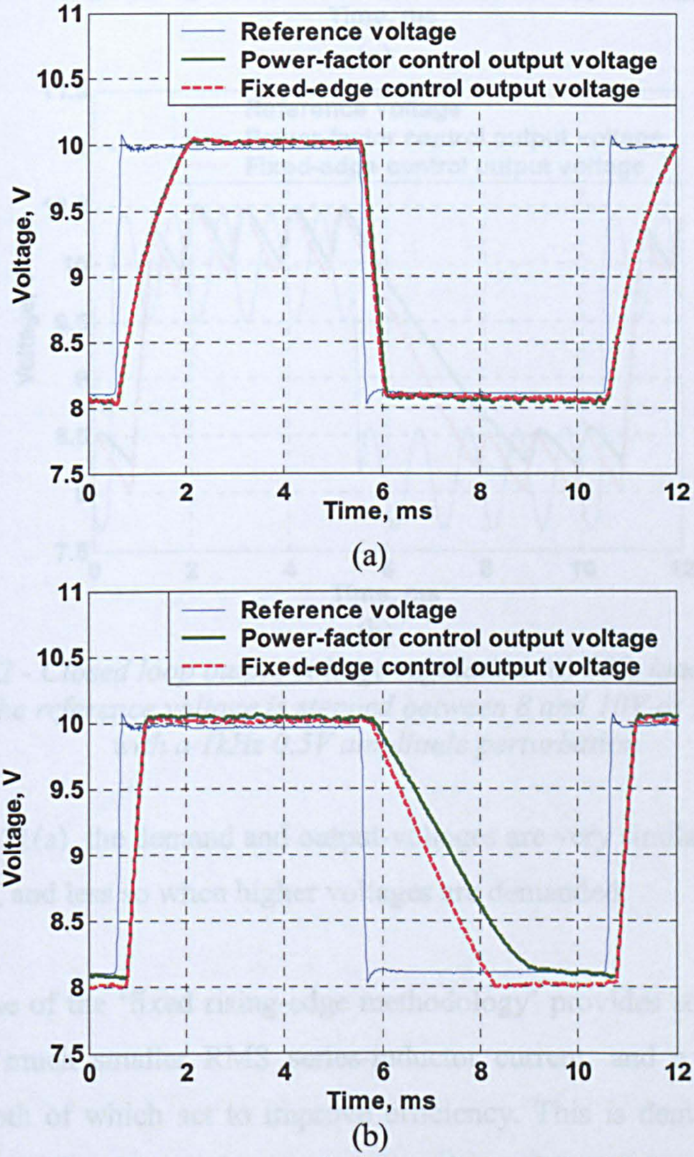

(a)

(b)

Figure 6.21 - Closed loop output voltage regulation (a) 10Ω load (b) 50Ω load. The reference voltage is stepped between 8 and 10V at 100Hz

Now including a sinusoidal perturbation in the square reference voltage demand signal, utilising the same feedback as in Figure 6.21, results in the response:

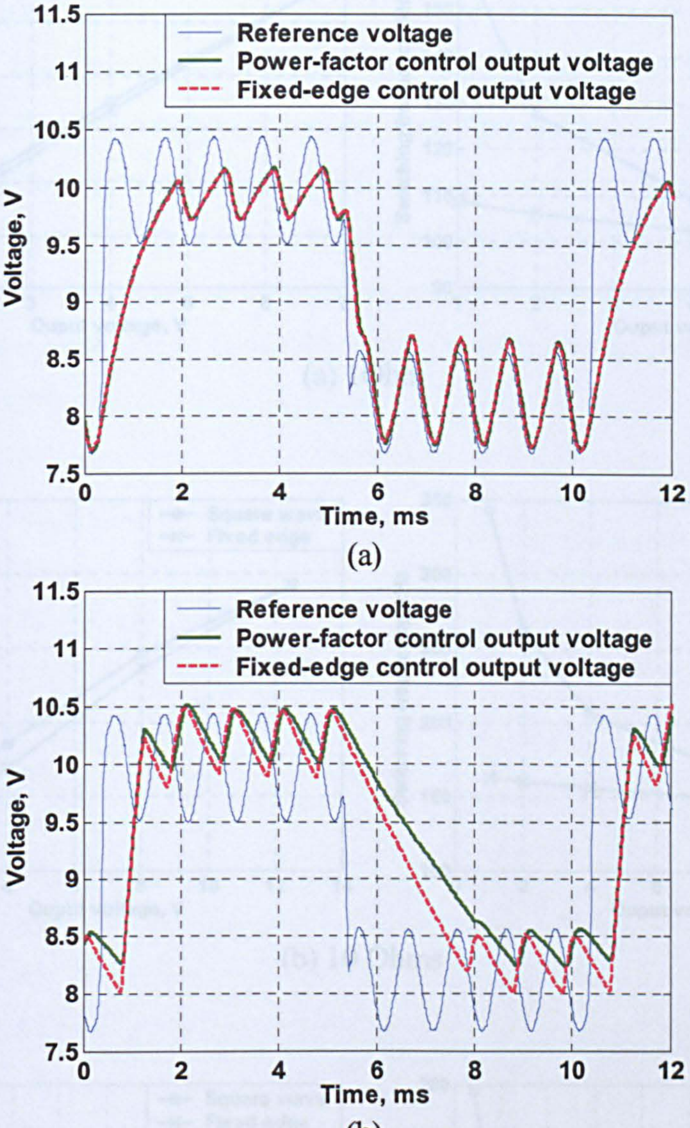

(a)

(b)

Figure 6.22 - Closed loop output voltage regulation (a) 10Ω load (b) 50Ω load. The reference voltage is stepped between 8 and 10V at 100Hz with a 1kHz 0.5V amplitude perturbation

As in Figure 6.21(a), the demand and output-voltages are very similar when the demand is less than 9V, and less so when higher voltages are demanded.

Of note, the use of the 'fixed rising-edge methodology' provides some merit since the qualities of a much smaller RMS series-inductor current, and a reduced switching bandwidth—both of which act to improve efficiency. This is demonstrated in Figure 6.23 where the RMS series-inductor current and switching frequency, are shown for both control methodologies.

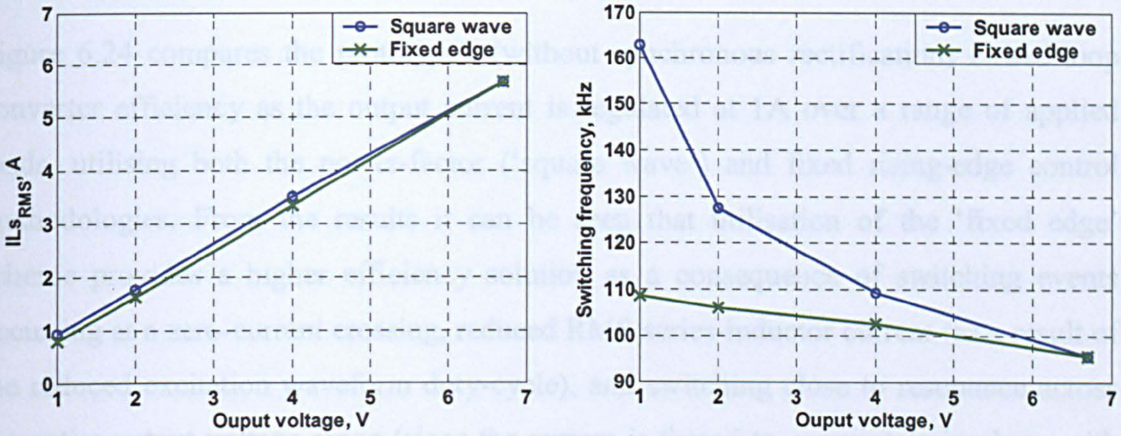

(a) 1Ohm

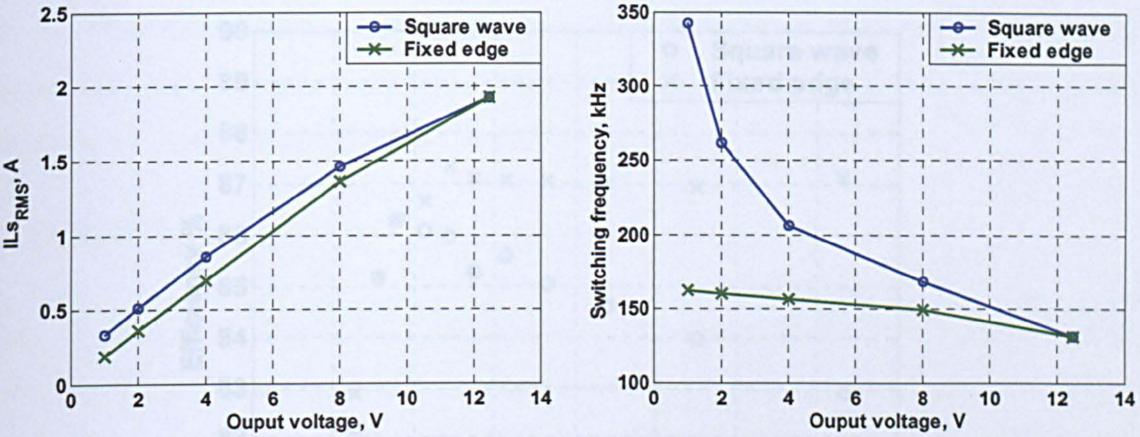

(b) 10 Ohms

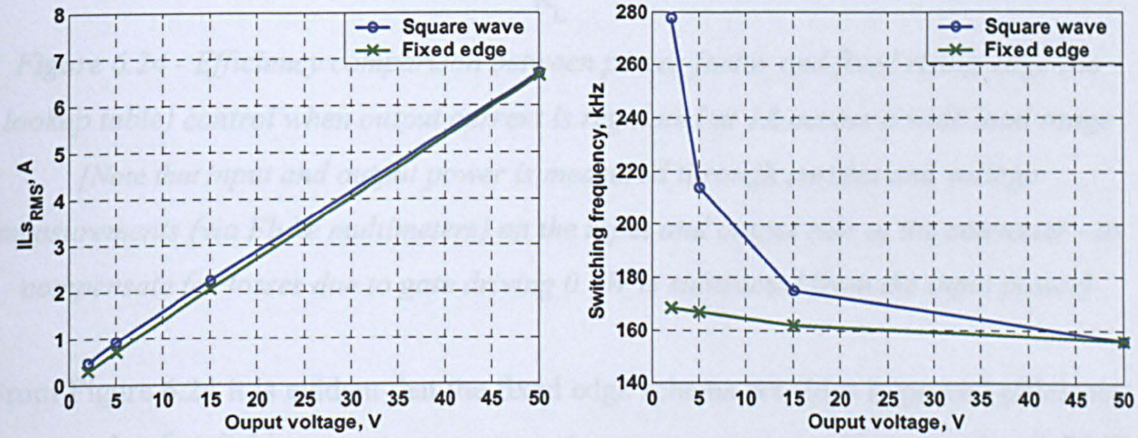

(c) 50 Ohms

Figure 6.23 - Simulated RMS series-inductor current and switching frequency for an applied load of (a) 1Ω (b) 10Ω (c) 50Ω across a range of output voltages when utilising power-factor and fixed-edge (no lookup table) control.

Figure 6.24 compares the prototype's (without synchronous rectification) closed-loop converter efficiency as the output current is regulated at 1A over a range of applied loads, utilising both the power-factor ('square wave') and fixed rising-edge control methodologies. From the results it can be seen that utilisation of the 'fixed edge' scheme provides a higher efficiency solution as a consequence of switching events occurring at a zero-current crossing, reduced RMS series-inductor current (as a result of the reduced excitation waveform duty-cycle), and switching close to resonance across the entire output-voltage range (since the system is forced to commutate in phase with the resonant current).

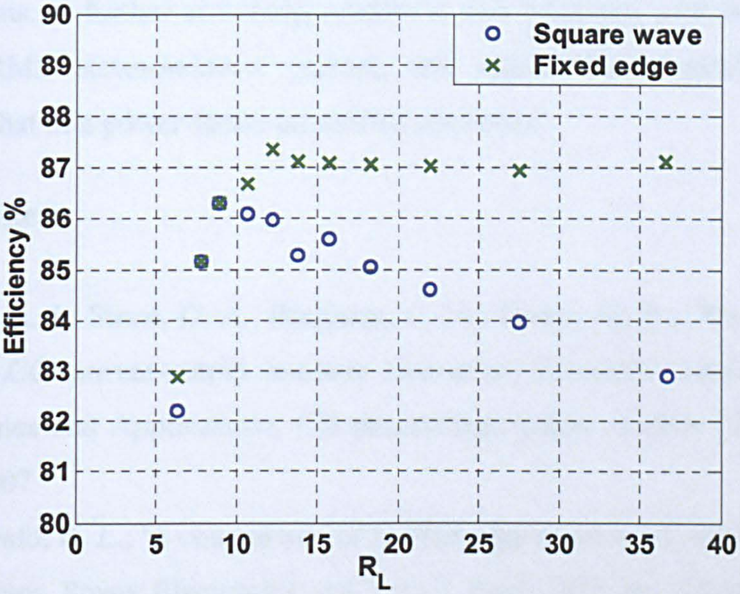

Figure 6.24 - Efficiency comparison between power-factor and fixed rising-edge (no lookup table) control when output current is regulated at 1A across a wide load range [Note that input and output power is measured through current and voltage measurements (via Fluke multimeters) on the input and output side of the converter - to compensate for losses due to gate driving 0.7W is subtracted from the input power]

From Figure 6.24 it is evident that the fixed edge scheme provides improved efficiency as a result of switching events occurring at a zero-current crossing, a reduced RMS series-inductor current (as a result of the reduced excitation waveform duty-cycle), and a reduced switching frequency (since the system is forced to commutate in phase with the resonant current).

6.12 Conclusion

A control strategy for the LCC inductively-smoothed resonant converter is presented. The methodology is advantageous in that it initially linearises the steady-state input-to-output conversion ratio and, secondly, the large-signal converter dynamics become predominantly 3rd order. At present, no other reported control methodology can boast such simple linear behaviour. Through the well-defined behaviour of the power-factor controlled converter, the design of an additional controller to obtain closed-loop output-voltage/current control, is greatly simplified, allowing robust and/or well documented adaptive control methods to be applied. This, therefore, addresses one of the main drawbacks for the use of resonant converters viz. the lack of literature on robust control of such systems. A further switching scheme is also proposed with reduced switching bandwidth, RMS series-inductor current, and approximately similar large signal behaviour to that of a power-factor controlled converter.

6.13 References

[6.1] Gilbert, A. J.; Stone, D. A.; Bingham, C. M.; Foster, M. P.; 'Power factor control of the LCC current-output resonant converter', European Conference on Power Electronics and Applications, CD proceedings paper number 0204, Aalborg 2-5 Sept. 2007

[6.2] Steigerwald, R. L.; 'A comparison of Half-Bridge Resonant Converter Topologies', IEEE Trans. Power Electronics, vol.3, no.2, April 1988, pp.174-182.

[6.3] Kazimierczuk, M. K.; Czarkowski, D.; 'Resonant Power Converters', John Wiley sons, inc 1995, ISBN 0-471-04706-6 , Chapter 8 & 17.

[6.4] Castilla,M.; Garcia de Vicuna, L.; Guerrero, J. M.; Matas, J.; Miret, J.; 'Sliding-mode control of quantum series-parallel resonant converters via input-output linearization', IEEE Trans. Industrial Electronics, vol.52, no. 2, April 2005, pp.566-575

[6.5] Forsyth, A. J.; Ho, Y. K. E.; 'High performance control of the series-parallel resonant converter', IEE Proceedings Electric Power Applications, vol. 144, no. 2, March 1997, pp.131-139

Chapter 7 - Observer-based Output Voltage Regulation of Resonant Converters

A novel control strategy has been developed in Chapter 6 such that traditional linear control techniques can be readily applied to resonant converters. Here, the control of resonant converters from an alternative perspective is explored. Specifically, the application of an observer-based control scheme is investigated [7.1-7.2]. A control methodology is proposed that allows for the elimination of isolated feedback sensors, thereby reducing complexity and cost, facilitating the use of feed-forward control action to accommodate the effects of output load variations, and the detection of output short-circuit fault conditions. Both simulated results and measurements from a prototype converter, are included, to demonstrate the efficacy of the proposed techniques for enhanced regulation and disturbance rejection dynamics when the converter is subjected to transient load changes. Although 3^{rd} order converters are specifically considered, ultimately, the proposed techniques are again applicable to a wide range of other resonant converter topologies.

7.1 Introduction

Classically, in order to regulate the output of a power supply, the voltage (or current) is measured and employed in a feedback control loop to provide an output that is insensitive to changes in the load or primary supply. However, for reasons of safety, electromagnetic compatibility and electromagnetic interference suppression, some form of signal isolation is normally required between the sensed converter output, and the control circuitry, that can constitute a significant proportion of the component and production costs.

An alternative approach, proposed here, is to employ a state-observer to estimate the (nominally) isolated output of a converter, from a model of the dominant system dynamics and measurements of the non-isolated voltages and currents [7.3-7.4]. Previously, similar techniques have been reported [7.4] to estimate the inductor current from the measured inductor voltage, for incorporation within the current-mode control-loop of a buck converter. A feature of such state-estimators, however, is that their dynamics are assumed to have a much greater bandwidth than the dominant dynamics of the converter and input/load disturbances, thereby enabling the observed estimates to be employed directly as part of a closed-loop feedback system. Thus, the effects of exogenous disturbances can be accommodated without the dynamics of the observer contributing significantly to the resulting closed-loop system response.

The dominant output dynamics of classical, hard-switched converters are, for the most part, governed by the time constant of the output filter, with the average values of the non-isolated voltages and currents being employed for the calculation of observer estimates. This has significant practical advantages for the digital implementation of the observer since comparatively low sample rates can be employed, thereby facilitating the use of low cost digital processing hardware.

For resonant converters, however, where high switching frequencies (typically, in the range 100kHz to 2.6MHz) are employed to excite a tank circuit close to its resonant frequency, in order to facilitate low-loss switching of the power devices, the (nominally) non-isolated voltages and currents, which are of interest for use in observer calculations, vary sinusoidally at the switching frequency. This, therefore, precludes the direct use of the relatively basic sensing/signal-processing circuitry employed when implementing observers for hard-switched converter counterparts. A method of addressing this problem is to employ a classical Luenberger observer for output voltage estimation by assuming that the dominant dynamics of the converter, for control purposes, are governed by the output filter, and that the envelopes of the high-frequency tank voltages and currents contain sufficient information to accurately predict the output voltage. Whilst the underlying principles of this technique have been previously reported in [7.5], along with experimental validation, it is constrained to a treatment of the much simpler capacitively-smoothed converter (without a filter inductor), and the linear state-estimation scheme considered was only able to accommodate constant load operation.

Here then, the application of an Extended Kalman Filter (EKF), is proposed, to simultaneously estimate both the output-voltage and the output-load, R_L of the more complex 3rd-order LCC inductively-smoothed resonant converter, shown in Figure 7.1, from measurements of the non-isolated tank voltages and currents. The resulting estimates are subsequently employed as part of a closed-loop control scheme for output voltage regulation. Furthermore, the addition of a feed-forward control element is shown to enhance the disturbance rejection performance of the converter when subject to transient load changes, by utilising the observed estimate of R_L.

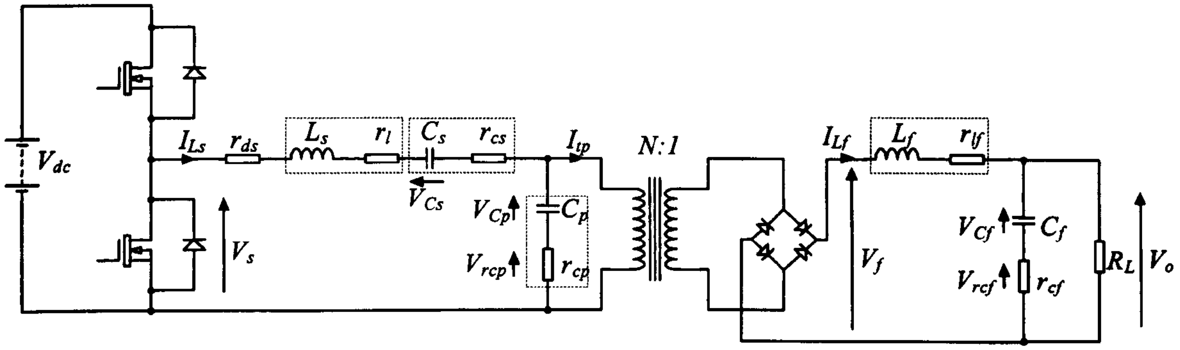

Figure 7.1 - 3^{rd}-order LCC inductively-smoothed resonant converter (including parasitic elements)

The bandwidth of the realised EKF is designed to be much higher than that of the output filter and the resulting closed-loop performance is therefore commensurate to that obtained when utilising a controller based on isolated feedback.

The classical structure of a closed-loop regulated, isolated power supply, is shown in Figure 7.2(a), whilst the structure of the proposed observer-based scheme, is shown in Figure 7.2(b).

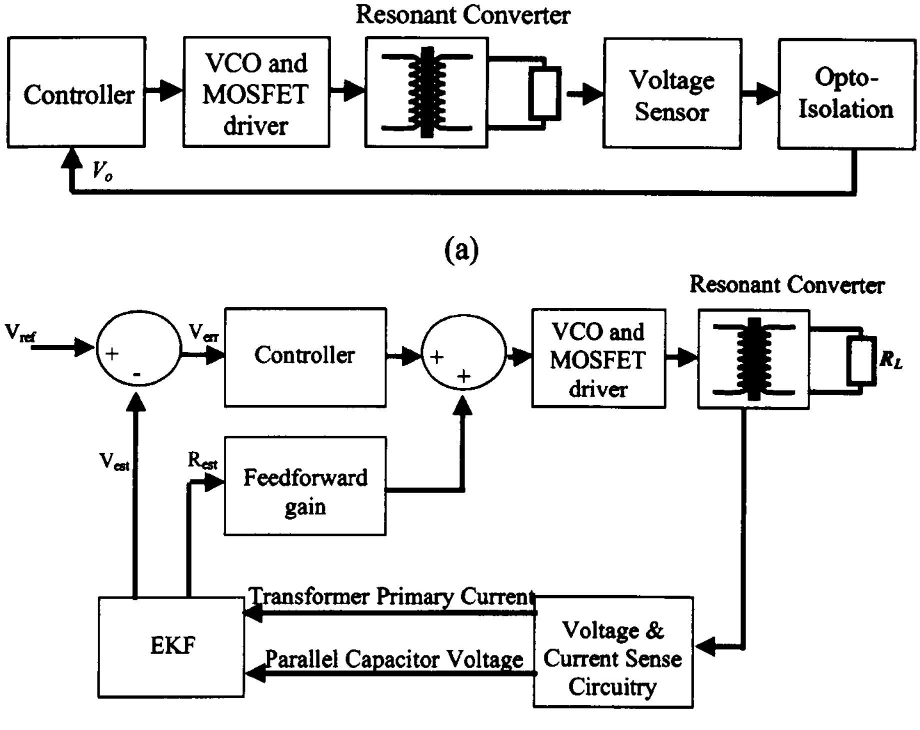

(a)

(b)

Figure 7.2 - Closed-loop feedback regulation schemes including Voltage Controlled Oscillator (VCO) (a) classical converter with isolated feedback sensors, and (b) proposed observer-based converter with feed-forward to enhance load disturbance rejection performance

7.2 Prototype converter

To provide a focus to the investigation, a prototype converter has been designed to meet the specifications given in Table 7.I, using the design procedure for 3rd-order LCC resonant converters described in [7.6-7.8]. Note that the design procedures presented in this thesis, see chapters 3 & 4, were developed after the work presented in this chapter, hence an alternative design methodology is utilised. Measured component values for the converter are summarised in Table 7.II, and the frequency response characteristics of the converter, for the specified load conditions, are given in Figure 7.3. For completeness, results obtained from SPICE simulations of the converter, under steady-state operation, and including the effects of parasitic elements in the circuit, are also included in Figure 7.3.

Table 7.I

Prototype LCC resonant converter specification

Input voltage range	V_{dc}	36→42V
Output voltage	V_o	12V
Load	R_L	8→40 Ω
Nominal switching frequency	f_s	150kHz

Table 7.II

Measured component values of prototype LCC resonant converter

Series tank inductor	L_s	48μH
Series tank capacitor	C_s	66nF
Parallel tank capacitor	C_p	44nF
Transformer turns ratio	N: 1	2.85 : 1
Filter inductor (current o/p)	L_f	1.6mH
Filter capacitor	C_f	2200μF

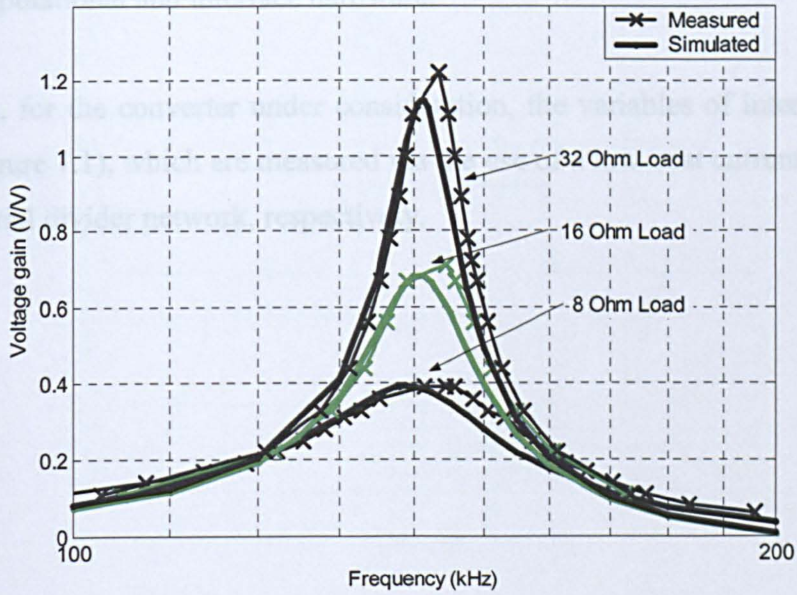

Figure 7.3 - Comparison of experimental and SPICE© simulated frequency response of prototype 3rd order LCC inductively-smoothed resonant converter

7.3 Sensing of primary-side variables

As previously described, the adoption of a resonant tank as the primary power transfer mechanism in resonant converters significantly complicates the use of digital observer schemes, since the resonant tank voltages and currents vary cyclically at the switching frequency (typically >100kHz)—Figure 7.4 shows typical voltage and current waveforms. Moreover, as seen, the waveforms are not necessarily sinusoidal, or rectangular, due to the action of the rectifier and output filter, see Chapters 3 and 4 [7.8]. As noted in [7.2- 7.3], after start-up, the transient behaviour of the tank voltages and currents are influenced, to a great extent, by the transient characteristics of the output filter and load. In this case, it is the 'envelopes' of the primary-side voltages and currents that are of key importance, and the bandwidth of the envelopes is dictated by the output filter bandwidth, which, by its very nature, is much lower than the resonant frequency of the tank. Consequently, by measuring the relatively low frequency 'behavioural' characteristics of the tank voltages and currents, a discrete-time observer/control scheme need only employ sampling frequencies that are commensurate with those of classical hard-switched power converters, thereby allowing the use of similar computational and interface hardware.

Specifically, for the converter under consideration, the variables of interest are I_{tp} and V_{Cp} (see Figure 7.1), which are measured via the use of a low-cost current sense resistor and a potential divider network, respectively.

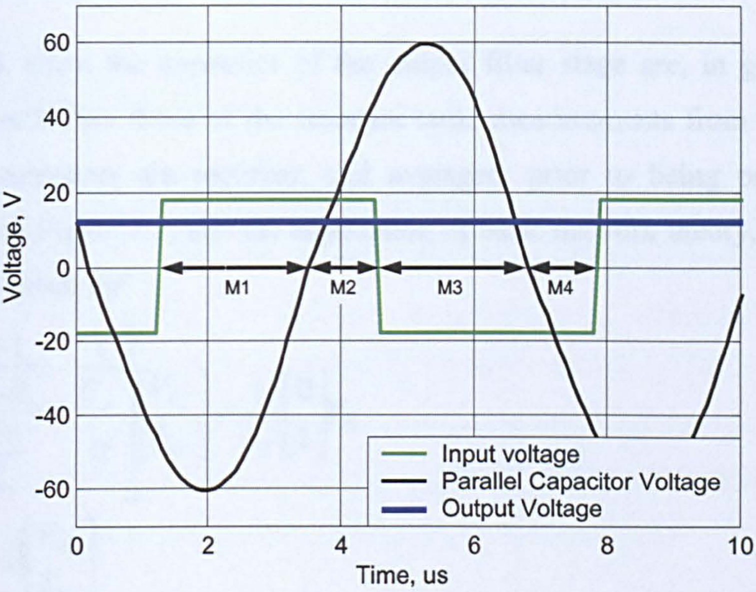

Mode 1: $V_s>0, V_{Cp}<0$ - (M1) Mode 3: $V_s<0, V_{Cp}>0$ - (M3)

Mode 2: $V_s>0, V_{Cp}>0$ - (M2) Mode 4: $V_s<0, V_{Cp}<0$ - (M4)

(a)

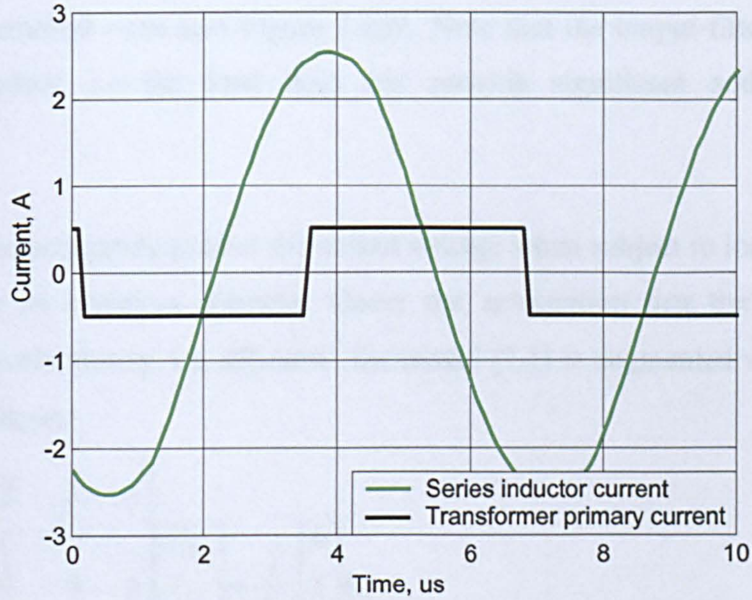

(b)

Figure 7.4. - Operating modes of a simulated (state-variable model) LCC converter with respect to (a) tank voltages, and (b) corresponding tank currents, during nominal rated load operation (12V, 8Ω) at 150kHz

7.4 Dynamic model of inductively-smoothed converter

As discussed, since the dynamics of the output filter stage are, in general, of much lower bandwidth than those of the resonant tank, measurements from the non-isolated side of the converter are rectified, and averaged, prior to being processed by the observer. From Figure 7.1, and the application of basic network theory, the output filter dynamics are given by:

$$\begin{bmatrix} \dot{V}_{Cf} \\ \dot{I}_{Lf} \end{bmatrix} = \begin{bmatrix} \dfrac{-1}{C_f R_L} & \dfrac{1}{C_f} \\ \dfrac{-1}{L_f} & 0 \end{bmatrix} \begin{bmatrix} V_{Cf} \\ I_{Lf} \end{bmatrix} + \frac{1}{L_f} \begin{bmatrix} 0 \\ 1 \end{bmatrix} V_f \qquad (7.1)$$
$$y = \begin{bmatrix} 0 & 1 \end{bmatrix} \begin{bmatrix} V_{Cf} \\ I_{Lf} \end{bmatrix}$$

where V_f is considered to be the cycle-by-cycle mean of the voltage presented to the filter inductor. It should be noted, that, whilst V_f is shown as an isolated variable, in Figure 7.1, its envelope is obtained from taking the absolute value, averaging, and appropriately scaling the parallel capacitor voltage, V_{Cp}, which is a non-isolated variable, as required—see also Figure 7.2(b). Note that the output-filter capacitance is assumed constant i.e the load does not provide significant additional reactive component.

For the EKF to accurately predict the output voltage when subject to load variations, R_L must also be an observed quantity. Under the assumption that the load resistance changes relatively slowly, i.e. $dR_L/dt \approx 0$, the model (7.1) is augmented with a new state, $\alpha = 1/R_L$, as follows:

$$\begin{bmatrix} \dot{V}_{Cf} \\ \dot{I}_{Lf} \\ \dot{\alpha} \end{bmatrix} = \begin{bmatrix} \dfrac{-\alpha}{C_f} & \dfrac{1}{C_f} & 0 \\ \dfrac{-1}{L_f} & 0 & 0 \\ 0 & 0 & 0 \end{bmatrix} \begin{bmatrix} V_{Cf} \\ I_{Lf} \\ \alpha \end{bmatrix} + \frac{1}{L_f} \begin{bmatrix} 0 \\ 1 \\ 0 \end{bmatrix} V_f \qquad (7.2)$$
$$y = \begin{bmatrix} 0 & 1 & 0 \end{bmatrix} \begin{bmatrix} V_{Cf} \\ I_{Lf} \\ \alpha \end{bmatrix}$$

Since V_{Cf} is effectively the output voltage, and α is an estimation of the load, an observer scheme to estimate the states of (7.2) provides sufficient information for closed-loop control purposes.

For a fixed load, the dynamics matrix is a constant, allowing linear observer principles to be applied, as in [7.5]. However, to accommodate variations in the load, (7.2) must be used, which is non-linear, and requires the adoption of non-linear state observer techniques. A further complication is that the representation in (7.2) does not provide a fully observable realisation for fixed values of R_L. However, by noting that both V_{Cf} and α are dependent on R_L, an alternative, observable formulation is readily obtained at the expense of introducing an additional term in the dynamics matrix:

$$\begin{bmatrix} \dot{V}_{Cf} \\ \dot{I}_{Lf} \\ \dot{\alpha} \end{bmatrix} = \begin{bmatrix} \frac{-\alpha}{2C_f} & \frac{1}{C_f} & \frac{-V_{Cf}}{2C_f} \\ \frac{-1}{L_f} & 0 & 0 \\ 0 & 0 & 0 \end{bmatrix} \begin{bmatrix} V_{Cf} \\ I_{Lf} \\ \alpha \end{bmatrix} + \frac{1}{L_f} \begin{bmatrix} 0 \\ 1 \\ 0 \end{bmatrix} V_f \tag{7.3}$$

Applying the Euler transformation, an equivalent discrete-time model of (7.3) is obtained (7.4), where the square bracketed terms denote discrete-time states:

$$x[k+1] = \mathbf{A}_d x[k] + \mathbf{B}_d u[k] \text{ where,}$$

$$\mathbf{A}_d = \begin{bmatrix} 1-\frac{\alpha\Delta T}{2C_f} & \frac{\Delta T}{C_f} & \frac{-V_{Cf}\Delta T}{2C_f} \\ \frac{-\Delta T}{L_f} & 1 & 0 \\ 0 & 0 & 1 \end{bmatrix}, \mathbf{B}_d = \frac{1}{L_f} \begin{bmatrix} 0 \\ \Delta T \\ 0 \end{bmatrix} \tag{7.4}$$

$$x[k] = \begin{bmatrix} V_{Cf}[k] \\ I_{Lf}[k] \\ \alpha[k] \end{bmatrix}, u[k] = V_f[k]$$

For the inductively-smoothed converter, the discrete-time output equation is given by:

$$\begin{aligned} I_{Lf}[k+1] &= \begin{bmatrix} 0 & 1 & 0 \end{bmatrix} \begin{bmatrix} V_{Cf}[k+1] \\ I_{Lf}[k+1] \\ \alpha[k+1] \end{bmatrix} \quad \text{where } \mathbf{C}_d = \begin{bmatrix} 0 & 1 & 0 \end{bmatrix} \\ &= \mathbf{C}_d x[k+1] \end{aligned} \tag{7.5}$$

7.5 Extended Kalman Filter (EKF)

The EKF is an extension of the well-known Kalman Filter (KF) [7.9], and has evolved specifically for systems described by non-linear equations. Although no formal stability and tuning procedures are available for initialising the EKF, its use is, nevertheless, widespread, in the hope that some of the optimal properties attributed to the KF, for linear systems, can be transferred to non-linear systems.

Since the underlying predictor-corrector principles of the EKF, are well documented [7.10-7.13], only the algorithmic structure of the EKF is summarised here, for completeness, in Figure 7.5, where the 'Kalman gain', K, is updated during each sampling period to minimise the error covariance between the system states and the estimator states, from a knowledge of the measured input and output data.

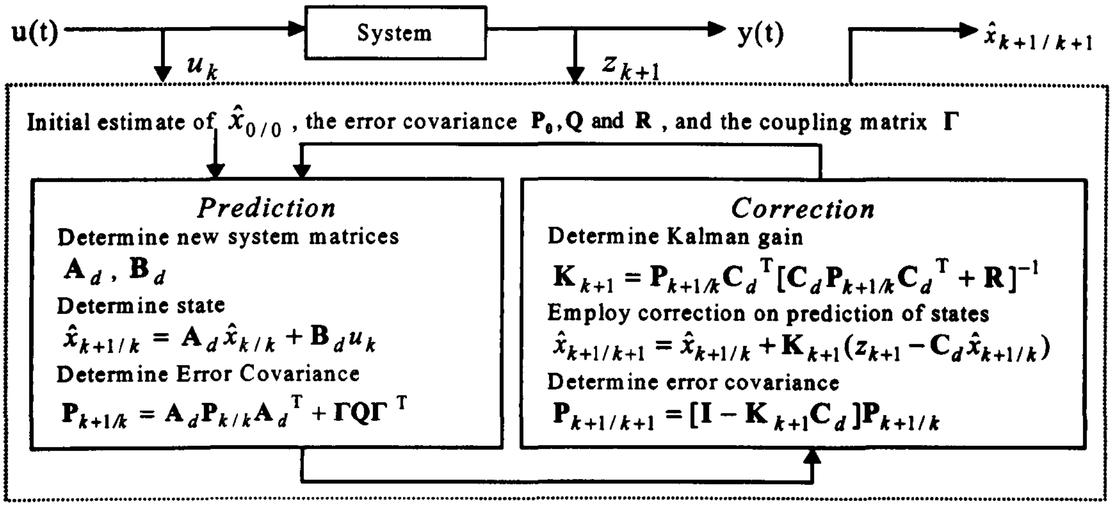

Figure 7.5 - Structure of the EKF (z is the vector of measured outputs)

7.6 Simulated and measured results

For comparison purposes, a Luenberger observer designed to be operated with a fixed load, as described in [7.5], is also considered, in order to clearly highlight the benefits of the proposed EKF solution. The discrete-time eigenvalues of the linear Luenberger observer, which govern the estimation error-convergence dynamics, are designed for a constant output load of 16Ω and are assigned to be $\lambda=[-0.75, 0.75]$ which were found to provide the best error-convergence dynamics. Both the EKF and classical Luenberger observers are realised using a sampling frequency of 1kHz.

Due to the lack of formal tuning procedures, initial values for the EKF covariance matrices are determined empirically (as is commonplace), from simulation studies, giving rise to the following initial conditions:

$$\begin{aligned}
&\mathbf{\Gamma Q \Gamma}^T = \begin{bmatrix} 1 & 0 & 0 \\ 0 & 3 & 0 \\ 0 & 0 & 1\times10^{-2} \end{bmatrix} \\
&\mathbf{R} = 0.1 \\
&\mathbf{P}_0 = 1\times10^{-2}\begin{bmatrix} 1 & 0 & 0 \\ 0 & 1 & 0 \\ 0 & 0 & 1 \end{bmatrix}
\end{aligned} \tag{7.6}$$

A simulation study is undertaken using the converter model and observers described above, simulated to steady-state, giving an output voltage of 12V with a 16Ω load, and subsequently subjected to transient load variations of between 16Ω→8Ω→16Ω at 150ms intervals, whilst maintaining a constant switching frequency. The estimated R_L resulting from the EKF during the transient load change, is shown in Figure 7.6(a), and demonstrates excellent state convergence. Notably, the EKF load estimation provides a faster response time to that generated by utilising the absolute average sensor measurements directly ($N^2\ V_{Cp}\ /\ I_{tp}$), termed 'Calculated' in Figure 7.6(b). When calculating the load directly from the sensor measurements, the load estimation has a slower response due to the presence of the output filter. The output filter inductor, L_f, reduces the instantaneous effects of any change in load resistance upon the load current, thereby having a 'delayed' effect on V_{Cp}. The net result is a relatively slow calculation of R_L from measurements. The EKF, however, employs a model of the output filter along with measurements to provide a more rapid estimate.

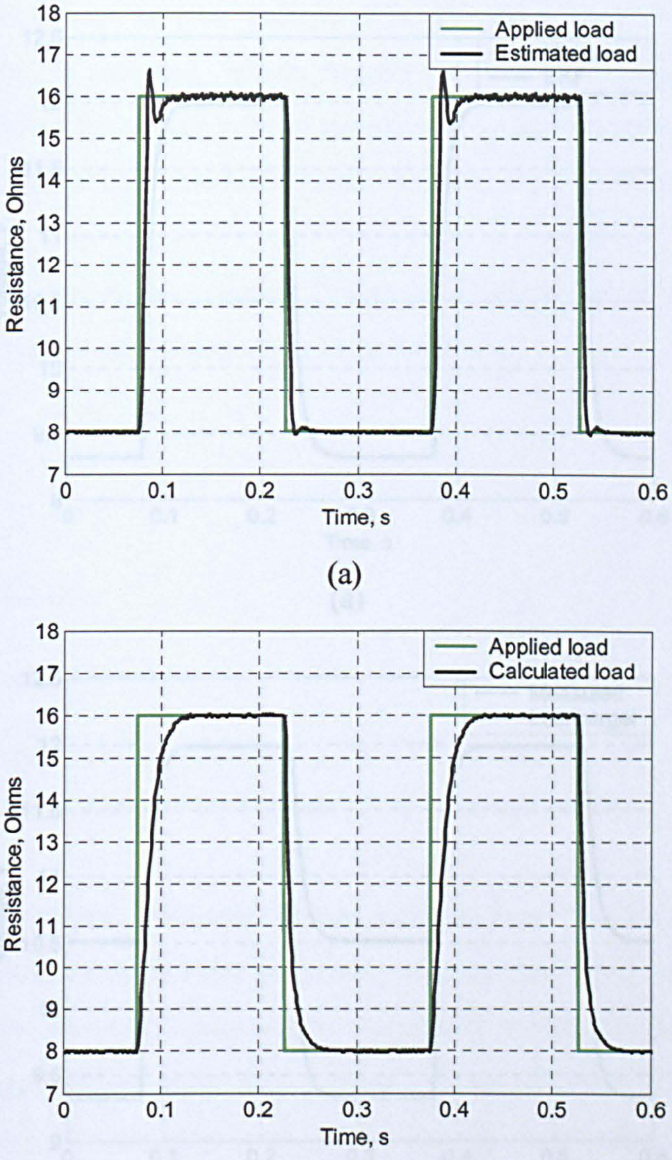

(a)

(b)

Figure 7.6 - Simulation results comparing applied load and (a) EKF observed (b) Calculated load resistance ($N^2 V_{Cp} / I_{tp}$)

Figure 7.7 compares measurements of output voltage from the prototype converter, with estimates from both the EKF and Luenberger observers, from which, it can be seen that the EKF observer provides superior performance to the Luenberger observer, in all respects. In particular, when the load resistance deviates from the nominal 16Ω design value, which was assumed for the design of Luenberger, the accuracy of the output voltage estimate deteriorates markedly, whilst the EKF observer, which incorporates the observed value of R_L, does not suffer such degradation.

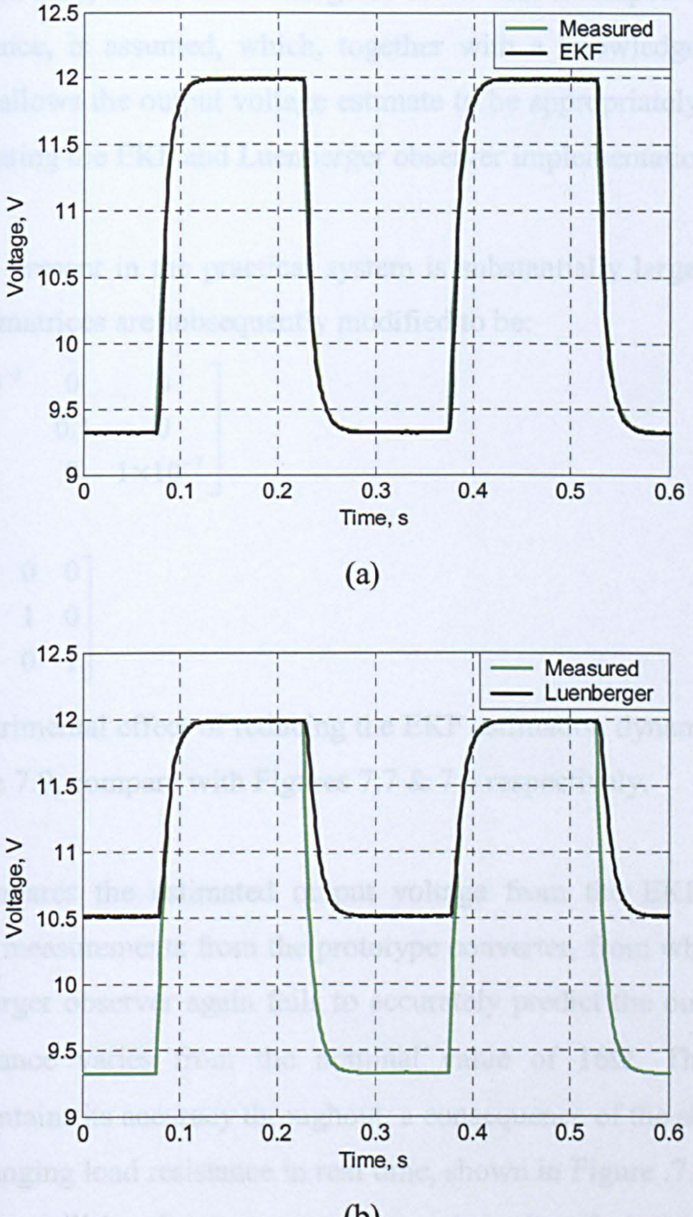

Figure 7.7 - Simulation study comparing measured output voltage with (a) EKF and (b) Luenberger observed output voltage [Note that the term measured here refers to the simulated actual output voltage of the converter, as opposed to the simulated estimator output voltage]

From a practical perspective, in order to ensure that the observers accurately estimate the output voltage and load resistance, consideration must also be given to the effects of additional parasitic elements in the circuit, Figure 7.1, since they can significantly influence the operation of the resonant tank [7.7,7.14]. Typically, for low-voltage converters, it is necessary to at least account for the diode forward voltage and filter parasitics. In this case, an on-state voltage of 0.74V and a lumped 1.28Ω output filter inductor resistance, is assumed, which, together with a knowledge of the estimated output current, allows the output voltage estimate to be appropriately modified without further complicating the EKF and Luenberger observer implementations.

Since the noise present in the practical system is substantially larger, the initial noise and covariance matrices are subsequently modified to be:

$$\begin{aligned}
&\mathbf{\Gamma Q \Gamma}^T = \begin{bmatrix} 1\times10^{-3} & 0 & 0 \\ 0 & 0.1 & 0 \\ 0 & 0 & 1\times10^{-7} \end{bmatrix} \\
&\mathbf{R} = 0.1 \\
&\mathbf{P_o} = 1\times10^{-2}\begin{bmatrix} 1 & 0 & 0 \\ 0 & 1 & 0 \\ 0 & 0 & 1 \end{bmatrix}
\end{aligned} \tag{7.7}$$

This has the detrimental effect of reducing the EKF estimation dynamics as can be seen in Figures 7.8 & 7.9, compare with Figures 7.7 & 7.6 respectively.

Figure 7.8 compares the estimated output voltage from the EKF and Luenberger observers, with measurements from the prototype converter, from which it will be seen that the Luenberger observer again fails to accurately predict the output voltage when the load resistance varies from the nominal value of 16Ω. The EKF observer, conversely, maintains its accuracy throughout, a consequence of the ability to accurately estimate the changing load resistance in real time, shown in Figure .7.9(a). Furthermore, it can be seen that utilising the sensor measurements to directly estimate load resistance ($N^2\ V_{Cp}\ /\ I_{tp}$) again provides relatively poor results that are corrupted by noise, Figure 7.9(b). The noise is a consequence of aliasing due to sampling the absolute value of the averaged quantities that contain remnant high frequency ripple components.

Note that the delay between measured and EKF estimated output voltage in Figure 7.8 can cause significant control difficulties. As a result of the noise present in the system, the EKF must compromise between accuracy of output voltage and accuracy of load estimate. The EKF in Figure 7.8 is tuned for fast load estimation.

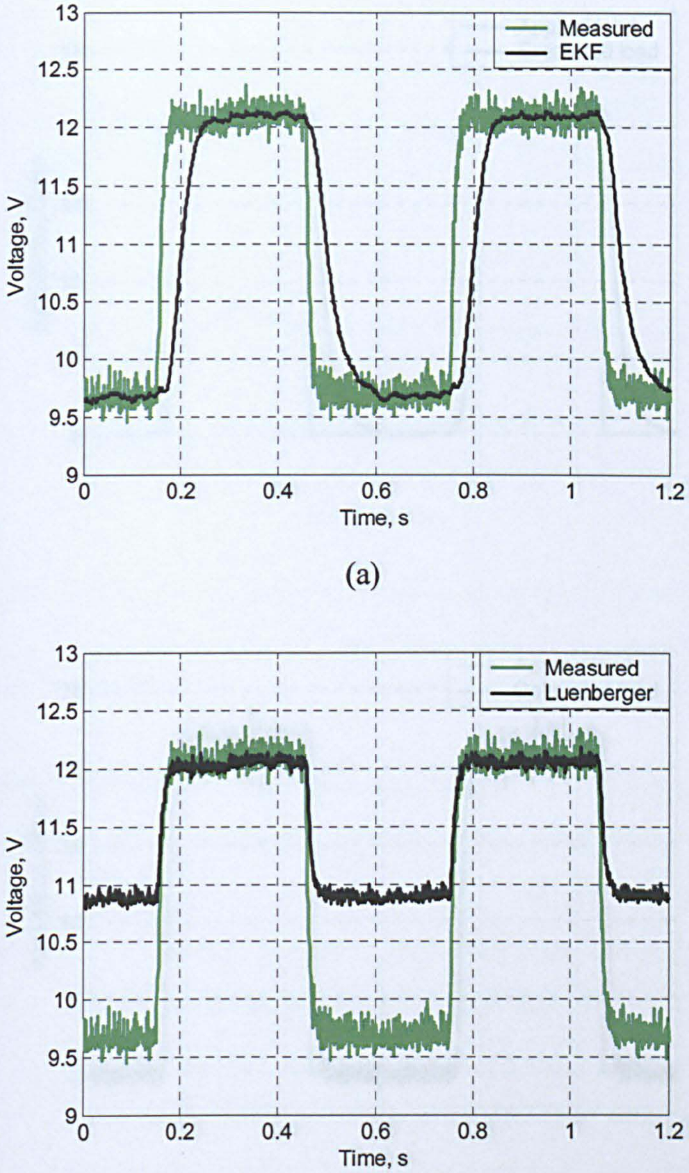

(a)

(b)

Figure 7.8 - Experimental result showing a comparison of measured and (a) EKF (b) Luenberger observed output voltage

[Note that the term measured here now refers to the practically measured output voltage of the converter, as opposed to the practically measured estimator output voltage]

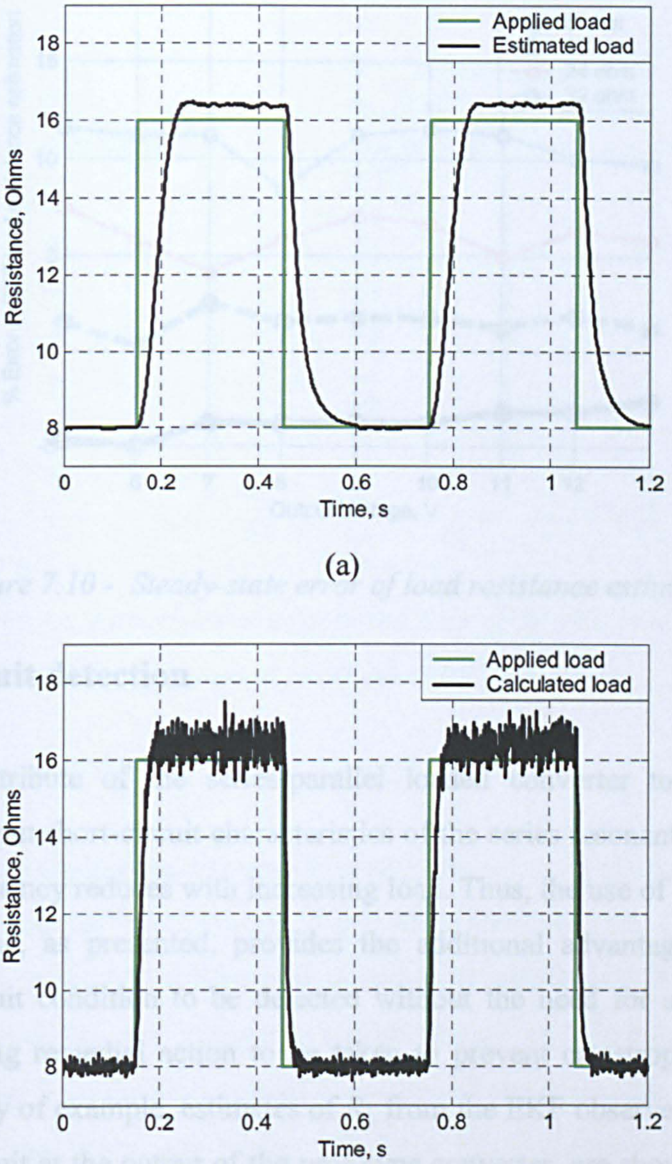

(a)

(b)

Figure 7.9 - Experimental results comparing applied and (a) EKF based observed (b) Calculated load resistance ($N^2 V_{Cp} / I_{tp}$)

In order to appraise the steady-state performance of the EKF based observer, the converter is operated over an extended output-voltage range, from 5V to 13V, and an extended load range, from 8Ω to 32Ω, at 1V and 8Ω intervals, respectively. Figure 7.10 shows the resulting error between the estimated and measured load resistance, for various output voltage levels, from which it will be seen that the prediction errors are <12%. Moreover, estimates of output voltage were <2% of that measured at the output, for all operating conditions.

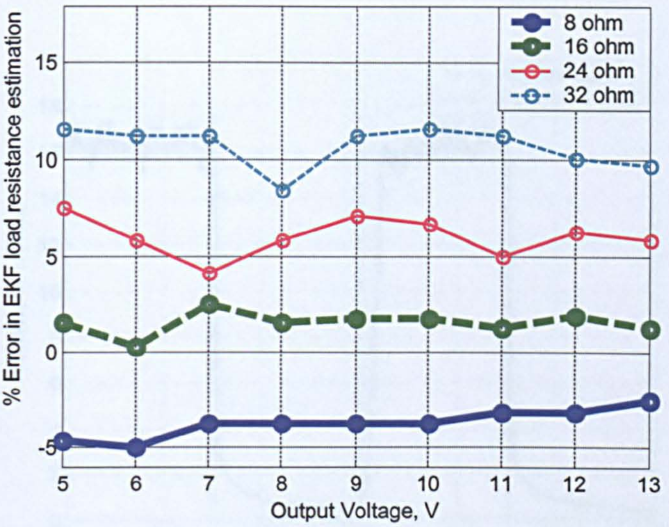

Figure 7.10 - Steady-state error of load resistance estimation

7.7 Short-circuit detection

A convenient attribute of the series-parallel loaded converter topology is that it possesses the output short-circuit characteristics of the series resonant converter, in that the resonant frequency reduces with increasing load. Thus, the use of a non-linear state-estimation scheme, as presented, provides the additional advantage of enabling an output short-circuit condition to be detected without the need for additional sensors, thereby facilitating remedial action to be taken to prevent catastrophic failure of the converter. By way of example, estimates of R_L from the EKF observer, in response to a sudden short-circuit at the output of the prototype converter, are shown in Figure 7.11, where, a resistance of 0Ω indicates a short-circuit at the output. The steady-state error of 0.5Ω in the load estimation during short-circuit, is a result of the lumped parasitic model becoming less accurate during this mode of operation. The rise- and fall-times of ≈ 15ms and 18ms, respectively, demonstrate that such faults can be rapidly detected to allow remedial action to be taken, such as increasing the switching frequency [7.15] or using harmonic excitation of the tank [7.16]. However, whilst some degree of control of the estimate convergence may be obtained by varying element (3,3) of $\mathbf{\Gamma Q \Gamma}^T$ (see (7.6)), the trade-off for this additional bandwidth is increased susceptibility to measurement noise. In particular, decreasing element (3,3) indicates more noise is present on the measured signal (voltage) and more emphasis should be placed on the system model and states for corrective action.

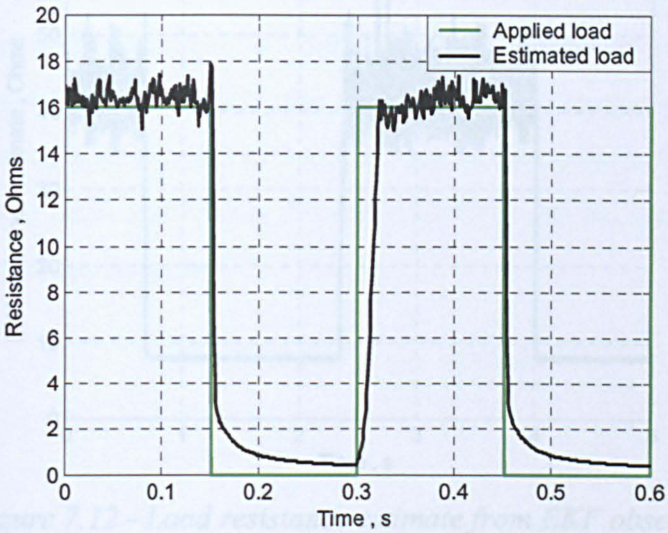

Figure 7.11 - Comparison of actual, and EKF observed, load resistance during transient short-circuit of the output

7.8 Closed-loop regulation

To benefit from the application of state-observers, the resulting estimates must facilitate closed-loop regulation of the converter to provide a stable output. Thus, the prototype converter is used to provide a regulated closed-loop output of 12V, and its dynamic performance evaluated by subjecting it to sudden changes in load between 8Ω and 40Ω, at 150ms intervals. A basic proportional-plus-integral (P+I) scheme is implemented to provide nominal regulation, see Figure 7.2 for a block diagram of the closed loop system. Additionally, the control action is augmented by feeding forward a proportion of the estimated load resistance from the EKF observer, thereby effectively implementing a composite feed-back/feed-forward control scheme, as illustrated in Figure 7.2(b).

The load resistance estimates, from the EKF, are shown in Figure 7.12, which are seen to correlate extremely well with measured values, albeit with increased noise sensitivity, to 20% pk-pk, as converter operation tends to the open-circuit condition.

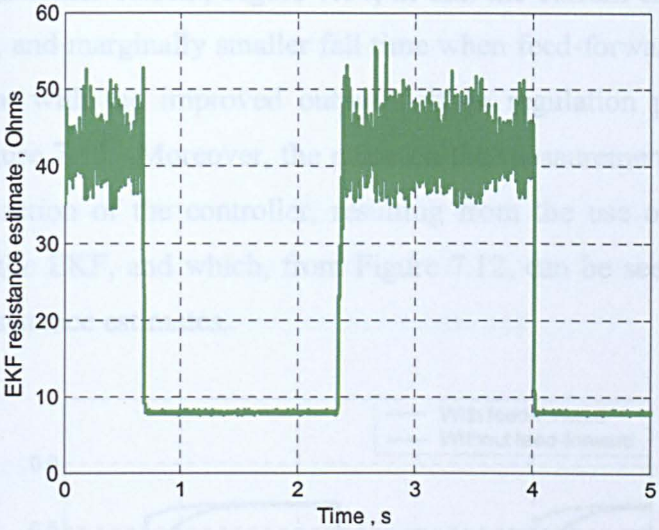

Figure 7.12 - Load resistance estimate from EKF observer

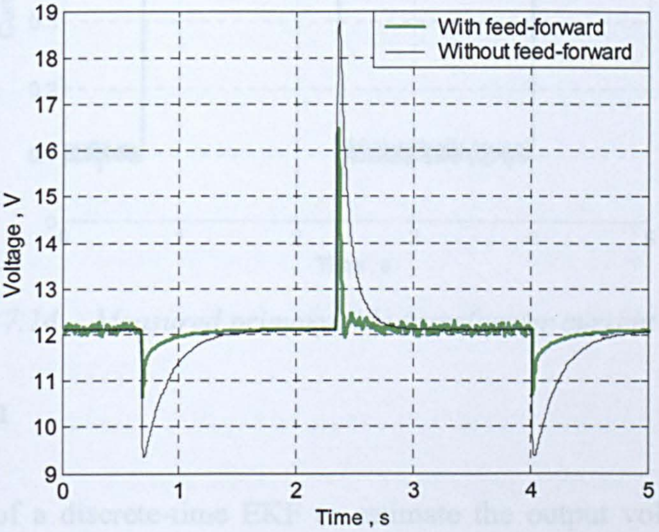

Figure 7.13 - Closed-loop regulation performance of converter under sudden load changes, both with and without feed-forward of estimated load resistance

The corresponding regulation performance of the converter, when subject to the load variations, is shown in Figure 7.13, where the benefit of incorporating a proportion of the EKF estimated load resistance, into the control action (giving a feed-forward contribution), is evident. In particular, it can be seen that the feed-forward action can enhance the transient response with regard to both damping (reduces peak under-/over-shoot) and settling time. Note however that a much lower bandwidth controller is used, hence the large overshoot and large time base. The results presented are simply proof of principle. It is also interesting to note the effect of the feed-forward action on the primary side transformer current, Figure 7.14, in that the current envelope has a much smaller rise time, and marginally smaller fall time when feed-forward action is utilised. This is consistent with the improved output voltage regulation performance shown previously in Figure 7.13. Moreover, the noise on the measurements is a consequence of feed-forward action of the controller, resulting from the use of estimates of load resistance, from the EKF, and which, from Figure 7.12, can be seen to be more noise prone for high resistance estimates.

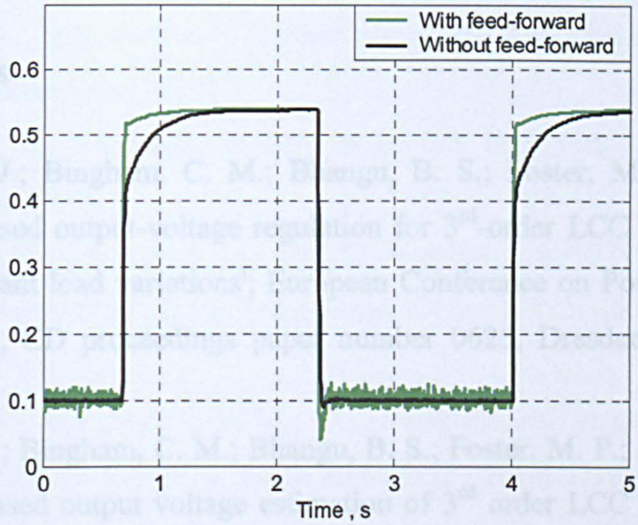

Figure 7.14 - Measured primary side transformer current envelope

7.9 Conclusion

The application of a discrete-time EKF to estimate the output voltage of a 3^{rd}-order LCC converter which is subject to variable load conditions, has been proposed, and demonstrated. Although resonant converters operate at high-switching frequencies, it has been shown that a digital observer/controller can be implemented using relatively low sample rates by utilising measurements of non-isolated peak- and averaged- values of the resonant circuit currents and voltages.

Measurements from a prototype converter show that the proposed EKF observer can provide accurate estimates of the output voltage, and load resistance, over a wide operating envelope. Moreover, performance comparisons, based on measurements from the proposed EKF state-estimation scheme and those from a classical linear Luenberger-type observer, show that the EKF observer provides significant performance benefits. In addition, it has been shown that the added flexibility afforded by incorporating estimates of the load into a closed-loop control scheme, by virtue of using feedforward control action, can significantly improve the settling time and damping of the output voltage when the converter is subject to load transients.

Although an EKF based estimation scheme has been demonstrated to have useful properties, alternative estimation schemes should be investigated since there is much room for improved dynamics and enhanced noise immunity.

7.10 References

[7.1] Gilbert, A. J.; Bingham. C. M.; Bhangu, B. S.; Foster, M. P.; Stone, D. A.; 'Observer-based output-voltage regulation for 3^{rd}-order LCC resonant converters with significant load variations', European Conference on Power Electronics and Applications, CD proceedings paper number 0625, Dresden, 11-14 September 2005

[7.2] Gilbert, A. J.; Bingham, C. M.; Bhangu, B. S.; Foster, M. P.; Stone D. A.; Howe, D.; 'EKF-based output voltage estimation of 3^{rd} order LCC resonant converters with significant load variations', EPE-PEMC 2004 Conference, CD proceedings, Latvia, 2-4 September 2004

[7.3] Kamas, L.A., Sanders, S.R.; 'Parameter and state estimation in power electronic circuits', PESC 91 Record IEEE Power Electronics Specialists Conference, 1991, pp.57-61.

[7.4] Midya, P., Krein, P.T., Greuel, M.F.; 'Sensorless current mode control - An observer-based technique for DC-DC converters', IEEE Trans Power Electronics, Vol. 16, No.4, 2001, pp.522 –526.

[7.5] Foster, M.P., Sewell, H.I., Bingham, C.M., Stone, D.A.; 'Observer based feedback control of 3rd order LCC resonant converters' , Proc. EPE-2003, CD-ROM.

[7.6] Sewell, H.I., Foster, M.P., Bingham, C.M., Stone, D.A., Hente, D., Howe, D.; 'Analysis of voltage output LCC resonant converters, including boost mode operation', IEE Proc. Electric Power Applications, Vol.150 , No.6, 2003, pp.673–679.

[7.7] Kazimierczuk, M.K., Czarkowski, D.; 'Resonant power converters', John Wiley & Sons, 1995, ISBN 0-471-04706-6 , Chapter 8 & 17.

[7.8] Forsyth, A.J., Ward, G.A., Mollov, S.V.; 'Extended fundamental frequency analysis of the LCC resonant converter', IEEE Trans. Power electronics, Vol.18, 2003, pp.1286-1292.

[7.9] Kalman, R.E.; 'A new approach to linear filtering and prediction problems', Trans. of ASME - Journal of Basic Engineering, 1960, pp.35-45

[7.10] Bucy, R., Kalman, R., Selin, L.; 'Comment on the Kalman filter and nonlinear estimates of multivariate normal processes', IEEE Trans. Auto. Cont. Vol.10, No.1, 1965, pp.118-119.

[7.11] Billings, S.A.; 'Introduction to Kalman filters', IEE Colloquium on Kalman filters and their Applications (1980).

[7.12]Maybeck, P. S.; 'Stochastic models, estimation and control', Vol.1, Academic Press, London 1979.

[7.13]Reif, K Reif, K., Günther, S. and Yaz, E.; 'Stochastic stability of the discrete-time extended Kalman filter', IEEE Trans. Auto. Control, Vol. 44, No.4, 1999 pp.714-728.

[7.14]Bhat, A.K S., and Swamy, M.M.: "Loss calculations in transistorized parallel resonant converters operating above resonance", IEEE Trans. Power electronics, Vol. 4, (4), 1989, pp.391-401.

[7.15]Yang, B., Lee, F. C., and Concannon, M.: "Over current protection methods for LLC resonant converter" 18th Annual IEEE Applied Power Electronics Conference and Exposition(Proceedings), 2003 , pp.605-609.

[7.16]Gould, C., Stone, D.A., Foster, M.P., and Bingham, C.M. "State-variable modelling of CLL resonant converter", Proc. 2nd International IEE Power Electronics, Machines & Drives Conference, 2004, pp.214-219

Chapter 8 - Conclusions and Future work

8.1 Conclusions

This thesis has developed techniques for the design, analysis and control of LCC resonant converters. Specifically, Chapter 3 has considered the design of LCC inductively-smoothed resonant converters by extending the underlying principles of classical FMA. The resulting design process provides simple equations relating component values to design specifications. Of note, is that the analysis demonstrates that the output-current of the converter tends to a constant value as the load resistance is increased and the converter switched at the resonant frequency - a very useful characteristic for current-source applications such as aluminium anodising, for instance. Chapter 4 focuses on the design and analysis of the LCC capacitively-smoothed variant. Using a state-plane analysis technique, a generalised set of equations relates the behavioural characteristics of the converter to the tank gain at the resonant frequency and the resonant tank capacitor ratio. Converters with similar tank gain at the resonant frequency and capacitor ratio are then shown to behave identically, from a steady-state normalised perspective, allowing a number of design curves to be derived for component value selection, electrical stresses, and switching frequency requirements as the load is varied and the converter gain regulated at a nominal level. Both design methodologies provide considerable new insight into the behaviour of resonant converters, and greatly simplify their design. For instance, it was demonstrated how to select preferred component values with minimum impact on the converter behaviour.

Chapter 5 considers the high speed transient analysis of LCC inductively-smoothed resonant converters. The method is shown to provide simulation results a 100× faster than for component based integration methods such as SPICE, at the expense of providing only the waveform envelopes. By reducing the protracted simulation times, such techniques greatly aid the designer during an iterative design process. Chapter 6 extends the transient analysis technique presented in Chapter 5, to provide a novel control methodology that linearises the overall resonant converter behaviour. This addresses one of the main drawbacks for the use of resonant converters viz. the lack of literature and tools for the simple, robust control of such systems. Chapter 7, alternatively, considered control of resonant converters when the cost of isolated sensors are prohibitive, thereby requiring observer based techniques to be realised. It was shown that the output resistance and output filter states can be quickly estimated whilst using low sampling rates, allowing for cost effective control methods to be applied.

8.2 Future work

A number of key ideas for future research have been identified. For instance, the LCC capacitively-smoothed analysis, presented in Chapter 4, could be developed into a constrained optimisation problem. As an example, it would be useful to obtain the 'minimum cost' solution for given power specifications. Alternatively, when considering equation (4.6), if it were possible to maintain the $f_r R_L C_p$ product, the tank gain at the resonant frequency (G_{tr}) would remain constant. Although this may appear unfeasible, as discussed within the literature review (Chapter 2) some authors have indeed varied the components in the resonant tank via use of voltage-controlled capacitors or current-controlled inductors. If the converter could be switched continuously at the resonant frequency, with all regulation control achievable through resonant tank component control, part-load efficiencies could be greatly enhanced since power flow from source to tank at resonance would be purely real (no circulating currents). Additionally, the power-factor control technique, presented in Chapter 6, requires further analysis for alternative converter topologies. The LCC inductively-smoothed converter was shown to behave in a predominately 3rd order dynamic manner under the power-factor control scheme. Since the capacitively-smoothed converter topology consists of one less reactive component in the output-filter, it would be useful to know whether the order of the dynamics would reduce likewise, or indeed increase. Within Chapter 6, alternative switching schemes were provided. The fixed rising edge scheme appeared to offer significant promise for the minimisation of converter losses by reducing converter bandwidth and through additional ZCS. The technique, however, has reduced linearity when compared to the power-factor control scheme. If, however, $\int V_s(t) I_{Ls}(t)dt$ could be calculated in real-time, the power-flow into the converter could be accurately controlled, thereby allowing simple linearization procedures to be applied. Although obtaining the time integral may appear unreasonable, if the supply-voltage is assumed to vary slowly compared to the switching frequency, it may be removed from the integral, and the voltage across the series-capacitor provides the required information. Chapter 6 also provided further insight into the limitations of the uni-directional power flow from tank to output-filter. Output-voltage regulation dynamics for the inductively-smoothed topology could be greatly enhanced via the use of a bi-directional rectifier. The work in Chapter 7 could be developed by considering alternative estimator schemes and their relative merits. Other more general ideas should also be considered, for instance, performing an analysis such as that provided in Chapter 4, for the change of converter states over a given switching period, thus allowing for a high sped transient solution to be obtained. A mixed s-z description of the converter may also enable the development of an alternative analysis methodology [8.1].

8.3 References

[8.1] Biolek, D.; 'Modelling of periodically switched networks by mixed s-z description', IEEE Transactions on Circuits and Systems I: Fundamental Theory and Applications, Vol.44, No.8, Aug. 1997, pp.750-758

Appendix A - Analysis of LCC Capacitively-smoothed resonant converter during heavy loading operation

Equations (4.38),(4.39) can be solved simultaneously to give:

$$Q_{M1} = \frac{V_{dc}G_o\left(2G_o - f_m\left(2G_{tr} - 1\right) - 1\right)}{4f_r f_m N^2 R_L} \tag{A.1}$$

$$Q_{M3} = \frac{V_{dc}G_o\left(2G_o - f_m\left(2G_{tr} - 1\right) + 1\right)}{4f_r f_m N^2 R_L} \tag{A.2}$$

Since all the tank current flows through C_s:

$$V_{Cs_{M4}}(t_{M4}) = -V_{Cs_{M2}}(0) = V_{Cs_{M2}}(0) + \frac{1}{C_s}\left(-Q_{M1} + Q_{M2} + Q_{M3}\right) \tag{A.3}$$

An expression for V_{Cs} at the start of M2 can be obtained from (4.6), (4.7), (4.39), (A.1), (A.2), (A.3) as follows:

$$V_{Cs_{M2}}(0) = \frac{-AV_{dc}G_o\left(1 + \left(2G_{tr} - 1\right)f_m\right)}{\left(2G_{tr} - 1\right)f_m} \tag{A.4}$$

An expression for I_{Ls} during M1 is determined by noting that $C_e = C_s$, since the V_{Cs} is clamped, see Figure 4.9(a),

$$I_{Ls_{M1}}(t) = \hat{I}_{M1}\sin\left(\sqrt{\frac{1}{L_s C_e}}(t - t_{M1})\right) = \hat{I}_{M1}\sin\left(\sqrt{\frac{A}{L_s C_P}}(t - t_{M1})\right) \tag{A.5}$$

At the end of M1, V_{Ls} is given by:

$$V_{Ls_{M2}}(0) = L_s\frac{di_{Ls_{M1}}\left(t_{M1}\right)}{dt} = \frac{V_{dc}}{2} + NV_o - V_{Cs_{M2}}(0) \tag{A.6}$$

Substituting (4.36), (A.4) into (A.6) and solving for the derivative gives:

$$\frac{dI_{Ls_{M2}}(0)}{dt} = \frac{V_{dc}}{2L_s} + \frac{V_{dc}G_o}{L_s} + \frac{AV_{dc}G_o\left(1 + \left(2G_{tr} - 1\right)f_m\right)}{L_s\left(2G_{tr} - 1\right)f_m} \tag{A.7}$$

Equating the derivative in (A.7) with the time derivative in (A.5), at $t = t_{M1}$, and solving for $\hat{I}_{M1}$ gives:

$$\hat{I}_{M1} = \frac{V_{dc}\left(f_m\left(2G_{tr} - 1\right)\left(1 + 2(A+1)G_o\right) + 2AG_o\right)}{4f_m N\sqrt{R_L A L_s f_r}\left(2G_{tr} - 1\right)} \tag{A.8}$$

It is now possible to calculate the time spent in M1 (t_{M1}). Substituting (4.6), (A.1), (A.5), (A.8) into (4.1) and solving for t_{M1} gives:

$$t_{M1} = \frac{1}{2N}\sqrt{\frac{L_s\left(2G_{tr} - 1\right)}{R_L A f_r}}\cos^{-1}\left(\frac{f_m\left(2G_{tr} - 1\right)\left(1 + 2G_o\right) + 4AG_o^2}{f_m\left(2G_{tr} - 1\right)\left(1 + 2(A+1)G_o\right) + 2AG_o}\right) \tag{A.9}$$

Substituting (A.8),(A.9) into (A.5) gives I_{Ls} during M1.

The tank current during M2 is now derived by noting that during M2 C_e is the series combination of C_s and C_p, see Figure 4.9(b). The tank current then takes the form:

$$I_{Ls_{M2}}(t) = \hat{I}_{M2}\sin\left(t\sqrt{\frac{1}{L_s C_e}}\right) = \hat{I}_{M2}\sin\left(t\sqrt{\frac{A+1}{L_s C_P}}\right) \tag{A.10}$$

Equating the time derivative of (A.10) at $t=0$ to (A.7), and solving for $\hat{I}_{M2}$ provides:

$$\hat{I}_{M2} = \frac{V_{dc}\left(f_m(2G_{tr}-1)(1+2(A+1)G_o)+2AG_o\right)}{4f_m N\sqrt{R_L(A+1)L_s f_r(2G_{tr}-1)}} = \hat{I}_{M1}\sqrt{\frac{A}{A+1}} \tag{A.11}$$

and, substituting (4.6),(4.39),(A.10),(A.11) into (4.1) and solving for t_{M2} gives:

$$t_{M2} = \frac{1}{2N}\sqrt{\frac{L_s(2G_{tr}-1)}{R_L(A+1)f_r}}\left(\pi - \cos^{-1}\left(\frac{f_m(2G_{tr}-1)(-1+2(1+A)G_o)-2AG_o}{f_m(2G_{tr}-1)(1+2(A+1)G_o)+2AG_o}\right)\right) \tag{A.12}$$

I_{Ls} at the end of M2 is obtained by substituting (4.6),(A.11),(A.12) into (A.10) (i.e t $=t_{M2}$).

$$I_{Ls_{M3}}(0) = \frac{V_{dc}}{N}\sqrt{\frac{G_o((2G_{tr}-1)f_m+2AG_o)}{2R_L f_r f_m L_s}} \tag{A.13}$$

The derivative of I_{Ls} at the end of M2 is obtained by substituting (4.6),(A.11),(A.12) into the time derivative of (A.10) (i.e $t=t_{M2}$).

$$\frac{dI_{Ls_{M3}}(0)}{dt} = \frac{V_{dc}\left(f_m(2G_{tr}-1)(1-2(A+1)G_o)+2AG_o\right)}{2L_s(2G_{tr}-1)f_m} \tag{A.14}$$

During M3, $C_e = C_s$ see Figure 4.9(c), and, by application of Laplace transforms, the tank current during M3 will have the following form:

$$I_{Ls_{M3}}(t) = \hat{I}_{M3}\cos\left(t\sqrt{\frac{1}{L_s C_e}}+\phi\right) = \hat{I}_{M3}\cos\left(t\sqrt{\frac{A}{L_s C_P}}+\phi\right)$$

$$\text{where } \hat{I}_{M3} = I_{Ls_{M3}}(0)\sqrt{1+\frac{L_s C_P\left(\frac{dI_{Ls_{M3}}(0)}{dt}\right)^2}{A\, I_{Ls_{M3}}(0)^2}}, \tag{A.15}$$

$$\phi = -\tan^{-1}\left(\frac{1}{I_{Ls_{M3}}(0)}\sqrt{\frac{L_s C_P}{A}}\frac{dI_{Ls_{M3}}(0)}{dt}\right)$$

where $I_{Ls_{M3}}(0)$, $\frac{dI_{Ls_{M3}}(0)}{dt}$ are the initial conditions of the mode and have been calculated in (A.13),(A.14) respectively. Substituting (4.6),(A.13),(A.14) into (A.15) provides the expression for I_{Ls} during M3.

The magnitude of $I_{L_{M3}}(t)$ is as follows:

$$\hat{I}_{M3} = \frac{V_{dc}}{4f_m N\sqrt{R_L A L_s f_r (2G_{tr}-1)}}\sqrt{\begin{array}{l} f_m{}^2(2G_{tr}-1)^2\left(4(A+1)^2 G_o{}^2 + 4(A-1)G_o + 1\right) \\ \ldots + f_m(2G_{tr}-1)4G_o A(2(A-1)G_o+1) + 4A^2 G_o{}^2 \end{array}} \qquad \text{(A.16)}$$

Substituting (4.6),(A.2),(A.13),(A.14),(A.15),(A.16) into (4.1) and solving for t_{M3} finally provides the time spent in M3:

$$t_{M3} = \frac{1}{2N}\sqrt{\frac{L_s(2G_{tr}-1)}{R_L A\, f_r}}\left(\begin{array}{l} \sin^{-1}\left(\dfrac{f_m(2G_{tr}-1)(-1+2G_o)+4G_o{}^2 A}{\sqrt{\begin{array}{l} f_m{}^2(2G_{tr}-1)^2\left(4(A+1)^2 G_o{}^2 + 4(A+1)G_o - 8G_o + 1\right) \\ \ldots + f_m(2G_{tr}-1)4G_o A(2(A-1)G_o+1) + 4A^2 G_o{}^2 \end{array}}}\right) \\ \ldots - \tan^{-1}\left(\dfrac{\sqrt{2}\left(f_m(2G_{tr}-1)(-1+2(1+A)G_o) - 2AG_o\right)}{4\sqrt{f_m(2G_{tr}-1)AG_o\left(2AG_o + f_m(2G_{tr}-1)\right)}}\right) \end{array}\right) \qquad \text{(A.17)}$$

Appendix B - Analysis of LCC Capacitively-smoothed resonant converter during light loading operation

Equations (4.40),(4.41) can be solved simultaneously to give the following:

$$Q_{M1} = \frac{V_{dc}G_o\left(2G_o - f_m\left(2G_{tr} - 1\right) + 1\right)}{4f_r f_m N^2 R_L} \tag{B.1}$$

$$Q_{M2} = \frac{-V_{dc}G_o}{2f_m f_r N^2 R_L} \tag{B.2}$$

$$Q_{M3} = \frac{V_{dc}G_o\left(2G_o + f_m\left(2G_{tr} - 1\right) + 1\right)}{4f_r f_m N^2 R_L} \tag{B.3}$$

Since all the tank current flows though C_s, the change in V_{Cs} during the positive half-cycle of the tank current is:

$$V_{Cs_{M5}}(t_{M5}) = -V_{Cs_3}(0) = V_{Cs_{M3}}(0) + \frac{1}{C_s}\left(-Q_{M1} - Q_{M2} + Q_{M3}\right) \tag{B.4}$$

V_{Cs} at the start of M3 follows from (4.6),(4.7),(B.1),(B.2),(B.3),(B.4):

$$V_{Cs_{M3}}(0) = \frac{-AV_{dc}G_o\left(1 + \left(2G_{tr} - 1\right)f_m\right)}{\left(2G_{tr} - 1\right)f_m} \tag{B.5}$$

Notably, this is the same for V_{Cs} at the start of M2 for operation under heavy loading (B.4).

During M2, $C_e = C_s$, see Figure 4.11(b), and:

$$I_{Ls_{M2}}(t) = \hat{I}_{M2}\sin\left(\sqrt{\frac{A}{L_s C_P}}\left(t - t_{M2}\right)\right) \tag{B.6}$$

At the end of M2, V_{Ls} is given by:

$$V_{Ls_{M2}}(t_{M2}) = L_s\frac{dI_{Ls_{M2}}\left(t_{M2}\right)}{dt} = \frac{V_{dc}}{2} + NV_o - V_{Cs_{M3}}(0) \tag{B.7}$$

Substituting (4.36),(B.5)into (B.7) and solving for the derivative gives:

$$\frac{dI_{Ls_{M2}}(t_{M2})}{dt} = \frac{V_{dc}}{2L_s} + \frac{V_{dc}G_o}{L_s} + \frac{AV_{dc}G_o\left(1 + \left(2G_{tr} - 1\right)f_m\right)}{L_s\left(2G_{tr} - 1\right)f_m} \tag{B.8}$$

Equating the derivative of (B.6) at $t=t_{M2}$ with (B.8) and solving for $\hat{I}_{M2}$ provides:

$$\hat{I}_{M2} = \frac{V_{dc}\left(f_m\left(2G_{tr} - 1\right)\left(1 + 2(A+1)G_o\right) + 2AG_o\right)}{4f_m N\sqrt{R_L A L_s f_r\left(2G_{tr} - 1\right)}} \tag{B.9}$$

Again, this is the same result as for $\hat{I}_{M1}$ during heavily loaded operation.

The time spent in M2 (t_{M2}) can be obtained by substituting (4.6),(B.2),(B.6),(B.9) into (4.1) and solving for t_{M2}:

$$t_{M2} = \frac{1}{2N}\sqrt{\frac{L_s(2G_{tr}-1)}{R_L A f_r}}\cos^{-1}\left(\frac{f_m(2G_{tr}-1)(1+2(A+1)G_o)-2AG_o}{f_m(2G_{tr}-1)(1+2(A+1)G_o)+2AG_o}\right) \qquad \text{(B.10)}$$

Substituting (B.9),(B.10) into (B.6) also gives I_{Ls} during M2.

I_{Ls} at the start of M2 is now be calculated by substituting (4.6),(B.9),(B.10) into (B.6) and evaluating at *t=0*, giving:

$$I_{Ls_{M2}}(0) = -\frac{V_{dc}}{N}\sqrt{\frac{G_o(2(A+1)G_o+1)}{2R_L f_r f_m L_s}} = I_{L_{M1}}(t_{M1}) \qquad \text{(B.11)}$$

The derivative at the start of M2 is similarly found by substituting (4.6),(B.9),(B.10) into the derivative of (B.6) and evaluating at *t=0*.

$$\frac{dI_{Ls_{M2}}(0)}{dt} = \frac{V_{dc}(f_m(2G_{tr}-1)(2G_o(1+A)+1)-2G_oA)}{2f_m(2G_{tr}-1)L_s} = \frac{dI_{Ls_{M1}}(t_{M1})}{dt} \qquad \text{(B.12)}$$

I_{Ls} during M3 is obtained by noting that C_e is the series combination of C_s and C_p (see Figure 4.11(c) and equation (4.9)), and, therefore:

$$I_{Ls_{M3}}(t) = \hat{I}_{M3}\sin\left(t\sqrt{\frac{1}{L_sC_e}}\right) = \hat{I}_{M3}\sin\left(t\sqrt{\frac{A+1}{L_sC_P}}\right) \qquad \text{(B.13)}$$

Equating the derivative of I_{Ls} at the start of M3 with that at the end of M2, gives $\hat{I}_{M3}$. Consequently, equating the derivative of (B.13) at *t=0* with (B.8) (the derivative of (B.6) at $t=t_{M2}$), and solving for $\hat{I}_{M3}$, ultimately provides:

$$\hat{I}_{M3} = \frac{V_{dc}(f_m(2G_{tr}-1)(1+2(A+1)G_o)+2AG_o)}{4f_mN\sqrt{R_L(A+1)L_sf_r(2G_{tr}-1)}} = \hat{I}_{M2}\sqrt{\frac{A}{A+1}} \qquad \text{(B.14)}$$

Finally, substituting (B.14) into (B.13) gives I_{Ls} during M3, and substituting (4.6),(B.3),(B.13),(B.14) into (4.1) and solving for t_{M3} gives:

$$t_{M3} = \frac{1}{2N}\sqrt{\frac{L_s(2G_{tr}-1)}{R_L(A+1)f_r}}\cos^{-1}\left(\frac{f_m(2G_{tr}-1)-2G_o(1+2(A+1)G_o)}{f_m(2G_{tr}-1)(1+2(A+1)G_o)+2AG_o}\right) \qquad \text{(B.15)}$$

I_{Ls} at the end of M3 is obtained by substituting (4.6),(B.14),(B.15) (i.e t $=t_{M3}$) into (B.13), as follows:

$$I_{Ls_{M3}}(t_{M3}) = \frac{V_{dc}}{2Nf_m}\sqrt{\frac{G_o\begin{pmatrix}(Go(A+1)+1)f_m{}^2(2G_{tr}-1)^2+(2G_o(A+1)+1)f_m(2G_{tr}-1)\\ \ldots-(2G_o+1)G_o(2G_o(A+1)-A+1\end{pmatrix}}{R_Lf_rL_s(2G_{tr}-1)}} \qquad \text{(B.16)}$$

The derivative of I_{Ls} at the start of M3 is similarly found by substituting (4.6),(B.14),(B.15) (i.e $t=t_{M3}$) into the derivative of (4.71):

$$\frac{dI_{Ls_{M3}}(t_{M3})}{dt}=\frac{V_{dc}\left(f_m(2G_{tr}-1)-2G_o\left(2(A+1)G_o+1\right)\right)}{2(2G_{tr}-1)f_m L_s} \tag{B.17}$$

Since the converter is assumed to be operating in steady-state, I_{Ls} at the start of M1 is of opposite polarity to that at the end of M3, i.e.:

$$I_{Ls_{M1}}(0)=-I_{Ls_{M3}}(t_{M3}) \tag{B.18}$$

and the derivative of I_{Ls} at the start of M1 is also related to the derivative of I_{Ls} at the end of M3, by:

$$\frac{dI_{Ls_{M1}}(0)}{dt}=-\left(\frac{dI_{Ls_{M3}}(t_{M3})}{dt}-\frac{V_{dc}}{L_s}\right) \tag{B.19}$$

The tank current during M1 takes the following form:

$$I_{Ls_{M1}}(t)=\hat{I}_{M1}\cos\left(t\sqrt{\frac{A+1}{L_sC_P}}+\phi\right)$$

$$\text{where } \hat{I}_{M1}=I_{Ls_{M1}}(0)\sqrt{1+\frac{L_sC_p\left(\frac{dI_{Ls_{M1}}(0)}{dt}\right)^2}{(A+1)I_{Ls_{M1}}(0)^2}} \text{ and} \tag{B.20}$$

$$\phi=-\tan^{-1}\left(\frac{1}{I_{Ls_{M1}}(0)}\sqrt{\frac{L_sC_p}{(A+1)}}\frac{dI_{Ls_{M1}}(0)}{dt}\right)$$

with initial conditions $I_{Ls_{M1}}(0)$, $\frac{dI_{Ls_{M1}}(0)}{dt}$ that have been calculated in (B.18),(B.19), respectively. Consequently, substituting (4.6),(B.16),(B.17),(B.18),(B.19) into (B.20) provides the tank current during the M1, $i_{Ls_{M1}}(t)$, and the amplitude is:

$$\hat{I}_{M1}=\frac{-V_{dc}\left(\sqrt{f_m^{\,2}(2G_{tr}-1)^2(2G_o(1+A)+1)^2+f_m(2G_{tr}-1)(4G_o(A+2)(2G_o(1+A)+1)+4G_o^{\,2}A}\right)}{4f_mN\sqrt{R_L(A+1)L_sf_r(2G_{tr}-1)}} \tag{B.21}$$

Substituting (4.6),(B.1),(B.16),(B.17),(B.18),(B.19),(B.20) into (4.1) and solving for t_{M1} finally gives:

$$t_{M1}=\frac{1}{2N}\sqrt{\frac{L_s(2G_{tr}-1)}{R_L(A+1)\ f_r}}\left(\begin{array}{l}\sin^{-1}\left(\dfrac{f_m(2G_{tr}-1)(2G_o(A+1)+1)-2G_oA}{\sqrt{\begin{array}{l}f_m^{\,2}(2G_{tr}-1)^2(2G_o(A+1)+1)^2\\ \ldots+f_m(2G_{tr}-1)(4G_o(A+2)(2G_o(1+A)+1))+4G_o^{\,2}A^2\end{array}}}\right)\\ \ldots-\tan^{-1}\left(\dfrac{f_m(2G_{tr}-1)+4G_o^{\,2}(A+1)+2G_o}{2\sqrt{\begin{array}{l}G_o(2G_o+1+f_m(2G_{tr}-1))(A+1)\\ \ldots\times(((A+1)G_o+1)f_m(2G_{tr}-1)-G_o(2G_o(A+1)+1-A))\end{array}}}\right)\end{array}\right) \tag{B.22}$$

Appendix C - Design curves for alternative *A* values

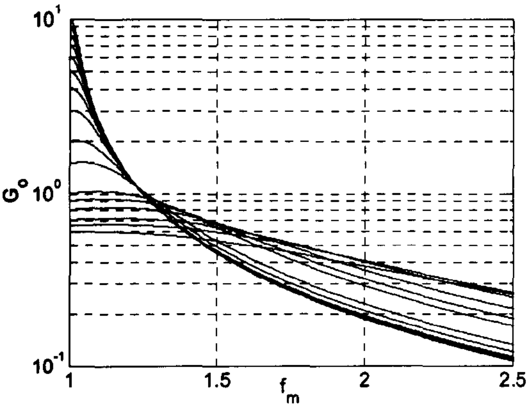

(a)

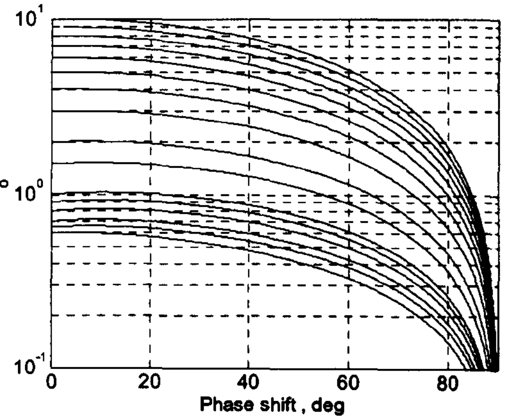

(b)

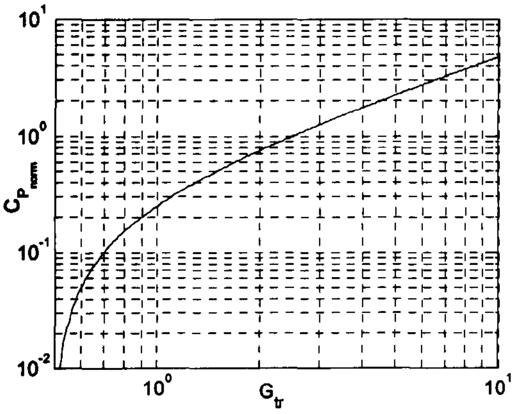

(c) $C_p = C_{p_{norm}} \frac{1}{N^2 R_L f_r} = \frac{2G_{tr} - 1}{4N^2 R_L f_r}$

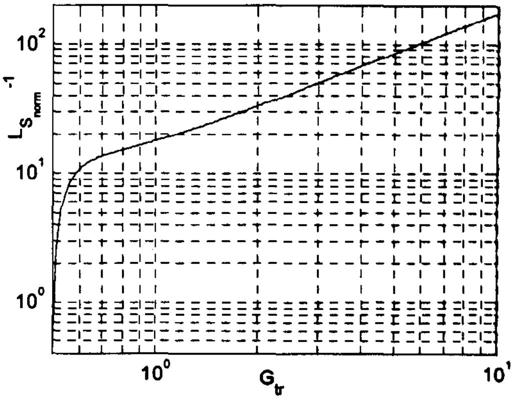

(d) $L_s = L_{s_{norm}} \frac{N^2 R_L}{f_r}$

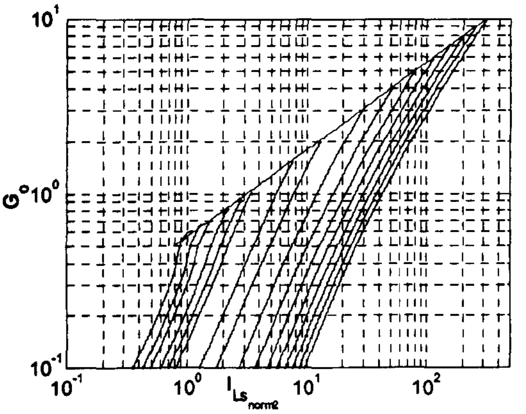

(e) $\hat{I}_{Ls} = I_{Ls_{norm2}} \frac{V_{dc}}{N^2 R_L}$

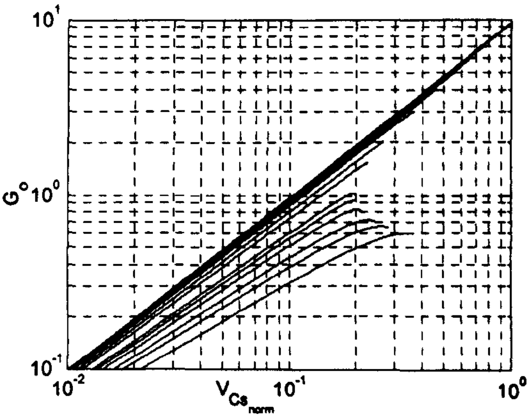

(f) $\hat{V}_{Cs} = V_{Cs_{norm}} V_{dc}$

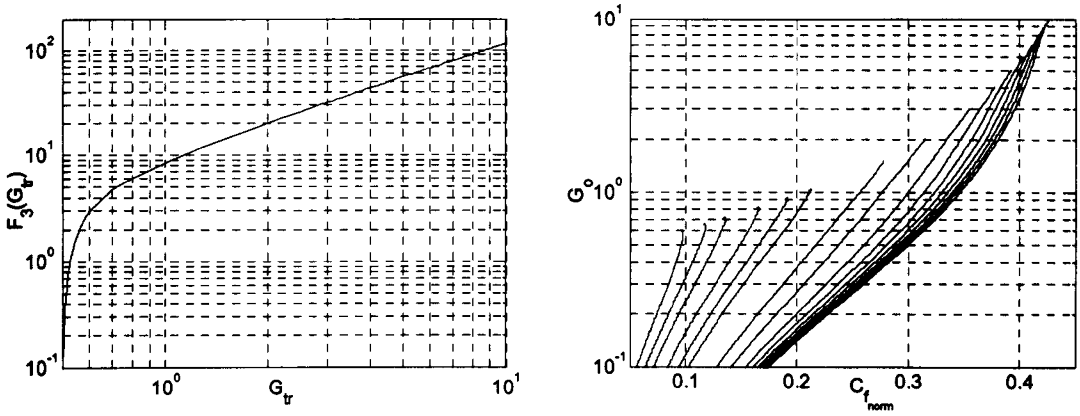

(g)

(h) $C_f = C_{f_{norm}} \frac{V_o}{R_L f_r V_{pp}}$

Figure C.1 – Design curves for A=0.1. (a) magnitude response (b) phase response (c) required parallel capacitor (d) required inductor (e) resonant inductor peak current (f) peak series capacitor voltage stress (g) resonant tank gain calculation curve (h) required filter capacitor

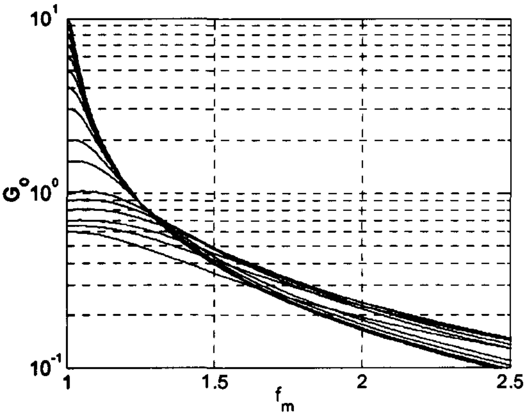

(a)

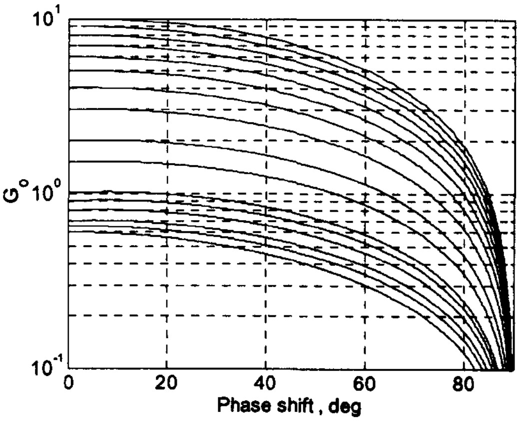

(b)

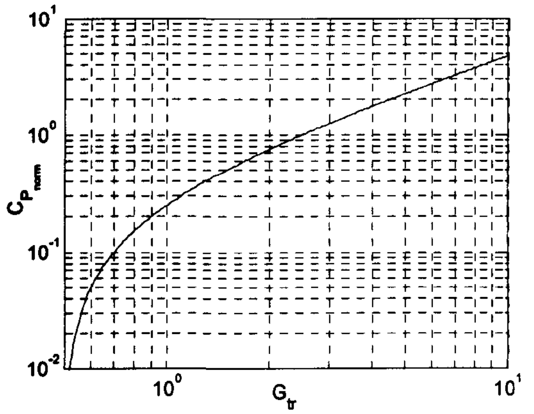

(c) $C_p = C_{p_{norm}} \frac{1}{N^2 R_L f_r} = \frac{2G_{tr} - 1}{4N^2 R_L f_r}$

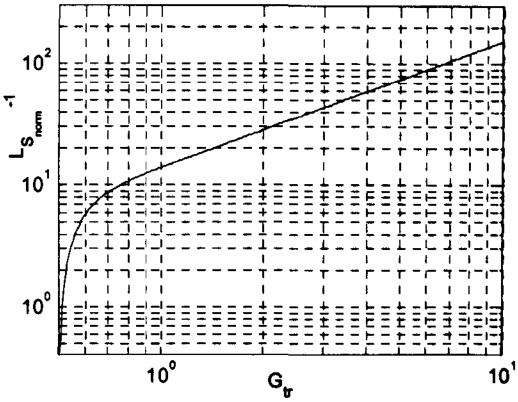

(d) $L_s = L_{s_{norm}} \frac{N^2 R_L}{f_r}$

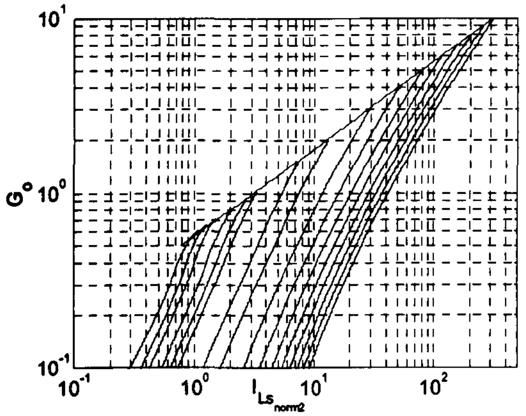

(e) $\hat{I}_{Ls} = I_{Ls_{norm2}} \frac{V_{dc}}{N^2 R_L}$

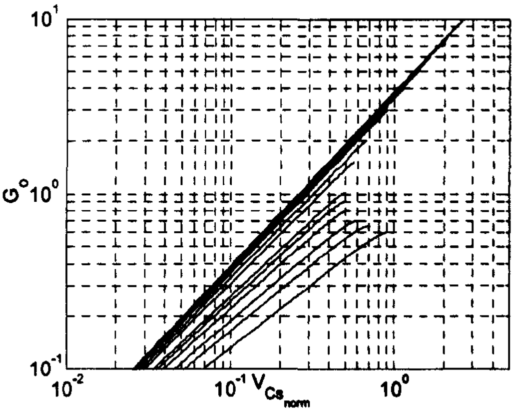

(f) $\hat{V}_{Cs} = V_{Cs_{norm}} V_{dc}$

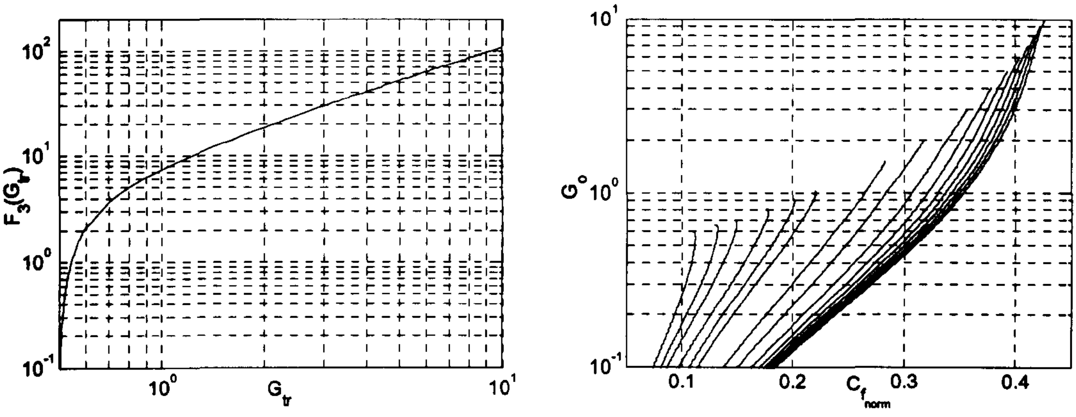

(g)

(h) $C_f = C_{f_{norm}} \frac{V_o}{R_L f_r V_{pp}}$

Figure C.2 –Design curves for A=0.25 (a) magnitude response (b) phase response (c) required parallel capacitor (d) required inductor (e) resonant inductor peak current (f) peak series capacitor voltage stress (g) resonant tank gain calculation curve (h) required filter capacitor

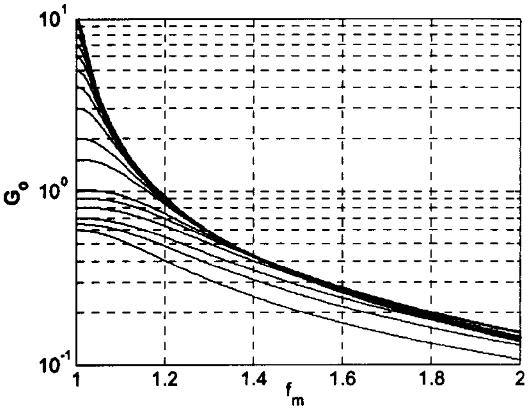

(a)

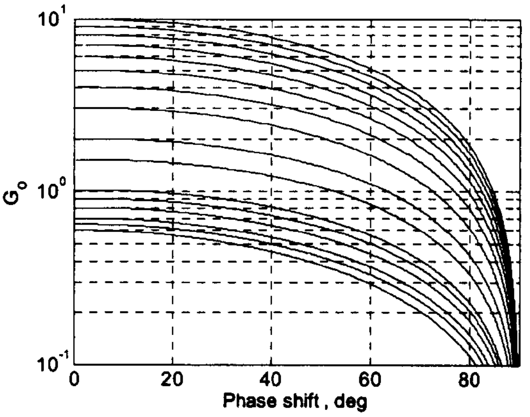

(b)

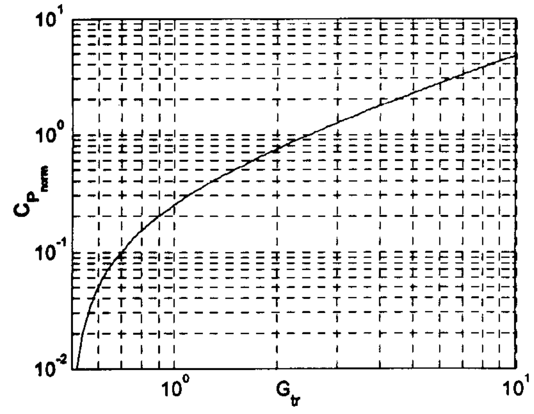

(c) $C_p = C_{P_{norm}} \frac{1}{N^2 R_L f_r} = \frac{2G_{tr}-1}{4N^2 R_L f_r}$

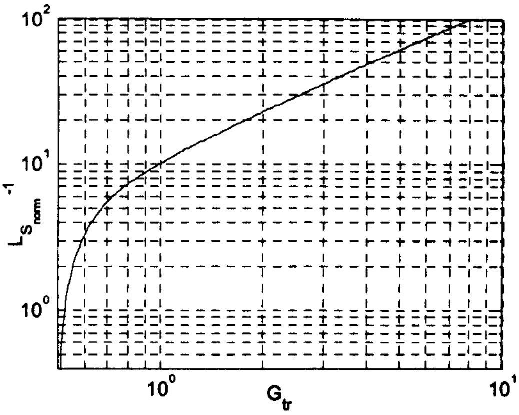

(d) $L_s = L_{s_{norm}} \frac{N^2 R_L}{f_r}$

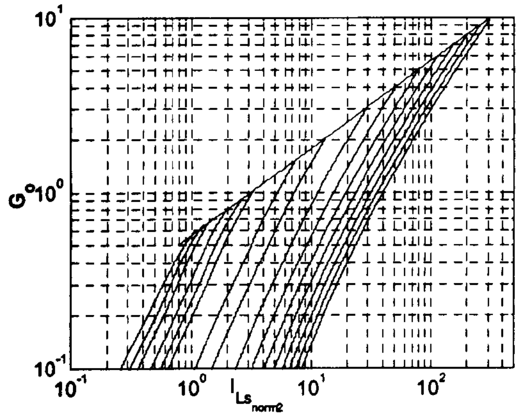

(e) $\hat{I}_{Ls} = I_{Ls_{norm2}} \frac{V_{dc}}{N^2 R_L}$

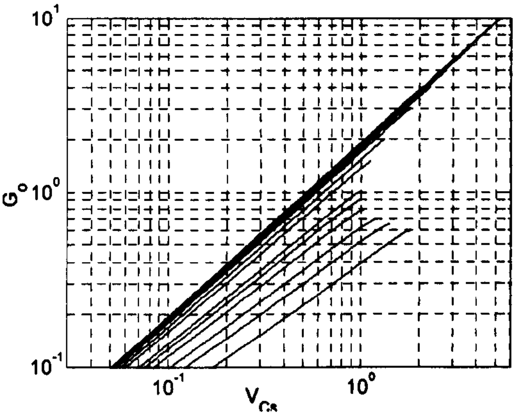

(f) $\hat{V}_{Cs} = V_{Cs_{norm}} V_{dc}$

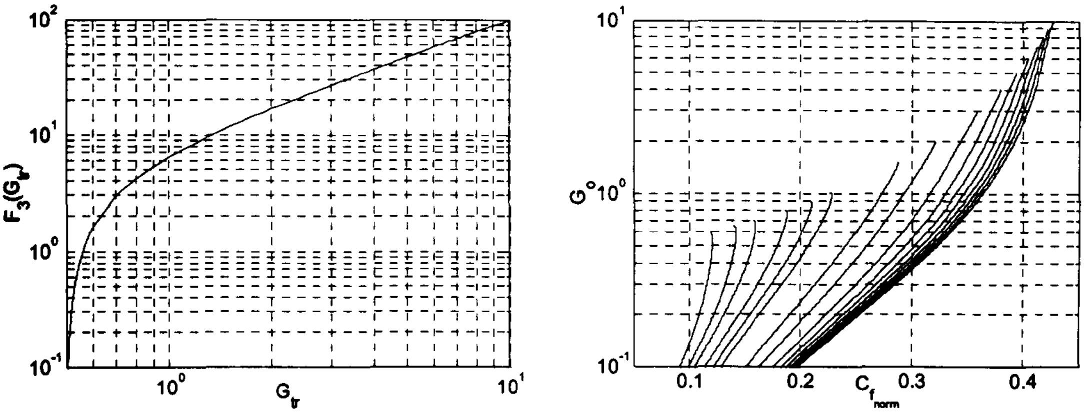

(g)

(h) $C_f = C_{f_{norm}} \frac{V_o}{R_L f_r V_{pp}}$

Figure C.3 –Design curves for A=0.5 (a) magnitude response (b) phase response (c) required parallel capacitor (d) required inductor (e) resonant inductor peak current (f) peak series capacitor voltage stress (g) resonant tank gain calculation curve (h) required filter capacitor

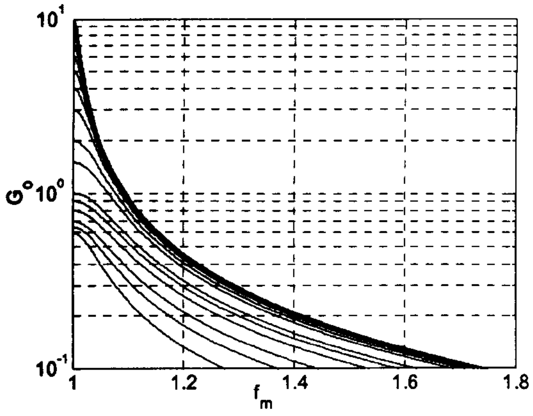

(a)

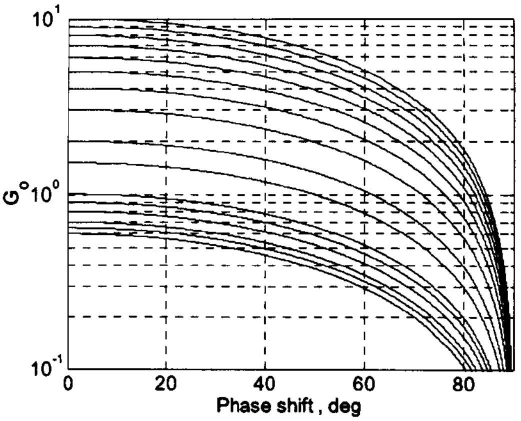

(b)

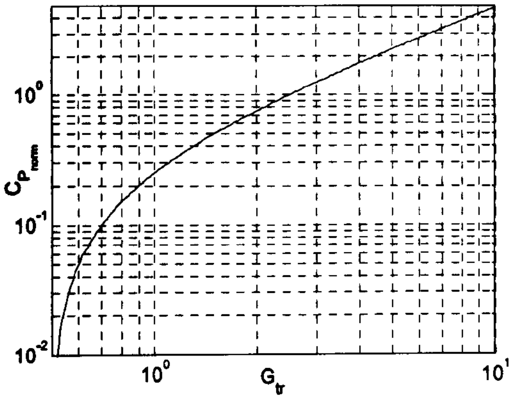

(c) $C_p = C_{p_{norm}} \frac{1}{N^2 R_L f_r} = \frac{2G_{tr}-1}{4N^2 R_L f_r}$

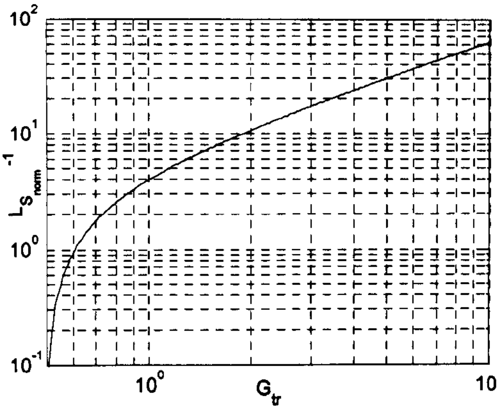

(d) $L_s = L_{s_{norm}} \frac{N^2 R_L}{f_r}$

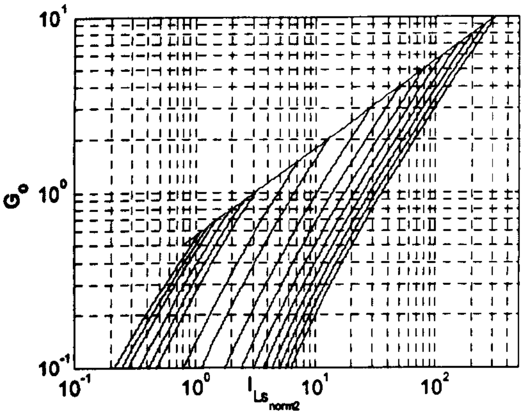

(e) $\hat{I}_{Ls} = I_{Ls_{norm2}} \frac{V_{dc}}{N^2 R_L}$

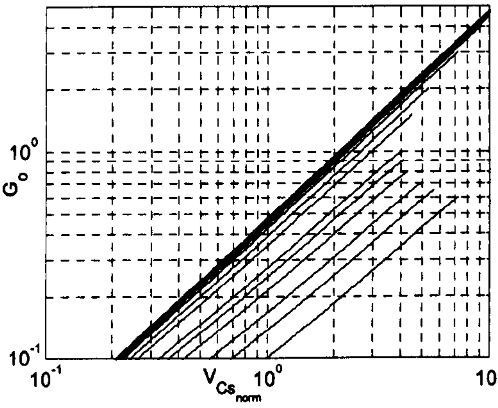

(f) $\hat{V}_{Cs} = V_{Cs_{norm}} V_{dc}$

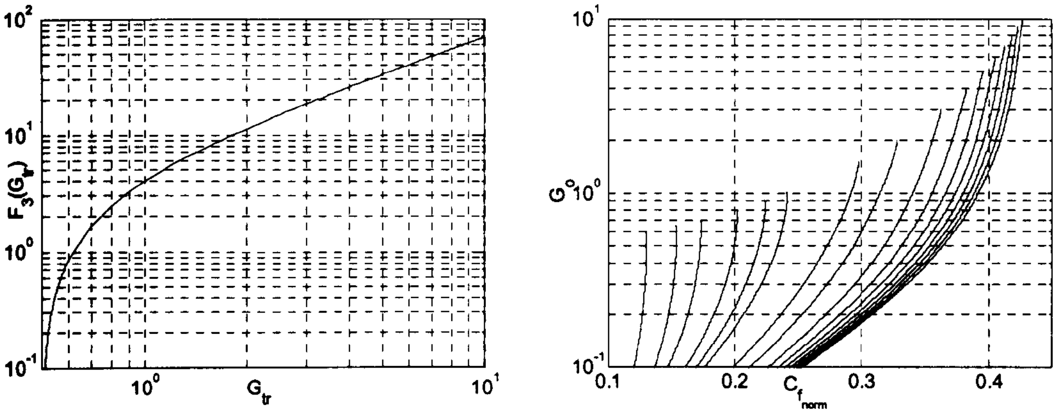

(g)

(h) $C_f = C_{f_{norm}} \frac{V_o}{R_L f_r V_{pp}}$

Figure C.4 –Design curves for A=2 (a) magnitude response (b) phase response (c) required parallel capacitor (d) required inductor (e) resonant inductor peak current (f) peak series capacitor voltage stress (g) resonant tank gain calculation curve (h) required filter capacitor

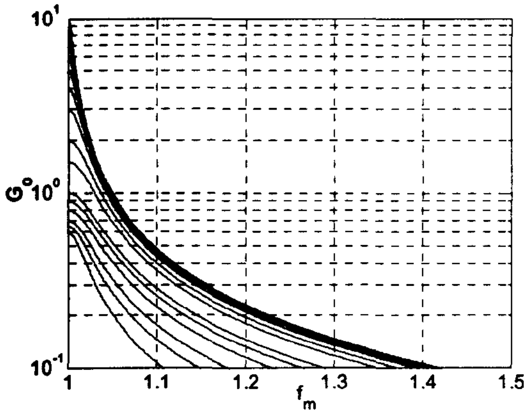

(a)

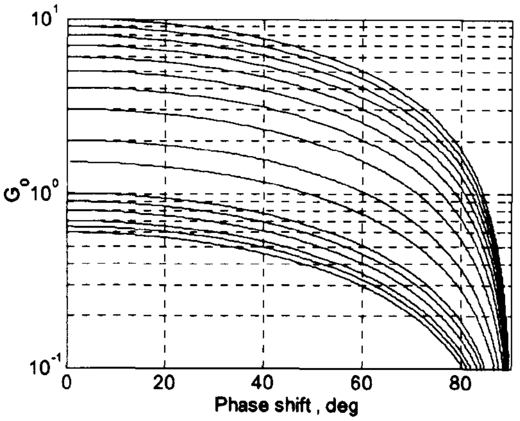

(b)

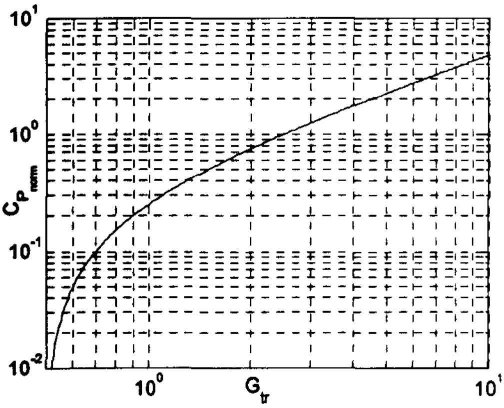

(c) $C_p = C_{p_{norm}} \frac{1}{N^2 R_L f_r} = \frac{2G_{tr}-1}{4N^2 R_L f_r}$

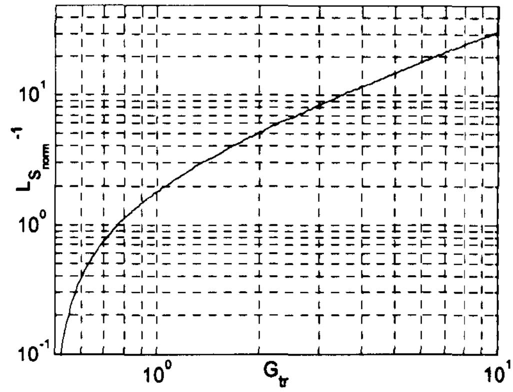

(d) $L_s = L_{s_{norm}} \frac{N^2 R_L}{f_r}$

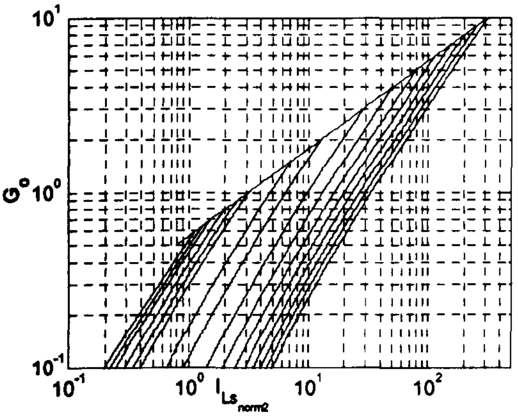

(e) $\hat{I}_{Ls} = I_{Ls_{norm2}} \frac{V_{dc}}{N^2 R_L}$

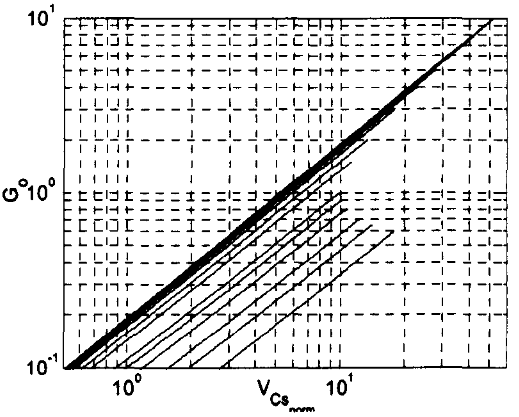

(f) $\hat{V}_{Cs} = V_{Cs_{norm}} V_{dc}$

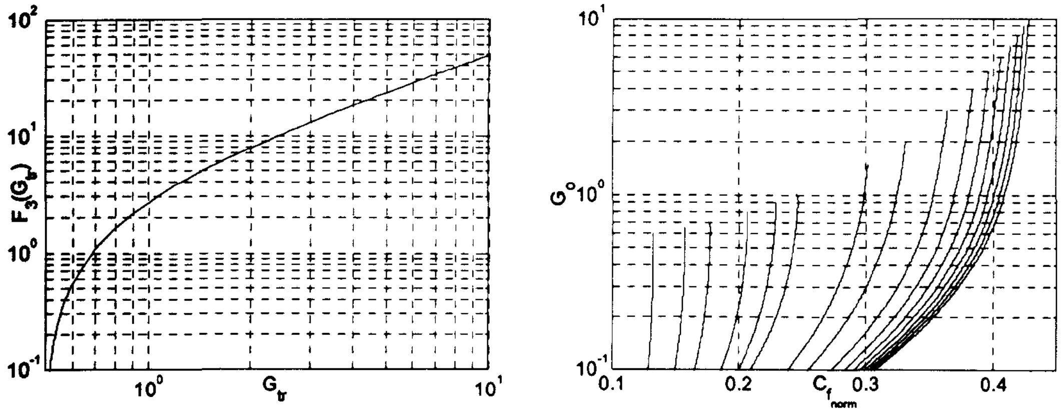

(g)

(h) $C_f = C_{f_{norm}} \frac{V_o}{R_L f_r V_{pp}}$

Figure C.5 –Design curves for A=5 (a) magnitude response (b) phase response (c) required parallel capacitor (d) required inductor (e) resonant inductor peak current (f) peak series capacitor voltage stress (g) resonant tank gain calculation curve (h) required filter capacitor

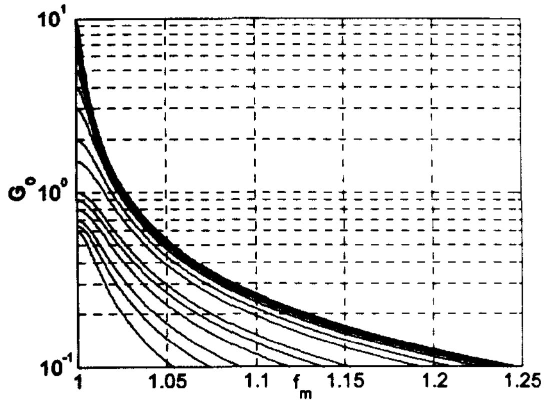

(a)

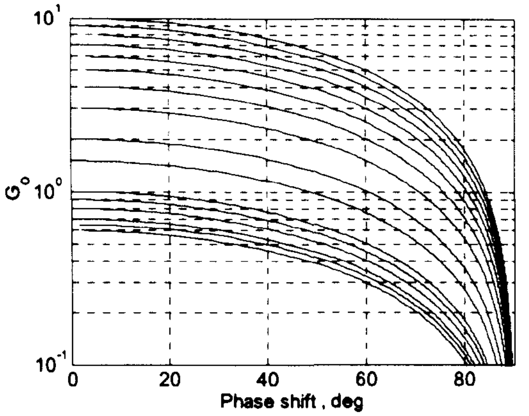

(b)

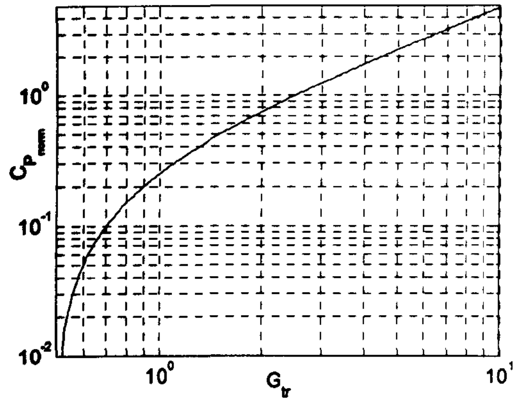

(c) $C_p = C_{p_{norm}} \frac{1}{N^2 R_L f_r} = \frac{2G_{tr}-1}{4N^2 R_L f_r}$

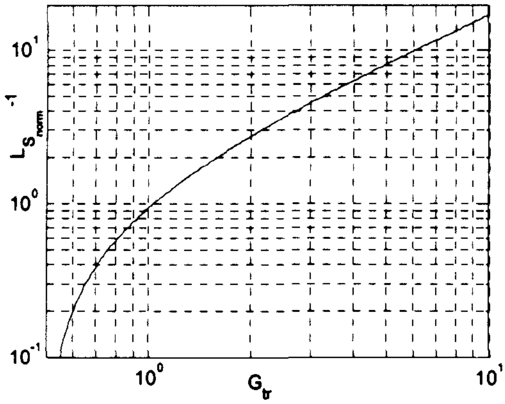

(d) $L_s = L_{s_{norm}} \frac{N^2 R_L}{f_r}$

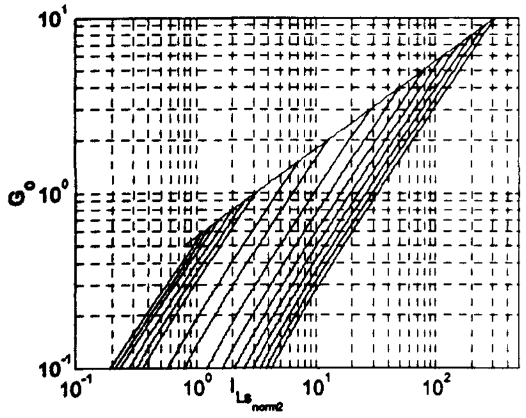

(e) $\hat{I}_{Ls} = I_{Ls_{norm2}} \frac{V_{dc}}{N^2 R_L}$

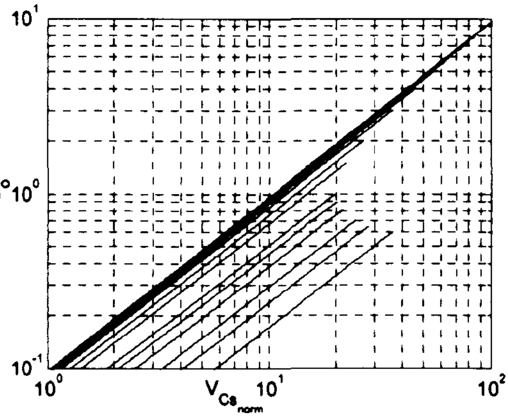

(f) $\hat{V}_{Cs} = V_{Cs_{norm}} V_{dc}$

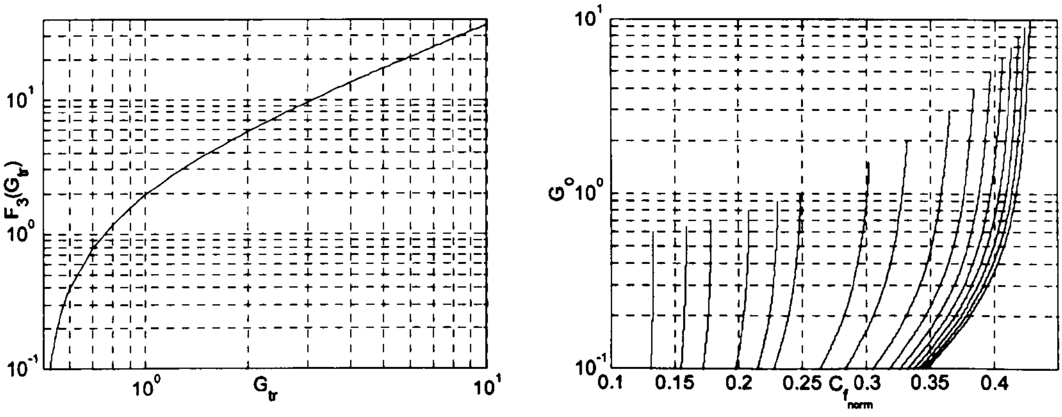

(g)

(h) $C_f = C_{f_{norm}} \frac{V_o}{R_L f_r V_{pp}}$

Figure C.6 –Design curves for A=10 (a) magnitude response (b) phase response (c) required parallel capacitor (d) required inductor (e) resonant inductor peak current (f) peak series capacitor voltage stress (g) resonant tank gain calculation curve (h) required filter capacitor

Appendix D - Resonant converter schematics/components

D.1 Gate drive schematics

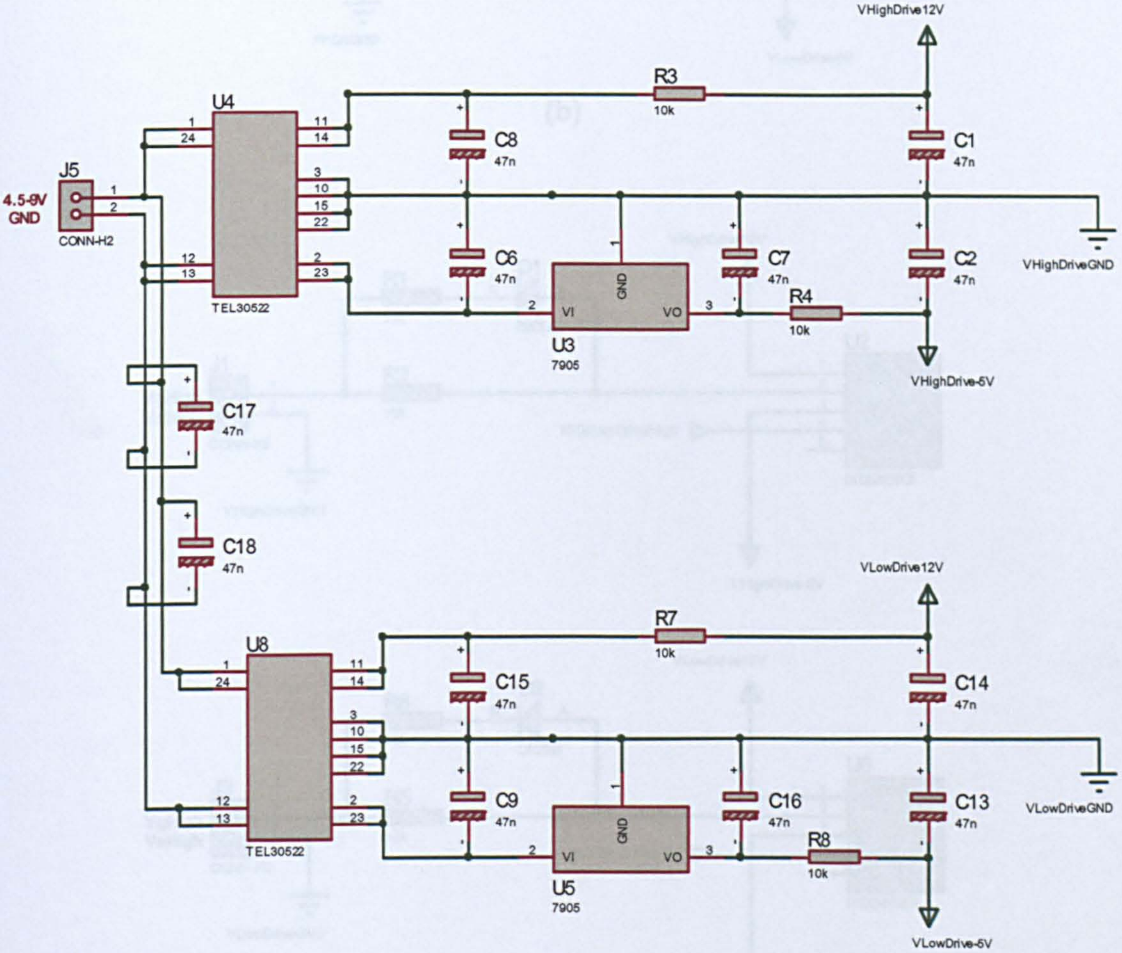

(a)

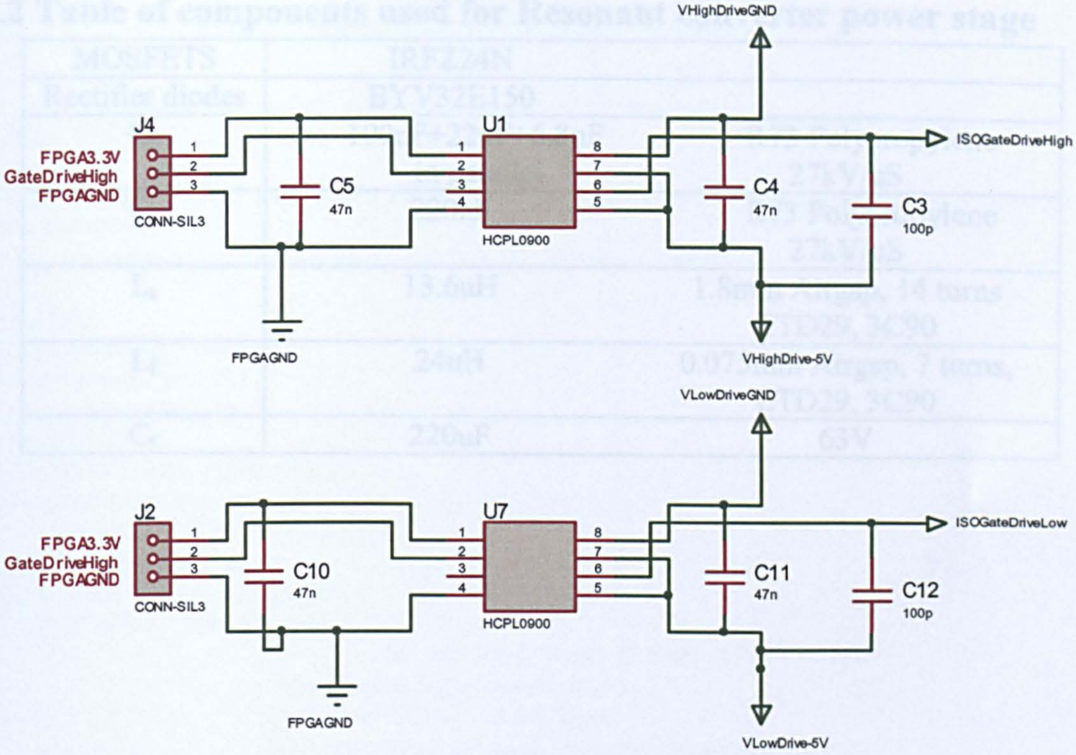

(b)

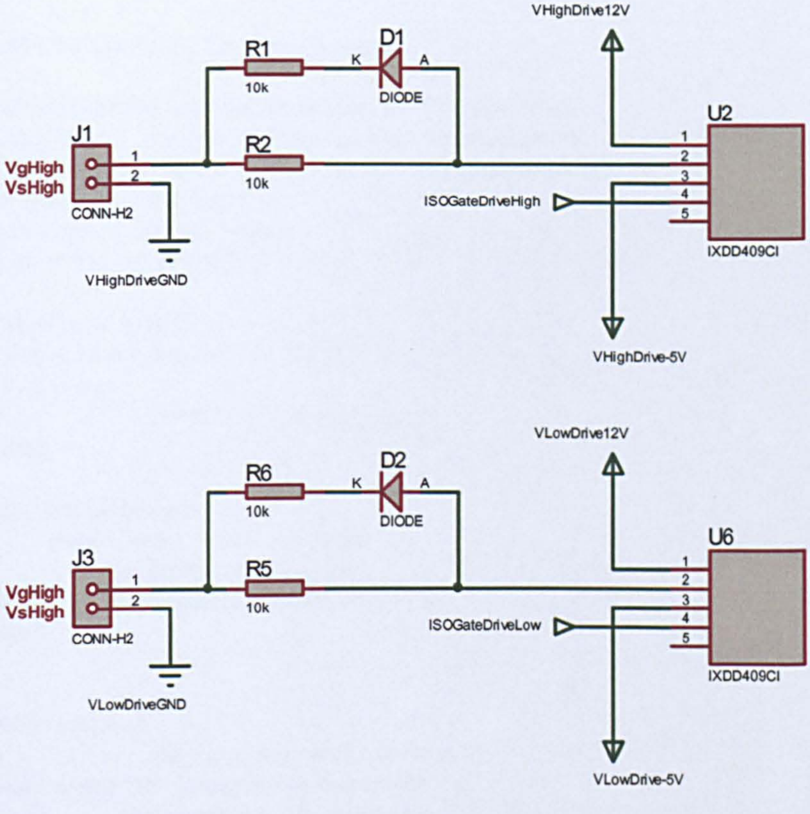

(c)

Figure D.1 - Gate drive (a) power supply (b) isolation (c) driving stage

D.2 Table of components used for Resonant converter power stage

MOSFETS	IRFZ24N	
Rectifier diodes	BYV32E150	
C_s	100nF+22nF+6.8nF in parallel	R73 Polypropylene 27kV/uS
C_p	220nF	R73 Polypropylene 27kV/uS
L_s	13.6uH	1.8mm Airgap, 14 turns ETD29, 3C90
L_f	24uH	0.075mm Airgap, 7 turns, ETD29, 3C90
C_f	220uF	63V

Appendix E - FPGA VHDL Code

```
---------------------------------------------------------------------------
-- TopLevelVHDL
--
----Implements Method 1 and 2 on the FPGA (Method 1 square wave original, Method -----2 dutycle>0.5
aprox linearised)
---------------------------------------------------------------------------

library ieee;
use ieee.std_logic_1164.ALL;
use ieee.numeric_std.ALL;
-- synopsys translate_off
library UNISIM;
use UNISIM.Vcomponents.ALL;
-- synopsys translate_on

entity TopLevelSchem is
  port ( Clock       : in    std_logic;
       SgnCurrent  : in    std_logic;
                         PF          : in    std_logic_vector (7 downto 0);
                         SwitchingSigHigh : out std_logic;
                         SwitchingSigLow: out std_logic;
                         ReduceDelay: in std_logic_vector (5 downto 0);
                         DeadTime: in std_logic_vector(5 downto 0)
                        );

end TopLevelSchem;


architecture BEHAVIORAL of TopLevelSchem is

signal HalfPeriodLengthSig: unsigned(9 downto 0):="0000000000";
signal DelayLengthOut  :  unsigned (10 downto 0):="00000000000";
signal AngleSig : std_logic_vector (11 downto 0):="000000000000";
signal PhaseSwitchingSig: std_logic;
signal SelectedSwitchingSig: std_logic;
signal StartBackUpSig: std_logic;

  component StartBackUp is
  port ( SgnCurrent: in std_logic;
       Clock: in std_logic;
                         Switching: out std_logic);
  end component;

  component HalfPeriodLength
                 port( Clock     : in    std_logic;
                    SgnCurrent: in  std_logic;
        NumCycles : out   unsigned(9 downto 0));
  end component;


component DelayLength is
  port ( Angle           : in    std_logic_vector (11 downto 0);
       HalfPeriodLength : in    unsigned (9 downto 0);
       NumCycles         : out   unsigned (10 downto 0);
                         Clock : in std_logic);
end component;
```

```
component VariableDelay is
   Port ( DelayLength : in  unsigned (10 downto 0);
        Clock : in  STD_LOGIC;
        SgnCurrent : in  STD_LOGIC;
        SwitchingSig: out STD_LOGIC;
        ReduceDelay: in std_logic_vector (5 downto 0);
        HalfPeriodLength : in    unsigned (9 downto 0));
end component;

component  Lookupangle
   Port ( PF : in  std_logic_vector (7 downto 0);
        Angle : out  std_logic_vector (11 downto 0));
end component;

component DeadTimeGen is
   Port ( SwitchingSig : in  STD_LOGIC;
        DeadTime : in  std_logic_vector (5 downto 0);
        SwitchingSigHigh : out  STD_LOGIC;
        SwitchingSigLow : out  STD_LOGIC;
        Clock: in std_logic);
end component;


begin

  StartBackUpInst: StartBackUp
         port map( Clock=>Clock, SgnCurrent=>SgnCurrent, Switching=>StartBackUpSig);

  HalfPeriodLengthInst : HalfPeriodLength
         port map (Clock=>Clock,SgnCurrent=>SgnCurrent,NumCycles=>HalfPeriodLengthSig);

  DelayLengthInst: DelayLength
         port map(Angle=>Anglesig, HalfPeriodLength=>HalfPeriodLengthSig,
                    NumCycles=>DelayLengthOut,Clock => Clock);

 VariableDelayInst: VariableDelay
                    port map(DelayLength=>DelayLengthOut, Clock=>Clock,  SgnCurrent=>SgnCurrent,
                              SwitchingSig=>PhaseSwitchingSig, ReduceDelay=>ReduceDelay,
                              HalfPeriodLength=>HalfPeriodLengthSig);

 LookupangleInst: Lookupangle
                    port map( PF=>PF, Angle=>AngleSig);

DeadTimeGenInst: DeadTimeGen
         port map ( SwitchingSig =>SelectedSwitchingSig, DeadTime=>DeadTime,
                      SwitchingSigHigh=>SwitchingSigHigh, SwitchingSigLow=>SwitchingSigLow,
                      Clock=>Clock);


 p10: process(StartBackUpSig, PhaseSwitchingSig ) is
 begin
               SelectedSwitchingSig<=PhaseSwitchingSig xor StartBackUpSig;

 end process;

end BEHAVIORAL;
```

```
-----------------------------------------------------------------------------
--  StartBackUp - Ensures that system will begin self oscillation
-----------------------------------------------------------------------------
library ieee;
use ieee.std_logic_1164.ALL;
use ieee.numeric_std.ALL;
-- synopsys translate_off
library UNISIM;
use UNISIM.Vcomponents.ALL;
-- synopsys translate_on

entity StartBackUp is
  port ( SgnCurrent: in std_logic;
       Clock: in std_logic;
                              Switching: out std_logic);
end StartBackUp;



architecture BEHAVIORAL of StartBackUp is
signal count1: unsigned(12 downto 0):="0000000000000";
signal count2: unsigned(7 downto 0):="00000000";
signal NeedStartUp: std_logic;
signal PreviousSgnCurrent:std_logic;

begin
p1: process(Clock, SgnCurrent)

begin
          if rising_edge(Clock) then
                    PreviousSgnCurrent<=SgnCurrent;

                    if (SgnCurrent='0' and PreviousSgnCurrent='1') or (SgnCurrent='1' and
                     PreviousSgnCurrent='0') then

                              count1<="0000000000000";
                              NeedStartUp<='0';
                    else
                              if count1<"1111111111111" then
                                        count1<=count1+1;
                                        NeedStartUp<='0';
                              else
                                        NeedStartUp<='1';
                              end if;

                    end if;

                    count2<=count2+1;
                    Switching<= NeedStartUp and count2(7);

          end if;

          end process p1;

end BEHAVIORAL;
```

```
----------------------------------------------------------------------------
--  HalfPeriodLength - Measures the half period of the current waveform
----------------------------------------------------------------------------
library ieee;
use ieee.std_logic_1164.ALL;
use ieee.numeric_std.ALL;
-- synopsys translate_off
library UNISIM;
use UNISIM.Vcomponents.ALL;
-- synopsys translate_on

entity HalfPeriodLength is
  port ( Clock     : in    std_logic;
              SgnCurrent : in std_logic;
       NumCycles : out   unsigned (9 downto 0):="0000000000");
end HalfPeriodLength;

architecture BEHAVIORAL of HalfPeriodLength is
signal NumCyclesTemp: unsigned(10 downto 0):="00000000000";
signal PreviousSgnCurrent: std_logic;

begin
        p1: process(Clock)
        variable Count: unsigned(10 downto 0):="00000000000";


        begin

            if rising_edge(Clock)then
                Count:=Count+1;
                PreviousSgnCurrent<=SgnCurrent;

                if SgnCurrent='0' and PreviousSgnCurrent='1' then

                        NumCycles<=Count(10 downto 1);
                        Count:="00000000001";            --We loose 1 cycle otherwise
               end if;
            end if;

        end process p1;
end BEHAVIORAL;
```

```
-----------------------------------------------------------------------------
--  DelayLength - Calculates the required delays
------------------------------------------------------------------------------
library ieee;
use ieee.std_logic_1164.ALL;
use ieee.numeric_std.ALL;
-- synopsys translate_off
library UNISIM;
use UNISIM.Vcomponents.ALL;
-- synopsys translate_on

entity DelayLength is
  port ( Angle          : in    std_logic_vector (11 downto 0);
       HalfPeriodLength : in    unsigned (9 downto 0);
       NumCycles        : out   unsigned (10 downto 0);
                              Clock: in std_logic);
end DelayLength;



architecture BEHAVIORAL of DelayLength is
begin

p3: process(Clock, Angle, HalfPeriodLength)
variable temp: unsigned(21 downto 0):="0000000000000000000000";
begin
                if rising_edge(Clock) then
                                temp:=(   unsigned(Angle)*unsigned(HalfPeriodLength));
                                NumCycles<=temp(21 downto 11);
                end if;
end process p3;

end BEHAVIORAL;
```

```
--------------------------------------------------------------------------------
--  VariableDelay - Implements the required delays
--------------------------------------------------------------------------------
library ieee;
use ieee.std_logic_1164.ALL;
use ieee.numeric_std.ALL;
-- synopsys translate_off
library UNISIM;
use UNISIM.Vcomponents.ALL;
-- synopsys translate_on

---- Uncomment the following library declaration if instantiating
---- any Xilinx primitives in this code.


entity VariableDelay is
   Port ( DelayLength : in  unsigned (10 downto 0);
         Clock : in  STD_LOGIC;
         SgnCurrent : in  STD_LOGIC;
                              SwitchingSig: out STD_LOGIC:='1';
                              ReduceDelay: in std_logic_vector(5 downto 0);
                              HalfPeriodLength : in    unsigned (9 downto 0));
end VariableDelay;


architecture behavioral of VariableDelay is
signal SwitchingSigTemp: std_logic:='1';
signal StartUp: std_logic:='1';
signal RaisingCountTemp: unsigned(10 downto 0);
signal FallingCountTemp: unsigned(10 downto 0);
signal PreviousSgnCurrent: std_logic;

begin
   p4: process (Clock, SgnCurrent) is
          variable RaisingCount:unsigned(10 downto 0):="00000000000";
   variable FallingCount:unsigned(10 downto 0):="00000000000";
          variable DelayLengthTemp:unsigned(10 downto 0):="00000000000";
          begin
                   if rising_edge(Clock) then
                    PreviousSgnCurrent<=SgnCurrent;

                   if SgnCurrent='0' then
                       SwitchingSig<='0';
                   else
                       if SgnCurrent='1' and PreviousSgnCurrent='0' then --Raising SgnCurrent edge
                              SwitchingSig<='1';
                              RaisingCount:="00000000100";
                       else  --normal opperation per clock cycle

                             if RaisingCount<=DelayLength-unsigned(ReduceDelay) then
                                  RaisingCount:=RaisingCount+1;
                             else
                                    SwitchingSig<='0';
                             end if;
                        end if;
                    end if;
          end if;
   end process;
end behavioral;
```

```
----------------------------------------------------------------------------
--  Lookupangle - Peforms       Theta=arcos(PF)
----------------------------------------------------------------------------
library IEEE;
use IEEE.STD_LOGIC_1164.ALL;
use IEEE.STD_LOGIC_ARITH.ALL;
use IEEE.STD_LOGIC_UNSIGNED.ALL;

---- Uncomment the following library declaration if instantiating
---- any Xilinx primitives in this code.
--library UNISIM;
--use UNISIM.VComponents.all;

entity lookupangle is
   Port ( PF : in  std_logic_vector (7 downto 0);
              Angle : out  std_logic_vector (11 downto 0));
end lookupangle;

architecture Behavioral of lookupangle is
begin
          p5: process(PF)
          variable tableresult: std_logic_vector (11 downto 0);
  begin

                      tableresult:='0'&PF&"000";
                     Angle<=tableresult;
   end process;
end Behavioral;
```

```
--------------------------------------------------------------------------------
--  DeadTimeGen - Creates a user defined deadtime
--------------------------------------------------------------------------------
library IEEE;
use IEEE.STD_LOGIC_1164.ALL;
use IEEE.STD_LOGIC_ARITH.ALL;
use IEEE.STD_LOGIC_UNSIGNED.ALL;

---- Uncomment the following library declaration if instantiating
---- any Xilinx primitives in this code.
--library UNISIM;
--use UNISIM.VComponents.all;

entity DeadTimeGen is
   Port ( SwitchingSig : in  STD_LOGIC;
          DeadTime : in  std_logic_vector (5 downto 0);
          SwitchingSigHigh : out  STD_LOGIC;
          SwitchingSigLow : out  STD_LOGIC;
                                   Clock: in std_logic);
end DeadTimeGen;

architecture Behavioral of DeadTimeGen is
begin
          process(Clock)
          variable shiftreg: unsigned(63 downto
0):="0000000000000000000000000000000000000000000000000000000000000000";
          variable DelayedSig: std_logic;
          --variable DeadTimeNot: unsigned (5 downto 0);
          begin
            if rising_edge(Clock) then
                      shiftreg:=shiftreg(62 downto 0) & SwitchingSig;
                              --DeadTimeNot:=not(DeadTime);
                              case DeadTime is
                               when "000000" =>DelayedSig:=SwitchingSig;
                               when "000001" =>DelayedSig:=shiftreg(1);
                               when "000010" =>DelayedSig:=shiftreg(2);
                               when "000011" =>DelayedSig:=shiftreg(3);
                               when "000100" =>DelayedSig:=shiftreg(4);
                               when "000101" =>DelayedSig:=shiftreg(5);
                               when "000110" =>DelayedSig:=shiftreg(6);
                               when "000111" =>DelayedSig:=shiftreg(7);
                               when "001000" =>DelayedSig:=shiftreg(8);
                               when "001001" =>DelayedSig:=shiftreg(9);
                               when "001010" =>DelayedSig:=shiftreg(10);
                               when "001011" =>DelayedSig:=shiftreg(11);
                               when "001100" =>DelayedSig:=shiftreg(12);
                               when "001101" =>DelayedSig:=shiftreg(13);
                               when "001110" =>DelayedSig:=shiftreg(14);
                               when "001111" =>DelayedSig:=shiftreg(15);
                               when "010000" =>DelayedSig:=shiftreg(16);
                               when "010001" =>DelayedSig:=shiftreg(17);
                               when "010010" =>DelayedSig:=shiftreg(18);
                               when "010011" =>DelayedSig:=shiftreg(19);
                               when "010100" =>DelayedSig:=shiftreg(20);
                               when "010101" =>DelayedSig:=shiftreg(21);
                               when "010110" =>DelayedSig:=shiftreg(22);
                               when "010111" =>DelayedSig:=shiftreg(23);
                               when "011000" =>DelayedSig:=shiftreg(24);
                               when "011001" =>DelayedSig:=shiftreg(25);
                               when "011010" =>DelayedSig:=shiftreg(26);
```

```
                         when "011011" =>DelayedSig:=shiftreg(27);
                         when "011100" =>DelayedSig:=shiftreg(28);
                         when "011101" =>DelayedSig:=shiftreg(29);
                         when "011110" =>DelayedSig:=shiftreg(30);
                         when "011111" =>DelayedSig:=shiftreg(31);
                         when "100000" =>DelayedSig:=shiftreg(32);
                         when "100001" =>DelayedSig:=shiftreg(33);
                         when "100010" =>DelayedSig:=shiftreg(34);
                         when "100011" =>DelayedSig:=shiftreg(35);
                         when "100100" =>DelayedSig:=shiftreg(36);
                         when "100101" =>DelayedSig:=shiftreg(37);
                         when "100110" =>DelayedSig:=shiftreg(38);
                         when "100111" =>DelayedSig:=shiftreg(39);
                         when "101000" =>DelayedSig:=shiftreg(40);
                         when "101001" =>DelayedSig:=shiftreg(41);
                         when "101010" =>DelayedSig:=shiftreg(42);
                         when "101011" =>DelayedSig:=shiftreg(43);
                         when "101100" =>DelayedSig:=shiftreg(44);
                         when "101101" =>DelayedSig:=shiftreg(45);
                         when "101110" =>DelayedSig:=shiftreg(46);
                         when "101111" =>DelayedSig:=shiftreg(47);
                         when "110000" =>DelayedSig:=shiftreg(48);
                         when "110001" =>DelayedSig:=shiftreg(49);
                         when "110010" =>DelayedSig:=shiftreg(50);
                         when "110011" =>DelayedSig:=shiftreg(51);
                         when "110100" =>DelayedSig:=shiftreg(52);
                         when "110101" =>DelayedSig:=shiftreg(53);
                         when "110110" =>DelayedSig:=shiftreg(54);
                         when "110111" =>DelayedSig:=shiftreg(55);
                         when "111000" =>DelayedSig:=shiftreg(56);
                         when "111001" =>DelayedSig:=shiftreg(57);
                         when "111010" =>DelayedSig:=shiftreg(58);
                         when "111011" =>DelayedSig:=shiftreg(59);
                         when "111100" =>DelayedSig:=shiftreg(60);
                         when "111101" =>DelayedSig:=shiftreg(61);
                         when "111110" =>DelayedSig:=shiftreg(62);
                         when "111111" =>DelayedSig:=shiftreg(63);


                         when others =>
                          null;
                        end case;
                        SwitchingSigHigh<=SwitchingSig and DelayedSig;
                        SwitchingSigLow<=(not(SwitchingSig) and not(DelayedSig));
                end if;
        end process;

end Behavioral;
```